

Journal of Energy

ISSN 1849-0751 (On-line)
ISSN 0013-7448 (Print)
UDK 621.31

VOLUME 66 Number 1–4 | 2017 Special Issue

- 04** J. Konjevod, S. Krajcar, P. Ilak
The real-time coordination of a wind-hydro power generation
- 18** T. Baškarad, I. Kuzle, S. Tešnjak
Nonlinear mathematical model of hydroelectric power plant
- 40** B. Jurišić, L. Bučar, I. Uglešić
Calculation of voltage distribution along the transformer winding using the wide band transformer model
- 52** A. Drandić, A. Marušić, M. Drandić, J. Havelka
Power system neutral point grounding
- 69** M. Krpan, I. Kuzle
The mathematical model of a wind power plant and a gas power plant
- 87** M. Pongrašić, Ž. Tomšić
Cost-benefit analysis of smart grids projects implementation
- 99** J. Đaković, D. Grgić
Analysis of spent fuel pool loss of coolant inventory accident progression
- 108** K. Pandžić, A. Marušić
SMV to COMTRADE data conversion
- 117** M. Pikutić, G. Grdenić, M. Delimar
Comparison of results and calculation speeds of various power system power flow methods
- 128** S. Raos, Ž. Tomšić, I. Rajšl
The role of pumped-hydro storage power plants and large penetration of electric cars to increase the flexibility of the system with a large share of renewable energy sources
- 150** I. Pavić, T. Capuder, I. Kuzle
Generation scheduling in power systems with high penetration of renewable energy
- 165** A. Stošić, A. Marušić, J. Havelka
Transmission lines protection using SIPROTEC numerical relays
- 184** G. Grdenić, Ž. Tomšić
Renewable energy sources and other energy technologies as a measure for mitigating the impact of urban heat islands
- 195** M. Gržanić, M. Delimar, T. Capuder
Financial transmission and storage rights
- 226** B. Pošta, S. Šadek
Mathematical model of the NPP Krško PCFV system for the RELAP5 computer code
- 241** N. Holjevac, C. Soares, I. Kuzle
Short-term power system hourly load forecasting using artificial neural networks

Published by

HEP d.d., Ulica grada Vukovara 37, HR-10000 Zagreb

HRO CIGRÉ, Berislavićeva 6, HR-10000 Zagreb

Publishing Board

Robert Krklec, (president) HEP, Croatia,

Božidar Filipović-Grčić, (vicepresident), HRO CIGRÉ, Croatia

Editor-in-Chief

Goran Slipac, HEP, Croatia

Associate Editors

Helena Božić HEP, Croatia

Stjepan Car Končar-Electrical Engineering Institute, Croatia

Tomislav Gelo University of Zagreb, Croatia

Davor Grgić University of Zagreb, Croatia

Mićo Klepo Croatian Energy Regulatory Agency, Croatia

Stevo Kolundžić Croatia

Vitomir Komen HEP, Croatia

Marija Šiško Kuliš HEP, Croatia

Dražen Lončar University of Zagreb, Croatia

Goran Majstrovic Energy Institute Hrvoje Požar, Croatia

Tomislav Plavšić Croatian Transmission system Operator, Croatia

Dubravko Sabolić Croatian Transmission system Operator, Croatia

Mladen Zeljko Energy Institute Hrvoje Požar, Croatia

International Editorial Council

Anastasios Bakirtzis University of Thessaloniki, Greece

Eraldo Banovac J.J. Strossmayer University of Osijek, Croatia

Franjo Barbir University of Split, Croatia

Tomislav Barić J.J. Strossmayer University of Osijek, Croatia

Frank Bezzina University of Malta

Srećko Bojić Power System Institute, Zagreb, Croatia

Tomislav Capuder University of Zagreb, Croatia

Ante Elez Končar-Generators and Motors, Croatia

Dubravko Franković University of Rijeka, Croatia

Hrvoje Glavaš J.J. Strossmayer University of Osijek, Croatia

Mevludin Glavić University of Liege, Belgium

Božidar Filipović Grčić University of Zagreb, Croatia

Dalibor Filipović Grčić Končar-Electrical Engineering Institute, Croatia

Josep M. Guerrero Aalborg Universitet, Aalborg East, Denmark

Juraj Havelka University of Zagreb, Croatia

Dirk Van Hertem KU Leuven, Faculty of Engineering, Belgium

Žarko Janić Siemens-Končar-Power Transformers, Croatia

Igor Kuzle University of Zagreb, Croatia

Niko Malbaša Ekoner, Croatia

Matislav Majstrovic University of Split, Croatia

Zlatko Maljković University of Zagreb, Croatia

Predrag Marić J.J. Strossmayer University of Osijek, Croatia

Viktor Milardić University of Zagreb, Croatia

Srete Nikolovski J.J. Strossmayer University of Osijek, Croatia

Damir Novosel Quanta Technology, Raleigh, USA

Hrvoje Pandžić University of Zagreb, Croatia

Milutin Pavlica Power System Institute, Zagreb, Croatia

Robert Sitar Končar-Electrical Engineering Institute, Croatia

Damir Sumina University of Zagreb, Croatia

Elis Sutlović University of Split, Croatia

Zdenko Šimić Joint Research Centre, Petten, The Netherlands

Damir Šljivac J.J. Strossmayer University of Osijek Croatia

Darko Tipurić University of Zagreb, Croatia

Bojan Trkulja University of Zagreb, Croatia

Nela Vlahinić Lenz University of Split, Croatia

Mario Vražić University of Zagreb, Croatia

INTRODUCTION

This special issue of the Journal of Energy is dedicated to the selected graduation thesis on Graduate study programme, profile »Electrical Power Engineering« prepared at the **Department for Energy and Power Systems (ZVNE)**, University of Zagreb Faculty of Electrical Engineering and Computing in last five years (2013. to 2017.). In these five years at ZVNE were defended 169 diploma thesis (masters in engineering) and 282 BSc Thesis (bachelors).

The articles were created in wide cooperation between former students and mentors based on graduation thesis prepared by students and showing the main results of the graduation thesis. Table shows besides paper title and authors also graduated engineer thesis (FER2) number; graduation thesis title in English and original title in Croatian; date of defence and mentor(s) of graduated engineer thesis.

Journal of Energy Special issue 2017 presents **16 papers** selected for publication in Journal of Energy after having undergone the peer review process. I would like to thank the authors for their contributions and the reviewers who dedicated their valuable time in selecting and reviewing these papers. We hope this special issue will provide you valuable information of some student's achievements in preparing graduation thesis at Department of Energy and Power Systems, Faculty of Electrical Engineering and Computing.

1. Short introduction of the Master of Science programs of Electrical Engineering and Information Technology and the profile Electrical Power Engineering

1.1. Master of Science programs at FER

Admission to the Master of Science programs at FER is open to persons holding the bachelor degree in electrical engineering and information technology, in computing and in electrical engineering or other related bachelor degree. To follow this program, first cycle study programs at other faculties or universities, in technical and natural sciences or similar fields, are completely or partially sufficient.

1.2. Electrical Engineering and Information Technology study program

Nowadays, it is almost impossible to come across an activity within electrical engineering that is not interconnected with information technology. Thus, these areas have been joined into the second cycle study program of Electrical engineering and information technology. This program enables a student to acquire the competencies to solve difficult engineering problems, to design complex systems, to act as a leader of a team and to conduct research and development in one of five profiles.

Within the study program, a student immediately decides for a profile. One of profile is »**Electrical Power Engineering**«.

1.3. Electrical Power Engineering profile

Electrical Power Engineering is a professional and scientific field of electrical engineering and power systems. It studies and promotes areas of power generation, transmission and distribution of electric energy as well as electric usage and energy management.

By studying power systems engineering, students gain knowledge of fundamentals and applications of electrical power engineering in a wide range of topics: theory of power systems control; optimization methods applied to power systems; energy efficiency methods; reactive power control; electric facilities automation; reliability theory; expert systems; environmental protection; efficient use of energy and energy conservation; economic analysis; disturbances and transient phenomena in power systems; power system protection; transmission and distribution networks network planning; development, stability, availability, reliability and operational safety of electric power system subsystems; mathematical modelling of power plants components and subsystems; deterministic and reliability analysis of operational safety; development modelling and analysis of environmental impact of electric power systems; establishment of open market environment, risk management and electrical energy trading; economy modelling, business and human resources management, microeconomics, marketing, etc.

Besides education, research is a crucial factor determining the power systems engineering progress with emphasis on the development of new power system technologies.

1.3.1. The graduation thesis

The graduation thesis is a comprehensive and highly independent task where the student has to demonstrate the ability to analyse the given problem from theoretical and practical aspects, devise a solution using the knowledge acquired in multiple courses and literature, implement the solution, write the documentation and instructions for use and/or for further work, to present his or her work in written and oral form. The accent is

given on demonstration of ability in all these aspects rather than to force students to pursue some work intensive repetitive activities in order to fully complete a product.

Students are to achieve self confidence in their acquired knowledge, ability to additionally consult the mandatory or supplementary textbooks, consult the advisor with well-structured and prepared questions and, in most cases, devise a practical solution of moderate but representative functionality. Last, but not least, they have to present it in a written form, formally, linguistically and ethically correct, prepared on computer, according to instructions, of the average overall size of 30

single spaced A4 pages, what raises their awareness of importance of this ability. Computer prepared transparencies and a 10 minutes oral presentation both serve to train the students how to present their work to specific audience within a given time frame.

Guest Editor

prof. dr. sc. Željko Tomšić

Department of Energy and Power Systems

University of Zagreb Faculty of Electrical Engineering and Computing

Table

Papers based on selected graduation engineer thesis on profile »Electrical Power Engineering« at the Department for Energy and Power Systems (ZVNE) in last five years (2013.-2017.)

	Paper title	Authors	Graduated Engineer Thesis (FER2) number:	Graduation Thesis TITLE (Original Title in Croatian) Date of defence	Mentor(s)
1	THE REAL-TIME COORDINATION OF A WIND-HYDRO POWER GENERATION	Jure Konjevod; Slavko Krajcar; Perica Ilak	Graduated Engineer Thesis (FER2) number: 1367	The real-time coordination of a wind-hydro power generation (Koodinirani rad u stvarnom vremenu vjetrene i hidroelektrane) July 2016	Slavko Krajcar
2	NONLINEAR MATHEMATICAL MODEL OF HYDROELECTRIC POWER PLANT	Tomislav Baškarad, Igor Kuzle, Sejid Tešnjak	Graduated Engineer Thesis (FER2) number: 1231	Nonlinear mathematical control systems in Hydroelectrical Power Plants (Nelinearni matematički modeli regulacijskih sustava u hidroelektrani) July 2017	Sejid Tešnjak
3	CALCULATION OF VOLTAGE DISTRIBUTION ALONG THE TRANSFORMER WINDING USING THE WIDE BAND TRANSFORMER MODEL	Bruno Jurišić; Luka Bučar; Ivo Uglešić	Graduated Engineer Thesis (FER2) number: 1599.	Transformer models for calculation of high frequency transmitted over-voltages (Model transformatora za proračun prenesenih prenapona visokih frekvencija) June 2017	Ivo Uglešić
4	POWER SYSTEM NEUTRAL POINT GROUNDING	Ana Drandić; Ante Marušić; Marino Drandić; Juraj Havelka	Graduated Engineer Thesis (FER2) number: 967	Power system neutral point grounding (Uzemljenje neutralne točke razdjelne mreže) July 2014	Ante Marušić
5	THE MATHEMATICAL MODEL OF A WIND POWER PLANT AND A GAS POWER PLANT	Matej Krpan; Igor Kuzle	Graduated Engineer Thesis (FER2) number: 1330	The mathematical model of a wind power plant and a gas power plant (Matematički model vjetroelektrane i plinske elektrane) September 2016	Igor Kuzle
6	COST-BENEFIT ANALYSIS OF SMART GRIDS PROJECTS IMPLEMENTATION	Marijana Pongračić; Željko Tomšić	Graduated Engineer Thesis (FER2) number: 1017	Economic analysis of benefits and costs of implementing smart systems in electricity transmission and distribution systems (Ekonomska analiza dobiti i troškova implementaciji naprednih sustava u prijenosu i distribuciji) July 2014	Željko Tomšić
7	ANALYSIS OF SPENT FUEL POOL LOSS OF COOLANT INVENTORY ACCIDENT PROGRESSION	Josip Đaković; Davor Grgić	Graduated Engineer Thesis (FER2) number: 1552	Mitigation of Spent Fuel Pool Loss of Coolant Inventory Accidents Using Spray Nozzles (Ograničavanje posljedica akcidenta gubitka hladioca iz bazena za istrošeno gorivo korištenjem sprej mlaznica) July 2017	Davor Grgić
8	SMV TO COMTRADE DATA CONVERSION	Kristina Pandžić; Ante Marušić	Graduated Engineer Thesis (FER2) number: 965	SMV to COMTRADE data conversion (Konverzija podataka iz SMV u COMTRADE format) July 2014.	Ante Marušić
9	COMPARISON OF RESULTS AND CALCULATION SPEEDS OF VARIOUS POWER SYSTEM POWER FLOW METHODS	Marko Pikutić; Goran Grdenić; Marko Delimar	Graduated Engineer Thesis (FER2) number: 1435	Comparison of results and calculation speeds of various power system power flow methods (Usporedba rješenja i brzine izvođenja različitih metoda za proračun tokova snaga u elektroenergetskim mrežama) February 2017	Marko Delimar
10	THE ROLE OF PUMPED-HYDRO STORAGE POWER PLANTS AND LARGE PENETRATION OF ELECTRIC CARS TO INCREASE THE FLEXIBILITY OF THE SYSTEM WITH A LARGE SHARE OF RENEWABLE ENERGY SOURCES	Sara Raos; Željko Tomšić; Ivan Rajšl	Graduated Engineer Thesis (FER2) number: 1594	The role of pumped-hydro storage power plants and large penetration of electric cars to increase the flexibility of the system with a large share of renewable energy sources (Uloga velike penetracije elektroautomobila u povećanju fleksibilnosti sustava s velikim udjelom obnovljivih izvora) September 2017.	Željko Tomšić; Ivan Rajšl
11	GENERATION SCHEDULING IN POWER SYSTEMS WITH HIGH PENETRATION OF RENEWABLE ENERGY	Ivan Pavić; Tomislav Capuder; Igor Kuzle	Graduated Engineer Thesis (FER2) number: 944	Generation scheduling in power systems with high penetration of renewable energy (Raspodjela opterećenja na agregate u elektroenergetskom sustavu s velikim udjelom obnovljivih izvora energije) July 2014	Igor Kuzle
12	TRANSMISSION LINES PROTECTION USING SIPROTEC NUMERICAL RELAYS	Andrea Stošić; Ante Marušić; Juraj Havelka	Graduated Engineer Thesis (FER2) number: 1082	Transmission lines protection using Siprotec numerical relays, (Zaštita prijenosnih vodova pomoću numeričke zaštite serije Siprotec) February 2015.	Ante Marušić
13	RENEWABLE ENERGY SOURCES AND OTHER ENERGY TECHNOLOGIES AS A MEASURE FOR MITIGATING THE IMPACT OF URBAN HEAT ISLANDS	Goran Grdenić; Željko Tomšić	Graduated Engineer Thesis (FER2) number: 1016	Renewable energy and other energy technologies as a measure for reducing the impact of urban heat islands (Obnovljivi izvori energije i druge energetske tehnologije kao mjera za smanjivanje utjecaja gradskih toplinskih otoka) July 2014.	Željko Tomšić
14	FINANCIAL TRANSMISSION AND STORAGE RIGHTS	Mirna Gržanić; Marko Delimar; Tomislav Capuder	Graduated Engineer Thesis (FER2) number: 1324	Financial Transmission and Storage Rights (Financijska prava u prijenosnoj mreži) September 2016	Marko Delimar
14	MATHEMATICAL MODEL OF THE NPP KRŠKO PCFV SYSTEM FOR THE RELAP5 COMPUTER CODE	Borna Pošta; Siniša Šadek	Baccalaureus Thesis number: 5025	The RELAP5 Computational Model of the PCFV System for the NPP Krško (Matematički model PCFV sustava NE Krško za program RELAP5) July 2017	Siniša Šadek
16	SHORT-TERM POWER SYSTEM HOURLY LOAD FORECASTING USING ARTIFICIAL NEURAL NETWORKS	Ninoslav Holjevac; Catarina Isabel Nunes Soares; Igor Kuzle	Erasmus student Seminar work, Electric Power System Operation and Planning course	Artificial Neural Network Based Short Term Load Forecasting, ac. year 2016/17 summer semester	Igor Kuzle

JURE KONJEVOD SLAVKO KRAJCAR PERICA ILAK
jure.konjevod@fer.hr slavko.krajcar@fer.hr perica-ilak@fer.hr

**University of Zagreb Faculty of Electrical Engineering and
Computing**

THE REAL-TIME COORDINATION OF A WIND-HYDRO POWER GENERATION

SUMMARY

This paper introduces the real-time coordination of the wind and hydro power plants in the case of a part of the Croatian Power System where hydro–wind coordination is represented by Vrataruša wind farm and Senj and Vinodol hydropower plants. The model uses real data which represent generation units that make the power system. Also, the paper describes the general problem which is specific for these type of energy sources. For modeling hydro-wind coordinated generation, the MATLAB/Simulink model is developed. Obtained results, rotor speed, an active and reactive power of wind power plant, voltages, rotor speed, rotor speed deviation, active output power, and stator current of a hydroelectric generator are presented and analyzed.

Keywords: excitation voltage, hydropower plant, output power, rotor speed, wind-hydropower generation system

1. NOMENCLATURE

P	<i>Active power</i>
P_{max}	<i>Total capacity of plant (MW)</i>
P_{eo}	<i>Output power of hydro turbine</i>
Q	<i>Reactive power</i>
Q_i	<i>Installed flow of plant (m³/s)</i>
ω_r	<i>Angular (rotation) speed of wind turbine</i>
ω_m	<i>Angular (rotation) speed of hydro turbine</i>
$d\omega_m$	<i>Angular (rotation) speed deviation of hydro turbine</i>

2. INTRODUCTION

Increasing popular hybrid systems (coordinate generation of two or more energy sources) is due to increased integration of renewable energy sources into existing power systems. Renewable energy technologies enable implementation of hybrid systems [2]. In this paper, we have analyzed a part of the Croatian power system which has a significant share of hydro and wind energy. A characteristic of Croatian power system is that more than a half of all energy sources are produced by hydropower plants [3]. Analyzed part of power system consists of two hydropower plants (HPP Vinodol and HPP Senj) and one wind power plant (WPP Vrataruša). HPP Vinodol is connected to 110 kV transmission grid via three power blocks "generator-transformer" and external switchgear. Total capacity of HPP is 94,5 MW (3 x 31,5 MW) with installed flow $Q_i=16,7$ m³/s. HPP Senj is diversion HPP with total capacity $P_{max}= 216$ MW (3 x 72 MW). Further, HPP Sklope is part of hydro-power system Senj and has $P_{max}= 22,5$ MW with installed flow $Q_i=45$ m³/s. WPP Vrataruša is the first WPP in Croatia which is connected to a transmission line. It has fourteen turbines with a nominal capacity of 3 MW each, having a total capacity of 42 MW. WPP Vrataruša is connected to the transformer station (TS) Crikvenica and HPP Vinodol on the one side, and to the HPP Senj on the other side. According to that, WPP is located between HPP Vinodol and HPP Senj and unavoidably affect their work [4]. The described part of the power system is shown in the Fig.1 (a) where in the Fig. 1 (b) the single pole scheme and the exact values of the analyzed power flows are shown. This example has been analyzed in this paper. Moreover, for simulating and analyzing all relevant parameters, of such a wind-hydro system, MATLAB/Simulink model is used.

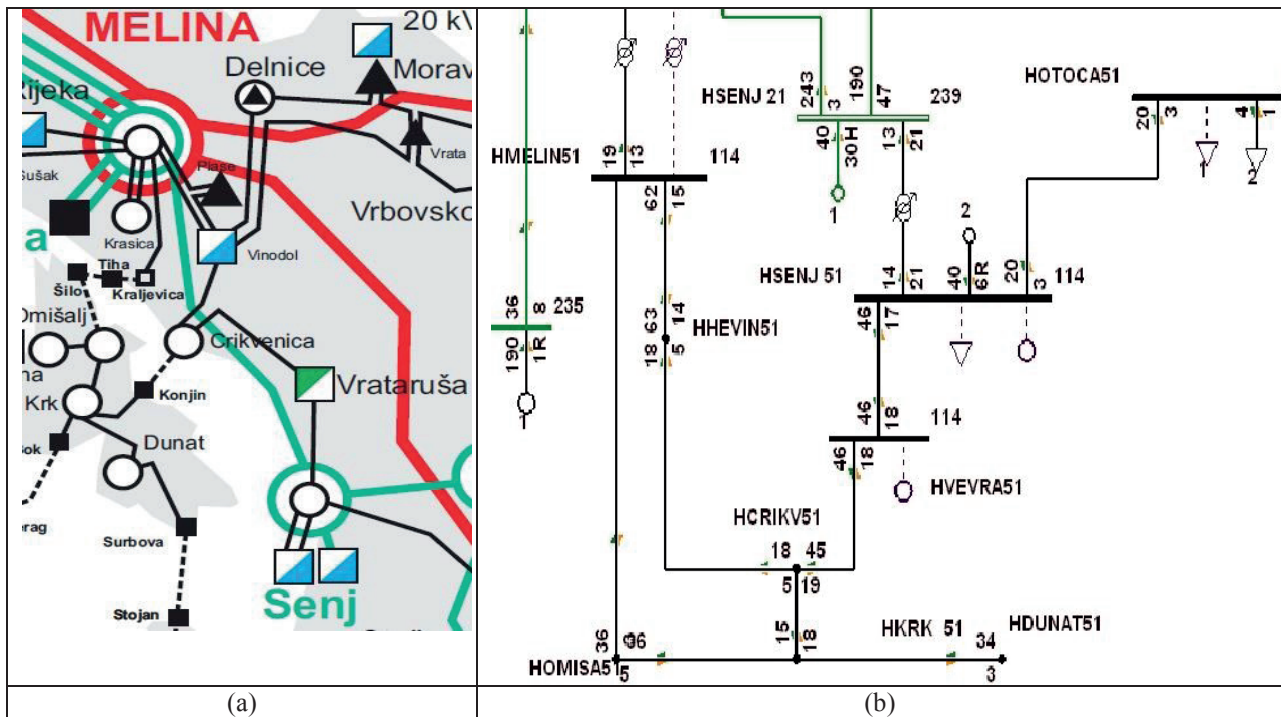


Figure 1. The: a) Analyzed part of the Croatian power system and b) the values of the power flows in the analyzed part of the grid in MW.

3. PROBLEM DESCRIPTION AND FORMULATION

3.1. Connecting wind power to the grid

Connecting wind power plants to the grid remains a significant problem as WPP can meaningfully influence on the system stability and quality of electrical energy (dynamical changes of voltage, i.e., flickers) [5]. Criteria of connecting are defined in the form of “Wind Grid Codes”. Since different types of wind generators are in use, there are also different types of “Wind Grid Codes”. The first one refers to connecting to the transmission system (nominal voltage 110 kV) and the second one refers to connecting to the distribution system (nominal voltage 35 or 20(10) kV).

3.2. Wind power plant grid work

“Problem of surplus wind” is possible to appear during WPP grid work. It is defined as wind energy repulsion for power which exceeds load minus baseload power plants (Figure 1).

Baseload power plants are, for example, nuclear power plants and run-of-the-river plants. Solution to the problem is on the level of international interconnection. When WPP is connected to the grid, the active power dependence of v^3 wind velocity. Since regulation of voltage, active and reactive power depends on operation and excitation of synchronous generator, wind generator represents energy source which causes voltage and power fluctuations in the grid. Also, wind speed is changeable. Wind predictability is a problem which can be reduced using improved wind forecast methods as well as wind turbine blade design and control.

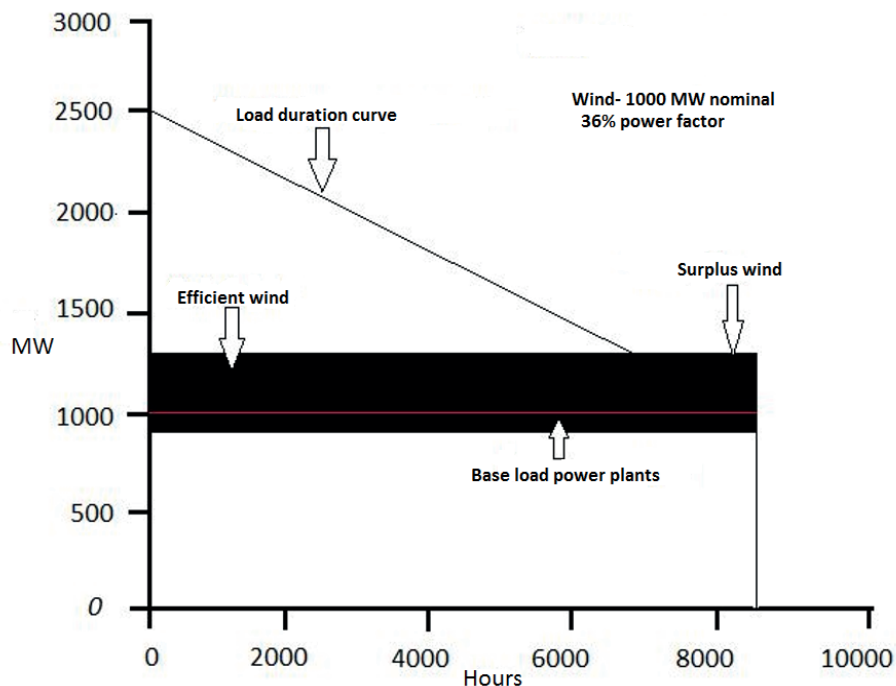


Figure 2. The depiction of load curve with a representation of “problem of surplus wind”

3.2. Hydro energy resources

It is possible to estimate hydro energy resources with knowing or estimation of flow duration curve and net head. There are three types of hydro energy resources: total (theoretical), technical and economically usable. Technical potential is a few times lower than total and about 30% greater than economic. Final usability is determined by ecological, economic and social factors [6].

3.3. Methodology

As mentioned before, for analyzing all relevant parameters the MATLAB/Simulink model is developed. The depiction of MATLAB/Simulink model is shown in the Fig. 3. In addition to that, it is important to say that transformer station 400/220/110 kV Melina, TS 110/20 kV Dunat and switchgear 110 kV Omišalj are considered as well as their mutual connection. Besides, it is modelled connection of HPP Senj to the TS 110/35 kV Otočac and HPP Sklope. All that units are modelled in that way to get a more realistic situation of the grid. Also, basic power flows data of each bus are used. In model are entered values for generation and consumption of active and reactive power of each bus.

Generally, in power flow calculation there are three types of buses: P-Q bus, P-V bus, and slack bus. For P-Q bus known values are active power P and reactive power Q [7]. In this model, P-Q buses are: Crikvenica, Melina, Omišalj, Krk, Dunat, and part of the grid on which HPP Senj is connected. Further, known values for P-V buses are voltage $|V|$ and active power P. Generation units, HPP Vinodol and HPP Senj, are modelled as P-V buses or slack buses what depends on the observed case. 42 MW wind farm is shaped using Doubly-Fed Induction Generator (DFIG). Simulation for the developed model is conducted under certain conditions. Thus, two different cases are analyzed and described in this paper. For hydroelectric generator are analyzed voltages, rotor speed, rotor speed deviation, active output

power and stator current and for wind power plant rotor speed, an active and reactive power.

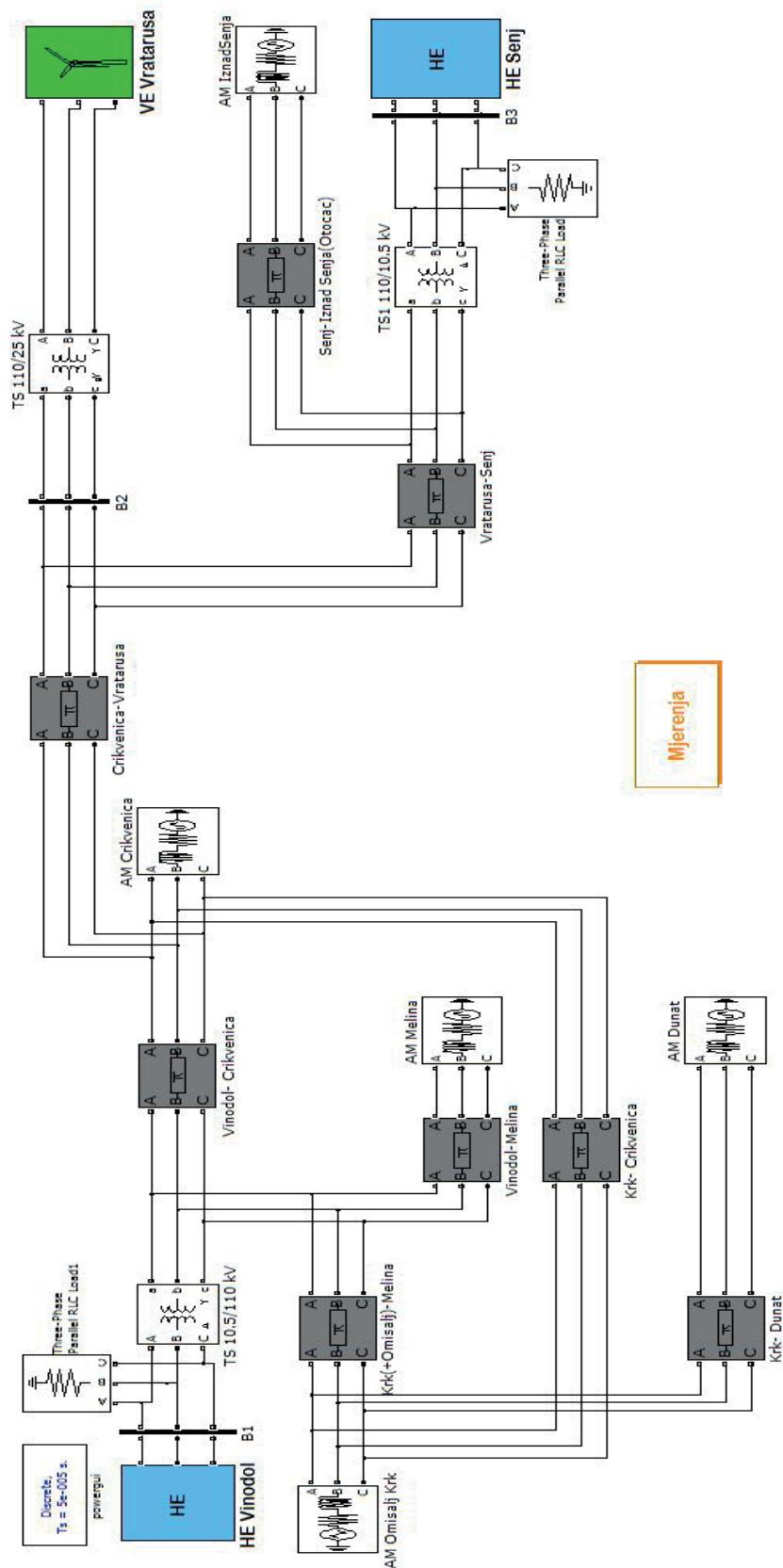


Figure 3. The depiction of the developed MATLAB/Simulink model

4. RESULTS AND DISCUSSION

In the first case, initial conditions are set via *Machine Initialization* block and *Powergui* tool. Further, it is defined that HPP Senj injects 200 MW active power into the grid, HPP Vinodol injects 90 MW, and WPP Vinodol injects 40 MW. In the second case, it is observed 3-phase short circuit which is located on the transmission line Vratarusa-Senj. Fault time is set to appear at 1,6 s of simulated time and has a duration of 0,1 s. Short circuit of three phases, generally, is shown in Figure 4.

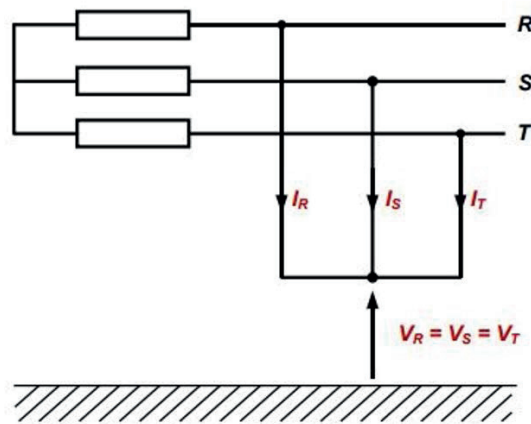


Figure 4. Three phase short circuit

Also, it is defined wind speed function using real data for one day in the year (Figure 5). The function is used in both analysed cases. After simulating the model, obtained results are shown in graphs. The angular speed of wind turbine in the first case (“normal” occasions without short circuit) is provided in Fig. 6 (a). The angular speed had a small collapse at that moment, but when fault elapsed, it came back to stable state (Fig. 6 (b)). Apparently, on both figures, angular speed reaches the steady value at 1,2 s of simulated time. Also, both functions are equal until the fault moment.

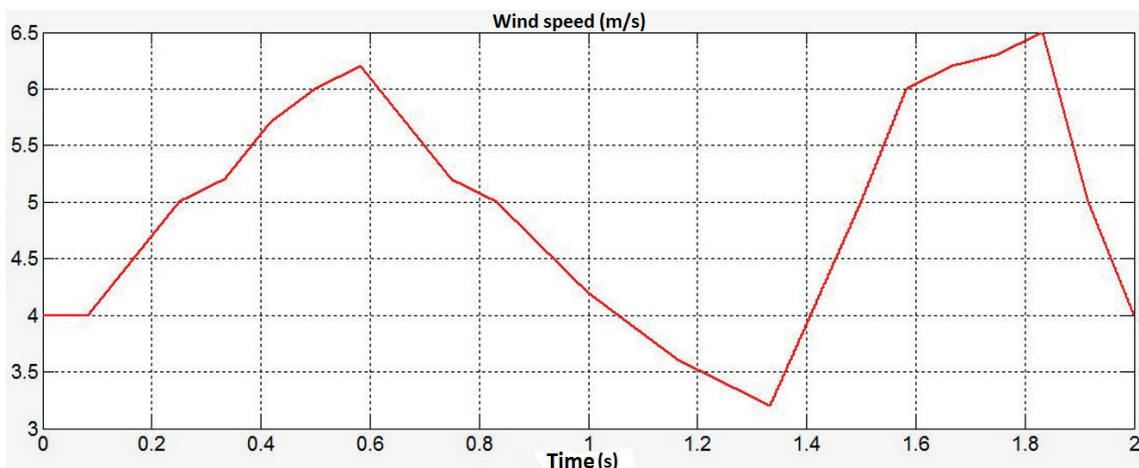


Figure 5. Wind speed function

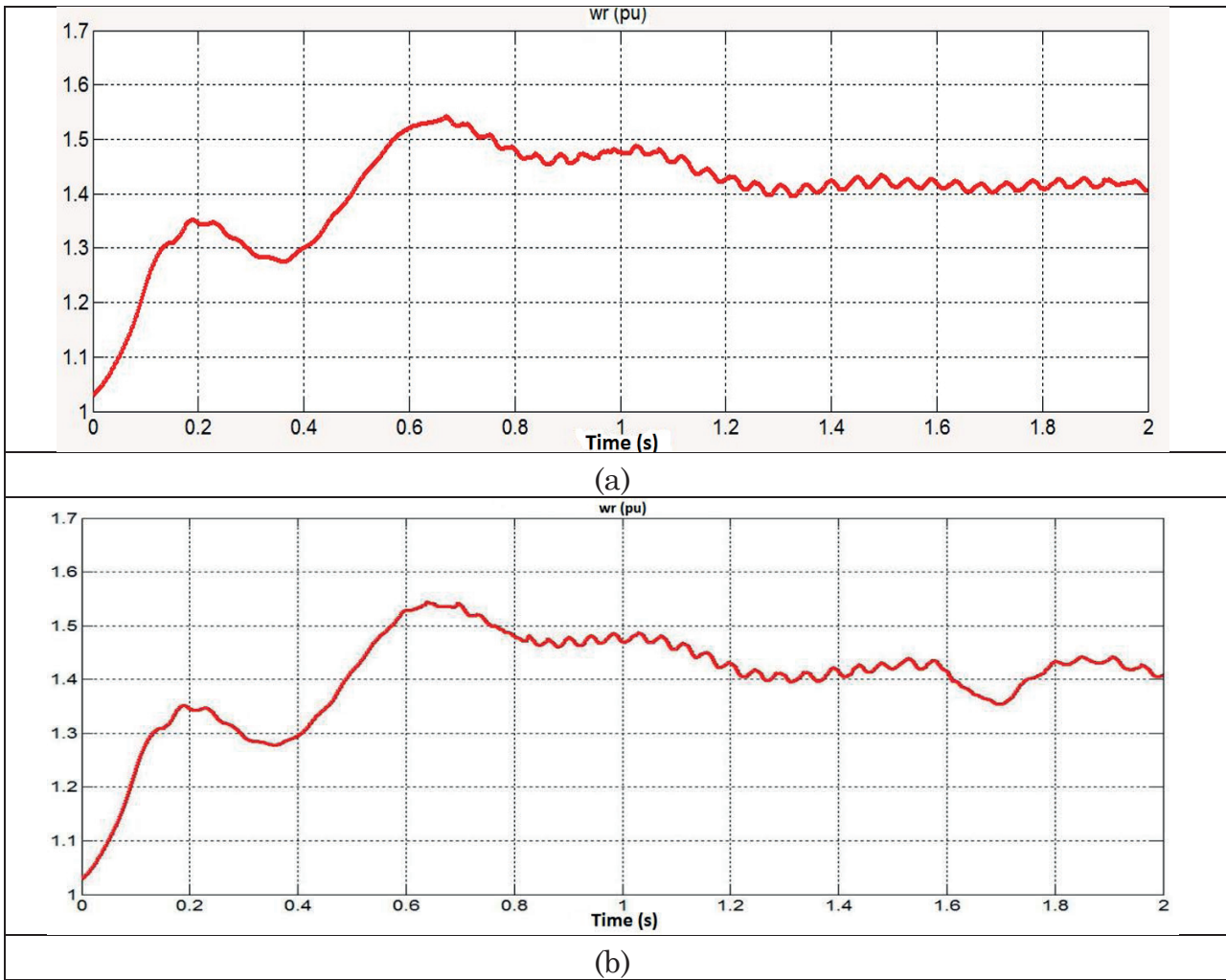


Figure 6. Angular (rotation) speed of wind turbine ω_r in the: a) first case; b) in the second case.

Dependence of angular speed and active power is visible in graphs in the Fig. 7 and Fig. 8. Larger change of angular speed affects larger change of active and reactive power. Noticeable difference in graphs of active and reactive power between two cases is during the fault time. During this period, wind power plant does not inject active power into the grid. Also, it is visible (Fig. 9 and Fig. 10) that reactive power of WPP is about 0 MVar during the fault.

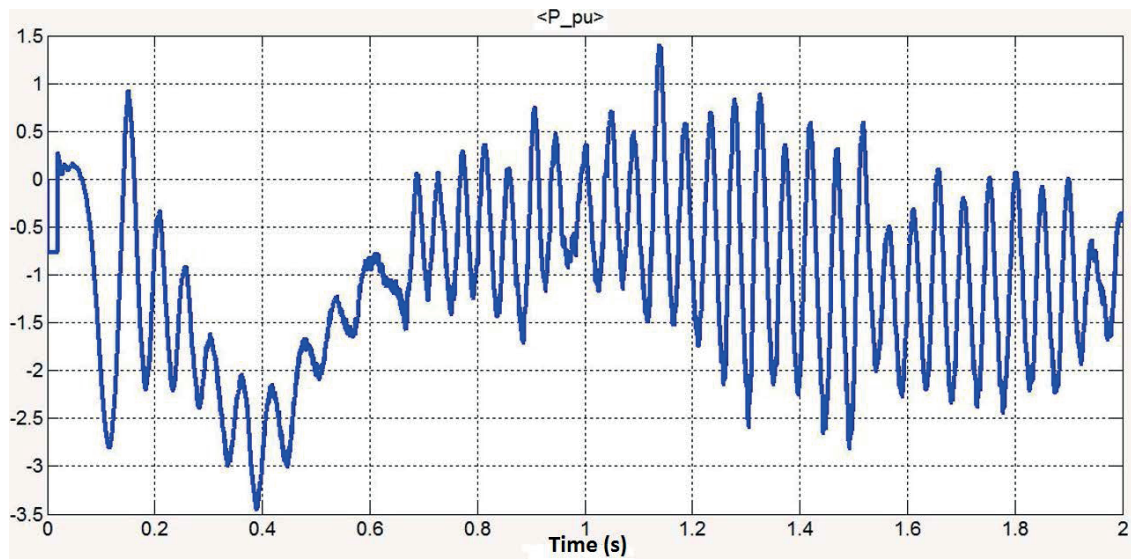


Figure 7. Active power of wind power plant in the first case

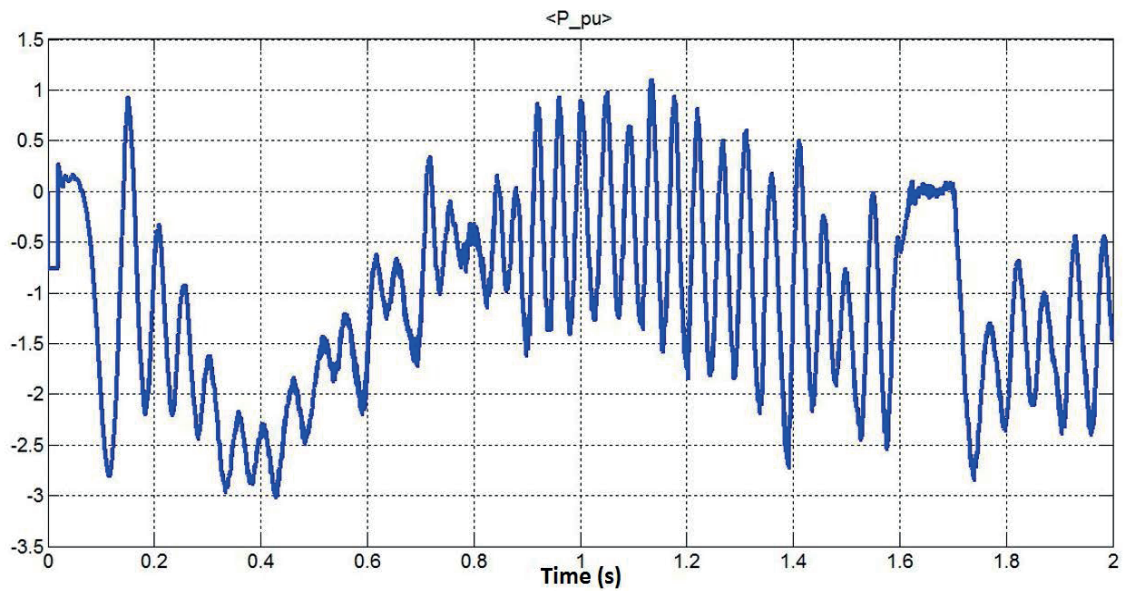


Figure 8. Active power of wind power plant in the second case

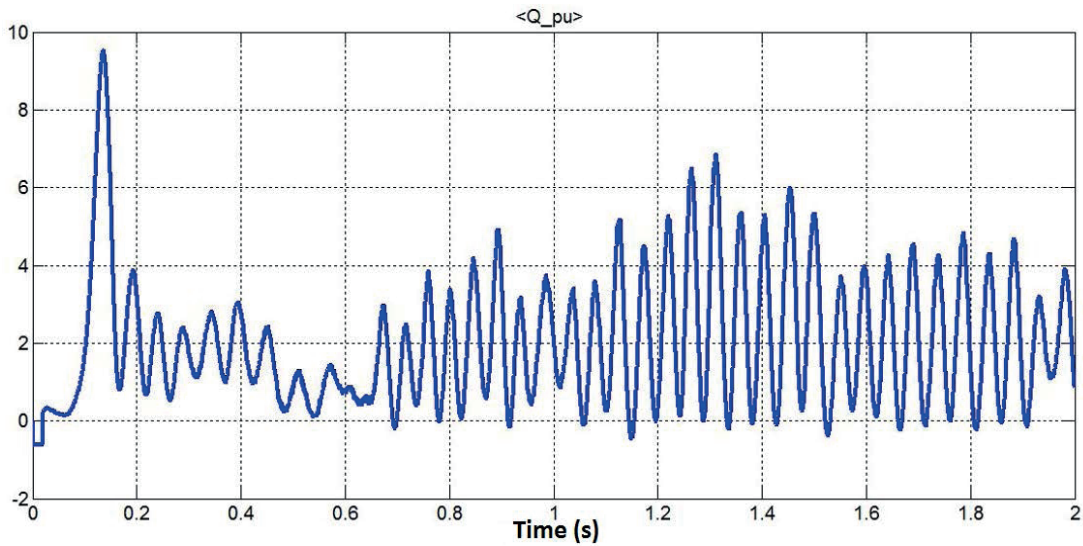


Figure 9. Reactive power of wind power plant in the first case

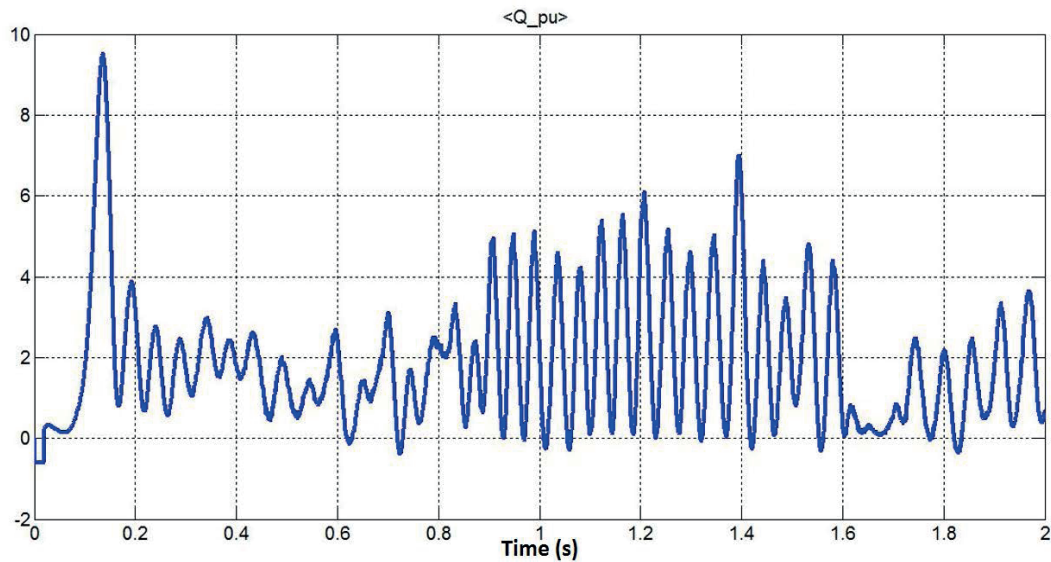


Figure 10. Reactive power of wind power plant in the second case

Excitation system provides generator voltage quality and reactive power. Also, it provides stable work of generator on the grid or in parallel work with other machines. Change of excitation voltage (Fig. 11) and reactive power of asynchronous wind generator (Fig. 10) are mutually connected. It is especially noticeable at 0,1 s when wind generator takes a large amount of reactive power for producing rotating magnetic field (peak of reactive power in Fig.10).

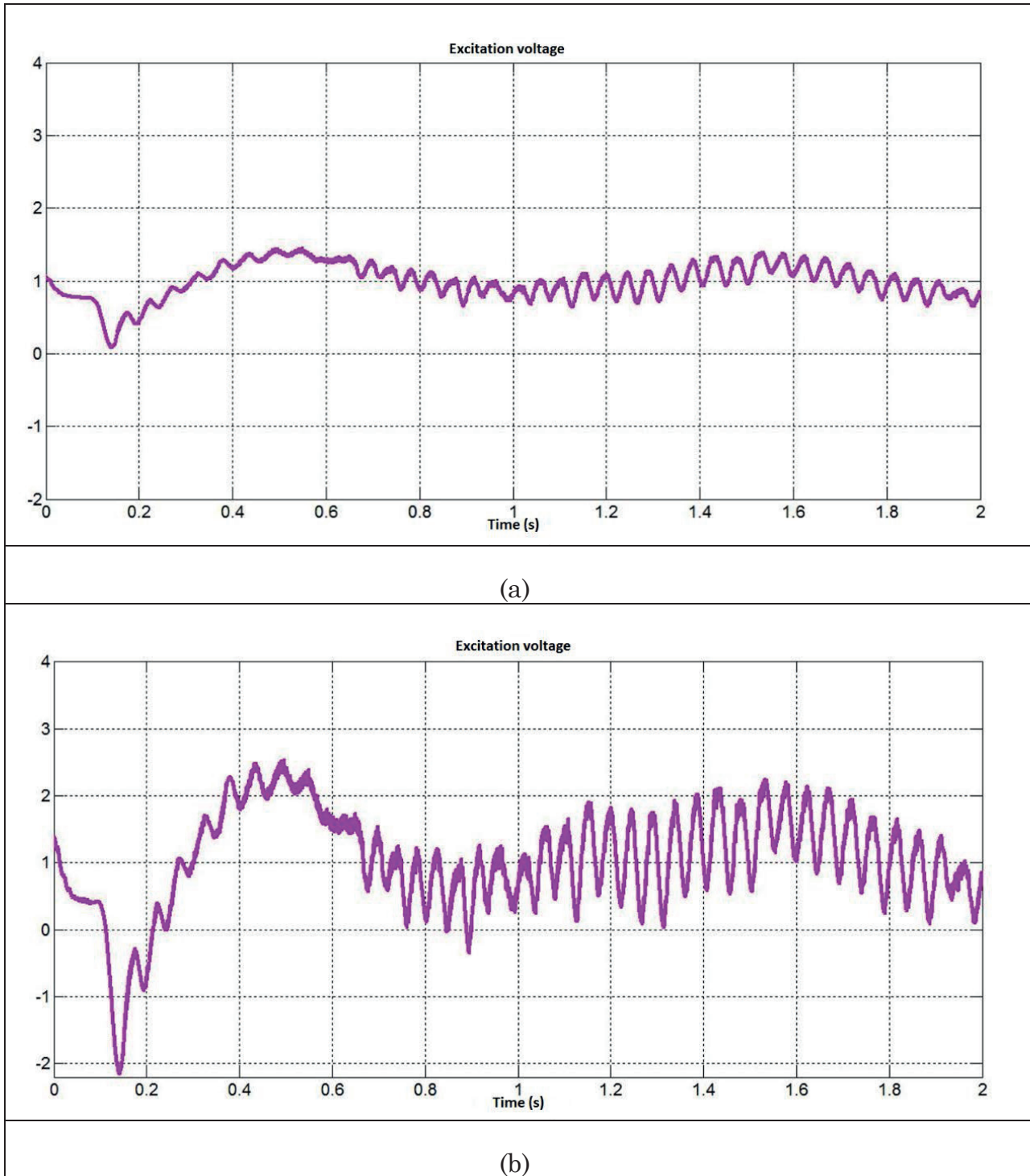


Figure 11. Excitation voltage of hydro power plants of tha: a) Vinodol and; b) Senj for the first case.

Also, on the graphs it is noticeable that excitation voltage of HPP Senj takes more oscillations than HPP Vinodol. It is important to mention that power of HPP Senj is 235 MVA and 105 MVA of HPP Vinodol. Thus, in parallel work, the load is proportional to the power of generators. Also, the connection of this wind-hydro system affects change of excitation voltage at 0,1 s because HPP Senj is directly connected to the WPP via transmission line Senj-Vratarusa. While HPP Vinodol is connected to the WPP with two transmission lines (Vinodol-Crikvenica and

Crikvenica-Vratarusa) and TS Crikvenica is located between that lines. When a fault occurs (Fig. 12), the growth of excitation voltages of synchronous generators is visible on graphs. During the fault time, values of excitation voltages reach the maximum upper limit. As mentioned before, excitation system is trying to provide a final voltage within the limits as it was during normal occasions without a short circuit.

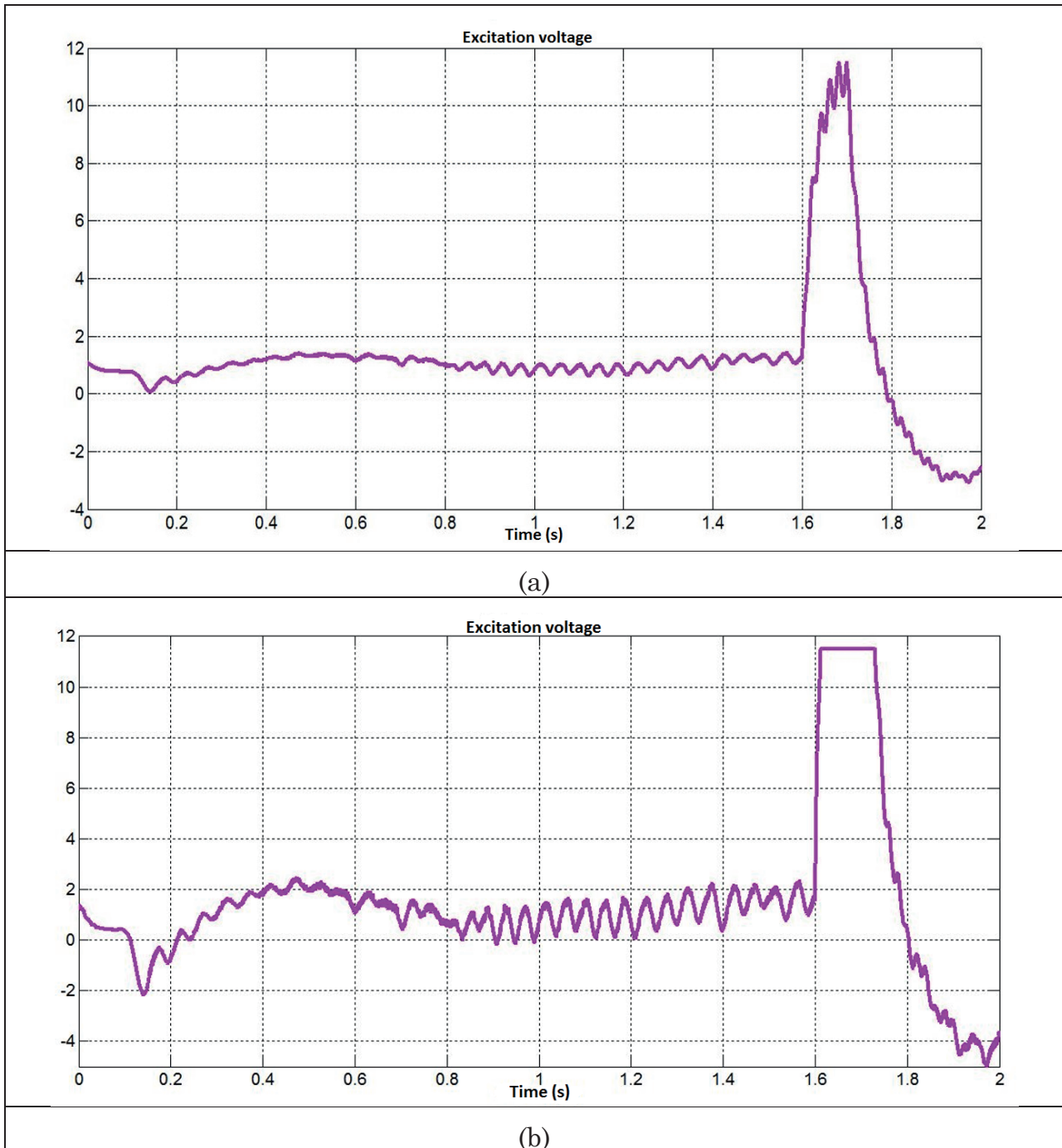


Figure 12. Excitation voltage of hydro power plants: a) Vinodol and; b) Senj for the second case

Angular speed has minimal changes until the fault occurs. When the fault occurs angular speed as well as its deviation has growth slightly and then collapse as noticeable in the graph in the Fig. 12. Angular speed affects output power of HPP which means that machine is trying to increase angular speed to compensate decreasing of output power. When a short circuit elapsed, output power increases slightly in relation to state before the fault had occurred (Fig. 13). That is the reason why angular speed gets a decrease. Parameters shown on graphs (Fig. 13) are related to HPP Senj. But functions for HPP Vinodol, which are not shown on graphs, has the same trend just with smaller oscillations. Causes of significant oscillations for HPP Senj are short circuit location, machine inertness and size of nominal power.

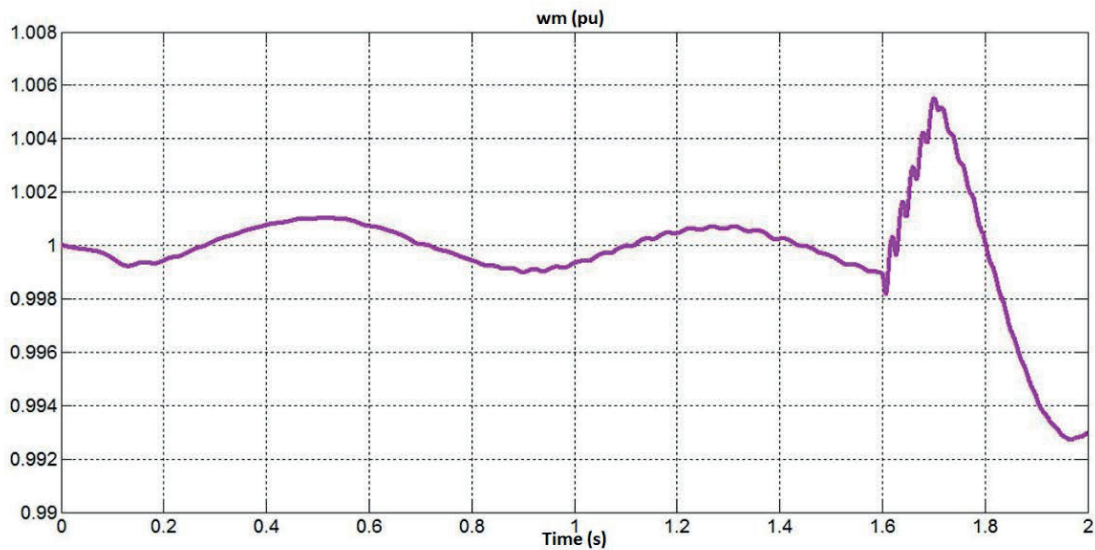


Figure 12. Angular (rotation) speed of hydro turbine for HPP Senj in the second case

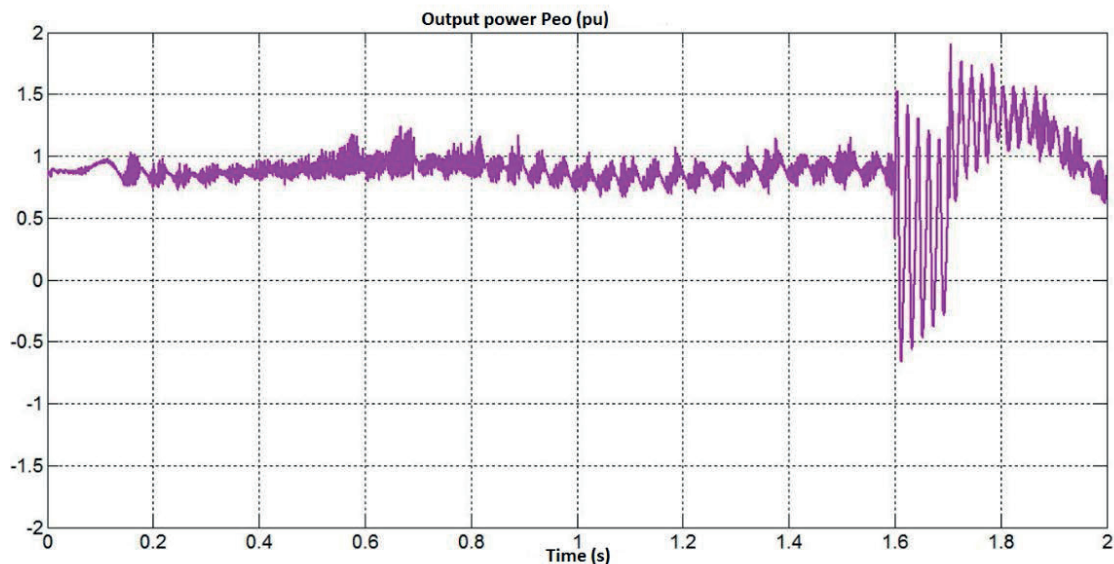


Figure 13. Output power of hydro turbine for HPP Senj in the second case

Three-phase stator current is shown in Fig. 14. Three single-phase alternating currents had sine waveform, equal amplitudes and separated by 120° until the fault occurs. Distortion is visible during the fault time. Three-phase stator current for HPP Vinodol has the same trend, but with smaller distortion. Since the HPP Senj is nearer the fault location, fault affects much more its generator rotation speed. Thus, fault affects rotating magnetic field which is produced by excitation winding. That rotating magnetic field acts via electromagnetic induction to induce a voltage in the armature windings of the stator. Further, the stator's output to the system is a three-phase alternating current (Fig. 14).

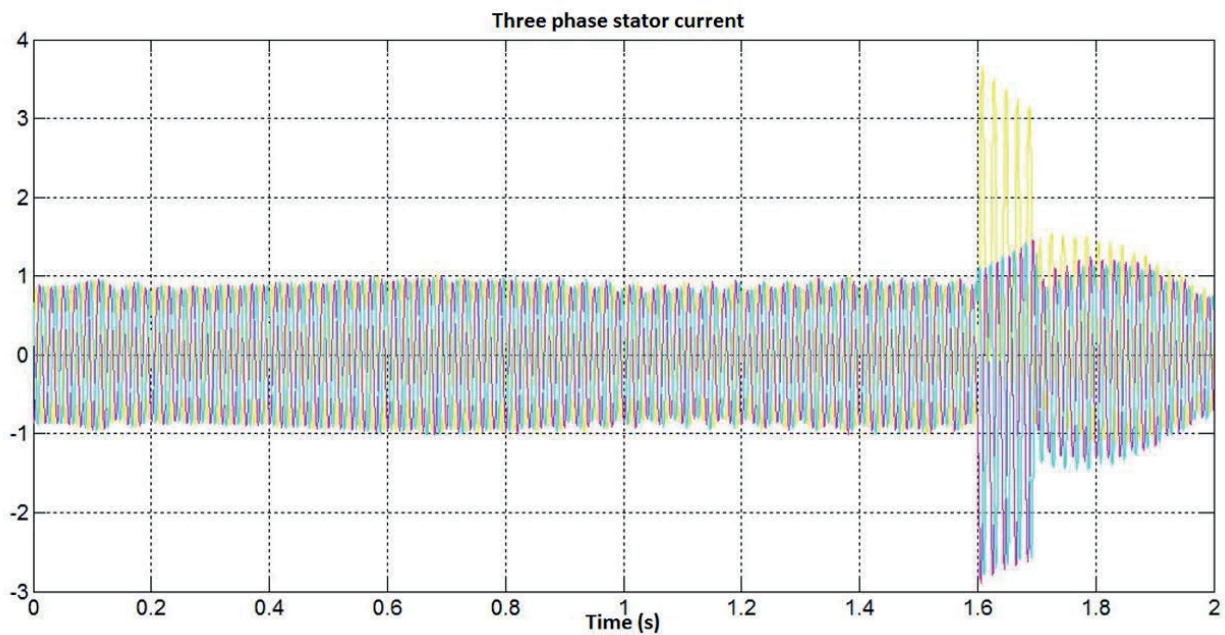


Figure 14. Three phase stator current of hydro generator for HPP Senj in the second case

5. CONCLUSION

After observing and analyzing modelled power system, it can be concluded that active output power of WPP is much more dependent on wind speed than on the load. Also, regulation of voltage, active and reactive power depends on operation and excitation of synchronous HPP generators. WPP is a fluctuating source of energy and causes voltage and power fluctuations as wind speed changes. It is necessary to install much more capacities on a wider area to improve the stability of this energy source. Besides, wind generator affects voltage increasing at the connection point of wind power plant to the grid. According to that, wind energy has a potential for more efficient use within hybrid wind-hydro systems. This can be implemented with storing wind energy when it is available and then supply the power to the grid if there is a demand. Energy storage in observed hybrid systems enables compensating those periods when there is no wind to fulfill market or grid obligations.

6. REFERENCES

- [1] Jure Konjevod, *Koordinirani rad u stvarnom vremenu vjetrene i hidroelektrane* (eng. *The Real-Time Coordination of a Wind-Hydro Power Generation*), Diplomski rad, Fakultet elektrotehnike i računarstva Sveučilište u Zagrebu, 2016. Mentor: S. Krajcar
- [2] K. Kumar, M. A. Ansari, *Design and Development of Hybrid Wind-Hydro Power Generation System*, *IEEEExplore*, 2013.
- [3] Osnovni podaci, Hrvatska Elektroprivreda, HEP-Proizvodnja, <http://proizvodnja.hep.hr/osnovni/hidroelektrane/default.aspx>, 2016.
- [4] Shema EES-a, Hrvatski operator prijenosnog sustava-HOPS, <https://www.hops.hr/wps/portal/hr/web/hees/podaci/shema>, 2016.
- [5] M. Lasic, D. Škrlec, *Influence of variable-speed wind turbine on voltage quality*, Konferencija HO CIRED, Šibenik, Croatia, 2008.
- [6] D. Šljivac, Z. Šimić, *Obnovljivi izvori energije - vrste, potencijal i tehnologija*, DOOR, Zagreb, 2009.
- [7] I. Pavić, M. Delimar, *Predavanje 5: Proračun tokova snaga*, Predmet - Analiza EES-a, predavanja FER 2015.

TOMISLAV BAŠKARAD

tomislav.baskarad@fer.hr

IGOR KUZLE

igor.kuzle@fer.hr

SEJID TEŠNJAK

sejid.tesnjak@fer.hr

**University of Zagreb Faculty of Electrical Engineering and
Computing**

NONLINEAR MATHEMATICAL MODEL OF HYDROELECTRIC POWER PLANT

SUMMARY

Mathematical and simulation models enable hydroelectric power unit dynamic behavior analysis using computers. In this paper, nonlinear mathematical models of all elements in hydroelectrical power plant are detailed described. Basic elements of hydroelectric power unit are water supply tunnel, surge tank, penstock, water turbine and synchronous generator. If we want more credible simulations models and calculation results, we have to use nonlinear differential equations. Using these nonlinear differential equations, a simulation model was developed for Zakucac HPP.

Key words: block-diagram model, nonlinear mathematical models, tunnel, surge tank, penstock, water turbine, synchronous generator, Zakucac HPP

1 INTRODUCTION

Hydroelectric power plant (HPP) plays an important role in the electric power system. Power from HPP is required to provide the grid regulation services. Considering that, HPP should have high availability level in all operation regimes and good dynamics behavior. The system is divided into several parts which are modeled and then simulated together. By combining individual simulation blocks of a unique simulation model of hydroelectric power plant regulation is obtained. In this paper, basic block structure of the hydro power plant is defined (fig. 1). First, a mathematical model of water supply system (tunnel, surge tank, penstock) [5], a model of water turbine [1,3], and detailed model of a synchronous generator [2,4] are described. Then, using the obtained nonlinear differential equations, a simulation model of all elements is developed using software package MATLAB and SIMULINK. Finally, based on HPP Zakucac, simulation results were obtained and show power plant response at:

- load step disturbance of increased or decreased active power
- a case of change of reference voltage

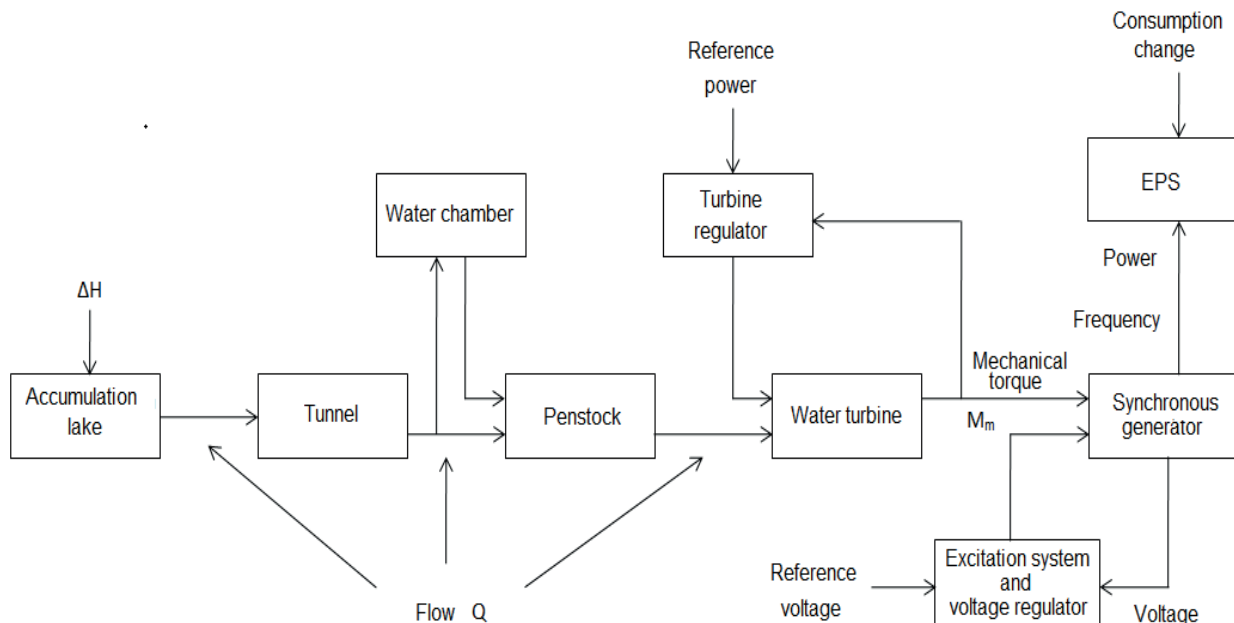


Figure 1. Basic block structure of hydro power plant

2 MATHEMATICAL MODELS OF WATER SUPPLY SYSTEM

2.1 Model of water supply tunnel

A water supply tunnel connects the accumulation lake with the surge tank. The tunnel length goes from one kilometer to several kilometers. In stationary mode, the flow through tunnel is equal to the flow through penstock. Disturbance caused by turbine power change, affects on flow changes and leads to the oscillations in a tunnel – surge tank system. Figure 2. shows the schematic representation of a water supply tunnel.

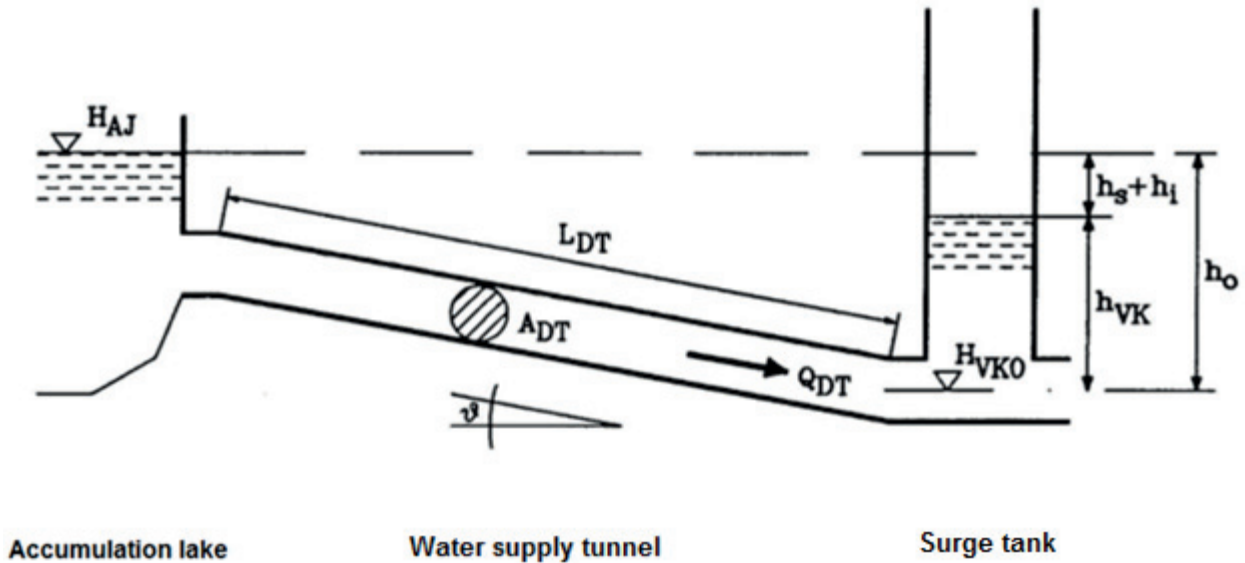


Figure 2. Schematic representation of water supply tunnel [5]

If we consider the water level of the accumulation lake constant, then the rate of change of flow in tunnel is [5]:

$$\frac{dq_{DT}}{dt} = -g \frac{A_{DT}}{L_{DT}} \frac{H_B}{Q_B} (h_{vk} - h_0 + k_{DT} |q_{DT}| q_{DT}) \quad (1)$$

$$h_0 = \frac{H_{AJ} - H_{VK0}}{H_B} \quad (2)$$

$$k_{DT} = \frac{1}{2} \frac{f_{DT}}{g} \frac{L_{DT}}{D_{DT} A_{DT}^2} \frac{Q_B^2}{H_B} \quad (3)$$

$$T_{WDT} = \frac{L_{DT} Q_B}{g A_{DT} H_B} \quad (4)$$

where q_{DT} is the flow through tunnel [p.u.], g is acceleration due to gravity force [m/s^2], A_{DT} is the tunnel cross section area [m^2], D_{DT} is the tube diameter [m], L_{DT} is the length of tunnel [m], H_B is rated head [m], Q_B is rated flow [m^3/s], h_{vk} is the head at surge tank [p.u.], h_0 is the static head of the water column [p.u.], T_{wDT} is the water time constant [s], k_{DT} is the factor of the head loss, f_{DT} is the friction coefficient in the conduit.

2.2 Model of the surge tank

Surge tank is an open tank which is often used with the pressure conduit of considerable length. It is required in hydro power plants for regulating the water flow during load reduction and sudden increase in the load on the hydro generator and thus reducing the pressure on the penstock. Surge tanks are generally built high enough so that the water cannot overflow even with a full load on the turbine. Figure 3. shows the surge tank with two different tanks.

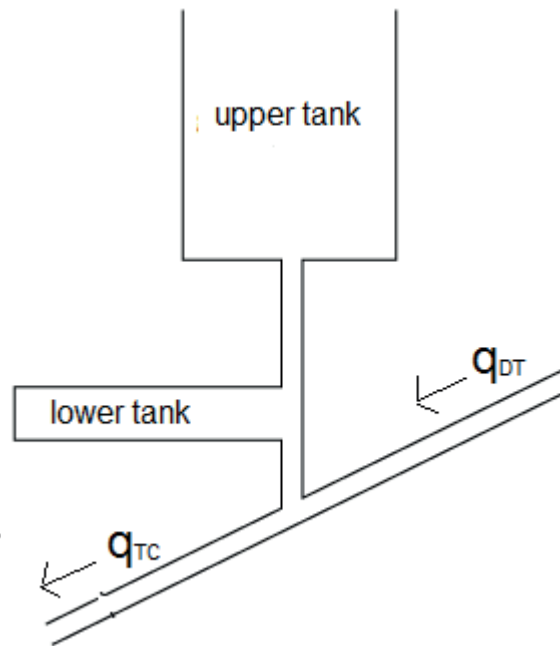


Figure 3. The surge tank

Change in the amount of water in chamber corresponds to the differences in flow through the tunnel and flow through the penstock so the rate of change of water level can be described by differential equations [5]:

$$\frac{dh_{VK}}{dt} = \frac{1}{A_{VK}(h_{VK})} \frac{Q_B}{H_B} (q_{DT} - q_{TNL}) \quad (5)$$

where $A_{VK}(h_{vk})$ [m^2] is the function of the surge tank cross section area depending on the water level h_{vk} in the surge tank.

2.3 Model of the tunnel between the surge tank and the common surge tank

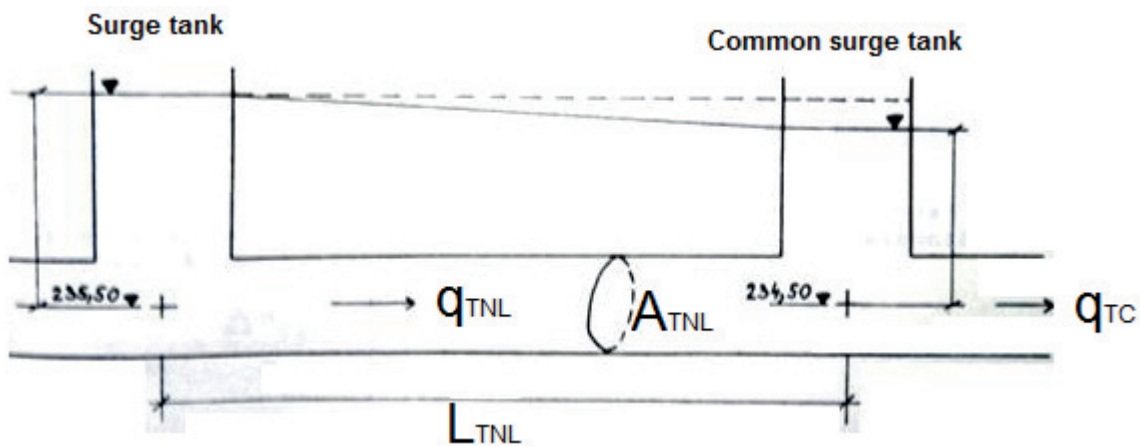


Figure 4. A schematic representation of the tunnel between the surge tank and the common surge tank

The rate of change of flow in tunnel is:

$$\frac{dq_{TNL}}{dt} = \frac{g A_{TNL} H_B}{L_{TNL} Q_B} (h_{vzk} + h_{raz} - h_{zvz} - k_{TNL} |q_{TNL}| q_{TNL}) \quad (6)$$

where q_{TNL} is the flow through tunnel [p.u.], h_{zvz} is head at the common surge tank [p.u.], h_{raz} is the difference in the geodetic height of the tunnel center at the admission to the chamber and common surge tank [p.u.]

2.4 Model of the common surge tank

This complex surge tank proved to be more economical than the classic type of the surge tank. This solution enables the use of water from both tunnels at the operation of any aggregate.

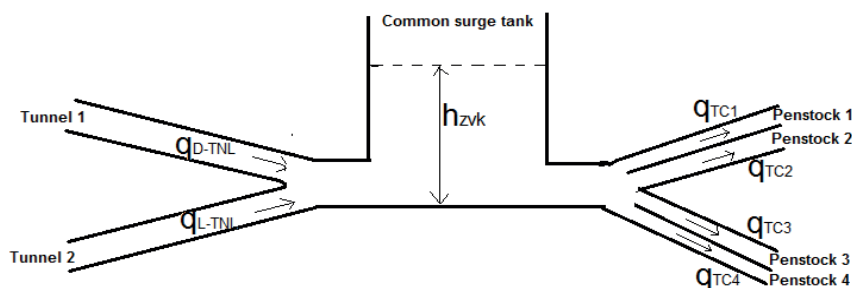


Figure 5. A schematic representation of the common surge tank

The rate of change of water level can be described by differential equation:

$$\frac{dh_{ZVK}}{dt} = \frac{1}{A_{ZVK}(h_{ZVK})} \frac{Q_B}{H_B} (q_{D-TNL} + q_{L-TNL} - q_{TC1} - q_{TC2} - q_{TC3} - q_{TC4}) \quad (7)$$

where Q_{D-TNL} and Q_{L-TNL} are flows through right and left tunnel, respectively [p.u.], $Q_{TC1...4}$ are flows through penstocks [p.u.], $A_{ZVK}(h_{zv_k})$ [m²] is the function of the surge tank cross section area depending on the water level h_{zv_k} in the surge tank.

2.5 Model of the penstock

Penstocks are long channels that carry water down from the hydroelectric reservoir to the turbines. Generally, they are made of steel and water under high pressure flows through the penstock. The penstock is modeled assuming an incompressible fluid and a rigid conduit.

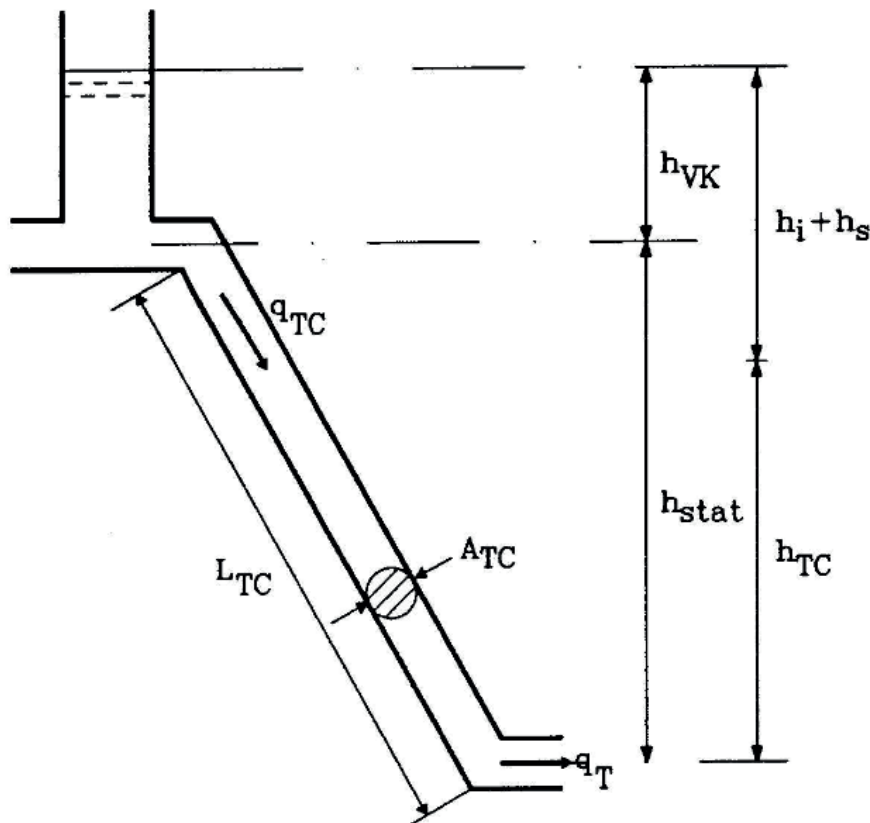


Figure 6. A schematic representation of the penstock [5]

Differential equations are [5]:

$$\frac{dq_{TC}}{dt} = \frac{1}{T_{wTC}} (h_{STAT} + h_{VK} - h_{TC}) - h_{GTC} \quad (8)$$

$$\frac{dh_{TC}}{dt} = k(q_{TC} - q_T) \quad (9)$$

$$h_{GTC} = k_{TC} \frac{Q_B^2}{H_B} |q_{TC}| q_{TC} \quad (10)$$

$$k = \frac{\pi^2}{4} \frac{a^2 Q_B}{g L_{TC} A_{TC} H_B} \quad (11)$$

$$T_{WTC} = \frac{L_{TC} Q_B}{g A_{TC} H_B} \quad (12)$$

$$a = \frac{a_0}{\sqrt{1 + \frac{E_V D_{TC}}{b E_C}}} \quad (13)$$

Where,

h_{STAT} is the static head of the water column [p.u.], h_{GTC} is the head loss due to friction in the conduit [p.u.], h_{TC} is the head at turbine admission [p.u.], q_{TC} is the flow through penstock [p.u.], q_T is the turbine flow [p.u.], L_{TC} is the length of penstock [m], A_{TC} is the penstock cross section area [m²], k_{TC} is the loss coefficient in penstock, T_{WTC} is the water time constant [s], a_0 is the speed of sound in water [1428 m/s], E_v is the modulus of elasticity of water [20.4 * 10⁸ kg/ms²], E_{TC} is the modulus of elasticity of penstock [19.6 * 10¹⁰ kg/ms² for the steel, and 19.6 * 10⁹ kg/ms² for the concrete], b is the penstock wall thickness [m].

3 MATHEMATICAL MODEL OF WATER TURBINE

Basic elements of hydroelectric power unit as dynamic system are hydraulic turbine with conduit, governor and generator. Fig. 7 shows functional relations between elements of hydroelectric power unit with double-regulated turbine [3]:

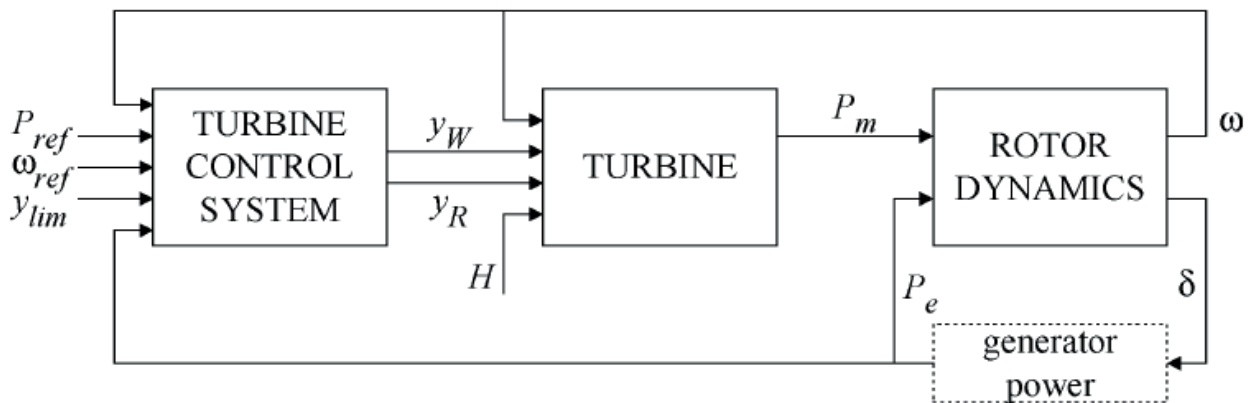


Figure 7. Structure of hydroelectric power unit with double regulated model [3]

If hydraulic turbines are installed in low head HPP with short pipelines, water and conduit can be taken as incompressible so the inelastic water column equation can be used [1,3]:

$$\frac{q_T - q_0}{h_{TC} - h_0} = - \frac{1}{s * T_{WTC}} \quad (14)$$

Where, q_T is the turbine discharge [p.u.], q_0 is the turbine discharge, initial value [p.u.], s is the Laplace operator, h_{TC} is the turbine head [p.u.], h_0 is the turbine head, initial value [p.u.].

Discharge and efficiency of double-regulated turbine are functions of head, speed, guide vanes, and runner blades opening so the mechanical power is also a function of these four variables [1,3]:

$$q = q(h, \omega, y_W, y_R) \quad (15)$$

$$\eta_t = \eta_t(h, \omega, y_W, y_R) \quad (16)$$

$$P_m = P_m(h, \omega, y_W, y_R) \quad (17)$$

In hydroelectric power unit normal operation, speed is almost constant, specially when the unit is connected to electric power system. Neglecting speed deviation, turbine discharge (15) and efficiency (16) characteristics become three variables functions.

In this paper, single regulated turbine is analysed so the assumption of turbine discharge linear dependence on wicket gate opening is usually used. In this case the curve $q(y_w)$ is approximated with straight line through rated operating point [3].

The flow rate through turbine and mechanical power in per unit system are given by [2]:

$$q_T = y_W \sqrt{h_{TC}} \quad (18)$$

$$P_m = A_t h_{TC} (q_T - q_{NL}) \quad (19)$$

$$A_t = \frac{1}{y_{fl} - y_{nl}} \quad (20)$$

Where, y_W is per unit gate position, A_t is the turbine gain, q_{NL} is per unit no load flow, y_{fl} is the full load maximum per unit gate opening, y_{nl} is the no load per unit gate opening.

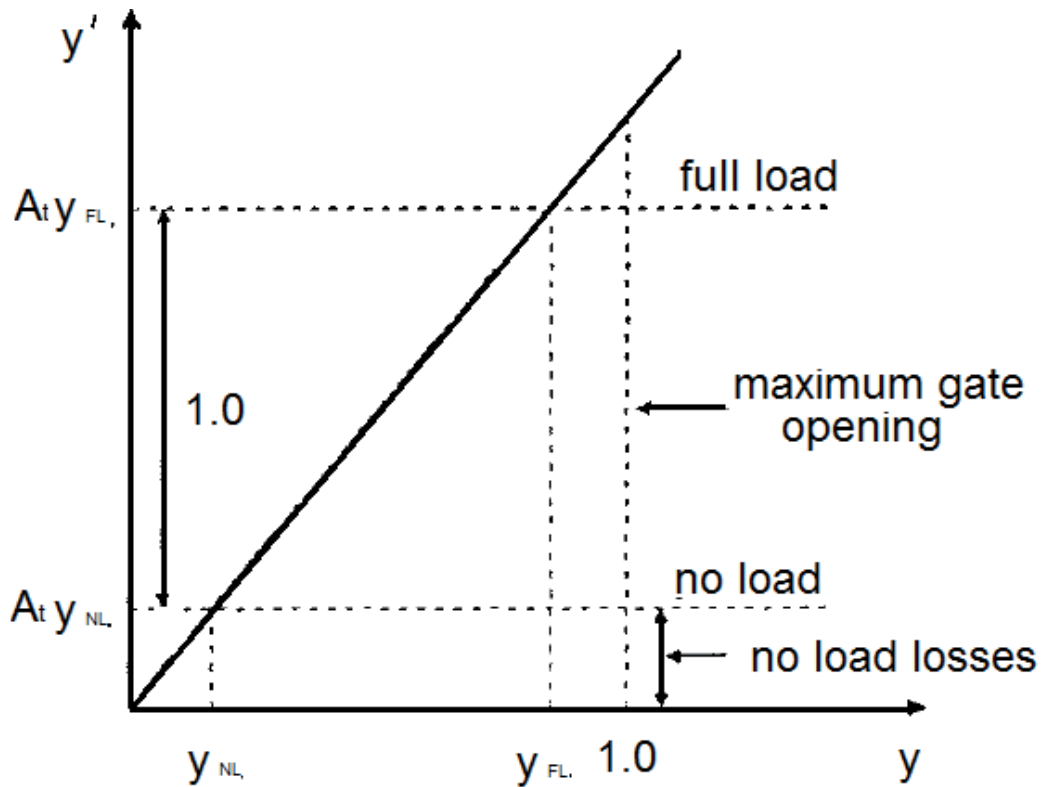


Figure 8. The relation between ideal wicket gate opening and real wicket gate opening [2]

3.1 Mathematical model of turbine governing system

Governing system or governor is the main controller of the hydraulic turbine. The governor varies the water flow through the turbine to control its speed or power output.

- Speed governing [2]:

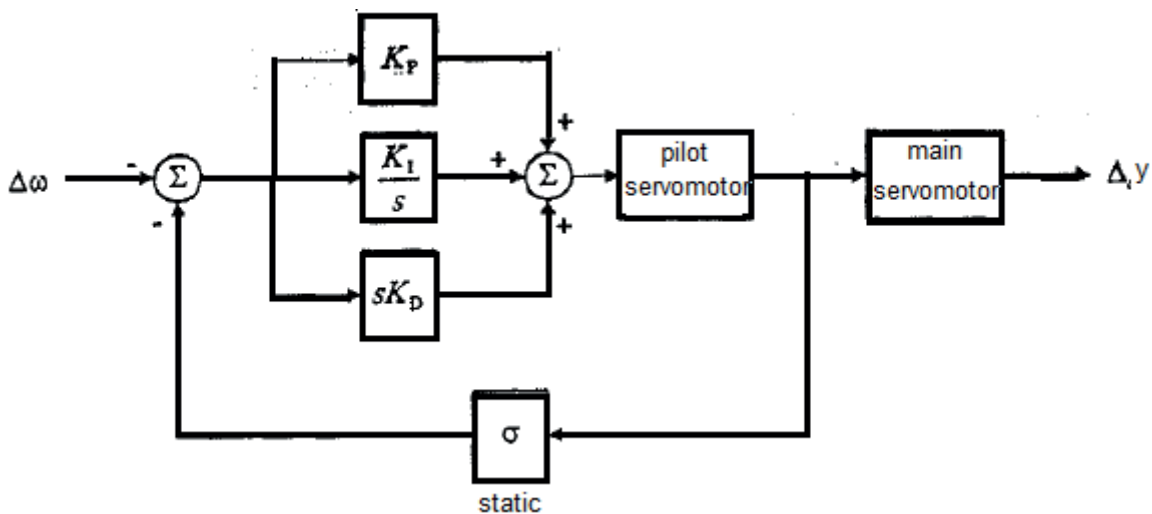


Figure 9. Block scheme of PID regulator [2]

Typical parameters values are [2] : $K_p = 3.0$; $K_i = 0.7$; $K_D = 0.5$

- Power governing:

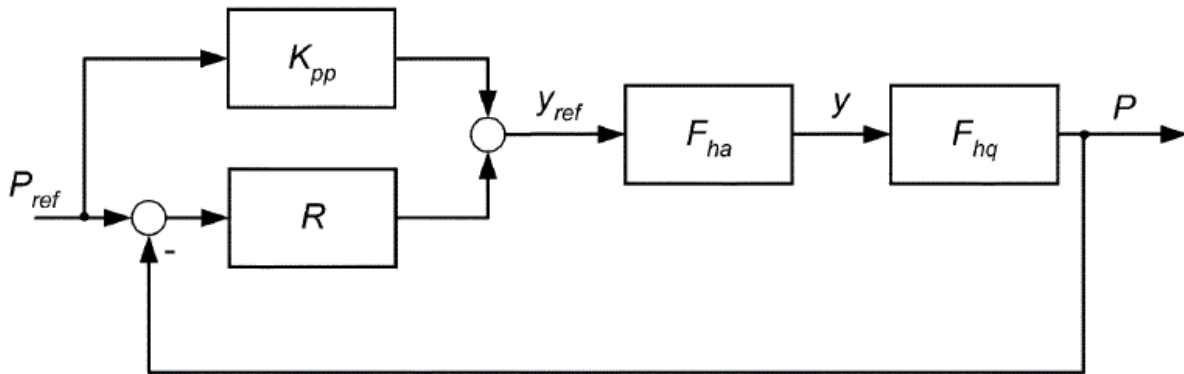


Figure 10. Block diagram of the active power control system [6]

Transfer functions of the blades positioning system and penstock system are [6]:

$$F_{ha} = \frac{y}{y_{ref}} = \frac{1}{T_a s + 1} \quad (21)$$

$$F_{hq} = \frac{\Delta h_{TC}(s)}{\Delta q_{TC}(s)} = -T_W S \quad (22)$$

and a PI controller:

$$R = K_p + \frac{K_i}{s} \quad (23)$$

where T_a [s] is the time constant of the hydraulic piston positioning control system.

3.2 Rotor dynamics model

Rotor swing equation is usually written in the following form [4]:

$$J \frac{d\omega_m}{dt} = M_m - M_e \quad (24)$$

where J is the moment of inertia [$\text{kg} \cdot \text{m}^2$], ω_m is the mechanical angular velocity [rad/s], M_m is the mechanical torque [Nm], M_e is the electrical torque [Nm].

Difference between mechanical and electrical torque is called an accelerating torque. Equation (24) can be written in terms of power instead of torque:

$$J\omega_m \frac{d\omega_m}{dt} = P_m - P_e \quad (25)$$

Introducing per unit values instead of real values, and with the assumption that angular velocity ω is approximately constant, the accelerating power is numerically approximately equal to the accelerating torque (p.u.), (25) becomes:

$$\frac{d\omega}{dt} = \frac{1}{2H^*\omega_r} (P_m - P_e) \quad (26)$$

Where ω is the electrical angular velocity [rad/s], ω_r is the rated electrical speed [rad/s], H is an inertia constant [MWs/MVA].

4 MATHEMATICAL MODEL OF SYNCHRONOUS GENERATOR

The modelling approach presented is carried out under the following assumptions:

- Saturation effects are neglected
- Stator winding currents are assumed to set up a magnetomotive force sinusoidally distributed in space around the air gap
- The effect of space harmonics in the field distribution is neglected
- The magnetomotive force acting along the d-axis and q-axis produces a sinusoidally distributed flux wave along that axis

The most common approach is based on general two-reaction theory upon which a three-phase winding of a generator is substituted by one equivalent, fictitious two-phase winding projected onto the direct (d) and quadrature (q) rotor axis. That transformation is known as Park's or d-q transformation [4]

$$[u_{abc}] = [C_{dq0}][u_{dq0}] \quad [i_{abc}] = [C_{dq0}][i_{dq0}] \quad (27)$$

Where the transformation matrix $[C_{dq0}]$ from the phase reference frame 'abc' to the rotor frame 'dq0' is given by [7]:

$$[C_{dq0}] = \begin{bmatrix} \cos\gamma & -\sin\gamma & 1 \\ \cos(\gamma - \beta) & -\sin(\gamma - \beta) & 1 \\ \cos(\gamma + \beta) & -\sin(\gamma + \beta) & 1 \end{bmatrix} \quad (28)$$

$$[C_{dq0}]^{-1} = \frac{1}{3} \begin{bmatrix} 2\cos\gamma & 2\cos(\gamma - \beta) & 2\cos(\gamma + \beta) \\ 2\sin\gamma & 2\sin(\gamma - \beta) & 2\sin(\gamma + \beta) \\ 1 & 1 & 1 \end{bmatrix} \quad (29)$$

Where γ is instantaneous generator voltage angle [rad], and angle $\beta = 120^\circ$

Voltage equations for these linked circuits can be written:

$$-u_d = r \cdot i_d + \frac{1}{\omega_s} \frac{d\psi_d}{dt} + \omega \cdot \psi_q \quad (30)$$

$$-u_q = r \cdot i_q + \frac{1}{\omega_s} \frac{d\psi_q}{dt} - \omega \cdot \psi_d \quad (31)$$

$$u_f = r_f \cdot i_f + \frac{1}{\omega_s} \frac{d\psi_f}{dt} \quad (32)$$

$$0 = r_D \cdot i_D + \frac{1}{\omega_s} \frac{d\psi_D}{dt} \quad (33)$$

$$0 = r_Q \cdot i_Q + \frac{1}{\omega_s} \frac{d\psi_Q}{dt} \quad (34)$$

where in per units: i_d, i_q are the d and q axis generator current; i_D, i_Q are the d and q axis damper winding current; i_f is the excitation current; u_d, u_q are the d and q axis generator voltage; r is the armature winding resistance; r_f, r_D, r_Q are the field winding resistance, d and q axis damper winding resistance; ψ_d, ψ_q are the stator winding flux linkages – $0, d, q$ system; ψ_f, ψ_D, ψ_Q are the field winding flux linkage, d and q axis damper winding flux linkage; ω_s is the synchronous angular frequency [rad/s].

The flux linkages equations are:

$$\psi_d = x_d \cdot i_d + x_{fd} \cdot i_f + x_{dD} \cdot i_D \quad (35)$$

$$\psi_q = x_q \cdot i_q + x_{qQ} \cdot i_Q \quad (36)$$

$$\psi_f = x_{fd} \cdot i_d + x_f \cdot i_f + x_{fD} \cdot i_D \quad (37)$$

$$\psi_D = x_{dD} \cdot i_d + x_{fD} \cdot i_f + x_D \cdot i_D \quad (38)$$

$$\psi_Q = x_{qQ} \cdot i_q + x_Q \cdot i_Q \quad (39)$$

Where in per units: x_d, x_q are the d and q axis synchronous reactance; x_f, x_D, x_Q are the field winding reactance, d and q axis damper winding reactance; x_{fD} is the field winding and damper winding mutual reactance; x_{fd} is the field winding and armature winding mutual reactance; x_{dD} is the armature winding and d axis

damper winding mutual reactance; x_{qQ} is the armature winding and q axis damper winding mutual reactance.

By substituting the expressions (35-39) in (30-34):

$$\begin{bmatrix} \frac{di_d}{dt} \\ \frac{di_f}{dt} \\ \frac{di_D}{dt} \end{bmatrix} = \omega_s \begin{bmatrix} x_d & x_{fd} & x_{dD} \\ x_{fd} & x_f & x_{fD} \\ x_{dD} & x_{fD} & x_D \end{bmatrix}^{-1} \begin{bmatrix} A_d \\ B_d \\ C_d \end{bmatrix} \quad (40)$$

$$\begin{bmatrix} \frac{di_q}{dt} \\ \frac{di_Q}{dt} \end{bmatrix} = \omega_s \begin{bmatrix} x_q & x_{qQ} \\ x_{qQ} & x_Q \end{bmatrix}^{-1} \begin{bmatrix} A_q \\ B_q \end{bmatrix} \quad (41)$$

Where are:

$$A_d = -u_d - \omega \cdot \psi_q - r \cdot i_d \quad (42)$$

$$B_d = u_f - r_f \cdot i_f \quad (43)$$

$$C_d = -r_D \cdot i_D \quad (44)$$

$$A_q = -u_q + \omega \cdot \psi_d - r \cdot i_q \quad (45)$$

$$B_q = -r_Q \cdot i_Q \quad (46)$$

Inverse matrix from (40) and (41) are, respectively:

$$A^{-1} = \frac{1}{\det[A]} \begin{bmatrix} x_f x_D - x_{fD}^2 & x_{dD} x_{fD} - x_{fd} x_D & x_{fd} x_{fD} - x_{dD} x_f \\ x_{dD} x_{fD} - x_{fd} x_D & x_d x_D - x_{dD}^2 & x_{dD} x_{fd} - x_d x_{fD} \\ x_{fd} x_{fD} - x_{dD} x_f & x_{dD} x_{fd} - x_d x_{fD} & x_d x_f - x_{fd}^2 \end{bmatrix} \quad (47)$$

$$\det[A] = x_d(x_f x_D - x_{fD}^2) - x_{fd}(x_{fd} x_D - x_{fD} x_{dD}) + x_{dD}(x_{fd} x_{fD} - x_{dD} x_f) \quad (48)$$

$$B^{-1} = \frac{1}{x_q x_Q - x_{qQ}^2} \begin{bmatrix} x_Q & -x_{qQ} \\ -x_{qQ} & x_q \end{bmatrix} \quad (49)$$

Standard generator parameters are reactances as seen from generator terminals associated with fundamental frequency during steady-state, transient and subtransient states along with corresponding time constants that determine the currents and voltages falloff gradient. Hence, it is necessary to determine the other model parameters from these standard generator parameters:

$$x_{fd} = x_{fD} = x_{dD} \quad (50)$$

$$x_{fd} = x_d - x_l \quad (51)$$

$$x_f = \frac{(x_d - x_l)^2}{x_d - x_{d'}} \quad (52)$$

$$x_D = x_{fd} + \frac{(x_{d'} - x_l)(x_{d''} - x_l)}{x_{d'} - x_{d''}} \quad (53)$$

$$x_{qQ} = x_q - x_l \quad (54)$$

$$x_Q = \frac{(x_q - x_l)^2}{x_q - x_{q''}} \quad (55)$$

$$r_f = \frac{x_f}{T_{d0} \omega_s} \quad (56)$$

$$r_D = \frac{(x_{d'} - x_l)^2}{x_{d'} - x_{d''}} \cdot \frac{x_{d''}}{x_{d'}} \cdot \frac{1}{T_{d''} \omega_s} \quad (57)$$

$$r_Q = \frac{(x_q - x_l)^2}{x_q - x_{q''}} \cdot \frac{x_{q''}}{x_q} \cdot \frac{1}{T_{q''} \omega_s} \quad (58)$$

Where $x_{d'}$ is the d-axis transient reactance in per unit; $x_{d''}$ is the d-axis subtransient reactance in per unit; $x_{q''}$ is the q-axis subtransient reactance in per unit; x_l is the stator leakage reactance in per unit; $T_{d''}$ is the d-axis open-circuit subtransient time constant [s]; $T_{q''}$ is the q-axis open-circuit subtransient time constant [s]

4.1 Load model

There are different ways to represent the load: constant impedance, constant power, constant current or any of the possible combinations of these three. For

generator modelling, the load representation that will define relations between voltages, currents and angular velocity (load angle) obtained by solving the load flow is required. To simplify the generator model analysis, the rest of the electric power system is replaced by an infinite bus, thus the system influence is reduced to an impedance, and magnitude and angle of the voltage phasor at the infinite bus [4].

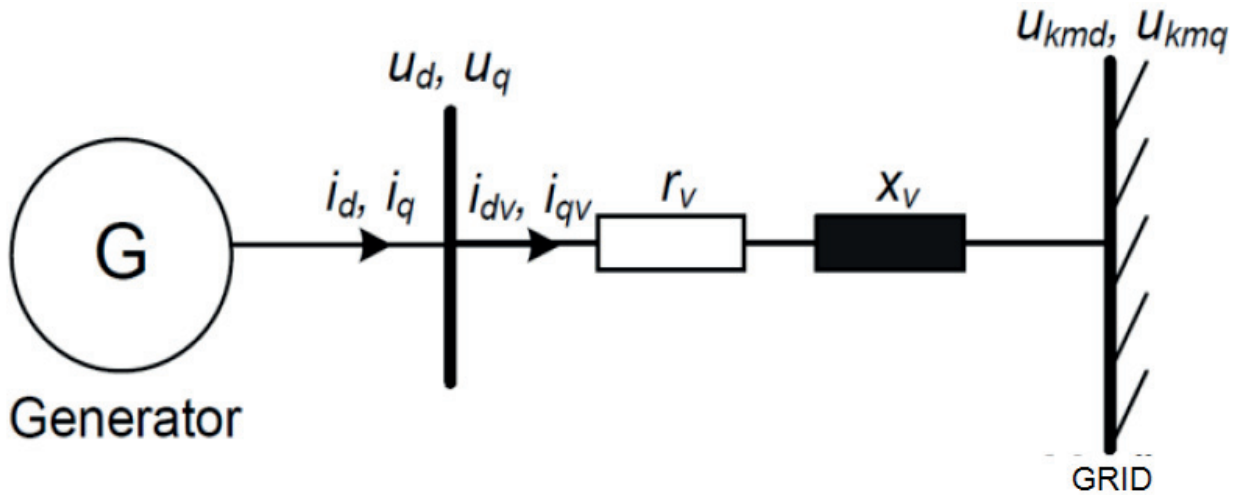


Figure 11. Generator grid connection

$$u_d = i_{dv} \cdot r_v + \frac{x_v}{\omega_s} \frac{di_{dv}}{dt} + \omega \cdot x_v \cdot i_{qv} + u_{kmd} \quad (59)$$

$$u_q = i_{qv} \cdot r_v + \frac{x_v}{\omega_s} \frac{di_{qv}}{dt} + \omega \cdot x_v \cdot i_{dv} + u_{kmq} \quad (60)$$

$$u_{kmd} = u_{km} \cdot \sin\delta \quad (61)$$

$$u_{kmq} = u_{km} \cdot \cos\delta \quad (62)$$

Where u_{kmd} is the grid voltage in d-axis [p.u.]; u_{kmq} is the grid voltage in q-axis [p.u.]; δ is the generator load angle [rad]

5 HPP ZAKUCAC PARAMETERS

BASE VALUES
$H_B = 250.4 \text{ m}$
$Q_B = 220 \text{ m}^3/\text{s}$
$S_B = 540 \text{ MVA}$
$U_B = 16 \text{ kV}$

Right water supply tunnel	Left water supply tunnel
$h_0 = 0.135 \text{ p.u.}$	$h_0 = 0.135 \text{ p.u.}$
$L_{DT} = 9876 \text{ m}$	$L_{DT} = 9894 \text{ m}$
$D_{DT} = 6.1 \text{ m}$	$D_{DT} = 6.5 \text{ m}$
$A_{DT} = 29.22 \text{ m}^2$	$A_{DT} = 33.18 \text{ m}^2$
$k_{DT} = 0.245 \text{ p.u.}$	$k_{DT} = 0.171 \text{ p.u.}$
$T_{wDT} = 30.27 \text{ s}$	$T_{wDT} = 26.70 \text{ s}$
Right and left surge tank	
$h_{vk} [m]$	$A_{vk}(h_{vk}) [m^2]$
3.05 - 5.45	7.06
5.45 - 12.75	$51.51 + 60.3\sqrt{3.65^2 - (h_{vk} - 9.10)^2}$
12.75 - 15.5	51.51
15.5 - 33	<i>right 28.27 and left 38.48</i>
33 - 33.5	233.85
33.5 - 35.9	$\frac{11000}{2.4} \cdot (h_{vk} - 33.5) + 2000$
35.9 - 36.5	$\frac{4000}{0.6} \cdot (h_{vk} - 35.9) + 13000$
36.5 - 41.5	$\frac{8700}{5} \cdot (h_{vk} - 36.5) + 17000$
> 41.5	25700
Right tunnel	
$L_{TNL} = 220 \text{ m}$	$L_{TNL} = 220 \text{ m}$
$A_{TNL} = 29.22 \text{ m}^2$	$A_{TNL} = 33.18 \text{ m}^2$
$h_{raz} = 0.004 \text{ p.u.}$	$h_{raz} = 0.004 \text{ p.u.}$
$k_{DT} = 0.018 \text{ p.u.}$	$k_{DT} = 0.032 \text{ p.u.}$
Common surge tank	
$h_{zvk} [m]$	$A_{zvk}(h_{zvk}) [m^2]$
1 - 7	7.07
7 - 14.2	$133 + 162\sqrt{3.6^2 - (h_{zvk} - 10.6)^2}$
14.2 - 43.5	133
43.5 - 47	$\frac{[9 - \frac{4}{3.5}(h_{zvk} - 47)]^2 \cdot \pi}{4}$

Right penstock 1,2	Left penstock 3,4
$h_{stat} = 0.942 \text{ p.u.}$	$h_{stat} = 0.942 \text{ p.u.}$
$L_{TC} = 366.83 \text{ m}$	$L_{TC} = 366.83 \text{ m}$
$A_{TC} = 10.25 \text{ m}^2$	$A_{TC} = 12.22 \text{ m}^2$
$T_{WTC} = 3.20 \text{ s}$	$T_{WTC} = 2.68 \text{ s}$
$k_{TC} = 0.16 \text{ p.u.}$	$k_{TC} = 0.16 \text{ p.u.}$

$k = 58.77 \text{ s}^{-1}$	$k = 49.29 \text{ s}^{-1}$
Right turbine 1,2	Left turbine 3,4
$Q_{NL} = 0.011 \text{ p.u.}$	$Q_{NL} = 0.013 \text{ p.u.}$
$A_t = 1.264$	$A_t = 1.267$
PID controller	PID controller
$T_a = 0.3 \text{ s}$	$T_a = 0.3 \text{ s}$
$T_m = 8.22 \text{ s}$	$T_m = 8.42 \text{ s}$
$K_p = 1.25$	$K_p = 1.18$
$K_i = 0.17$	$K_i = 0.18$
$K_d = 2$	$K_d = 1.33$
PI controller	PI controller
$K_p = 0.16$	$K_p = 0.12$
$K_i = 0.11$	$K_i = 0.11$
Generator 1,2	Generator 3,4
$S_n = 120 \text{ MVA}$	$S_n = 150 \text{ MVA}$
$U_n = 16 \text{ kV}$	$U_n = 16 \text{ kV}$
$I_d = 4330 \text{ A}$	$I_d = 5400 \text{ A}$
$\cos(\phi) = 0.9$	$\cos(\phi) = 0.9$
$x_d = 0.9 \text{ p.u.}$	$x_d = 0.902 \text{ p.u.}$
$x_q = 0.5 \text{ p.u.}$	$x_q = 0.541 \text{ p.u.}$
$x_l = 0.135 \text{ p.u.}$	$x_l = 0.135 \text{ p.u.}$
$r_a = 0.0025 \text{ p.u.}$	$r_a = 0.0025 \text{ p.u.}$
$x_d' = 0.4 \text{ p.u.}$	$x_d' = 0.341 \text{ p.u.}$
$x_d'' = 0.22 \text{ p.u.}$	$x_d'' = 0.216 \text{ p.u.}$
$x_q'' = 0.198 \text{ p.u.}$	$x_q'' = 0.216 \text{ p.u.}$
$T_d' = 1.2 \text{ s}$	$T_d' = 3.36 \text{ s}$
$T_d'' = 0.028 \text{ s}$	$T_d'' = 0.082 \text{ s}$
$T_q'' = 0.079 \text{ s}$	$T_q'' = 0.105 \text{ s}$
$H = 4.11 \text{ Ws/VA}$	$H = 4.21 \text{ Ws/VA}$

6 SIMULATION RESULTS

Responses of HPP Zakućac at load step disturbance of increase and decrease active power:

- A case of load step increased active power

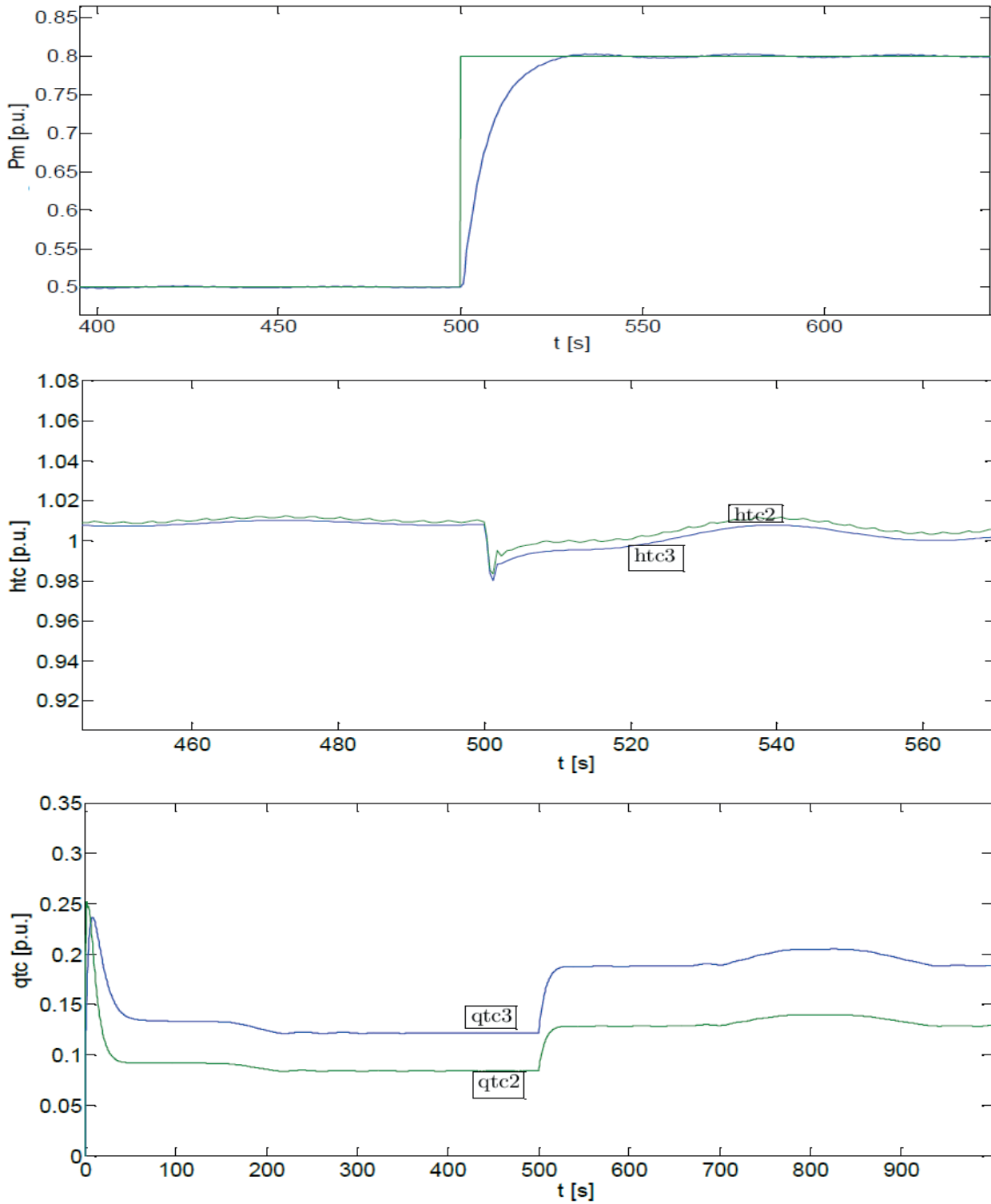


Figure 12. Responses of the power, head at turbine admission and flow through penstock

- A case of load step decreased active power:

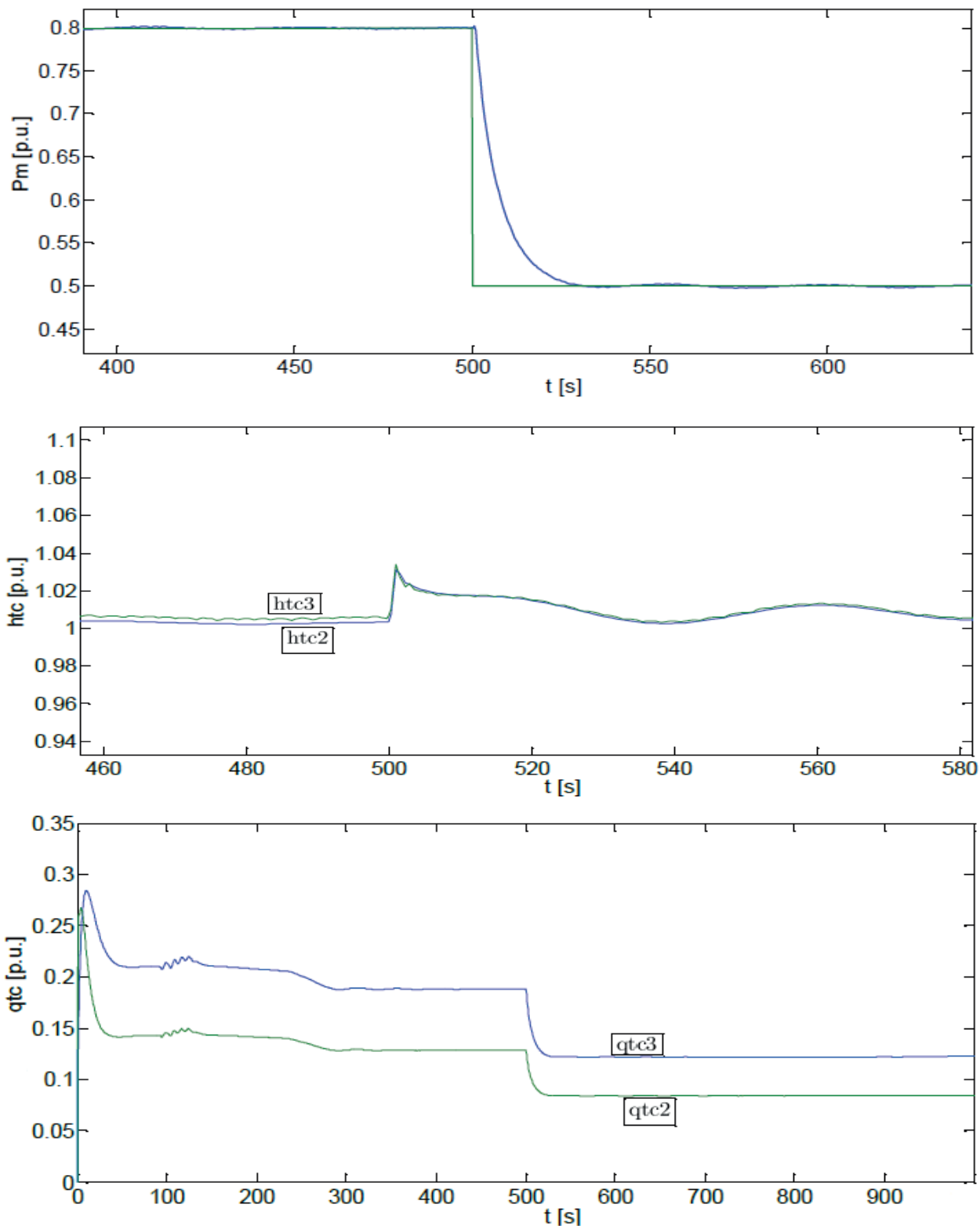


Figure 13. Responses of the power, head at turbine admission and flow through penstock

Responses of HPP Zakucac at a case of change of reference voltage:

- A case of the load step changes in voltage increase $1 - 1.05 - 1$ p.u.

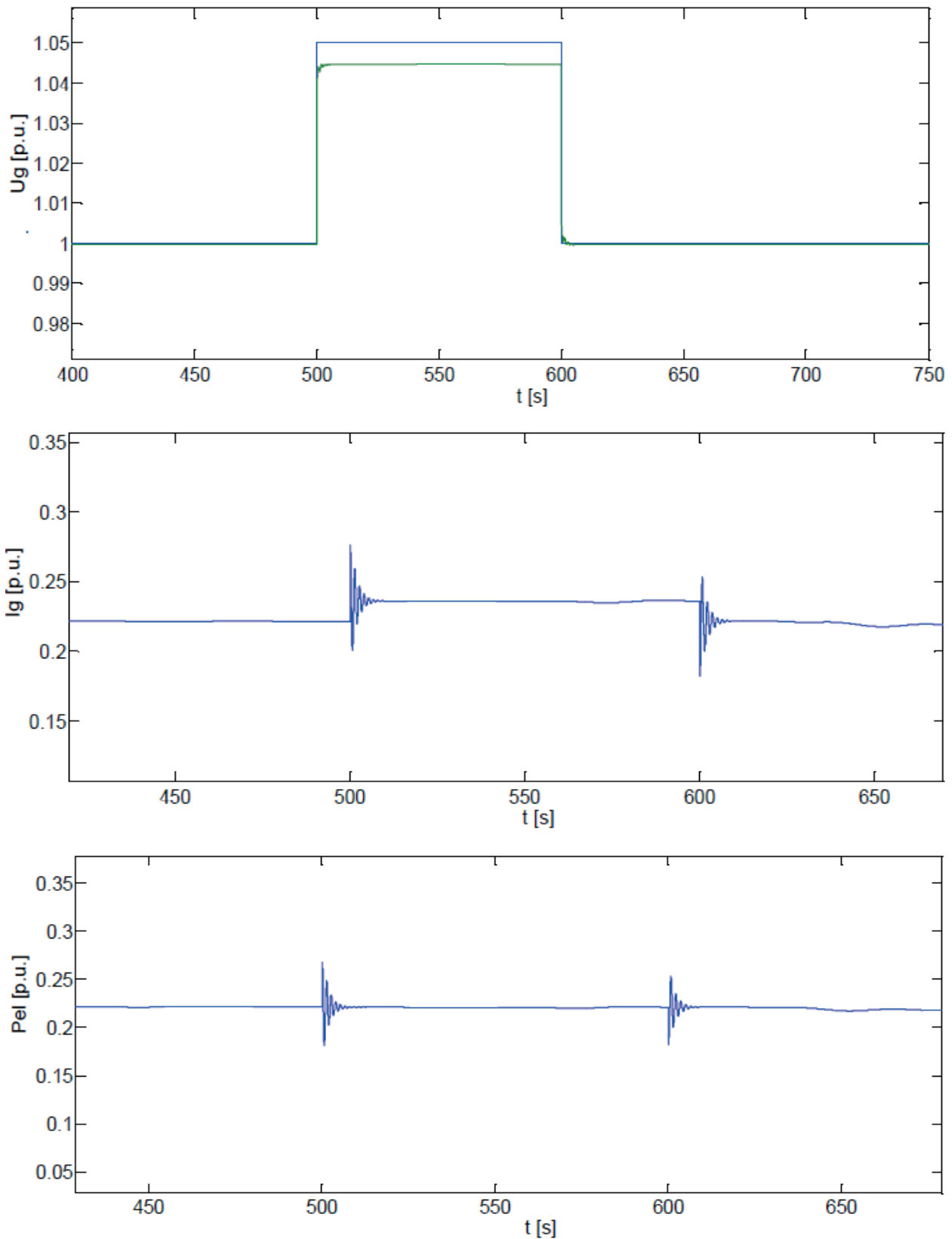


Figure 14. Responses of the voltage, current and electrical power

- A case of the load step changes in voltage decrease $1 - 0.95 - 1$ p.u.

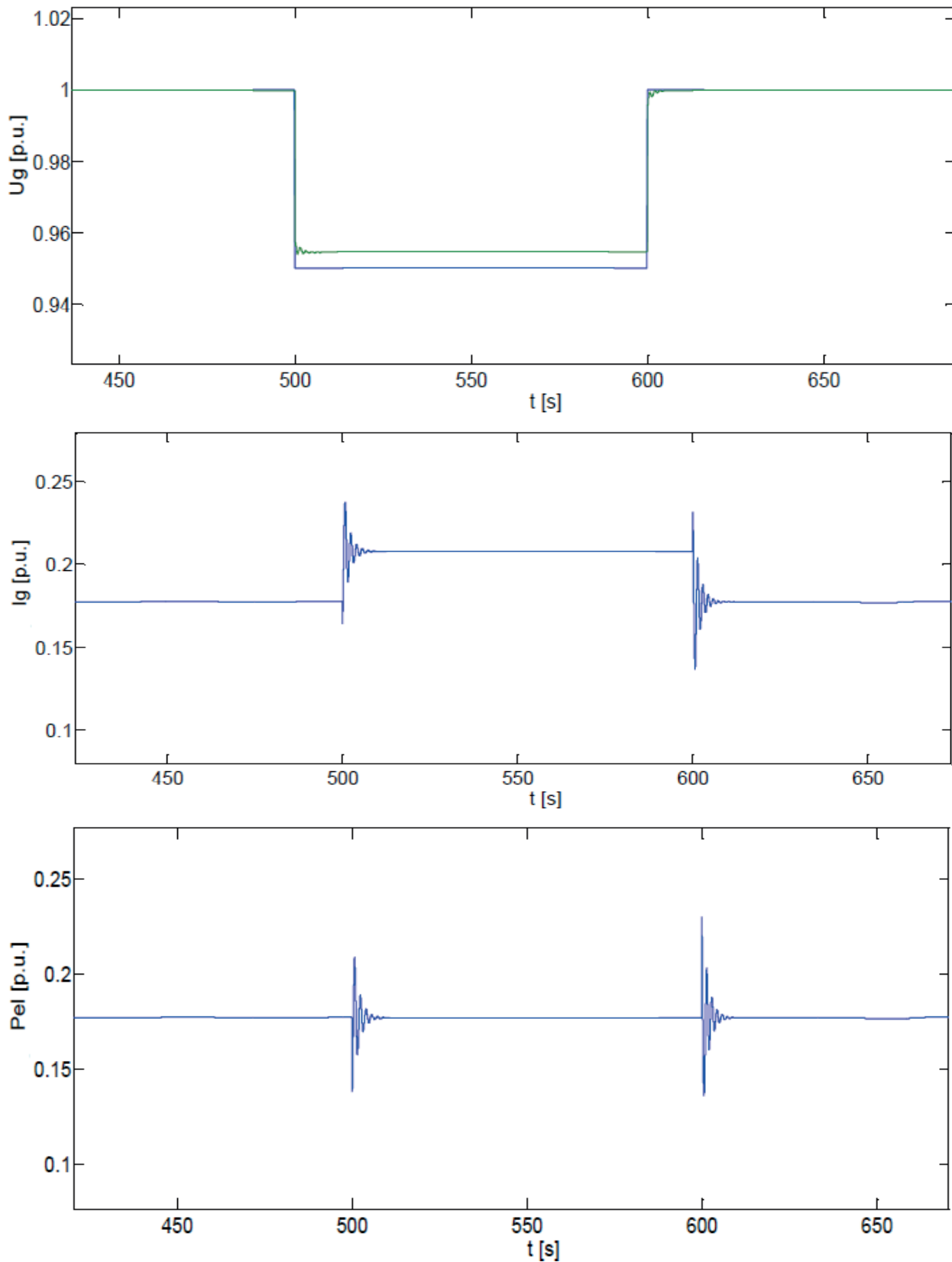


Figure 14. Responses of the voltage, current and electrical power

7. CONCLUSIONS

Hydroelectric power plant has the strongest influence on the dynamics of the electric power system so in the order to analysis and research dynamics characteristics it's necessary to have appropriate mathematical and simulation model. In some case, it's not possible to solve obtain differential equation and then certain assumptions and simplification are used. Another problem is a many data for power system calculations are usually hard to obtain. All this affects the accuracy of the model. The presented mathematical and simulation model of a hydroelectric power plant allows the analysis of all electrical and mechanical units during certain disturbances.

8. REFERENCES

- [1] M. Brezovec, I. Kuzle and S. Tešnjak. Matematički model hidroagregata s dvostruko reguliranom turbinom, *Energija*, Vol. 47, No. 5, 1998, pp. 345-356
- [2] S. Tešnjak, I. Kuzle and M. Brezovec. Modeliranje hidroelektrana, *Energija*, Vol. 46, No. 5, 1997, pp. 287-298
- [3] M. Brezovec, I. Kuzle and T. Tomiša. Nonlinear Digital Simulation Model of Hydroelectric Power Unit With Kaplan Turbine, *IEEE Transactions on Energy Conversion*, Vol. 21, No. 1, March 2006, pp. 235-241
- [4] M. Brezovec, I. Kuzle and M. Krpan, Detailed mathematical and simulation model of a synchronous generator, *Journal of Energy*, Vol. 64, Special issue 2015, pp.102-129
- [5] T. Tomiša. Identifikacija parametara dovodnog hidrauličkog sustava visokotlačne hidroelektrane, *Doktorska disertacija, ETF, Zagreb, 1995*
- [6] B. Strah, O. Kuljača and Z. Vukić. Speed and Active Power Control of Hydro Turbine Unit, *IEEE Transactions on Energy Conversion*, Vol. 20, No. 2, June 2006, pp. 424-433
- [7] Z. Sirotić and Z. Maljković, *Sinkroni strojevi, Element, Zagreb, 1996*

BRUNO JURIŠIĆ**LUKA BUČAR****IVO UGLEŠIĆ**bruno.jurismic@fer.hrluka.bucar@dalekovod.hrivo.uglesic@fer.hr**University of Zagreb Faculty of Electrical Engineering and
Computing**

CALCULATION OF VOLTAGE DISTRIBUTION ALONG THE TRANSFORMER WINDING USING THE WIDE BAND TRANSFORMER MODEL

SUMMARY

Electrical devices in transmission and distribution networks are submitted to fast front transients. These transients are often a cause of a failure in the power system. To simulate these phenomena, it is necessary to detailly model all the components of the power system. This paper concentrates on studding transformer internal failures due to voltage stress that can occur when fast front electromagnetic wave travels through the transformer. To prevent a failure, an internal insulation of the transformer has to be dimensioned to sustain these transient phenomena. Therefore, it is necessary to use advanced wideband transformer models for its dimensioning.

In this paper, a wide band transformer model based on limited transformer geometry is used to simulate evaluate the stresses on internal transformer insulation in the case of fast front transients. The model is validated for calculation of internal overvoltages with the test case from CIGRE brochure.

Key words: Fast front transients, transformer, Grey Box, internal insulation, voltage distribution.

1. INTRODUCTION

Electrical equipment is designed to work permanently at nominal values of frequency, voltage and current. However, transient phenomena occur in the power system affecting the normal operation of the system and its components. These phenomena can reduce life time of the equipment or cause permanent damage to the equipment which has not been dimensioned and protected properly.

In this paper, a power transformer and its behaviour during fast front transients has been studied. These transients include frequencies from few tens of kHz up to few hundreds of kHz. Such fast electromagnetic wave, that encounters transformer windings, is non-linearly distributed along the transformer winding, causing the stress on the inner insulation of the transformer. Therefore, in the design stage of the transformer as well as during the investigation system studies it is necessary to simulate these voltages correctly. To do so, complex wide band transformer models based on the transformer geometry have to be used [1], [2]. As the detailed geometry data needed for these models is not always available, the model that requires a limited information about the transformer geometry data has been developed recently [3], [4]. To validate it for studying the internal voltages, a model is used for modelling a CIGRE test case transformer and compared with the responses that have been calculated using the detailed transformer models that have been developed by different transformer manufacturers.

In the second section of this paper an electromagnetic behaviour of a power transformer has been described when fast front electromagnetic wave is applied to its terminals. In the third section, a “Grey Box” model used in the study is described. Then, in the fourth the test case geometry for a fictitious 100 MVA, 230/69 kV transformer is presented. It includes a validation based on the comparison with the results that have been calculated using the others, already validated models. Finally, the fifth is a conclusion.

2. ELECTROMAGNETIC BEHAVIOUR OF A TRANSFORMER WHEN SUBJECTED TO A FAST-FRONT ELECTROMAGNETIC WAVE

In this section of the paper an electromagnetic behaviour of a transformer, when it is subjected to the electromagnetic wave caused which contains high frequencies in the range of few tens or hundreds of kHz, is explained.

Fast-front transients in power systems are generally caused by lightning or more rarely by vacuum circuit breaker switching and they usually have an amplitude larger than the ones existing because of any other transients. They are critical for choosing the withstand voltage of the power system equipment. The maximum frequency of these transients ranges between 50 and 10000 kHz while its lowest frequency is less than 3.33 kHz [5]. The standard test voltage shape is 1.2/50 μ s lightning impulse test wave, defined in [6].

The response of a transformer submitted to high frequency overvoltages and the corresponding voltage distribution along its windings highly depend on the frequency spectrum of the overvoltages, which are applied to the transformer terminals. Table 1, which is extracted from [7], presents the influence of the main transformer parameters versus the type of transient:

Table 1: Transformer parameters sensitivity versus frequency [7].

Parameter/ Effect	Low- Frequency Transients	Slow-Front Transients	Fast-Front Transients	Very Fast- Front Transients
Short circuit impedance	Very important	Very important	Important	Negligible
Saturation	Very important	Important	Negligible	Negligible
Core losses	Very important	Important	Eddy currents losses are important*	Negligible
Capacitive coupling	Negligible	Important	Very important	Very important

Note that the element from Table 1 marked with an asterisk differs from the one of the table given in [7].

First parameter, shown in Table 1, refers to the leakage inductance and losses in the conductor when a current flows through it (Joules losses and eddy current losses). Eddy currents losses in the windings rise versus frequency as well as the impedance of the leakage flux reactance. Consequently, less current flows through the transformer windings. Therefore, the influence of the short circuit impedance diminishes with frequency. Nevertheless, for fast front transients it is important to model correctly eddy current losses (skin and proximity losses) in the copper of the windings, especially if the model is intended to have an accurate damping.

The two following parameters from Table 1, namely saturation and core losses, are related to the core influence. For fast front and very fast front transients it can be considered that the magnetic flux disappears from the core with high frequencies due to the rise of the eddy currents in the core's lamination which compensate the main flux, resulting in the low magnetic induction in the core. Consequently the core's permeability is considered to be in its initial zone (linear part of the saturation curve) so saturation effect and hysteresis losses can be neglected [8], [9].

The last parameter in Table 1, capacitive coupling between the windings and between the windings and the ground becomes important when modelling a transformer for fast front and very fast front transients.

3. GREY BOX TRANSFORMER MODEL

Following the observations in the previous section, a Grey Box model based on limited information about the transformer geometry has been developed to model high frequency overvoltages existing on outside and inside terminals of transformer [3], [4], [10].

The model is composed of lumped RLCG equivalent parameters whose values are calculated using finite element method software program [11]. In the model transformer geometry is divided in simple segments as shown in Figure 1.

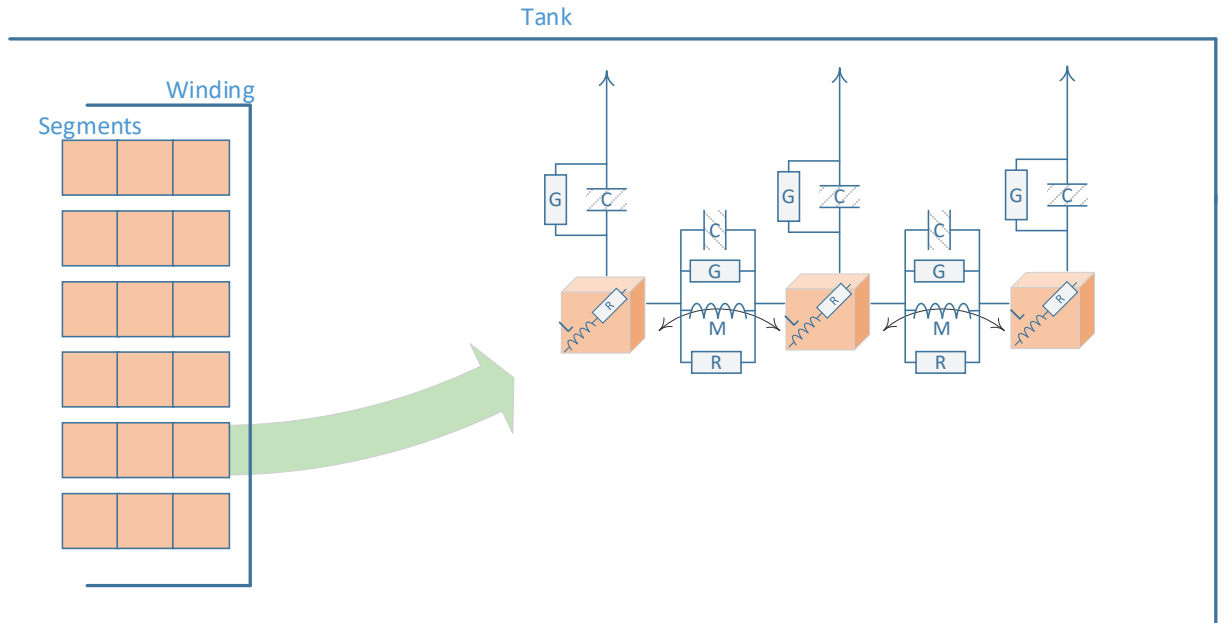


Figure 1: Segment of the Grey Box transformer model

Each segment represents a turn or a group of the turns depending on transformer size and the frequency range that needs to be simulated. Each segment consists of serial inductance, serial resistance, serial capacitances, mutual inductances, capacitances and resistances (related to the proximity effect), mutual capacitances and conductance to the ground. Resistance and inductance parameters are frequency dependent since eddy current effects (proximity and skin effect) are represented in the model. This is important to model if one wants to have accurate results at high frequencies.

Inductances and resistances are calculated from the magnetic field value given frequency by using the Maxwell Ampere's law for quasistatic magnetic fields ($\nabla \times \mathbf{B} = \mu \mathbf{J}$) from which the following equations can be extracted [12]:

$$R_{ij} = -\frac{\omega * n_j}{I_i} * \text{Im} \left\{ \oint_{C_j} \left(\frac{n_i}{a_j} \iint_{S_j} \mathbf{A}_{ij} d\mathbf{S}_j \right) dl_j \right\} \quad (1)$$

$$L_{ij} = \frac{n_j}{I_i} * \text{Re} \left\{ \oint_{C_j} \left(\frac{n_i}{a_j} \iint_{S_j} \mathbf{A}_{ij} d\mathbf{S}_j \right) dl_j \right\} \quad (2)$$

Capacitance values are calculated from the electrostatic electric field calculations, from the charge:

$$C_{ij} = \frac{Q_{ij}}{V_i} \quad (3)$$

Conductance parameters are calculated directly from capacitance parameters [3], [8].

When all the parameters are calculated, it is possible to form branch impedance matrix $\mathbf{Z}_{RLbranch}$ and nodal admittance matrix $\mathbf{Y}_{CGnodal}$ as follows:

$$\mathbf{Z}_{RLbranch}(f) = \mathbf{R}(f) + j\omega\mathbf{L}(f) \quad (4)$$

$$\mathbf{Y}_{CGnodal}(f) = \mathbf{G}(f) + j\omega\mathbf{C} \quad (5)$$

Both matrices $\mathbf{Z}_{RLbranch}(f)$ and $\mathbf{Y}_{CGnodal}(f)$ are symmetrical. All the elements of the matrices given above, except the capacitances, are frequency dependant. Dimension of $\mathbf{Z}_{RLbranch}(f)$ is determined by the number of segments taken into consideration while the dimension of $\mathbf{Y}_{CGnodal}(f)$ is determined by the number of nodes.

To calculate a transformer nodal admittance matrix, first, it is necessary to calculate \mathbf{RL} nodal matrix, $\mathbf{Y}_{RLnodal}(f)$ from the $\mathbf{Z}_{RLbranch}(f)$ matrix:

$$\mathbf{Y}_{RLnodal}(f) = \mathbf{A} * \mathbf{Z}_{RLbranch}(f)^{-1} * \mathbf{A}^T \quad (6)$$

\mathbf{A} is the incidence matrix which contains the relations between the inductive branch currents and the nodal currents [3]. The $\mathbf{Y}_{RLnodal}(f)$ matrix is a square matrix of the dimension equal to the number of nodes.

Complete nodal matrix of a transformer, $\mathbf{Y}_{nodal}(f)$ can be calculated as follows:

$$\mathbf{Y}_{nodal}(f) = \mathbf{Y}_{RLnodal}(f) * \mathbf{Y}_{RLnodal}(f) \quad (7)$$

$$\mathbf{Y}_{nodal}(f) = \begin{bmatrix} \mathbf{Y}_{ee}(f) & \mathbf{Y}_{ei}(f) \\ \mathbf{Y}_{ie}(f) & \mathbf{Y}_{ii}(f) \end{bmatrix} \quad (8)$$

$$\begin{bmatrix} \mathbf{Y}_{ee}(f) & \mathbf{Y}_{ei}(f) \\ \mathbf{Y}_{ie}(f) & \mathbf{Y}_{ii}(f) \end{bmatrix} * \begin{bmatrix} \mathbf{V}_e(f) \\ \mathbf{V}_i(f) \end{bmatrix} = \begin{bmatrix} \mathbf{I}_e(f) \\ \mathbf{I}_i(f) \end{bmatrix} \quad (9)$$

\mathbf{V}_e and \mathbf{I}_e respectively stand for the voltages at the external terminals and currents flowing into the external terminals while \mathbf{V}_i and \mathbf{I}_i stand for the voltages at the internal terminals and currents flowing into the internal terminals. To form a nodal matrix as it is shown in equation (8) the rows and columns of the nodal matrix have to be restacked.

If in equation (9) we set all the currents that are entering in internal transformer nodes, \mathbf{I}_i to 0, then it can be written:

Both windings are discs windings. The low voltage winding is modelled with 87 discs and 5 turn per discs while the high voltage winding is modelled with 84 discs per part of the winding and 20 turns per discs. The high voltage winding is interleaved. For more details on the transformer geometry, see [1].

For the simplicity, in the paper only one test scenario is described. It is assumed that 1050 kV lightning impulse wave hits HV terminal of high voltage winding, while all the other terminals are grounded. This scenario is similar to lightning impulse test that is a routine test for all the transformer with nominal voltage higher than 72.5 kV [13].

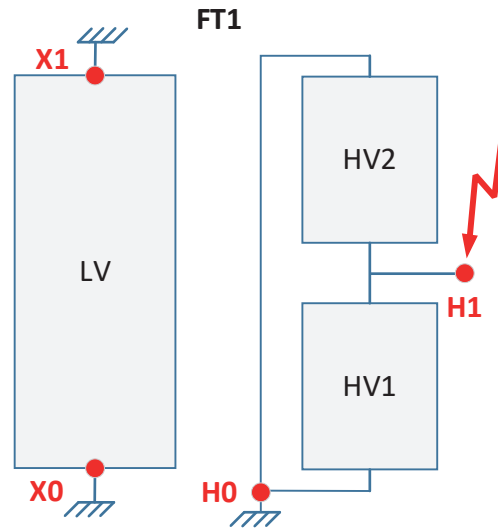


Figure 3: Test scenario

The transformer is modelled using the described Grey Box model, representing 5 turns as one segment. This approximation reduced number of the elements in the model from 2115 to 423. The accuracy of the model is maintained up to 780 kHz. As two parts of the HV winding are connected in parallel, the model is constructed in the way that the voltage distributions do not differ for two parallels. This has been done in order to reduce the simulation time. Therefore, the results are shown only for one parallel HV branch (see nodes from 45 to 68 in Figure 4). Associated numbers with the LV winding are 1 to 44. External nodes are named as follows: "LV1", "LV_mid", "H0" and "H1".

In the continuation the results are compared with the one provided in CIGRE brochure [1] for the maximum voltage amplitude that exist in all the internal nodes when LI is applied to terminal H1.

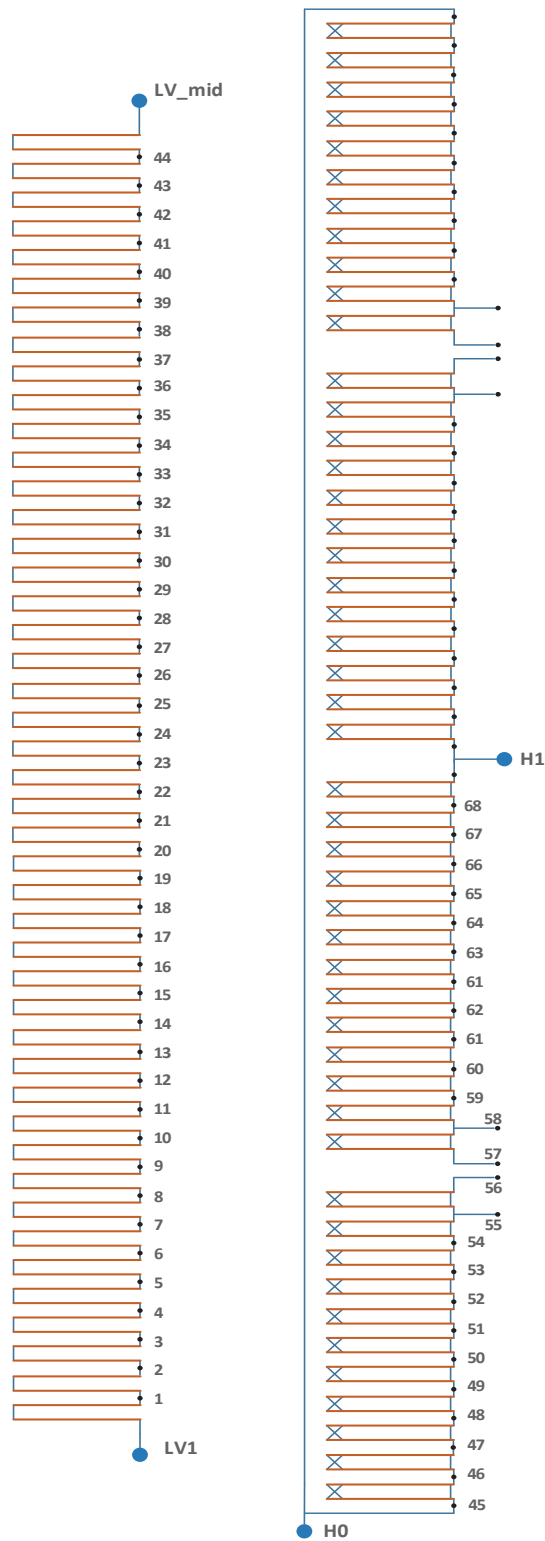


Figure 4: Names of internal and external nodes in LV and HV windings

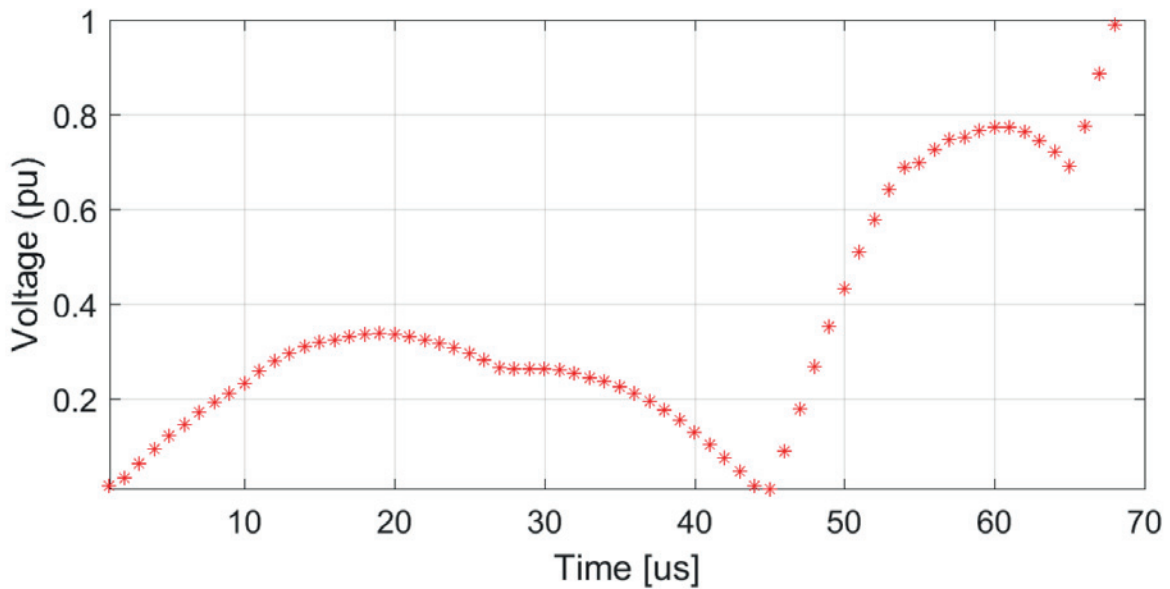


Figure 5: Maximum internal nodes voltages calculated with the Grey Box model

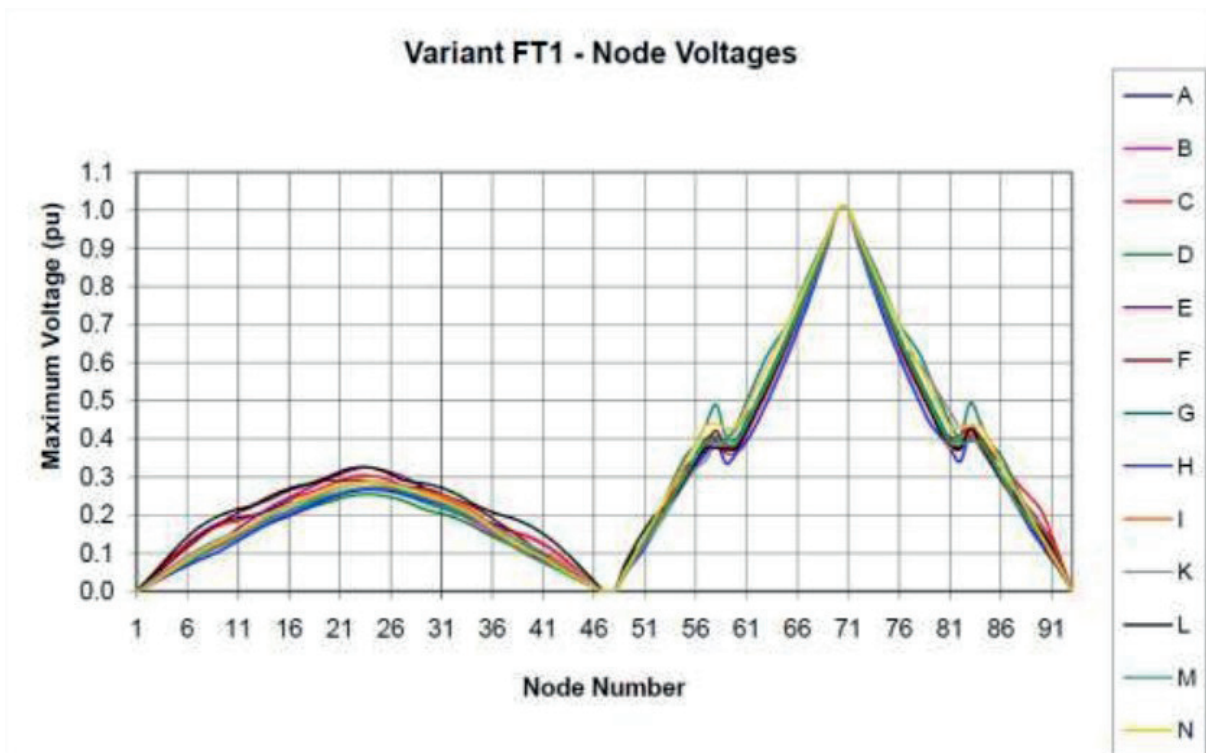


Figure 6: Maximum internal nodes voltages from CIGRE brochure [1]

In Figure 6 the results have been shown for 13 different transformer models developed by different universities, manufacturers or independent consultants. Note that the models used by CIGRE differs two parts of the HV winding. Consequently, the CIGRE results include voltages for more nodes. However, the numbers of the nodes correspond to each other in Figure 5 and Figure 6.

The presented model gave quite comparable results to the one provided by CIGRE especially if we take into account that the initial intention of the model was to study external voltages rather than the internal ones [3].

Furthermore, the comparison has been made for the voltage shapes existing at the first disc of the HV winding, seen from the point of the LI impact.

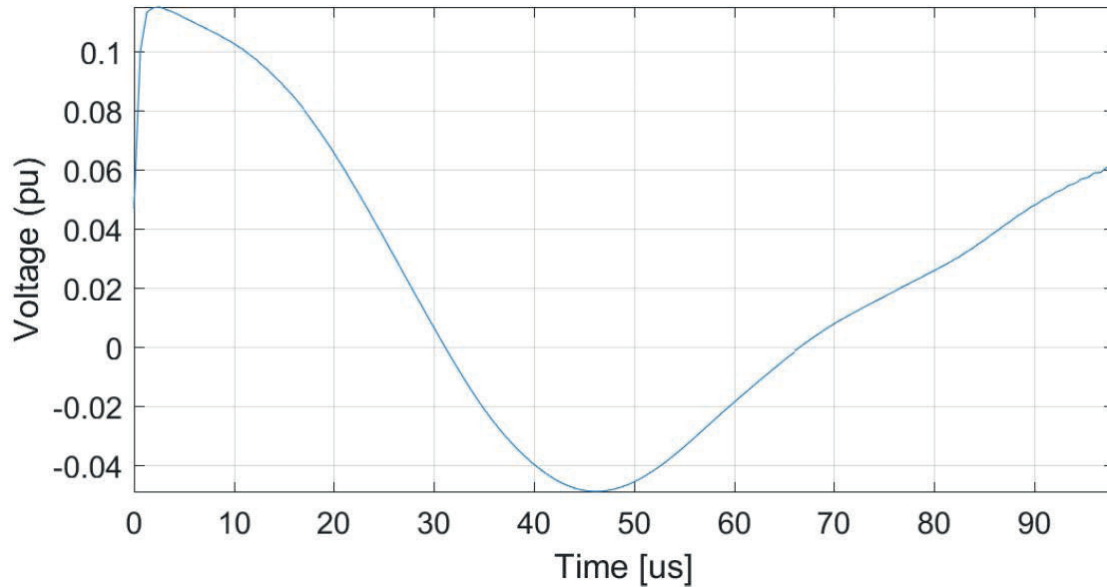


Figure 7: Voltage across the first discs of the HV winding calculated using the Grey Box model

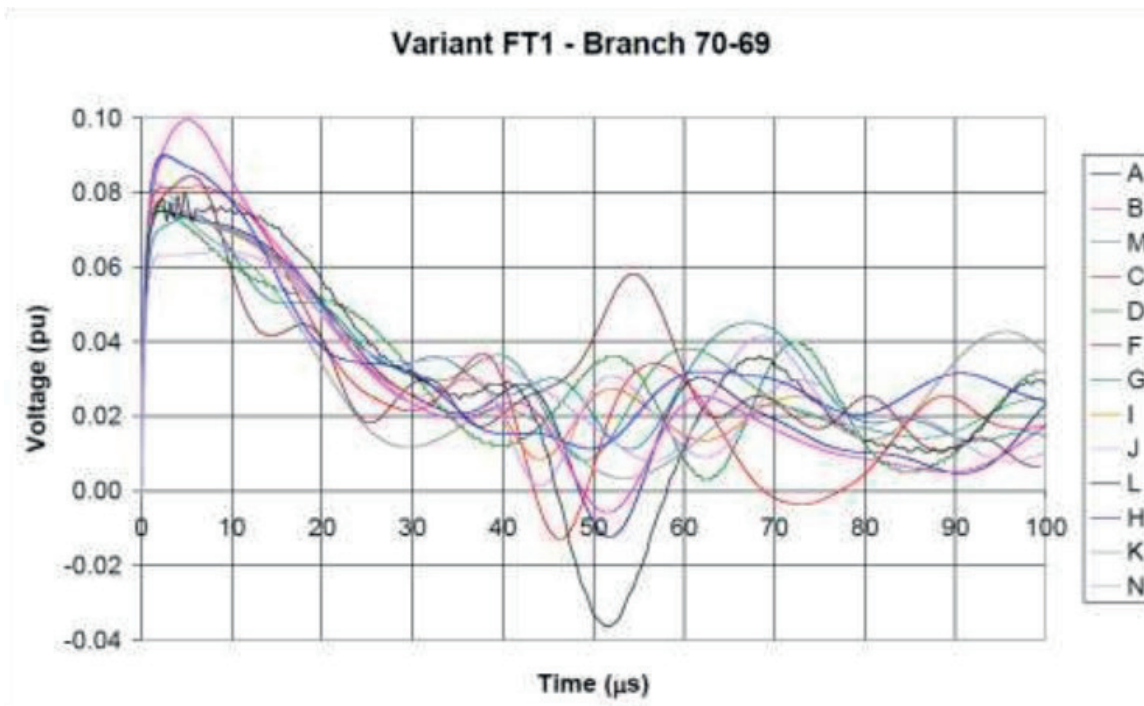


Figure 8: Voltage across the first discs of the HV winding from CIGRE brochure [1]

The model showed once again comparable results with the one provided by CIGRE.

Discrepancies between the results of the models could be explained by the validity range of the Grey Box model or due to the way parallel HV winding is presented.

5. CONCLUSIONS

In this paper a Grey Box model based on limited information about a transformer geometry has been presented. It has been validated, using the example from CIGRE brochure [1] for calculation of internal overvoltages along the transformer winding. It gave comparable results in terms of voltage amplitude and wave shapes, when compared to more advanced transformer models developed by different universities, manufacturers or independent consultants.

The models such as the one that is presented can help power utilities to detect the cause of transformer failure or to improve the design and protection of the power network.

6. REFERENCES

- [1] CIGRE WG A2/C4.39, *Electrical Transient Interaction Between Transformers and the Power Systems*. 2013.
- [2] S. V. Kulkarni and S. A. Khaparde, *Transformer Engineering Design and Practice*. 2004.
- [3] B. Jurisic, "Methods for Calculations of High Frequency Transmitted Overvoltages through a Power Transformer," Ph.D. dissertation, University of Zagreb, University Blaise Pascal, 2016.
- [4] B. Jurišić, P. Poujade, A. Xemard, I. Uglesic, and F. Paladian, "Calculation of internal overvoltages using a wide band transformer model based on limited information about transformer design," in *4th International Colloquium "Transformer Research and Asset Management,"* 2017, vol. 0, pp. 1–9.
- [5] International Electrotechnical Commission, *IEC 60071-4 Insulation Co-ordination - Part 4: Computational Guide to Insulation Co-ordination and Modelling of Electrical Networks*. 2004.
- [6] International Electrotechnical Commission, *IEC 60060-1 High-Voltage Test Techniques Part 1: General Definitions and Test Requirements*. 2010.
- [7] J. a. Martinez-Velasco, *Power System Transients*. United States: CRC Press, 2010.

- [8] E. Bjerkan, “High Frequency Modeling of Power Transformers,” Ph.D. dissertation, Norwegian University of Science and Technology, 2005.
- [9] E. Bjerkan, H. K. Høidalen, and O. Moreau, “Importance of a Proper Iron Core Representation in High Frequency Power Transformer Models,” *IEEE Trans. Magn.*, vol. 34, no. 5, 1998.
- [10] B. Jurisic, I. Uglesic, A. Xemard, and F. Paladian, “High frequency transformer model derived from limited information about the transformer geometry,” *Int. J. Electr. Power Energy Syst.*, vol. 94, pp. 300–310, 2018.
- [11] M. David, “Finite Element Method Magnetics.” 2014.
- [12] O. Moreau, L. Popiel, and J. L. Pages, “Proximity Losses Computation with a 2D Complex Permeability Modelling,” *IEEE Trans. Magn.*, vol. 34, no. 5, pp. 3612–3615, 1998.
- [13] International Electrotechnical Commission, *IEC 60076-3- Power Transformers - Part 3: Insulation Levels, Dielectric Tests and External Clearances in Air*. 2013.

ANA DRANDIĆ¹ ANTE MARUŠIĆ¹ MARINO DRANDIĆ² JURAJ HAVELKA¹

ana.drantic@fer.hr ante.marusic@fer.hr marino.drantic@elput.hr juraj.havelka@fer.hr

¹ University of Zagreb Faculty of Electrical Engineering and Computing

² ELPUT d.o.o., Pula, Croatia

POWER SYSTEM NEUTRAL POINT GROUNDING

SUMMARY

The method used for neutral point grounding is very important for power network operation. There are many ways of grounding, which are used in practice, and the decision on the method of neutral grounding depends on the situation in the network connected to the substation. When deciding on the method of neutral grounding it is necessary to thoroughly consider all the advantages and disadvantages of individual modes of neutral grounding, and then choose the best technical and economical solution.

This paper analyzes the ways of neutral point grounding in medium voltage networks used in the current practice in Croatia which are isolated neutral point, low resistance earthing, partial compensation and resonant earthing. The use of shunt circuit-breaker is also described. Additionally, a survey of the relays used for the neutral point grounding system inside the substations was conducted and a brief analysis of the results is presented in the paper.

Key words: Neutral point grounding, compensation coil, shunt trip circuit-breaker, earth-fault protection, earth fault.

1. INTRODUCTION

Optimal selection of the grounding method for the neutral point is of great importance for the operation of the medium voltage networks since different concepts affect the different shapes and values of overvoltages and fault currents, which represent the most common type of malfunction in the network. The grounding mode selection directly affects network operating conditions, power quality, human security, and the choice of earthing protection concept.

In Europe, there is no unique concept of grounding the neutral point. There are many works that describe the possible grounding methods and the protection of networks depending on the grounding method [1-10]. Many factors influence the neutral point grounding. One them is the value of the capacitive current. In more developed distribution networks, with a relatively large number of electricity customers, and due to systematic cabling, the capacitive currents have reached such a level that the change of grounding system was necessary, such as switching from the low-ohmic resistor grounding to resonant grounding [3].

The reasons to ground the neutral point are:

- rise in the number of cable networks - leads to a higher value of capacitive current,
- single-phase failure current increase,
- network expansion,
- demand to increase the quality of electricity supply.

A large number of different grounding methods used for neutral point grounding is the result of concessions between two main and mutually opposite requirements [5]:

- reduction of the earth fault current amplitude, which can cause trouble when detecting faults,
- permitting larger earth fault current amplitudes, which makes it easier to detect earth faults, but can cause dangerous contact voltages, and cause more power outages.

In order to be able to adjust the relay protection of the network, it is necessary to know the voltage and current voltages that are established in the stationary state after a single-phase fault. In order to properly identify the type of fault and the reaction of the relay protection, it is necessary to know network configuration and the method of neutral point grounding.

Due to different conditions in networks and national regulations, there are various technical solutions for grounding the neutral point in Europe [5]:

- isolated neutral point,
- direct grounding,
- low-impedance grounded neutral point,
- low-ohmic grounded neutral point,
- high-impedance grounded neutral point,

- partial compensation,
- resonant grounded neutral point.

The use and protection of network with low-ohmic grounded neutral point is presented in [11], a proposal of partial compensation use is presented in [12], examples of the use of resonant grounded neutral point are given in [13-15], and [16] presents the usefulness of the shunt circuit-breaker.

This paper gives the technical overview of the grounding methods for neutral point in medium voltage networks used in Croatia and is based on the information in [1] and [2]. Additionally, the use of shunt circuit-breaker is also described since its' use in the networks grounded by low-ohmic resistor or networks with partial compensation means that it is possible, depending on the capacitive currents, to use it as a more economical alternative to resonant grounding. Analysis of the protective relays used for protection in 35/10(20) kV substations is also presented.

2. THEORETICAL OVERVIEW

In Croatia, four ways of grounding the neutral point are used in medium voltage networks:

- isolated neutral point,
- low-ohmic grounded neutral point,
- partial compensation,
- resonant grounded neutral point.

In addition to these solutions, it is also necessary to observe the solution where the shunt trip circuit breaker is used. Its use can achieve similar effects as resonant grounding as it solves the problem of earth fault. As each phase can be individually switched on and off, the shunt trip circuit breaker is used as a solution for reducing the number of transient failures.

2.1. Isolated neutral point

The use of the isolated neutral point in the power system is the simplest and cheapest solution. In such a system, the neutral point is separated from the ground, and the only connection with the earth is realized through the earth capacitances of cables and overhead lines. During the earth fault, the currents flow through those capacitances of the healthy phases. The fault current depends on the capacitive current of the network and on the transient resistance [7]. In single-phase earth fault the voltages of the healthy phases can increase to the size of the line voltage. Then there is a danger of the occurrence of a two-phase earth fault in which the values of the currents are similar to the currents of the three-phase short circuit. If the network works in the state of earth fault for more than two hours, it is considered that the conditions for a two-phase earth fault to occur are met.

The insulated neutral point provides a continuous operation in the event of an earth fault, so that the fault can be removed in the best time for consumers. However, by network expansion, the currents of the earth fault become larger than the maximally allowed currents for the network which is 10 A for the 35 kV network, 15 A for 20 kV, 20 A for 10 kV, and 30 A for 6 kV network. Then, the isolated neutral point use loses its main advantage, which is maintaining the conditions for single-phase earth fault to shut down itself without the need of relay protection or staff intervention [3]. This is particularly emphasized for cable networks that have large earth capacitances and the fault currents are greater than in overhead networks.

Figure 1 shows the current flow in the grid when there is an earth fault at phase L1 assuming that a stable earth fault without transient resistance has occurred. Vector diagram for this kind of earth fault is depicted in Fig.2. As shown on the vector diagram, the neutral point voltage towards earth is the phase voltage size, while the voltage levels of the healthy phases towards earth are of the line voltage size.

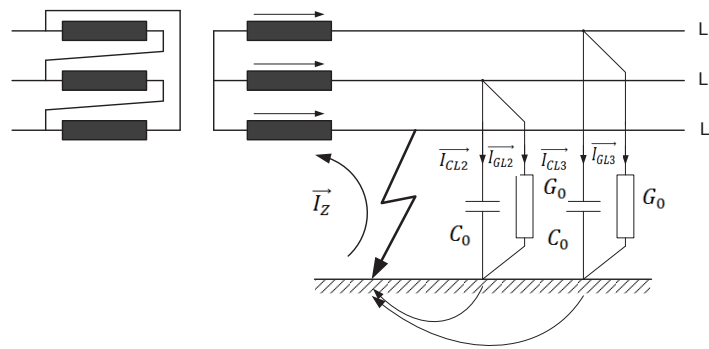


Figure 1 Current flows in the grid at earth fault in phase L1

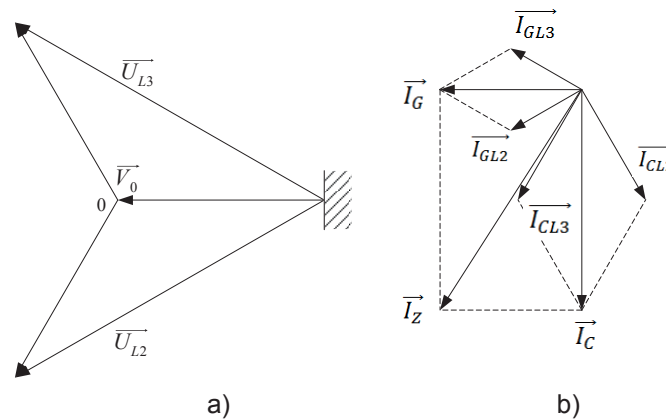


Figure 2 Vector diagram for a) voltages and b) currents at earth fault in phase L1

From Fig.1. and Fig.2 for the capacitive current \vec{I}_C and conductance current \vec{I}_G it can be easily written [8]:

$$\vec{I}_C = 3 * \vec{V}_F * C_0 * j\omega \quad (1)$$

$$\vec{I}_G = 3 * \vec{V}_F * G_0 \quad (2)$$

Where \vec{V}_F is the vector of the rated phase voltage, C_0 is the earth capacitance, and G_0 is the conductance.

Looking at the vector diagram it can be concluded that the earth fault current $|I_Z|$ is:

$$|I_Z| = \sqrt{|I_G|^2 + |I_C|^2} \approx |I_C|. \quad (3)$$

$|I_G|$ is usually not larger than a small percentage of $|I_C|$. \vec{V}_F je vektor nazivnog faznog napona.

As already mentioned, in isolated neutral point networks single-phase earth faults do not need to be switched off automatically since the currents are small and the network can remain in operation until the fault is detected. This allows the fault to turn off by itself. After the earth fault current is switched off, a return voltage occurs whose amplitude can be up to two times the amplitude of the rated phase voltage. This greatly obstructs the conditions of self-shutdown and can lead to reignition of the arc which will further cause intermittent overvoltages. Intermittent overvoltages are the consequence of the superposition of potentials after each reignition of the arc to a static potential from the previous shutdown of the arc. The occurrence of intermittent overvoltages in isolated neutral point networks can not be prevented. But it is rare in distribution networks and the surges themselves do not endanger properly dimensioned isolation. Only where the insulation is weaker due to improper design or damage there is a risk of expansion on a double earth fault.

Network protection under such conditions is often only signalization and personnel on duty have enough time to detect the earth fault and take measures to solve the problem. Networks with isolated neutral point are allowed operation if the capacitive earth current is not too large. If the capacitive current exceeds the previously mentioned values, it is recommended to divide the network or ground the neutral point.

The advantages of isolated neutral point networks are as follows [5]:

- the arc will be extinguished if it is a transient failure for earth fault with relatively low capacitive currents. This increases the quality of electricity supply,
- relatively easy earthing design,
- simplicity and economical design,
- possibility to resume network operation until the fault is located.

The disadvantages of these networks are:

- possibility of intermittent overvoltages with a high surge voltage factor,
- higher internal surges compared to when the grid is earthed,
- more difficult detection of faults compared to when the network is earthed,
- in case of high- capacitance earth fault currents, no self-shutdown of the fault.

2.2. Low-ohmic resistor grounding of neutral point

Distribution networks are grounded via low-ohmic resistance if the capacitive current exceeds the values mentioned in the previous subsection. This reduces the internal voltage surges, eliminates the possibility of intermittent overvoltages and provides a more reliable protection.

In this grounding system, the single-phase fault current is closed not only through the zero capacitances of the healthy phases, but also through the low-ohmic resistance. This earth fault current, which is increased in comparison to the current when neutral point is isolated, provides a stable electric arc at the place of fault, thus preventing the formation of intermittent overvoltages. Even with consecutive reignition of the arc no static potential can be achieved. With larger fault currents it is easier to detect the fault and design the protection, but there is a problem of network disconnection at each fault, which interrupts the supply of electricity to the consumers [9].

For networks grounded over a small resistor R_Z , shown in Fig.3, every earth fault in the network must be switched off as it is a short circuit. The earth fault current \vec{I}_Z is [8]:

$$\vec{I}_Z = \frac{3 \cdot \vec{V}_F}{\vec{Z}_d + \vec{Z}_i + \vec{Z}_0} \approx \frac{3 \cdot \vec{V}_F}{2 \cdot \vec{Z}_{v+T} + \vec{Z}_{0v+T} + 3 \cdot R_Z} \quad (4)$$

where $\vec{Z}_d, \vec{Z}_i, \vec{Z}_0$ are the vectors of the direct, inverse and zero impedance of the network in the location of the fault, \vec{V}_F is the vector of the rated phase voltage, and \vec{Z}_{v+T} and \vec{Z}_{0v+T} are the vectors of the operational and zero impedance of the transformer and faulty line.

Since following expression is usually valid:

$$3 \cdot R_Z \gg |2 \cdot \vec{Z}_{v+T} + \vec{Z}_{0v+T}|, \quad (5)$$

the earth fault current can be calculated with:

$$\vec{I}_Z \approx \frac{\vec{V}_F}{R_Z} \quad (6)$$

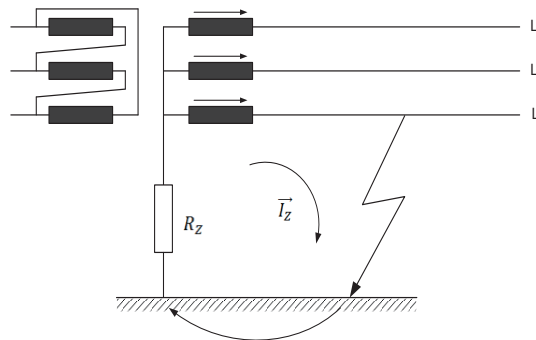


Figure 3 Current flows in the grid at earth fault in phase L1

When selecting the resistor size for neutral point grounding two conflicting criteria should be considered [10]:

- technical regulations on the dangerous contact voltages in substations,
- the values of the internal overvoltages occurring when single-phase faults occur.

According to the criteria for dangerous contact voltages it is desirable to have a low single-phase fault current so that the contact voltages are lower. On the other hand, it is desirable that the current is large as much as possible to allow the internal surge voltages, which can break the insulation during the faults, to be as low as possible. In order for the internal voltage surges to remain within the acceptable values, the resistor should be selected so that it satisfies the criterion $I_R:I_C \geq 3:1$, or $I_R:I_C \geq 1,5:1$ when the rounding conditions are difficult.

For networks grounded with a low-ohmic resistor the earth fault must be switched off as soon as possible due to high values of the fault current that are limited by the resistance value of the resistor. Compared to the isolated networks, in these networks there is a breakdown protection for the resistor itself. The resistor connection to the neutral point of the transformer along with the protection scheme is shown in Fig. 4.

For the selection of the protection, the relevant current is the earth fault current I_{K1} , the remaining current of the faulty line when earth capacitances are ignored \vec{I}_{k1} , and the residual current in the health line \vec{I}_{r1} . They can be calculated with the following equations [11]:

$$I_{K1} = \frac{\sqrt{3} * U_n}{2 * Z_d + Z_0 + 3 * R_n + 3 * Z_K'} \quad (7)$$

$$\vec{I}_{r1} = \vec{I}_{K1}, \quad (8)$$

$$\vec{I}_{r1} = 3 * \vec{I}_{02} = - \frac{3 * j\omega * C_{02} * R_Z * \vec{V}}{R_Z + R_K * (1 + 3 * j\omega * C_0 * R_Z)}, \quad (9)$$

where \vec{I}_{02} is the vector current of the healthy line, C_{02} is the earth capacitance of the healthy line, and C_0 is the total earth network capacitance.

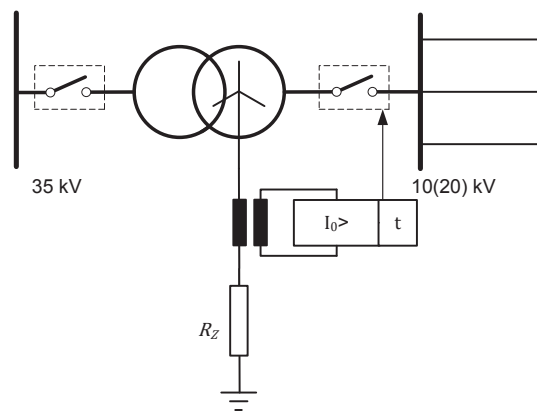


Figure 4 Low-ohmic grounded neutral point protection

The earthing resistor used in Croatia, depending on the network type, is chosen so it satisfies single-fault current limitation limits of 300 A, 150 A and 50 A. The relay protection of these networks consists of the protection of medium voltage lines, transformers protection, and resistors protection.

The advantages of grounding networks grounded via low-ohmic resistors are [11]:

- simple and reliable protection when compared to the isolated neutral point networks,
- no intermittent overvoltages,
- lower internal voltage surges when compared to the isolated neutral point networks,
- easier detection of fault location.

The disadvantages of such grounded networks are [11]:

- all faults cause power outages, which is undesirable due to reduced quality of electricity supply,
- higher values of fault currents when compared to the isolated neutral point networks which means dangerous contact voltages.

2.3. Partial compensation

Partial compensation is the name for type of network grounding by means of parallel coil and low-ohmic resistor. The neutral point grounding by means of a parallel coupling of a fixed coil and a low-ohmic resistor represents a technical solution that is of a transitional character depending on the magnitude of the capacitive current of the network. This solution is an upgrade to the technical solution of the grounding via the low-ohmic resistor. It is economically acceptable, especially for capacitive currents up to about 150 A after which the grounding should be done by means of an automatically adjustable arc suppression coil.

Owing to the power network expansion, especially the greater number of cable lines, the capacitive currents in the network are increased. When the capacitive current of the network exceeds 50 A for dangerous contact voltages it is preferable to limit the current of single-phase fault. A technical solution for the capacitive current cutoff consists of a parallel connection of a manually adjustable coil with an existing low-ohmic resistor. In Croatia, a 150 A and 50 A short-circuit current resistor is used in combination with a 30-to-150 A fixed coil with the ability of manual adjustments in seven degrees of 20 A.

Such a solution achieves partial compensation with the residual minimum reactive current, while still retaining other features of the low-ohmic resistor grounding and therefore no changes in protective devices are required. Manual regulation is carried out in a state without voltage.

Due to the inductive current, the system can be sub-compensated or overcompensated, and therefore a fault current can be found either in III. or II. quadrant compared to the reference voltage of the neutral point. Compared to the

automatically adjustable arc suppression coil, a manually adjustable coil, which is combined with a parallel low-ohmic resistor, is not designed to shut off short-term faults, but only serves for the compensation of the capacitive current component.

Resistor current selection depends on the size of the contact voltages defined by the technical regulations. A single-phase short circuit current through the neutral point is dictated by the current limited by the resistor. Inductive current of the coil reduces the capacitive current of the network. For partial compensation with a fixed coil and a low-ohmic resistor the residual value of the capacitive current I_C in the network is [12]:

$$I_C = I_{Cnetwork} - I_L, \quad (10)$$

where $I_{Cnetwork}$ is the network capacitive current and I_L is the inductive current of the coil. The current of the single-phase fault I_{1k} is then:

$$I_{1k} = \sqrt{I_R^2 + I_C^2}, \quad (11)$$

where I_R is the current limited by the resistor.

The relay protection located in power transformer cells consists of the protection of medium voltage lines, protection of transformers and protection of resistors in combination with a fixed coil. Transformers are usually protected by short-circuit protection, overload protection and single-phase fault protection, and larger units also with differential protection. Transformer protection is coupled to the primary side so that the single-phase transformer fault depends on the neutral point grounding of the voltage to which a transformer is connected. Medium voltage lines are protected by short-circuit protection, overload protection and single-phase short-circuit protection.

Relay protection of transformers, lines and the combination resistor-coil is the same as in the networks grounded with low-ohmic resistors. The protection of a single-phase short circuit in network with partial compensation is shown in Fig. 5. The protection of the resistor consists of a three-stage overcurrent protection, which ensures protection against breakdown, protection of single-phase fault in lines and protection against high-ohmic faults in the network.

The advantages of networks with partial compensation are [12]:

- It is an economically good solution if previously the network was grounded via a low-ohmic resistor,
- no additional investment is required,
- the internal voltage surges are slightly lower than in the low-ohmic resistor networks,
- it is not necessary to change the protection system if previously the network was grounded via a low-ohmic resistor,
- no intermittent overvoltages.

Disadvantages of these networks are [12]:

all faults cause power outages, which is undesirable due to reduced quality of electricity supply.

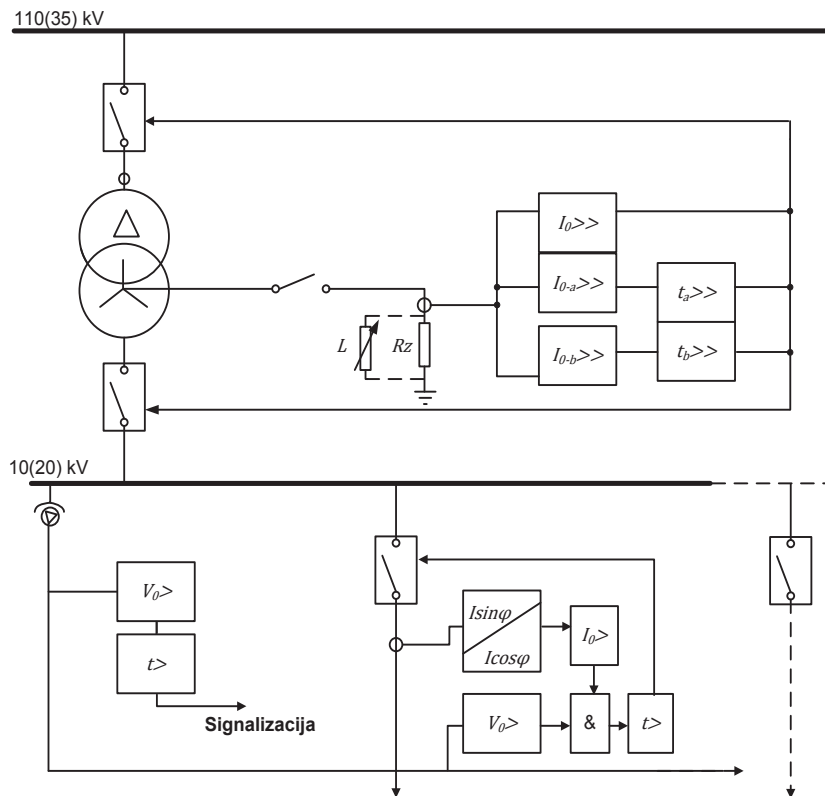


Figure 5 Schematic of protection for partial compensation network

2.4. Resonant grounded neutral point

As was already mentioned, more frequent use of cable lines in the power networks causes increase of capacitive currents [13]. The consequences are an increase of the internal voltage surges as well as the earth fault currents. When the single-phase earth fault current is greater than the maximum permissible, the operation of the network with the isolated neutral point is not possible because the likelihood of self-shutdown of the fault is reduced. This is just one of the reasons why lately the resonant grounding is considered more frequently. This type of grounding is achieved by the grounding of the neutral point via an automatic compensating coil also called Petersen coil [14].

The application of the resonant grounding shows the best results if the inductance of the compensating coil is adapted to the earth capacity of the network. Such grounding reduces currents of earth faults and slows down the recovery voltage over the fault location. This leads to higher maximum permissible fault currents compared to the isolated networks.

The principle of the compensating coil consists of compensating capacitive currents in the network by means of variable inductance as an active part of the network [13]. Fig. 6 shows conditions during the earth fault in phase L1 of the compensated network with negligible low resistance of the arc R_K at the fault location. It is assumed that the line impedance and admittance are negligible. Since

earth fault protection with time-specific or inverse characteristics is up to 15 k Ω , the vatmeter protection can selectively detect failures at resistance ranges up to 3 k Ω .

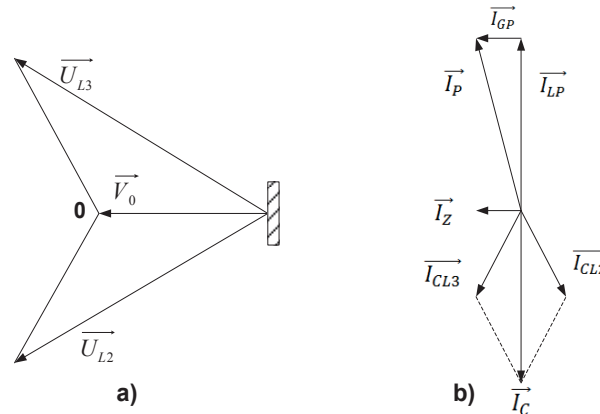


Figure 7 Vector diagram for a) voltages and b) currents for the case of full compensation

It should be noted that earthing via the coil is not efficient in the cable networks since there the earth fault presents a permanent fault and the cable must be switched off immediately.

The advantages of grounding through the compensating coil are:

- low current through the fault location enables self-shutdown of the fault, increasing the quality of electricity supply,
- a slower return voltage reduces the likelihood of intermittent overvoltage generation,
- the minimum risk of too high potential on transformer earthing leads to lower economic cost of the repairs,
- the least thermal stresses compared to other grounding systems,
- the current at fault location is reduced and the theoretically around zero,
- at fault location voltage is reduced to almost zero.

The disadvantages of resonant grounding are [14]:

- the need for more sensitive and therefore more expensive protection,
- considerable investment costs,
- a higher isolation level of equipment is needed as the healthy phase voltages rise to the line value of the voltage during earth fault.

2.5. Shunt circuit-breaker

As was mentioned in the previous chapters, numerous short-term faults can be technically solved by installing an automatic compensation coil. However, as the cost of installing the coil is high another way to reduce the number of power failures is needed. The solution is to use shunt circuit-breakers. Shunt circuit-breaker is a

three-phase circuit-breaker with three separate mechanisms, one for each pole. It is a technical solution developed in France, where it is mostly used.

If a single-phase short circuit occurs, the shunt circuit-breaker, along with the associated protective relay, detects the faulted phase. Then, the command for the corresponding pole of the circuit breaker is switched on connecting the faulty phase directly to the ground. The fault current, which was the arc current before, is then flowing through the pole of the shunt circuit breaker and a low-ohmic resistor with or without the parallel coil. This current is limited by the resistance of the low-ohmic resistors. At the fault location there is no longer any voltage to the ground, which would maintain an electric arc, and the arc will turn off if the failure is transient. After a certain time, which is usually set at a value between 150 and 300 ms, a command to switch off the pole of the shunt circuit-breaker is given. If the fault was transient, the network works normally after switching off the shunt circuit-breaker and consumers did not feel the fault existed because the line itself was not switched off. If it is not a transient fault, but a permanent one, the built-in earth fault protection switches off the faulty line after a certain set time.

Some of the criteria that should be considered when deciding to install shunt circuit-breakers are [16].:

- the number of transient faults,
- the share of overhead lines in the network,
- insulation level of the cable lines in the network,
- existing system of neutral point grounding,
- the power system user number and their requirements.

It is necessary to consider the event statistic of the network. Particular attention should be paid to the number of transient faults. The shunt circuit-breaker can solve this problem without the interruption of the electricity supply. If the insulation level of the cable part of the network is too low, after the installation and start of the shunt circuit-breaker operation malfunctions might be caused by overvoltages on the weakened parts of the network. Therefore, it is necessary that the insulation level is not too low or that the weakened cables are replaced.

The shunt circuit-breaker is installed in networks grounded via a low-ohmic resistance or partially compensated networks.

3. Analysis of protection relays used in 35/10(20) kV substations in Croatia

Protective relays and their functions are responsible for the protection of the power system apparatus. A survey was sent to the 21 domain operators of the Croatian distribution system operator. The survey was answered by 13 domain operators: Zagreb (DP Elektra Zagreb), Split (DP Elektrodalmacija), Rijeka (DP Elektroprimorje), Pula (DP Elektroistra), Osijek (DP Elektroslavonija), Zadar (DP Elektra Zadar), Šibenik (DP Elektra Šibenik), Dubrovnik (DP Elektrojug), Karlovca

(DP Elektra Karlovac), Sisak (DP Elektra Sisak), Zabok (DP Elektra Zabok), Križ (DP Elektra Križ) and Vinkovci (DP Elektra Vinkovci). The survey encompasses the relay protection of 35/10(20) kV substations which present around 90-95% of substations in Croatia. Here, the analysis of relays used for the protection of the neutral point grounding system field is presented [2].

The total number of analyzed relays is 53. It can be seen from table I that 60,15% of the substations are equipped with numerical relays, 35,85% of the substations have static relays, and there are no electromechanical relays. Graphical representation of this is given in Fig.1.

Table I Relay types used in substations

<u>Type of relays</u>	<u>Nb. Of substations for the relay type</u>	<u>Nb. Of lines where the relay is embedded</u>
NUMERICAL	27	34
STATIC	15	19
E-M	0	0
HV FUSE	91	118

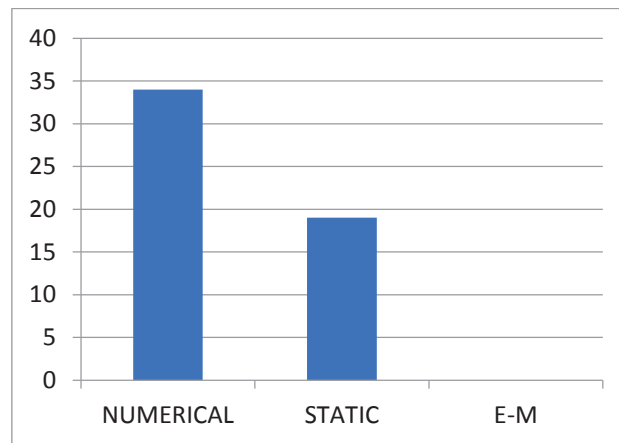


Figure 8 Graphical representation of used relays by type

Tables II and III give the data about the most used relays in substations and their activated functions. Table III gives data about most commonly used relays by operator domain. Operators of the domains usually prefer one or two manufacturers of the same relay as this means that it was easier for the communication between the remote-control center and the substations. Today, with the IEC 61850 standard used for communication this will no longer be necessary.

Table II The three most used relays in the substations for neutral point protection

<u>Manufacturer</u>	<u>Model (type)</u>	<u>Nb. Substations</u>	<u>Nb. Lines</u>	<u>Activated functions</u>
KONČAR	RIVC264E	5	9	I>, I>>
SIEMENS	7SJ600	7	8	I>, I>>, 50BF
ISKRA	TIF1220	7	7	I>

Table III The most common relay used in substations by operator domain

<u>Domain operator</u>	<u>Manufacturer</u>	<u>Model (type)</u>	<u>Nb. of substations</u>	<u>Nb. of fields</u>
KRIŽ				
VINKOVCI	SIEMENS	7SJ600	5	5
RIJEKA	KONČAR	RV117E	2	2
PULA	ISKRA	TFI1220	6	6
SISAK	SIEMENS	7SJ600	1	1
KARLOVAC	ALSTOM	P127	3	4
ZABOK	ALSTOM	P139	1	2
DUBROVNIK				
ZADAR	ABB	SPAJ324C4	3	3
ZAGREB				
OSIJEK	KONČAR	RIVC264E	4	8
SPLIT				
ŠIBENIK				

Data about relay manufacturers is given in Fig.2. The manufacturers are almost evenly represented, with a slight preference toward Končar.

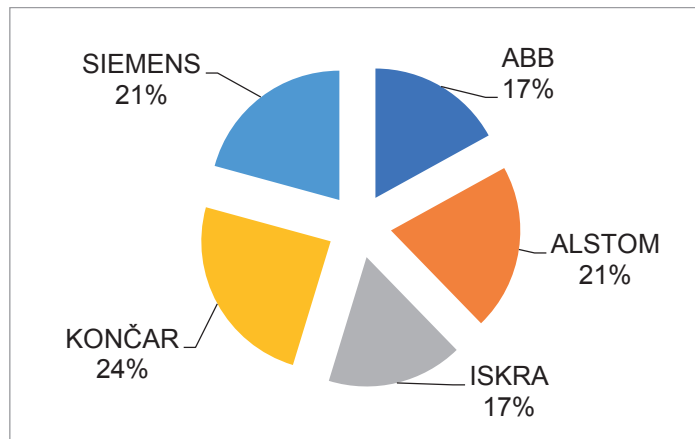


Figure 9 Graphical representation of used relays by manufacturer

Relay protection functions that are, according to the survey, used in the protection of the neutral point grounding system are:

- overcurrent protection ($I >$);
- instantaneous overcurrent protection ($I >>$);
- zero sequence overcurrent protection ($I0 >$);
- instantaneous zero sequence overcurrent protection ($I0 >>$);
- directional zero sequence overcurrent protection ($I0 > \square$);
- directional overcurrent protection ($I > \square$);
- breaker failure protection (50BF);
- overvoltage protection ($U >$);
- undervoltage protection ($U <$);
- zero sequence overvoltage protection ($U0 >$);
- zero sequence undervoltage protection ($U0 <$).

4. CONCLUSION

The neutral point grounding method significantly influences network operating conditions, power stability, human security, the type and cost of equipment, and the choice of network configuration and relay protection. Given that each method has certain advantages and disadvantages, there is no single approach to the grounding of the neutral point of the medium voltage networks. This paper gives the overview of several ways to ground the neutral point of the medium voltage network. Additionally, the paper presents the analysis of the protective relays used for the protection of the neutral point grounding system in 35/10(20) kV substations in Croatia. Since not all of the domain operators have answered the survey a further analysis with larger data should be part of future research.

5. REFERENCES

- [1]. A. Drandic, "Power system neutral grounding", M.S. thesis, FER Zagreb, 2014.
- [2]. M. Drandic, "Protective functions in substations 35/10(20) kV", M.S. thesis, FER Zagreb, 2012.
- [3]. J. Đerek, "Uzemljenje neutralne točke srednjenaponskih razdjelnih mreža", M.S. thesis, FER Zagreb, 2004.
- [4]. I. G. Kuliš, "Rezonantno uzemljenje neutralne točke srednjenaponskih mreža za distribuciju električne energije", M.Sc. thesis, FER, Zagreb, 2003.
- [5]. J. Ćurković, "Zemljospojna zaštita razdjelne mreže uzemljene preko kompenzacijske prigušnice", M.S. thesis, FER Zagreb, 2005.
- [6]. J.M. Nahman, *Uzemljenje neutralne tačke distributivnih mreža*, Naučna knjiga, Beograd, 1980.
- [7]. V. Komen, R. Ćučić, V. Sirotnjak, "Neutral point treatment in distribution networks", *HO CIRED 1.session*, Šibenik, 2008.
- [8]. F. Božuta, M. Golubović, *Aspekti zaštite elektroenergetskog sistema*, Svjetlost, Sarajevo, 1988.
- [9]. S. Žutobradić, M. Damianić M., "Konceptija uzemljenja zvjezdišta mreža 10(20) kV u budućnosti", *Journal of Energy*, nb.1, pp. 41-47., 1999.
- [10]. S. Žutobradić, "Aktualno stanje provedbe uzemljenja zvjezdišta srednjenaponskih mreža", *Journal of Energy*, nb. 4, pp. 203-208, 1993.
- [11]. S. Drandić, N. Rudan, "Izbor i podešavanje relejne zaštite maloohmskog otpornika za uzemljenje SN mreže primjenom digitalnih releja", *CIGRE 5. session*, Cavtat, 2001.

- [12]. E. Sterpin, "Prijedlog primjene kompenzacijske prigušnice s ručnom regulacijom u sprezi s otpornikom u mreži 10(20)kV Elektroistre", *Journal of Energy*, pp. 441.-446., 2005.
- [13]. G. Šagovac, I. Watson, "Improvement of quality of supply in medium voltage networks with resonant earthing of neutral point", *HO CIREĐ 1.session*, Šibenik, 2008.
- [14]. M. Damianić, "Analiza parametara uzemljenja zvjezdišta 10(20) kV mreže", M.Sc. thesis, FER Zagreb, 2001.
- [15]. D. Franković, "Određivanje parametara zaštitnih i regulacijskih uređaja u rezonantno uzemljenim srednjenaponskim mrežama", Ph.D. thesis, FER, Zagreb, 2009.
- [16]. V. Komen, R. Čučić, V. Sirotnjak, "Operating experiences in a distribution network with shunt circuit breaker", *HO CIREĐ 1.session*, Šibenik, 2008.

MATEJ KR PAN**IGOR KUZLE**matej.krpan@fer.hrigor.kuzle@fer.hr

**University of Zagreb Faculty of Electrical Engineering and
Computing**

THE MATHEMATICAL MODEL OF A WIND POWER PLANT AND A GAS POWER PLANT

SUMMARY

To enable conduction of quality research of power system dynamics using computer simulation software, appropriate mathematical and simulation models have to be developed. In the last two decades, an exponential increase of installed wind power capacity can be observed, while the gas power plant capacity and energy production has also seen an increase in the recent years. Consequently, their impact on power system dynamics is no longer negligible. Furthermore, the increased penetration of wind power has led to a lot of research concerning frequency support capabilities from wind power plants (WPPs). In this paper, after a brief theoretical introduction, simplified system frequency response (SFR) simulation models of a generic wind power plant and a gas power plant have been developed in MATLAB. These generic models have been integrated with existing SFR models of a steam and hydro unit. The model contains a representation of under-frequency load shedding (UFLS) and demand response, as well. Graphical user interface (GUI) has been developed to control this expanded model.

Key words: wind power plant; gas power plant; primary frequency regulation; power system; MATLAB

1. INTRODUCTION

To reduce the carbon footprint of the power & energy sector, many countries throughout the world introduced various measures encouraging the integration of renewable energy sources (RES). The most popular energy sources for renewable power generation are the photo-voltaic (PV) plants and the wind power plants (WPPs): in 2016, installed PV capacity was 291 GW and installed WPP capacity was 467 GW in the world [1] and will continue to rise. On the other hand, United States Energy Information Administration predicts a grow of 2.1% per year for electrical energy generation from natural gas from 2015 to 2017 [2]. In the grid frequency control context, the turbine dynamics dictate the frequency response dynamics after a disturbance. More precisely, grid inertia dictates the rate-of-change-of-frequency (RoCoF) while the turbine dynamics associated with the governor dynamics and mechanical dynamics dictate the behavior of primary frequency response.

Most wind turbines today are converter-connected to the grid which ensures electricity production at nominal grid frequency independent of the actual rotational speed of the turbine. However, this effectively decouples the mechanical and electrical frequency of the wind energy conversion system (WECS) [3] which means there will be no inertial response from WPPs after a disturbance occurs. Coupled with the fact that WPPs do not participate in primary frequency control, the frequency stability of a power system is getting more and more jeopardized. To combat this issue, a lot research has been conducted to utilize the kinetic energy of the wind turbine blades and high controllability of variable-speed drives for frequency support. The overview of the aforementioned research has been extensively covered in [4]–[7].

Gas power plants have also enjoyed an increase in their share of total electricity production since new materials and technologies with better thermodynamic efficiency are being constantly developed. Furthermore, natural gas is the least carbon-intensive of all fossil fuels (carbon dioxide emissions are about half the rate of coal) and it is also attractive for new power plants because of low capital costs and relatively low fuel cost [2]. Gas power plants are usually utilized as peaking power plants but can also be used as load following power plants in systems with an insufficient capacity of hydro power.

Low-order system frequency response (SFR) model provides a simple framework for studying power system frequency changes by considering only the most dominant time constants in the power system in the time scale of inertial response and primary frequency response. Based on the concept of average system frequency, it gives a good-enough estimate of the grid frequency behavior. As this is a very well-known and widely used approach, it will not be discussed anymore. For further reading, refer to [8]. In most of scientific literature, SFR model of a power system is used where only one type of turbine is represented, usually steam or hydro turbine. Rarely is there a mix of different turbines represented, e.g. steam-hydro (e.g. [9]), while gas turbines are rarely used for simulations, e.g. [10]–[12]. Wind turbines have not been represented so far because they did not participate in frequency response. The goal of thesis [4] was to research the existing literature

and expand the steam-hydro SFR model [9] in the way that, finally, it includes a model of a gas turbine as well as a model of a wind turbine (with frequency support capability). In this paper, the most important results of [4] will be summarized and discussed. Rest of the paper is structured as follows: in section 2 an SFR model of a gas turbine is presented; in section 3 an SFR model of a wind turbine is developed which exploits pitch angle control for primary frequency control; in section 4 an expanded power system SFR model is presented which includes a wind, gas, steam and hydro turbine along with a UFLS scheme and a demand response (DR) representation in the SFR context. Some examples of simulations are shown here. Section 5 concludes the paper.

2. A GENERIC GAS TURBINE MODEL FOR SFR SIMULATIONS

Gas turbine development lagged behind steam turbine development foremost because of material limitations (gas is burning at higher temperatures) and technical complexity of the design. From the conceptual standpoint, the gas turbine is similar to a steam turbine in a way that the output power is controlled by valves which govern the fuel supply. General theory of operation, main components and different types of gas turbines and gas power plants have been succinctly described in [4]. Conclusively, it is not necessary to individually model different types of gas power plants (GPPs) for this application because the gas turbines are virtually identical in the context of dynamic response: combined-cycle power plants use separate gas and steam turbines while cogeneration plants and big GPPs use gas turbines with similar if not identical dynamic properties.

A typical gas turbine model for power system stability studies is shown in Figure 1. According to Figure 1 [11], the control design consists of three control circuits: temperature control, speed control and acceleration control. To simplify the model even more, temperature and acceleration control will be ignored. The reasoning behind this simplification lies in the fact that these control circuits are active during abnormal conditions: temperature controller keeps the turbine blades from damaging when the temperature in the combustion chamber is too high by limiting the fuel supply. Acceleration controller is usually only active during start-up and shut-down. The temperature is assumed to be always in the normal range and that the turbine is operating in steady-state around normal operating point where small perturbations are applied to simulate the primary frequency response. Thus, only speed control and fuel-turbine dynamics will be considered. The generic low-order SFR model of a GPP is shown in Figure 2, where Δf , ΔP_m are the small change in frequency and active power, respectively. R_{GT} , T_g , T_{VP} , T_{FS} and T_{CD} are governor droop, governor servo time constant and time constants related to valve positioning, fuel dynamics and compressor discharge, respectively. Typical values of these constants are given in Table I.

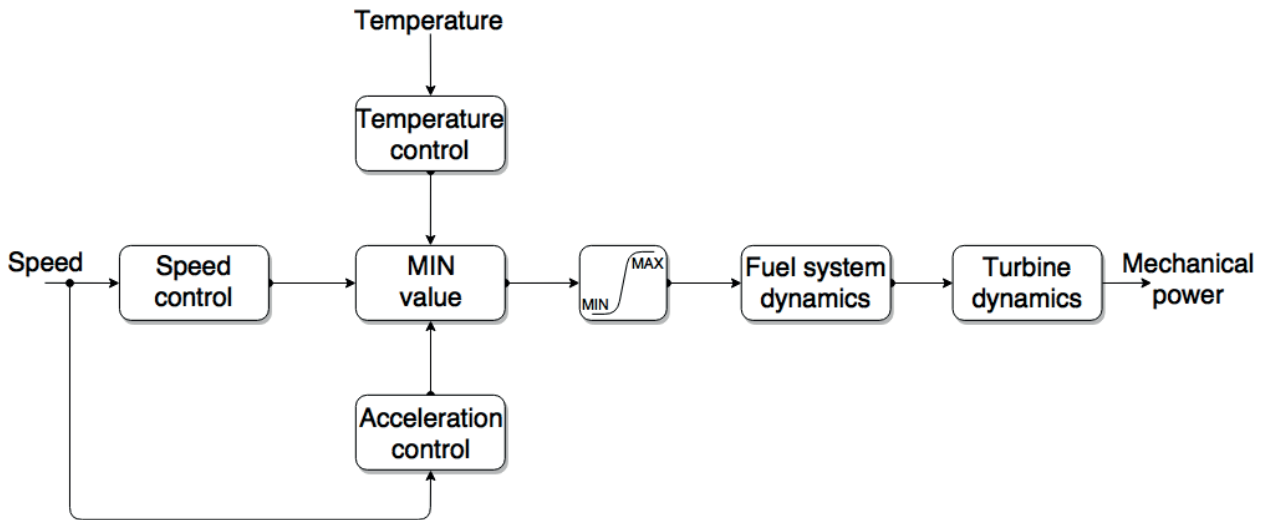


Figure 1. General gas turbine model for power system stability studies

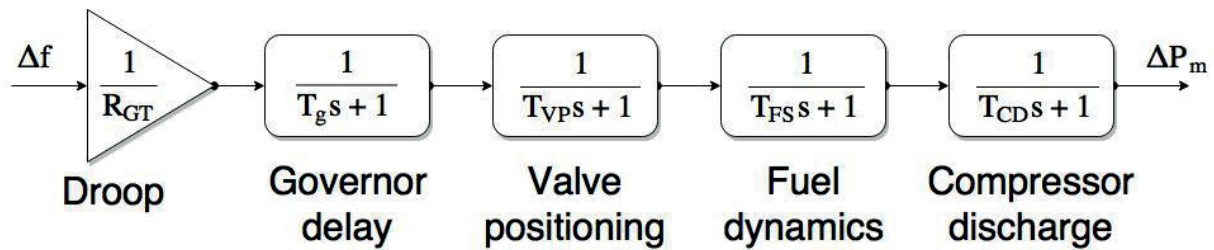


Figure 2. Gas power plant SFR model

Table I. Typical values of gas turbine parameters

According to:	R_{GT}	T_g [s]	T_{VP} [s]	T_{FS} [s]	T_{CD} [s]
Weimin <i>et al.</i> [10]	3 – 6%	-	0,1	-	0,94
Zhang and So [12]	2 – 10%	0,1	0,1	0,4	0,4

The difference in values can be explained by the fact that authors in [12] use standard IEEE governor models with typical recommended values, while authors in [10] used real gas turbine experimental data to identify the gas turbine parameters. A combined-cycle plant has been used in both [10] and [12].

3. A GENERIC WIND TURBINE MODEL FOR SFR SIMULATIONS

Before the SFR model of a wind turbine is developed, it is necessary to classify different types of wind turbines since they have different characteristics and dynamic behavior which determine how those turbines are modelled. After the brief overview of wind turbine generator topologies, frequency support from wind turbines is briefly discussed. Finally, the general assumptions which the simplified modelling is based upon are laid down and the generic wind turbine SFR model is developed.

3.1. Overview of wind turbine generator topologies

Different wind turbine generator topologies are shown in Figure 3. The wind turbine itself doesn't differ between different topologies since horizontal axis wind turbines have the same blade design concept. The difference between wind turbine topologies comes from the generator-converter pair.

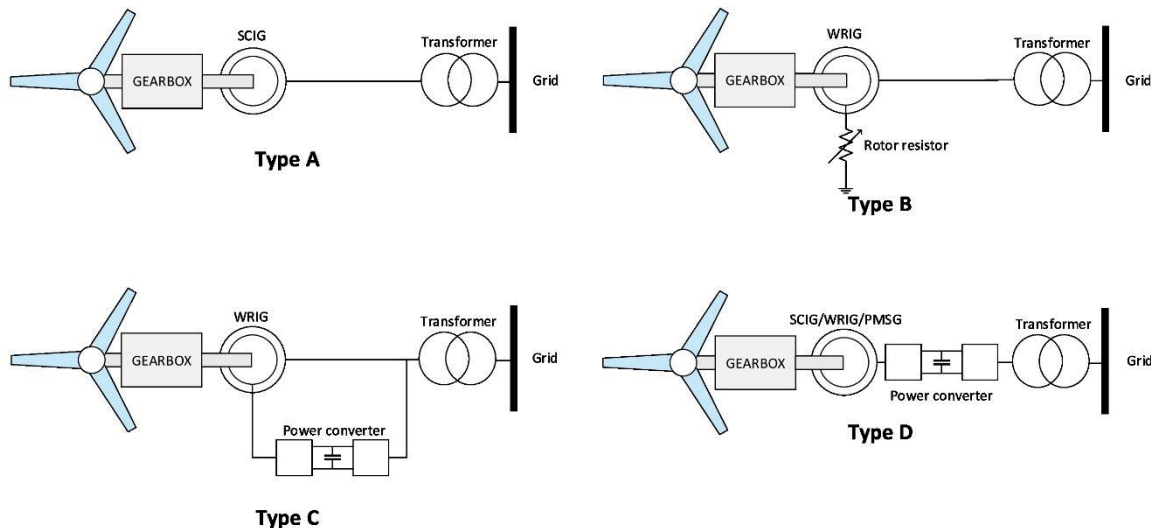


Figure 3. Wind turbine generator topologies

Type A is the fixed-speed wind turbine which utilizes a squirrel cage induction generator (SCIG). Rotor speed is quasi-fixed with the slip less than 1% and dictated by the grid frequency. Type A wind turbine is connected to the grid only through a transformer. Type B is the variable-slip wind turbine. It utilizes a wound rotor induction generator (WRIG) with a variable rotor resistor to control the slip between 0–10% in super-synchronous mode. It is also connected to the grid through a transformer.

Variable-speed wind turbines (VSWTs) can be divided into Type C (partially decoupled using partially rated frequency converter) and Type D (fully decoupled using fully-rated frequency converter). Both are connected to the grid through a power converter interface. The former topology is called a doubly-fed induction generator (DFIG) which uses a (WRIG), while the latter is in literature sometimes called full-scale converter (FSC) wind turbine generator which can utilize SCIG or permanent magnet synchronous generator (PMSG) for geared solutions; or PMSG and wound rotor synchronous generator (WRSG) for direct-drive solutions.

3.2. Grid frequency support provision from wind turbines

In this paper, the emphasis of frequency support is on the time scales of inertial response and primary frequency response. Capability of a wind turbine to provide frequency support depends on its topology. Type A and Type B wind turbines have inherent inertial response since they are directly connected to the grid. A spinning reserve can be obtained by pitch angle control in Type A and by

pitch angle control or variable rotor resistance in Type B [13], however the operating speed range is very limited, and it is difficult to control the spinning reserve with the pitch control, while the frequent use of rotor resistance generates more heat which is wanted minimized. Type C and D wind turbines are significantly more controllable, and the spinning reserve is achieved easier due to the power electronic interface. On the other hand, this power electronic interface, decouples the mechanical behavior of the turbine and electrical behavior on the grid side, thus removing the inertial response. More on inertial response and primary frequency control from wind turbines can be found in [13],[14]. Wind turbines do not usually participate in inertial or primary frequency response of a power system, but as the share of wind power in power systems worldwide keeps growing, system operators are recognizing the need to include WPPs in ancillary services related to frequency support and some have already implemented various measures[5].

3.3. Developing the wind turbine SFR model

Although Type A and Type B wind turbines still exist in power systems today, they are probably at the end of their life span and are being pushed out by types C and D due to their superior aerodynamic efficiency and controllability [4]. Therefore, in this paper, the focus is on VSWTs and they are the ones which will be modelled in the rest of the paper. WECS is a complex electromechanical system and the order and the type of modelling depends on the type of intended simulations. For power system dynamics & stability simulations (more precisely, for studying power system frequency changes by low-order SFR models in this case), certain assumptions have to be made which will enable the simplification and the reduction of the model order. These assumptions are very well documented in [15]–[18]:

- Rotor is modelled as a lumped-mass because shaft dynamics are hardly reflected on the grid side;
- flux dynamics in the stator and rotor voltage equations are neglected which results in algebraic generator equations. Therefore, the generator is modelled as an electrical torque source. Fast action of power electronic converters means the new set-point is reached almost instantaneously.

3.3.1. Rotor model

Mechanical power developed at the turbine shaft is expressed as:

$$P_m = \frac{1}{2} \rho R^2 \pi v^3 C_p(\lambda, \beta) \quad (1)$$

where ρ is the air density, R is the rotor radius, v is the wind speed, C_p is the aerodynamic coefficient which is a function of the pitch angle β and the tip-speed ratio λ . The tip-speed ratio is defined as the ratio of the blade tip velocity and the wind velocity:

$$\lambda = \frac{\omega_t R}{v} \quad (2)$$

where ω_t is the angular velocity of the turbine. A generic numerical expression for C_p from [17] is used:

$$C_p(\lambda, \beta) = 0.73 \left(\frac{151}{\lambda - 0.02\beta} - \frac{0.453}{\beta^3 + 1} - 0.58\beta - 0.002\beta^{2.14} - 13.2 \right) e^{-\left(\frac{18.4}{\lambda - 0.02\beta} - \frac{0.0552}{\beta^3 + 1} \right)}. \quad (3)$$

The $C_p - \lambda$ curves are shown in Figure 4 with pitch angle β in degrees as a parameter. It can be seen that for every pitch angle there exists an optimal tip-speed ratio for which the aerodynamic efficiency is maximized. This also holds true for every wind speed. Therefore, the generator speed is controlled in a way that will maximize the tip-speed ratio for a given wind speed. This is called maximum-power-point-tracking (MPPT).

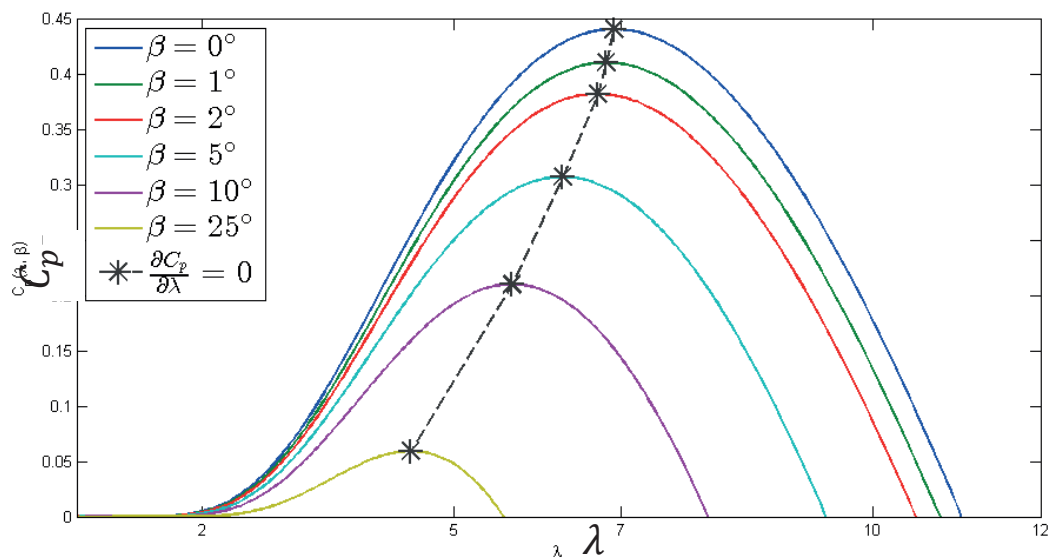


Figure 4. Graphical representation of $C_p - \lambda$ curves for β as a parameter [4]

In this paper, the achieved deloading has been achieved solely by pitch angle control and the extra active power injection after a disturbance is achieved by pitching the blades which most closely resembles a tradition turbine governing. However, this is not the most accurate approach nor the only approach: the wind turbine is controlled differently depending on the wind conditions [19], and the pitch angle controller is usually active only during high wind speeds. Moreover, a spinning reserve can be achieved by generator speed control during lower wind speeds. Nevertheless, to avoid taking into account different control modes, the pitch angle control has been chosen as a mechanism for primary frequency response of a wind turbine ignoring the actual wind conditions.

Generator power—rotor speed curve is described in [19] in more detail. Succinctly, it represents the control action by which the wind turbine generator speed and output power is controlled. The control action (e.g. minimum and maximum speed control, MPPT, power control) depends on the current wind conditions. However, in this paper, only MPPT mode is considered. Here, the generator power is proportional to the cube of generator speed

$$P_e = k_g \omega_g^3 - K_e \delta f \quad (4)$$

where k_g is the generator power—speed curve coefficient and ω_g is the generator mechanical (high-speed shaft) speed. The value of coefficient k_g depends on the turbine parameters, but also on the base values for which the equations are normalized in p.u. values. This MPPT curve is shown in Figure 5 for different wind speeds. This generator power reference is offset when a frequency disturbance δf occurs, with K_e being the gain of the proportional controller.

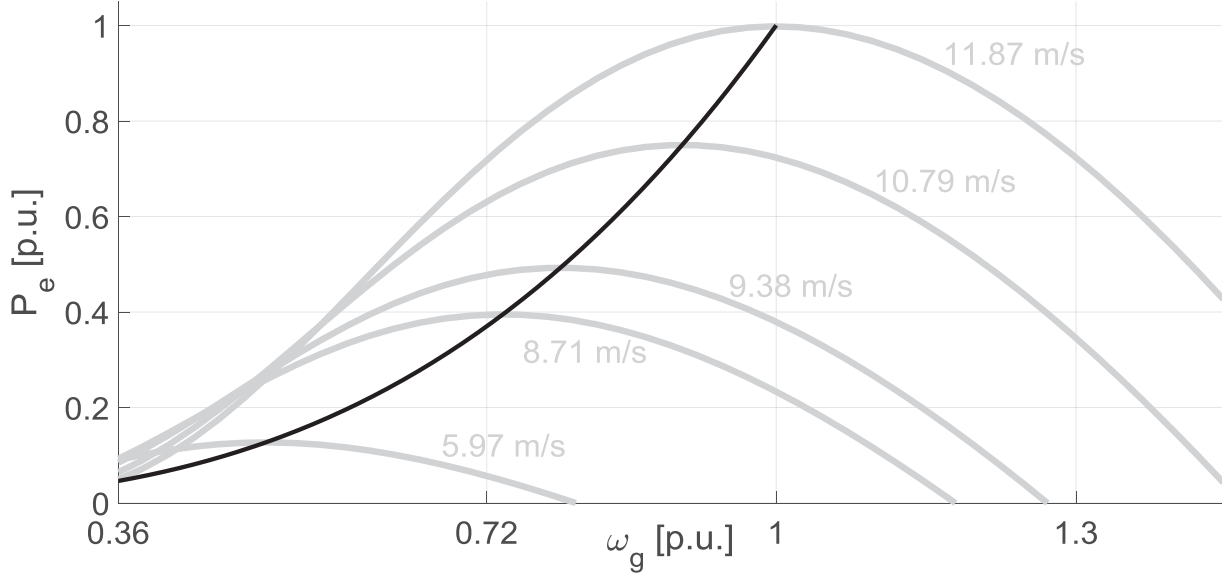


Figure 5. MPPT curve

Pitch angle is usually only active during high wind speeds to limit the aerodynamic torque exerted on the turbine, but here it will also be used to reserve a certain power margin and to control the pitch angle during a frequency disturbance. P controller is used instead of a PI controller to further simplify the model [17] and the pitch control servomechanism is modeled as a first-order lag as described by (5).

$$T_s \frac{d\beta}{dt} = -\beta + K_m \delta f \quad (5)$$

T_s is the servo time constant and the other half of frequency control is completed by the $K_m \delta f$ member, where K_m is the gain of the proportional controller. K_e and K_m can be considered analogous to the droop gain of conventional turbine systems, but here the former changes the generator setpoint, while the latter changes the mechanical power by controlling the aerodynamic torque.

The motion equation completes the wind turbine model:

$$2H_{WT} \frac{d\omega_g}{dt} = \frac{P_m - P_e}{\omega_g} \quad (6)$$

Rotor acts as a buffer and the high-frequency components of the wind speed signal is evened out over the rotor surface [18]:

$$T_w \frac{dv}{dt} = -v + u \quad (7)$$

where u is the raw wind speed signal, and low-pass filter time constant T_W is set to 4 seconds [18].

Equations (1), (4), (5), (6) and (7) represent the simplified mathematical model of the turbine. The aforementioned expressions are linearized around initial operating point to obtain the SFR model of a wind turbine. The state-space model is described by (8), (9), while the complete derivation can be found in [4]. Numerical values of coefficients $a_{1,1}$ – $a_{1,3}$ and c_1 – c_3 are given in the Table III in the Appendix.

$$\begin{pmatrix} \Delta \dot{\omega}_t \\ \Delta \dot{\beta} \\ \Delta \dot{v} \end{pmatrix} = \mathbf{A} \begin{pmatrix} \Delta \omega_t \\ \Delta \beta \\ \Delta v \end{pmatrix} + \mathbf{B} \begin{pmatrix} \Delta f \\ \Delta u \end{pmatrix} \quad (8)$$

$$\Delta P_m = \mathbf{C} \begin{pmatrix} \Delta \omega_t \\ \Delta \beta \\ \Delta v \end{pmatrix} + \mathbf{D} \begin{pmatrix} \Delta f \\ \Delta u \end{pmatrix}$$

$$\mathbf{A} = \begin{pmatrix} \frac{a_{1,1}}{2H_{WT}} & \frac{a_{1,2}}{2H_{WT}} & \frac{a_{1,3}}{2H_{WT}} \\ 0 & -\frac{1}{T_s} & 0 \\ 0 & 0 & -\frac{1}{T_W} \end{pmatrix} \quad \mathbf{B} = \begin{pmatrix} \frac{K_e}{2H_{WT}} & 0 \\ \frac{K_m}{T_s} & 0 \\ 0 & \frac{1}{T_W} \end{pmatrix} \quad (9)$$

$$\mathbf{C} = (c_1 \quad c_2 \quad c_3) \quad \mathbf{D} = (0 \quad 0)$$

From (8), (9) the transfer function that represents the generic low-order SFR model of a VSWT is derived:

$$\mathbf{G}(s) = \begin{pmatrix} K_m \frac{(2K_m(c_2 a_{11} - a_{12} c_1) - K_e c_1) - s(2K_m c_2 H_{WT} + K_e c_1 T_s)}{2(sT_s + 1)(a_{11} - sH_{WT})} \\ \frac{1}{sT_w + 1} \frac{c_3 a_{11} - a_{13} c_1 - c_3 H_{WT} s}{a_{11} - sH_{WT}} \end{pmatrix} \quad (10)$$

4. EXPANDED SFR MODEL OF A POWER SYSTEM

The final goal of [4] was to expand the existing SFR model of a power system which includes a steam turbine [20] and a hydro turbine [9] so that it includes the gas turbine and a wind turbine as well. This model developed in MATLAB/Simulink environment is shown in Figure 6, and it also includes the dynamic demand response (DR) model [21] and the UFLS scheme. The used steam and hydro turbine models, as well as the UFLS model and DR model are shown in the Appendix.

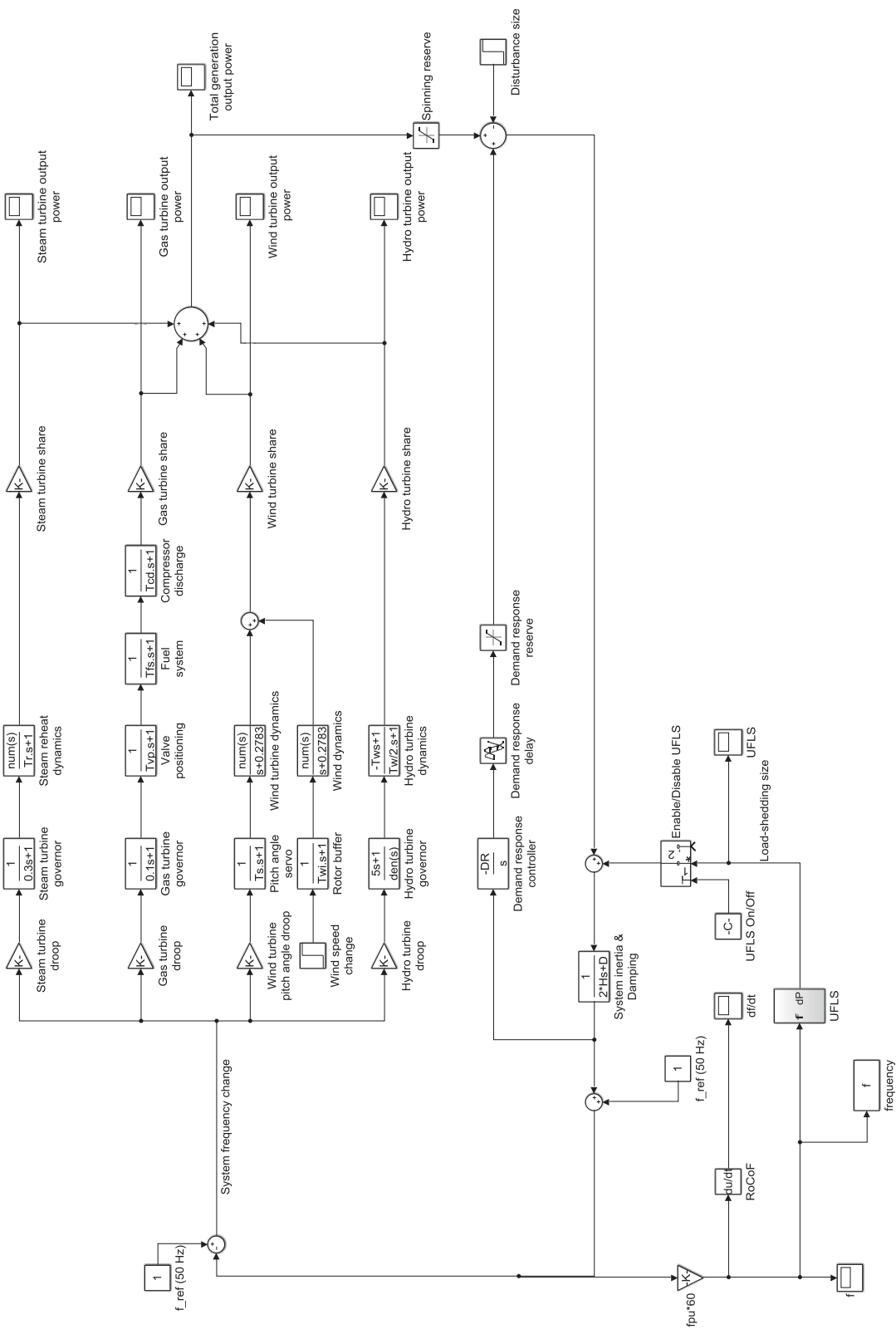


Figure 6. Expanded SFR model of a power system

4.1. Graphical user interface of the model

Graphical user interface has also been created in MATLAB GUIDE environment (Figure 7). It enables the user to easily change different parameters and run an arbitrary number of simulations while the results figures (system frequency and power output of power plants) are generated automatically (Figure 8).

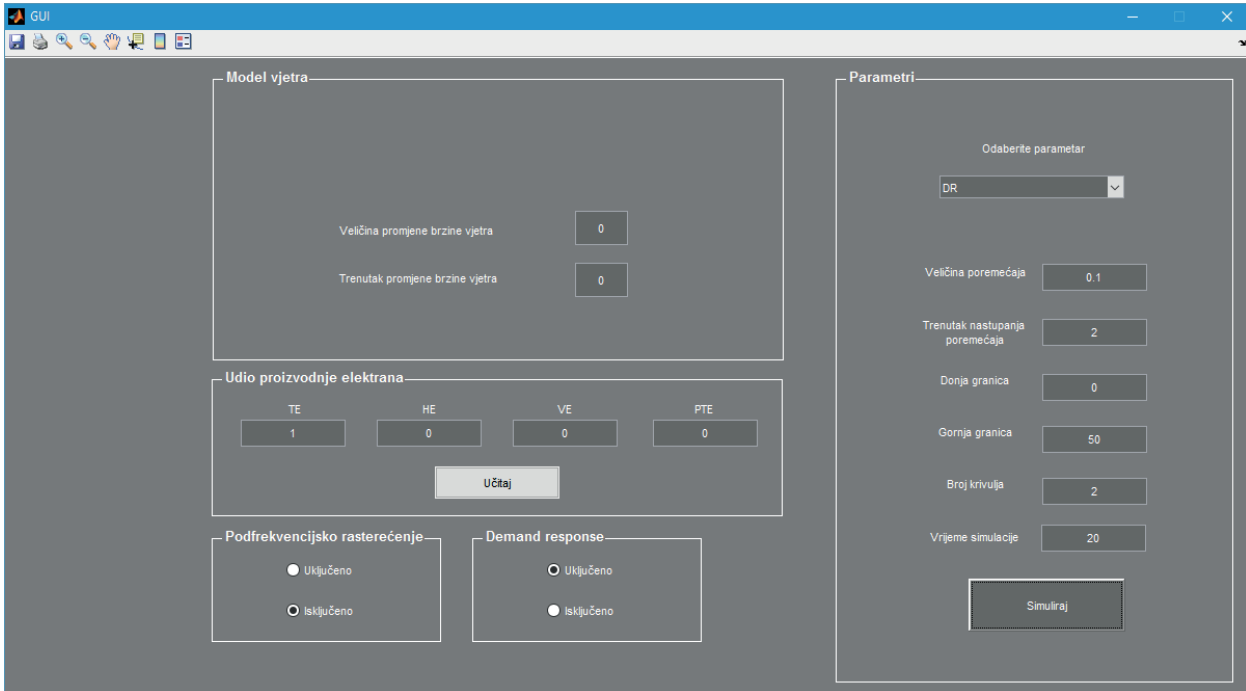


Figure 7. Screenshot of a graphical user interface of the developed model

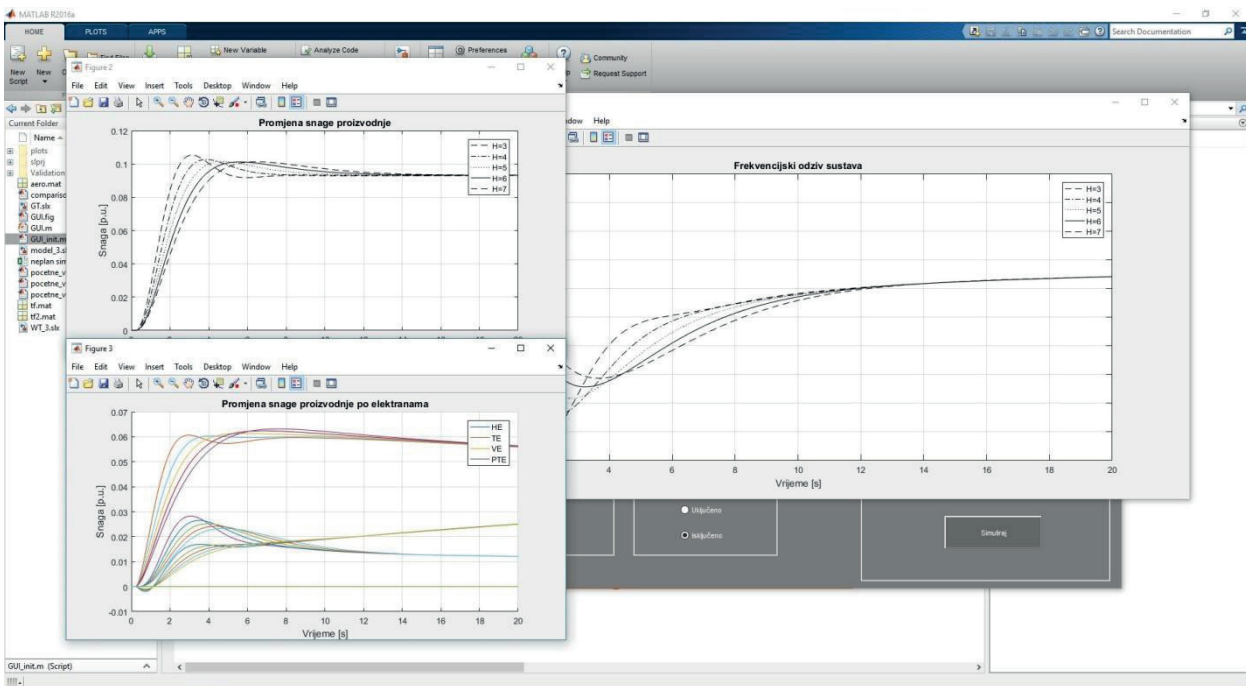


Figure 8. Screenshot of automatically generated figures

4.2. Simulation examples

Now, the presented SFR model can be used to study power system frequency dynamics for different operational scenarios (e.g. different generation mix, increase of wind power penetration, inertia reduction, etc.) and how different parameters influence the frequency dynamics (e.g. turbine droop, turbine time constants, etc.). Default simulation parameters are shown in Table II; if some parameter is changed during the simulations, the rest are held constant according to Table II.

Table II. Default simulation parameters

Steam turbine				Hydro turbine					Gas turbine				
R	T_2 [s]	F_H	T_R [s]	R	T_W [s]	T_2 [s]	T_3 [s]	T_4 [s]	R	T_g [s]	T_{VP} [s]	T_{FS} [s]	T_{CD} [s]
0.05	0.3	0.3	8	0.04	1	0.5	5	50	0.06	0.1	0.1	0.4	0.4
System				Demand response					Wind turbine				
H [s]	D	ΔP_D [p.u.]	K_{DR}		T_d [s]			H_{WT} [s]	K_m	K_e	T_s [s]		
4	1	0.05	10		0.2			3	20	20	0.25		

4.2.1. Impact of wind power share in the generation mix on the frequency response

Starting with a system with 50% hydro power and 50% thermal power (similar to the Croatian power system), the share of wind power capacity is increased in the increments of 5% (this is offset by the reduction of steam units), but the wind power plants do not have any frequency support capabilities. A load disturbance $\Delta P_D = 0.05$ p.u. is applied. From Figure 9, it can be seen that the increase of the wind power in the system worsens the frequency response of the system: nadir and steady-state error are larger.

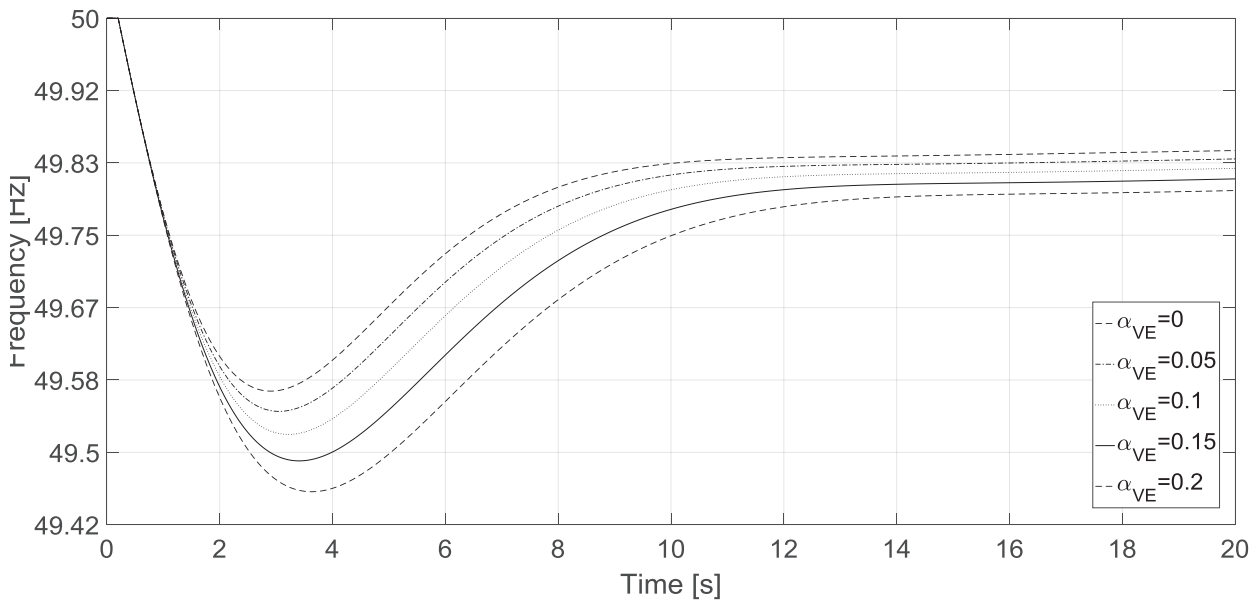


Figure 9. Frequency response of a system for different wind power penetration

4.2.2. Impact of participation of WPPs in primary frequency response

For a system with 40% thermal power, 40% hydro power and 20% wind power, the frequency response is studied for when there is no active power contribution from WPPs and for when the WPPs are deloaded 10% and they can inject extra active power after a disturbance. Results are shown in Figure 10. It can be seen that participation of WPPs in primary frequency response can significantly improve the system frequency response because the power set-point of a VSWT can be changed almost instantaneously. This is an illustrative example and the real contribution depends on WPP frequency controller gains as well as the instantaneous capability of WPPs to provide reserve power which depends on the wind conditions:

- if the wind speeds are too low they will not participate in frequency control;
- if the wind speeds are too high they will shut down to protect the turbine;
- the actual amount of power reserve may be lower since the 10% is quite high and a lot of wind energy is wasted in this case.

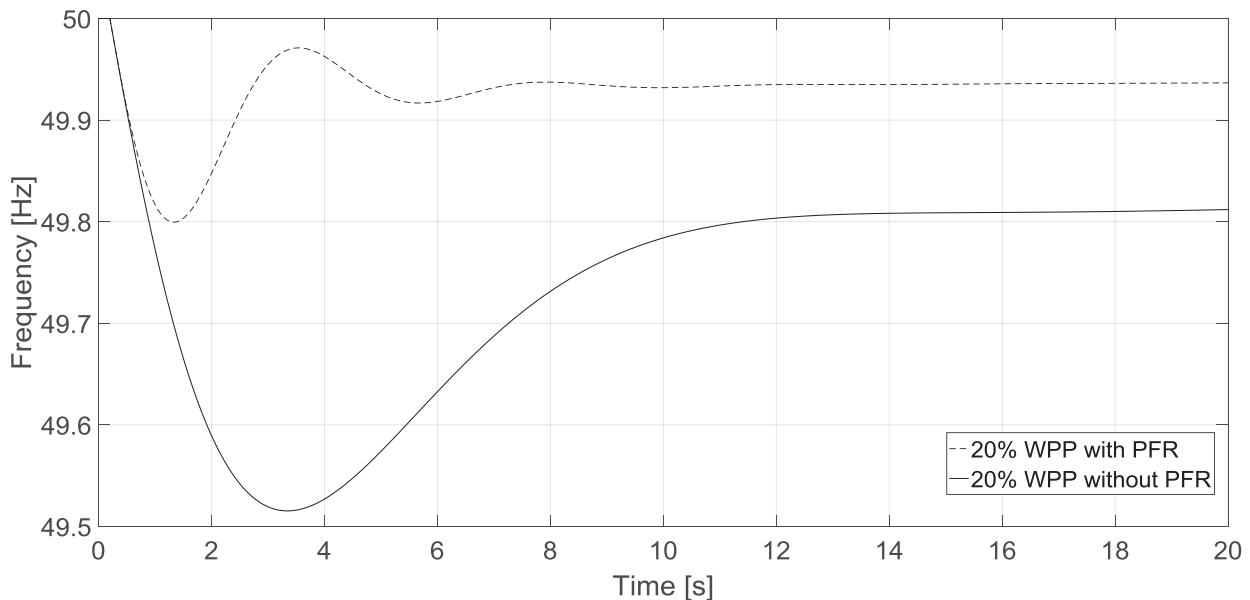


Figure 10. Impact of primary frequency response (PFR) from WPPs on system frequency

4.2.3. Impact of gas turbine share in the generation mix on the frequency response

Starting with a system with 50% hydro power and 50% thermal power, the share of gas power plants is increased in the increments of 5% (this is offset by the reduction of hydro units). From Figure 9, it can be seen that the increase of the gas turbines in the system reduces the frequency nadir since the gas turbines have a much faster response than hydro turbines, but also, hydro turbines are non-minimal phase shift systems due to the water inertia and the output power is reduced immediately after a disturbance which contributes to worse frequency response—gas turbines do not possess that characteristic.

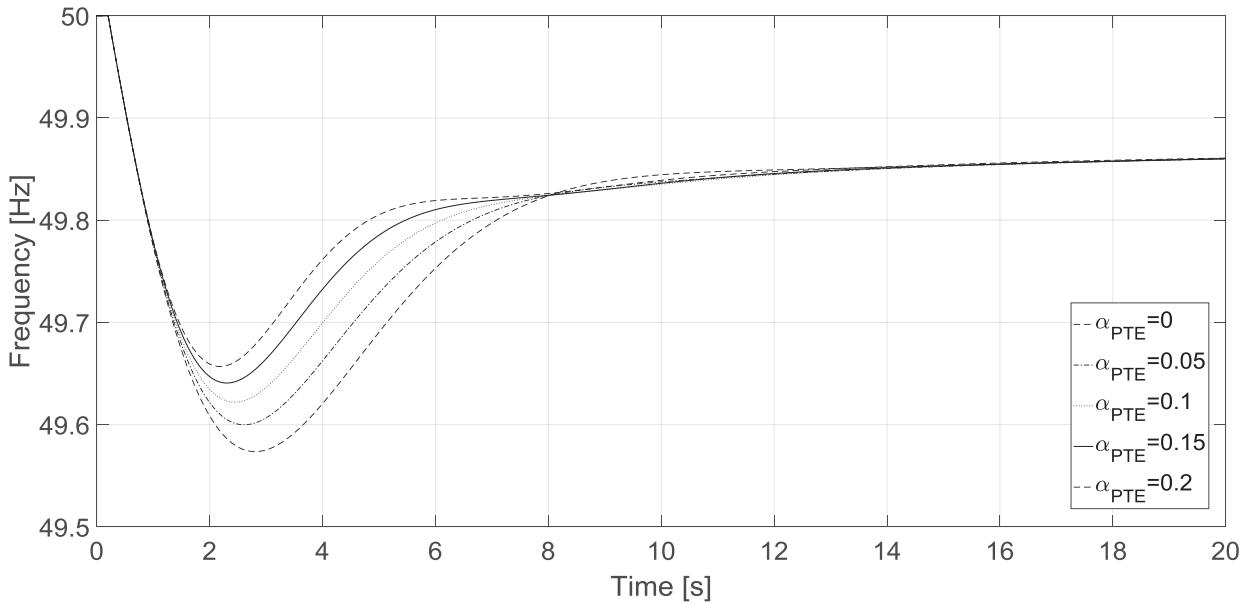


Figure 11. Impact of gas turbine share on frequency response

4.2.4. Impact of dynamic demand response on frequency response

Introduction of a dynamic demand response can improve frequency nadir and the steady-state error of frequency as seen in Figure 12. After a disturbance, smart, responsive loads lower their power consumption which can help in maintaining system stability. Some examples of these kinds of loads are electric water heaters or HVAC systems [21].

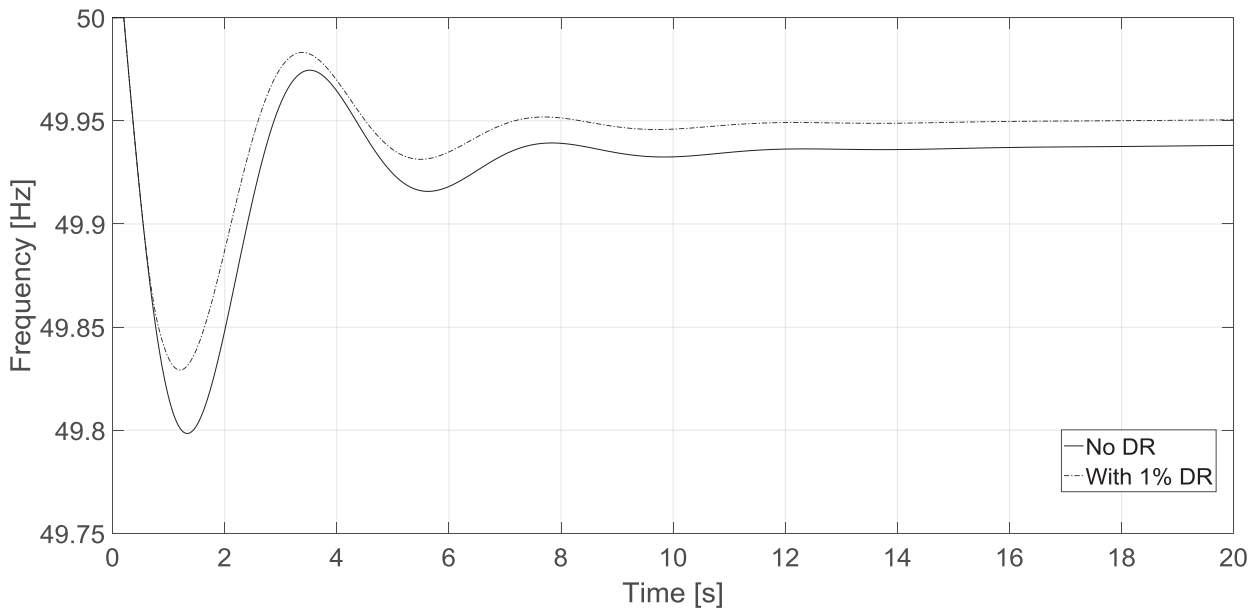


Figure 12. Impact of dynamic demand response on system frequency

5. CONCLUSION

This paper summarizes the main results of [4]. With the development of new energy technologies and smart grid technologies, power systems throughout the world are changing. Since not many power systems consist only of thermal or hydro units, the goal was to expand existing SFR model of a steam-hydro system to now include the gas turbines and wind turbines because their share is not anymore insignificant. Moreover, as smart, responsive loads also show great promise for balancing services, a dynamic model of a demand response has also been incorporated. Since modern wind turbines are converter-connected to the grid they are insensitive to changes in grid frequency. Therefore, a simplified model of a wind turbine which utilizes pitch angle control and generator-converter control to obtain an active power reserve which is injected to the grid upon an active power disturbance in the system by supplementary Δf control which is analogous to the turbine governor response for primary frequency control. The expanded SFR model now contains the 4 most common types of turbines (steam, hydro, gas and wind), dynamic demand response and an UFLS scheme to simulate load shedding. The SFR models are easy to implement and can be used to qualitatively study power system frequency changes without the need to model detailed grids in power system simulation software which requires knowledge of a lot of parameters. A graphical user interface has been created to quickly change simulation parameters, run numerous simulations and generate graphical results.

6. REFERENCES

- [1] International Renewable Energy Agency. "Renewable energy capacity statistics 2017", 2017. <http://www.irena.org>, accessed 12 November 2017.
- [2] U.S. Energy Information Administration. "International Energy Outlook 2017", 2017. <https://www.eia.gov/outlooks/ieo/>, accessed 3 January 2018.
- [3] J. G. Slootweg, S. W. H. de Haan, H. Polinder, and W. L. Kling, "General model for representing variable speed wind turbines in power system dynamics simulations," *IEEE Trans. Power Syst.*, vol. 18, no. 1, pp. 144–151, 2003.
- [4] M. Krpan, "The mathematical and simulation model of a wind power plant and a gas power plant", master thesis, University of Zagreb Faculty of Electrical Engineering and Computing, September 2016.
- [5] M. Krpan and I. Kuzle, "Inertial and primary frequency response model of variable-speed wind turbines," *Publ. J. Eng.*, 2017.
- [6] M. Krpan and I. Kuzle, "Linearized model of variable speed wind turbines for studying power system frequency changes," in *17th IEEE International Conference on Smart Technologies, EUROCON 2017 - Conference Proceedings*, 2017.
- [7] Z. Wu *et al.*, "State-of-the-art review on frequency response of wind power plants in power systems," *J. Mod. Power Syst. Clean Energy*, Sep. 2017.

- [8] P. M. Anderson and M. Mirheydar, "A low-order system frequency response model," *IEEE Trans. Power Syst.*, vol. 5, no. 3, pp. 720–729, 1990.
- [9] I. Kuzle, T. Tomisa, and S. Tesnjak, "A mathematical model for studying power system frequency changes," *IEEE AFRICON Conf.*, vol. 2, Gaborone, Botswana, pp. 761–764, 2004.
- [10] K. Weimin, X. Junrong, G. Lian, and D. Yiping, "Study on the mathematical model and primary frequency regulation characteristics of combined cycle plants," *2011 Second Int. Conf. Mech. Autom. Control Eng.*, pp. 2632–2635, 2011.
- [11] P. Centeno, I. Egido, and C. Domingo, "Review of gas turbine models for power system stability studies," *9th Spanish Port. Congr. Electr. Eng.*, pp. 1–6, 2005.
- [12] Q. Zhang and P. L. So, "Dynamic modelling of a combined cycle plant for power system stability studies," *Power Eng. Soc. Winter Meet. 2000. IEEE*, vol. 2, no. c, pp. 1538–1543 vol.2, 2000.
- [13] E. Muljadi, M. Singh, and V. Gevorgian, "Fixed-speed and variable-slip wind turbines providing spinning reserves to the grid," *IEEE Power Energy Soc. Gen. Meet.*, no. November 2012, 2013.
- [14] E. Muljadi, V. Gevorgian, and M. Singh, "Understanding Inertial and Frequency Response of Wind Power Plants," *2012 IEEE Power Electron. Mach. Wind Appl.*, no. July, pp. 1–8, 2012.
- [15] J. G. Slootweg, H. Polinder, and W. L. Kling, "Dynamic modelling of a wind turbine with doubly fed induction generator," *2001 Power Eng. Soc. Summer Meet. Conf. Proc. (Cat. No.01CH37262)*, vol. 1, pp. 644–649 vol.1, 2001.
- [16] J. G. Slootweg, H. Polinder, and W. L. Kling, "Dynamic modeling of a wind turbine with direct drive synchronous generator and back to back voltage source converter," *Conf. Eur. Wind Energy Conf. Copenhagen*, July, 2001.
- [17] J. G. Slootweg, S. W. H. de Haan, H. Polinder, and W. L. Kling, "General model for representing variable speed wind turbines in power system dynamics simulations," *IEEE Trans. Power Syst.*, vol. 18, no. 1, pp. 144–151, 2003.
- [18] J. G. Slootweg, H. Polinder, and W. L. Kling, "Representing Wind Turbine Electrical Generating Systems in Fundamental Frequency Simulations," *IEEE Trans. Energy Convers.*, vol. 18, no. 4, pp. 516–524, 2003.
- [19] G. Abad, J. Lopez, M. A. Rodriguez, L. Marroyo, and G. Iwanski, *Doubly fed induction machine: modeling and control for wind energy generation*, 1st ed. John Wiley & Sons, 2011.
- [20] M. Lukic, I. Kuzle and S. Tesnjak, "An Adaptive Approach to setting Underfrequency Load Shedding Relays for an Isolated Power System with Private Generation," *IEEE MELECON '98*, Tel-Aviv, Israel, pp. 1122–1125, 1998.
- [21] S. A. Pourmousavi and M. H. Nehrir, "Introducing dynamic demand response in the LFC model," *IEEE Trans. Power Syst.*, vol. 29, no. 4, pp. 1562–1572, 2014.

7. APPENDIX

7.1. Numerical values of linearized wind turbine model

Linearization of the presented wind turbine model includes some parameters that depend on the initial condition around which the model is linearized. Due to the high complexity (nonlinearity) of the mathematical expressions, only numerical values are given. These parameters are shown in Table III. The definition of these parameters is given in [4] and are not repeated here, but they originate during the Taylor's series expansion neglecting higher order terms during the linearization process.

Table III. Numerical values of the SFR wind turbine model parameters [4]

v [p.u.]	$a_{1,1}$	$a_{1,2}$	$a_{1,3}$	c_1	c_2	c_3
0.9	-1.1273	-0.0100	1.0547	-0.7233	-0.0200	2.1093
0.95	-1.2550	-0.0118	1.1751	-0.8064	-0.0236	2.3502
1.00	-1.3913	-0.0138	1.3021	-0.8931	-0.0275	2.6041
1.05	-1.5346	-0.0159	1.4355	-0.9843	-0.0318	2.8710
1.1	-1.6832	-0.0183	1.5755	-1.0809	-0.0366	3.1510

7.2. Steam reheat turbine model, hydro turbine model, dynamic demand response model and UFLS scheme model.

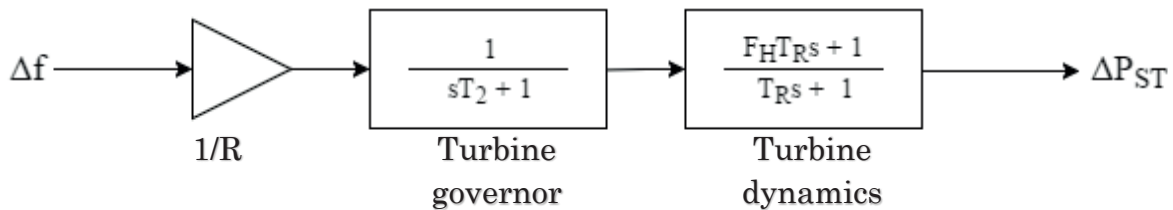


Figure 13. SFR model of a steam reheat turbine

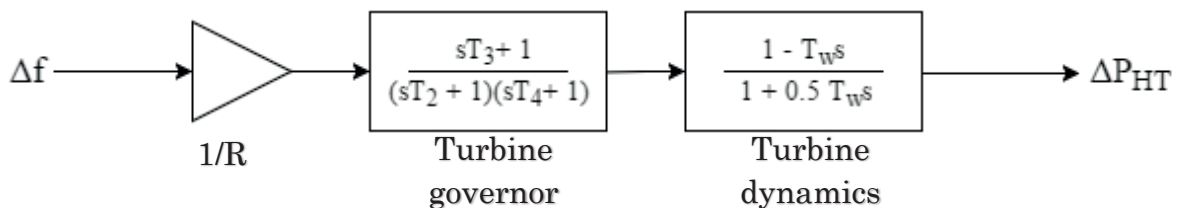


Figure 14. SFR model of a hydro turbine

Table IV. Typical values of turbine parameters [4]

Steam	R	T_2 [s]	F_H	T_R [s]	
	2% – 7%	0.2 – 0.3	0.3	4 – 11	
Hydro	R	T_2 [s]	T_3 [s]	T_4 [s]	T_w [s]
	2% – 4%	0.5	5	50	0.5 – 5

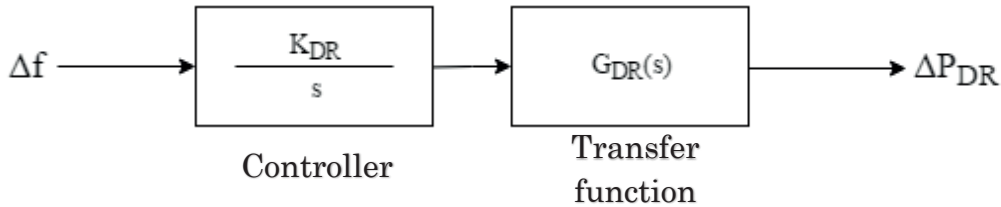


Figure 15. Dynamic demand response model of a hydro turbine

$G_{DR}(s)$ represents an 2nd order approximation of the transport delay e^{-sT_d} [21]:

$$G_{DR}(s) = \frac{\frac{3360}{T_d^3} s^2 - \frac{15120}{T_d^4} s + \frac{30240}{T_d^5}}{\frac{3360}{T_d^3} s^2 + \frac{15120}{T_d^4} s + \frac{30240}{T_d^5}} \quad (11)$$

where $T_d \leq 0.5$ s and K_{DR} is arbitrary.

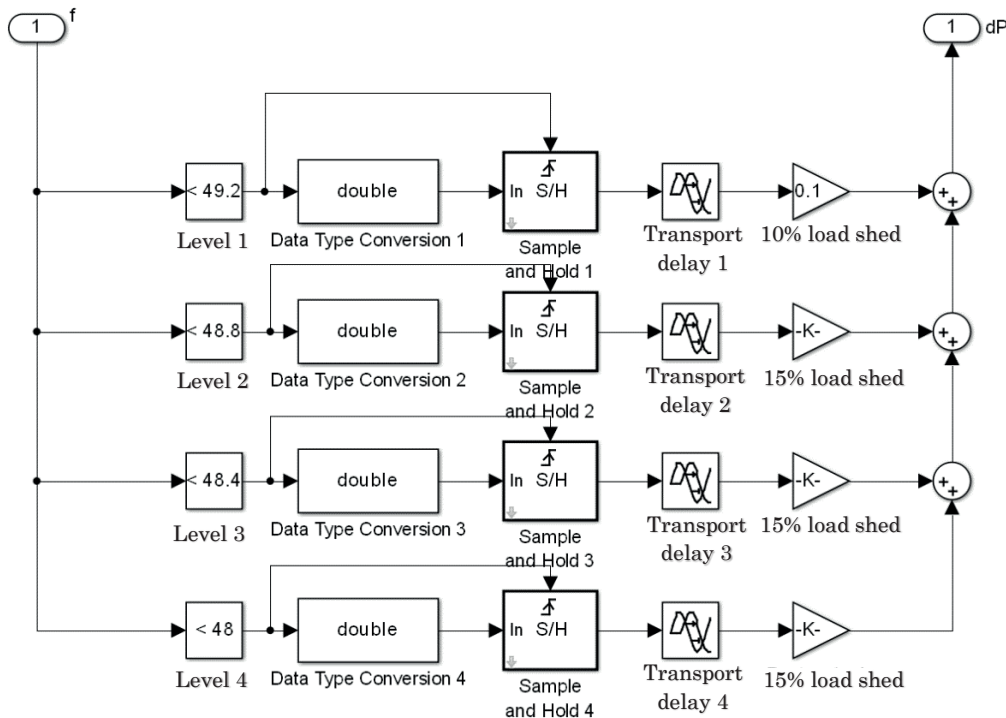


Figure 16. UFLS model in Simulink

UFLS transport delay is set to 400 ms which simulates circuit breaker action and under/frequency relays are set according to the Croatian grid code.

MARIJANA PONGRAŠIĆ¹ ŽELJKO TOMŠIĆ²

marijana.pongrasic@koncar-mjt.hr zeljko.tomsic@fer.hr

¹ Končar - Mjerni transformatori d.d.

² University of Zagreb Faculty of Electrical Engineering and Computing

COST-BENEFIT ANALYSIS OF SMART GRIDS PROJECTS IMPLEMENTATION

SUMMARY

Smart Grids are one of a key component of the EU strategy towards a low-carbon energy future and efficient energy use. From an economic point of view, it's main characteristic is big investment, and benefits are seen after some time with risk of being smaller than expected. Therefore it is important to make a comprehensive cost-benefit analysis of those projects.

Paper presents restrictions of current electric power networks along with solutions that are offered by Smart Grids. Guidelines for conducting the cost-benefit analysis of Smart Grid projects are compared and applied on pilot projects, to demonstrate use of methodologies for reducing uncertainties and incentivizing investments. As a part of qualitative analysis, social aspect of Smart Grid projects is described.

In the end of this paper, it is given an overview of what has been done and what will be done in European Union.

Key words: Smart Grids, cost-benefit analysis, electric power system, social aspect.

1 INTRODUCTION

From economic point of view, main goal of Smart Grids is implementation of new technologies and systems, exploiting current capacities, with minimal funds possible, to enable efficient usage of electric energy on all levels, from production to consumption. Primary characteristic of such grids are big initial costs and benefits manifest after some time with certain risk rate of savings being lower than costs. Problem is that such characteristic makes Smart Grids risky to invest into. So before implementation of the grid it is necessary to do cost-benefit analysis which will inform investors about profitability of their investments, as well as qualitative analysis which will show investors comprehensive picture of influence of the project to stakeholders, environment and society in general. Until now, many studies have tried to identify the benefits of the Smart Grid, but far fewer have focused on developing a systematic way of defining and estimating them. EPRI (Electric Power Research Institute, USA) developed first and so far the best methodology for economic analysis of Smart Grids with benefits and expenses for entire society, including qualitative impact analysis. Hypothesis is that systematic methodology would help in reducing uncertainties and incentivizing investments. The goal of this paper is to make a fair allocation of short-term costs, additional costs in projects of integrating electricity from variable renewable energy sources into the electric power system, long-term benefits among different players and social aspect of Smart Grid projects comparing existing methodologies and pilot projects.

2 DEFINITIONS, ADVANTAGES AND IMPORTANCE OF SMART GRIDS

In European Union Smart Grids are defined as grids that intelligently connect behavior and operation of all users connected to it (Figure 1.) in attempt to optimize the efficient, reliable, safe and secure delivery of electricity [1, 2]. Smart Grids are meant to improve global protection of environment and lower harmful effects on climate, such as emissions of CO₂, efficient use of electric energy of consumers, increase rate of renewable and distributed sources of energy in production, and finally strengthening of the electric energy market. It is expected that such Smart Grids would also contribute climate and energy policies in European Union until 2020, 2030 and 2050 [3]. Smart Grids are defined similarly in USA, but unlike European Union, main goal of USA politics is to introduce new jobs and increase economical worth and efficiency of electric power network.

Electric power network of today is facing problems caused by increased demand for electric energy, new technologies and system integrated into existing network (renewable energy sources, electric vehicles, energy storage), need to lower harmful emissions, fear of terrorist attacks on centralized units of energy production, and demand of consumers related to reliability and quality of electric supply. Smart Grids solve these problems and offer efficiency and reliability of supply and high quality energy services for all participants in electric power network.

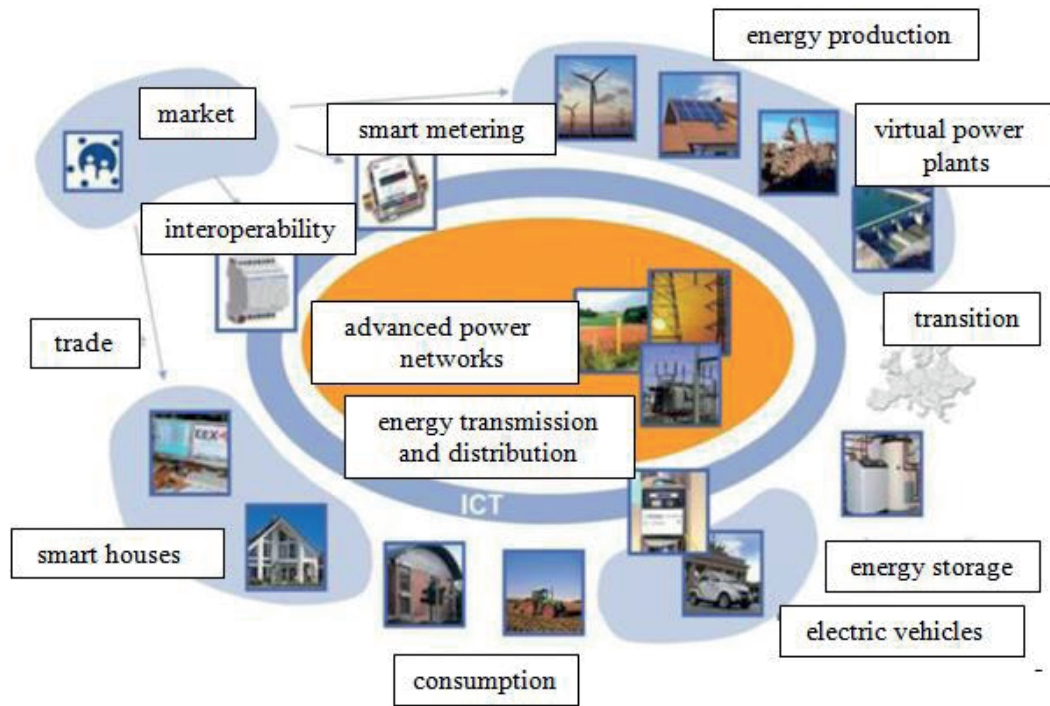


Figure 1. Parts of Smart Grids [2]

Fundamental difference between existing grids and Smart Grid, together with main advantages of Smart Grid, are summarized in Table 1.

Table 1. Comparison of key features of presented grids and Smart Grids [5]

	<i>Current Grid</i>	<i>Smart Grid</i>
Communications	None or one-way; typically not real-time	Two-way, real time
Customer interaction	Limited	Extensive
Metering	Electromechanical	Digital (enabling real-time pricing and net metering)
Operation and maintenance	Manual equipment checks	Remote monitoring, predictive, time-based maintenance
Generation	Centralized	Centralized and distributed
Power flow control	Limited	Comprehensive, automated
Reliability	Prone to failures and cascading outages; essentially reactive	Automated, pro-active protection; prevents outages before they start
Restoration following disturbance	Manual	Self-healing
System topology	Radial; generally one-way power flow	Network; multiple power flow pathways

3 COMPARISON OF METHODOLOGIES FOR COST-BENEFIT ANALYSIS OF SMART GRID IMPLEMENTATION PROJECTS

This article consist in brief, a fair allocation of short-term costs, additional costs in projects of integrating electricity from variable renewable energy sources into the power system, long-term benefits among different players and social aspect of Smart Grid projects comparing existing methodologies. There are steps in cost benefit analysis according to three most common methodologies.

3.1 EPRI methodology

EPRI methodology for economic analysis of costs and benefits of Smart Grid projects consists of ten steps (Table 2.) grouped into 3 categories: project description, definition of benefits and costs and comparison of defined costs and benefits.

Table 2. Ten-Step Approach for Cost-benefit analysis according to EPRI methodology [6]

	<i>TEN-STEP APPROACH FOR COST-BENEFIT ANALYSIS</i>	
Characterize the project	1.	Project's technologies/elements and goals
	2.	Smart Grid functions provided by project
	3.	Project's Smart Grid principal characteristics
	4.	Mapping functions to benefits
	5.	Establishing project baselines
Estimate benefits	6.	Identify and obtain the data needed to estimate the baseline and to calculate each type of benefit
	7.	Calculate quantitative estimates of the benefits
	8.	Estimate the monetary value of the benefits
Compare costs to benefits	9.	Estimating the relevant costs
	10.	Comparing costs to benefits

Review on the project's technologies/elements and goals. The first step is to summarize representation and description of technologies, elements and goals of the project. It involves defining grid size (annually power consumption, number of grid users), local characteristics of the grid, identification of participants of the grid that bear the costs and benefit from the grid, socio-economic impact of the grid and finally regulations of grid implementation. It is possible to define technologies from one of these categories:

- Advanced metering infrastructure
- Advanced technologies in distribution system
- Integration of advanced systems (renewable energy sources, electric vehicles)
- Consumption control system and smart houses
- Energy storage

Smart Grid functions provided by project. Second step is grouping components according to their function. There are 33 different functions possible separated into six groups [6]:

- Enabling the network to integrate users with new requirements
- Enhancing efficiency in day-to-day grid operation
- Ensuring network security, system control and quality of supply
- Better planning of future network investment
- Improving market functioning and customer service
- Enabling and encouraging stronger and more direct involvement of customers in their energy usage and management

Project's Smart Grid principal characteristics. Third step is defining main characteristics with which the project contributes to accomplishment of Smart Grid goals, which are:

- Possibility of involvement of consumers into consumption control
- Possibility of integration production facilities and power storage
- Improvement of the energy market
- Ensuring quality of electric energy
- Efficient control of grid elements
- Prevention, detection and removal of malfunctions
- Protection against damages and malfunctions

Mapping functions to benefits. Fourth step is grouping functions/functionality that grid components perform according to benefits they cause. There are four main benefit types, three perspectives and four levels of precisions of estimated benefits and costs listed in Figure 2.

Four main categories of benefits are:

- Economic – reduced costs, or increased production at the same cost
- Reliability and power quality – reduction in interruptions and power quality events
- Environmental – reduced impacts of climate change and effects on human health and ecosystems due to pollution
- Security and safety – improved energy security (reduced oil dependence); increased cyber security; and reductions in injuries, loss of life and property damage

Table 3. Four categories of uncertainty levels [7]

LEVEL OF PRECISION	PROBABILITY THAT THE ACTUAL VALUE IS WITHIN CERTAIN RANGE	RANGE WITHIN THE ACTUAL VALUE IS
MODEST	80%	±20%
SIGNIFICANT	80%	±40%
HIGH	95%	±100%
UNCERTAINTY RANGE	cannot be quantified	

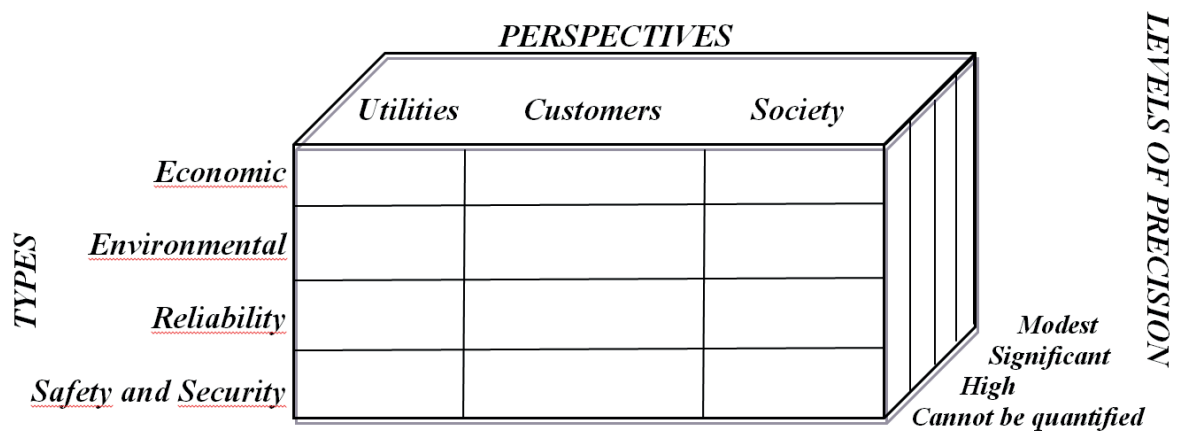


Figure 2. Types, perspectives and levels of precisions of estimated benefits and costs [7]

Establishing project baseline. Fifth step is establishment of referential (basic) state which all other states will be compared with. Referential state can be determined based on historical (for relatively stable conditions) or forecasted data (for conditions that are expected to vary over short time periods) about consumption. When testing new products or services referential data are reactions of consumer groups on such products or services. It is important to ensure that consumer group is random and represents all grid users realistically.

Benefits calculation. Sixth, seventh and eighth steps regard to quantification of benefits and identification of grid participants which are benefiting. Monetary worth of realized benefit is calculated as difference between referential state and state in Smart Grid.

Estimating the relevant costs. Ninth step is especially important in order to calculate time in which invested money will return. Essentially those are investments and operational expenses. During the integration of intermittent energy sources, because of their specific characteristics such as variability, unpredictability, modularity, small marginal cost, additional expenses are unavoidable:

- Balancing expenses - expenses of ensuring reserve capacities to satisfy demands
- Grid-related impacts and costs - expenses of reinforcement, expansion and connection to the network
- System adequacy impacts and costs - expenses to ensure reliability of supply considering reliability of production of intermittent power plants in time of peak load (Capacity credit), and decreasing usage of conventional power plants, and thus lowering their profitability (Utilization effect)

Table 4 provides a summary overview of total integration costs – including the three constituent components – for three technologies (wind offshore, wind onshore and solar) at the penetration levels (10% and 30%) in three selected EU countries (France, Germany and the UK), as estimated by NEA (2012). In general, the major component of total integration cost is accounted for by grid-related costs (ranging from about 45-65% of total costs), followed by adequacy costs (20-35%) and balancing costs (15-20%).

Table 4. Estimates of variable renewable energy integration costs in selected EU countries (in €/MWh) [8]

		<i>Wind onshore</i>		<i>Wind offshore</i>		<i>Solar</i>	
FRANCE	Penetration rate	10%	30%	10%	30%	10%	30%
	<i>Grid connection</i>	4.9	4.9	13.0	13.0	11.2	11.2
	<i>Grid reinforcement and extension</i>	2.5	2.5	1.5	1.5	4.0	4.0
	Total grid-related costs	7.3	7.3	14.6	14.6	15.2	15.2
	Adequacy (back-up) costs	5.7	6.1	5.7	6.1	13.6	13.9
	Balancing costs	1.3	3.5	1.3	3.5	1.3	3.5
	Total system integration costs	14.3	16.9	21.6	24.1	30.1	32.6
GERMANY	<i>Grid connection</i>	4.5	4.5	11.0	11.0	6.6	6.6
	<i>Grid reinforcement and extension</i>	1.2	15.6	0.6	8.3	2.6	33.2
	Total grid-related costs	5.7	20.0	11.6	19.3	9.2	39.8
	Adequacy (back-up) costs	5.6	6.2	5.6	6.2	13.5	13.8
	Balancing costs	2.3	4.5	2.3	4.5	2.3	4.5
	Total system integration costs	13.6	30.7	19.5	30.0	25.0	58.1
UK	<i>Grid connection</i>	2.8	2.8	13.9	13.9	10.9	10.9
	<i>Grid reinforcement and extension</i>	2.1	3.6	1.8	3.2	6.0	10.6
	Total grid-related costs	4.8	6.4	15.7	17.0	16.9	21.5
	Adequacy (back-up) costs	2.8	4.8	2.8	4.8	18.3	18.8
	Balancing costs	5.3	9.9	5.3	9.9	5.3	9.9
	Total system integration costs	13.0	21.2	23.8	31.8	40.5	50.2

Comparing costs to benefits. Tenth step in economic analysis is comparison of costs and benefits in order to determine profitability of the project. It is possible to conduct annual comparison, cumulative comparison or ratio of invested and obtained. Method of Net present value NPV is calculated as a difference between sums of discounted worth of savings (difference between benefits and costs over n years with the discount rate r) and investment costs I_0 . Investment is profitable if NPV is positive (1).

$$NPV = \sum_{t=0}^n \frac{(benefits - costs)_t}{(1+r)^t} - I_0 \quad (1)$$

Internal rate of profitability, IRR is discount rate with which NPV is zero, and investment is profitable if IRR is larger of equal than set discount rate [8].

3.2 JRC methodology

JRC¹ method of economic analysis of Smart Grids is composed of seven steps [6]. In comparison with EPRI methodology, third step in which main characteristics of Smart Grids are estimated is skipped. In second and fourth step terms of function and functionality are switched, because functions refer to technical benefits only and functionality on technical, environmental and societal. Another modification is grouping of the sixth, seventh and eighth steps because they all refer to definition of benefits. In addition to stated, for analysis of grids in Europe, it is suggested to define input parameters for analysis and conduction of parameter sensitivity analysis which define range of input parameters for which project is still profitable.

3.3 Analysis of implementation of smart metering projects

Implementation of smart meters is one of the oldest and most used technologies during construction of the Smart Grid, so it is often separately analysed. The analysis is conducted in five main steps [10].

First four steps contain economic analysis of implementation of smart meter projects. Description of the projects includes rate of implemented smart meter, time period of the analysis, and functionalities which are taken into account. Scenarios which observed projects are compared with are "Business as usual" (without implemented smart meters) and scenario predicted in year 2020 (advanced counters implemented in 80% of consumers, with minimal functionalities).

Some of the parameters that have to be defined before analysis of the project are assessment of energy consumption deviation, assessment of energy price deviation, reduction of peak load, estimated duration of supply termination, VOLL, discount rate, unit costs of equipment, amount of implemented advanced counters, price of installation, expected lifetime of the smart meter, expenses of consumption reading, share of communication technology, plan of implementation, implementation in urban or rural areas, taxes for CO₂ emissions...

As well as for any of the other implemented smart system, economic analysis of expenses and benefits is conducted through already stated seven steps. Specificity which differentiates analysis of smart meters implementation projects lies in functions, benefits and expenses.

Analysis of sensitivity, as with JRC methodology results in range of variables for which the project is still profitable.

With higher quality analyses of project one must take into account effect on external factors such as increase in number of jobs, increased reliability of supply, positive impact on environment, protection of privacy and increased comfort of consumers.

¹ The Joint Research Centre (JRC) is the European Commission in-house science service. It provides independent scientific and technical advice to the European Commission to support a wide range of European Union policies [9].

4 APPLIANCE OF METHODOLOGY ON SMART GRID PILOT PROJECTS

In the Netherlands KEMA and CE Delft (2012) made a report based on the social cost-benefit analysis of Smart Grids. [11] This analysis corresponds to economic analysis of above mentioned methodologies. There are allocated costs and benefits, including social aspect through external effects. Costs and benefits are compared using Net present value method.

They run three scenarios,

- (i) the business as usual (BAU 2050) with only a limited CO₂ emissions reduction,
- (ii) combination (C&N 2050) of Coal with carbon capture and storage & Nuclear (80-95% CO₂ reduction) and
- (iii) combination (R&G 2050) of renewables and gas (80-95% CO₂ reduction), represented in Table 5.

The benefits far outweigh the costs in every scenario. This means that Smart Grids are profitable, even under the scenario of little to no intermittent renewable energy sources on the market. The C&N scenario comes out as the most profitable choice as many of the energy sources as many of the electricity generation plants are already in place and the electricity produced is non-intermittent meaning there is less need for additional generation and grid investments.

Table 5. Cost-benefit of Smart Grid deployment in Denmark, in the three scenarios [11]

<i>NPV (€ billion)</i>	<i>BAU 2050</i>	<i>C&N 2050</i>	<i>R&G 2050</i>
COSTS			
Investments in Smart Grids	-2,10	-2,10	-2,10
Operation & maintenance Smart Grids	-2,50	-2,50	-2,50
Costs need to be determinate	Costs for new equipment, Welfare loss due to changes in timing in response to pricing		
Total costs	-4,60	-4,60	-4,60
BENEFITS			
Avoided grid investments	2,50	5,80	4,10
Avoided electricity losses	0,30	0,50	0,90
Avoided investments in centralised generating capacity	1,20	5,10	1,00
Avoided investments in large scale electricity storage	0,00	0,00	0,10
More efficient use of electricity	1,30	1,40	1,60
Energy savings	0,70	0,70	1,50

<i>NPV (€ billion)</i>	<i>BAU 2050</i>	<i>C&N 2050</i>	<i>R&G 2050</i>
COSTS			
Lower load issues	0,40	0,50	3,20
External effects	0,60	0,10	0,10
Benefits need to be determinate	Welfare loss due to comfort and time gain		
Total benefits	7,10	14,10	12,50
BALANCE	2,50	9,50	7,90
Internal interest rate	13%	28%	31%

5 SOCIAL EFFECT OF CONDUCTION OF SMART GRID IMPLEMENTATION

Social effect refers to inclusion of consumers into functioning of Smart Grid, as well as effect of Smart Grid on consumers, community and society in general. Degree of Smart Grid development is greatly dependent on inclusion of consumers into control of their own consumption, and main motivations are care about environment, lower bill for electrical energy, and finally feeling of comfort and satisfaction. Thus operators of electric power networks are trying to encourage consumers to be more included by introducing fixed and variable charges, rewards or competitions (e.g. Green offices).

Reasons for sceptical attitudes of consumers towards implementation of Smart Grids are large investments, risk of not achieving sufficient savings, concern about their health or privacy, fear of remote control over their access to energy and similar. However, Smart Grids have numerous advantages for consumers (comfort, lower receipts for used power, reliable supply, high quality energy, control over their own consumption), community (reliable supply, mutual exchange of energy at favourable prices), and society in general (care about environment, reliable supply) [12].

6 SMARTGRIDS IMPLEMENTATION PROJECTS IN EUROPEAN UNION SO FAR AND FUTURE PLANS

JRC (Joint Research Centre) in the newest catalogue [13] published analysis of projects of Smart Grid implementation in countries of European Union by June 2013. 459 projects of Smart Grid implementation were conducted, where 47 countries participated and total investment was 3.15 billion euros. According to IEA, for renewable power system from production to distribution Europe should in period from 2007 to 2030 invest 1.5 billion euros [1].

6.1 Systems of smart metering of electrical energy consumption in European Union

According to Directive 2009/72/EC, the goal of energetic grid of EU members is to supply at least 80% of consumers with smart meters by 2020. So far the plan of implementation was conducted in Finland, Sweden and Italy, which make 23% of

desired 80%. 16 members of EU have decided that Smart Grid implementation would be profitable investment, and started preparations for their integration into electric grid. 4 members of EU so far did not evaluate integration of Smart Grids profitable investment so far (Lithuania, Czech Republic, Belgium, Portugal), and 4 countries have not conducted the analysis so far (Slovenia, Hungary, Bulgaria, Cyprus). Germany, Latvia and Slovakia are conducting integration in some consumer groups only. It is estimated that by year 2020 72% of consumers have implemented smart meters, which involves 200 million consumers and requires investment of 35 billion euros [13]. As a part of EU, Croatia wants to implement smart meters into 80% of households until 2018. too.

7 CONCLUSION

Advanced technologies so far were developed in technical way, but were not harmonized with other systems on the grid, so optimal function of Smart Grid was not achieved so far. Hypothesis given at the beginning of this paper that systematic methodology would help in reducing uncertainties and incentivizing investments is confirmed with an example of Smart Grid implementation in Netherland. It is important to analyse conducted projects, publish reports and exchange knowledge and experiences so benefits to social goals would be more easily monitored, energy market opened, investors encouraged, consumer trust established and strategical plan of Smart Grid construction developed.

8 ABBRIVATIONS

IEA – International Energy Agency

EPRI - Electric Power Research Institute

NEA – Nuclear Energy Agency

NPV – Net Present Value

IRR - Internal Rate of Return

JRC - Joint Research Centre

VOLL – Value of Lost Load

KEMA - Keuring van Elektrotechnische Materialen te Arnhem

BAU - Business as Usual

C&N - Coal with Carbon Capture and Storage & Nuclear

R&G - Renewables and Gas

9 REFERENCES

- [1] European Commission, Joint research Centre, Assessing Smart Grid Benefits and Impacts: EU and U.S. Initiatives, 2012.
- [2] Dr.sc.Miletić S., Hrvatski ogranak međunarodne elektrodistribucijske konferencije: Kvaliteta električne energije u naprednim mrežama, 3. (9.) savjetovanje, Sveti Martin na Muri, 13. –16. svibnja 2012.
- [3] Smartgrid.gov,
<https://www.smartgrid.gov/document/guidebook arra smart grid program metrics and benefits smart grid investment grant program>, 19.4.2014.
- [4] http://en.wikipedia.org/wiki/Electric_Power_Research_Institute
- [5] ABB, Towards a smarter grid, ABB's Vision for the Power System of the Future, ABB White Paper. 2009.
- [6] European Commission, Joint research Centre, Guidelines for conducting a cost-benefit analysis of Smart Grid projects, 2012.
- [7] Electric Power Research Institute: Methodological Approach for estimating the benefits and Costs of Smart Grid Demonstration Projects, 2010
- [8] Sijm, J.P.M., ECN, Cost and revenue related impacts of integrating electricity from renewable energy into the power system – A review of recent literature
- [9] http://en.wikipedia.org/wiki/Joint_Research_Centre
- [10] Giordano, V., Joint Research Centre, Guidelines for Cost Benefit Analysis of Smart metering Deployment, 2012.
- [11] Vanderhaeghen W., The role of electricity grids in the energy transition: an economic analysis, 2012.
- [12] Mengolini, A., Vasiljevska, J., Joint Research Centre ,Scientific and policy reports, *The social dimension of Smart Grids*, 2013.
- [13] Giordano, V. et al., Joint Research Centre, Smart Grid projects in Europe: Lessons learned and current developments, 2014.

JOSIP ĐAKOVIĆ*

josip.djakovic@fer.hr

DAVOR GRGIĆ*

davor.grgic@fer.hr

*** University of Zagreb Faculty of Electrical Engineering
and Computing**

ANALYSIS OF SPENT FUEL POOL LOSS OF COOLANT INVENTORY ACCIDENT PROGRESSION

SUMMARY

The Spent Fuel Pool (SFP) in a nuclear power plant is a robust structure designed to withstand large seismic loads. After the terrorist attacks on September 11 and the accident in the Fukushima nuclear power plant, special attention was focused on safety assessments and taking measures to mitigate possible accidents related to the spent fuel pool. This paper will provide an insight into spent fuel pool loss of coolant phenomenology and consequence mitigation strategies. Model of NPP Krško SFP was presented in MELCOR code which has been used as a case-study for evaluating accident propagation. The calculations were carried out using the latest version of MELCOR code which was updated for the analysis of severe accidents in nuclear spent fuel pools.

Key words: Spent Fuel Pool; Loss of Coolant accident; fuel heatup, cladding oxidation, decay heat, NPP Krško

1. INTRODUCTION

Spent Fuel Pool (SFP) is a storage space in nuclear power plant where fuel elements are temporarily discharged (during fuel exchange) or permanently after the fuel reaches a certain burnup. The fuel is placed in metal racks which hold it in the vertical position in the pool. The purpose of the racks is to support fuel weight and ensure the subcritical conditions with adequate cooling. It is possible that the SFP in certain circumstances (disturbances or accidents) remains without an external cooling system, which is acceptable for a shorter period of time. If a cooling and water makeup has not been established for a long period of time (from a few days to a week), fuel uncovering can lead to zirconium rod oxidation, and in severe accidents ignition of fuel elements, radioactivity release and hydrogen explosion [1]. A sudden loss of water from the pool can be caused by a fracture of the pool walls due to a major earthquake or other catastrophic event. The probability of radiological release from the SFP due to severe seismic accidents is estimated at one in 10 million years (for some power plants). Despite the very low chance of such an event, experience has shown that weather disasters can lead to the severe accidents that can affect both nuclear reactor and spent fuel pool (Fukushima). The aim of this paper is to evaluate the response of a NPP Krško SFP to a loss-of-coolant inventory accident (LOCA). The paper is divided into three main sections. The first section explains phenomenology associated with different types of spent fuel pool failures, i.e. the rate of coolant leakage. In addition, measures for accidents mitigation and their effectiveness on a certain type of failure are listed. The second section describes the NPP Krško SFP model in the MELCOR code. The last section provides the results and discussion of accidental parameters for the different sizes and locations of the SFP cracks.

2. LOSS OF COOLANT INVENTORY ACCIDENTS

From the perspective of natural circulation and phenomenology, SFP loss of coolant accidents are divided into two categories:

- 1) Complete loss of coolant inventory accident;
- 2) Partial loss of coolant inventory accident.

In a complete-loss-of-pool-coolant scenario, most of the oxidation of zirconium cladding occurs in an air environment:



For a partial-loss-of-pool-coolant scenario (or slow drainage in a complete-loss-of-pool-coolant scenario), the initial oxidation of zirconium cladding will occur in a steam environment:



Both reactions are highly exothermic, although Zirconium oxidation in the steam produces less heat energy per mole of Zircaloy than in the air, since part of the energy is spent on water dissociation to hydrogen and oxygen. The zirconium-steam reaction leads to the formation of hydrogen, which can undergo rapid deflagration in the pool building, resulting in overpressures and structural damage. This damage can provide a pathway for air ingress to the pool, which can promote further zirconium oxidation and allow radioactive materials to be released into the environment. Debris from the damaged building can fall into the pool and block coolant passages.

2.1 Mitigation Strategies for Spent Fuel Pool LOCA

Loss of coolant accident has been analyzed through numerous tests, using data from operable PWR and BWR power plants. The recent study [2] analysed a wide spectrum of accidental scenarios and phenomenological uncertainties for determining the most important factors affecting the progression of accidents and fuel coolability. Based on the analyses carried out, activities that could influence the consequences of an accident are identified: adding makeup water, optimal pool configuration, dispersed fuel loading patterns, spray nozzles, building ventilation. At least two mitigation strategies are available to mitigate a loss-of-coolant event in a spent fuel pool: Repair the leak that is causing water to be lost and/or add makeup water. In the absence of leak repair, the location, size of the leak, magnitude of decay heat in the pool, and rate and timing of makeup water addition determines the effectiveness of the mitigation strategy. In the case where a spent fuel pool drains completely, adding makeup water will cover the lower portions of the fuel assemblies and block air convection. This could lead to rapid heat-up of the fuel and production of hydrogen as a result of zirconium-steam reaction, loss of coolable geometry in the assembly, and eventually self-sustaining oxidation of zirconium. The flow of makeup water must be high enough to cover a certain portion of the active fuel height before these conditions occur. Spraying water on top of the fuel assemblies may also be an effective strategy to provide additional cooling if makeup water capabilities are inadequate to maintain pool water levels above the tops of the fuel racks. Spraying the fuel can be an effective strategy for maintaining coolability of the fuel depending on droplet size, effect of counterflowing steam and fuel loading configuration.

3. SFP MODEL IN MELCOR

The MELCOR code was originally developed for analysis of severe accidents in BWR and PWR reactors [3]. The code is based on control volumes connected by

flow paths (junctions) with specified frictional losses. Flow areas are either given or are determined as degraded material relocates. Generally, one-dimensional (1D) flows are considered. Since the version 1.8.6 MELCOR has been updated for use in investigating conditions in spent fuel pools under various loss-of-coolant conditions. The last version of MELCOR includes models for:

- Air and steam oxidation;
- Radiative, convective, and conductive heat transfer;
- Hydrogen production and combustion;
- Fuel degradation;
- Boiling and two-phase thermal hydraulics;
- Fission-product release and transport.

3.1 NPP Krško Spent Fuel Pool model

Spent fuel pool and associated building has been modeled as control volumes with the lumped parameters. The control volume geometry is mostly rectangular or cylindrical. The pool volume is divided into 9 control volumes, while the building is divided into 2 volumes, as shown in Fig 1. The outer space is modeled as a time-independent volume ('ENVIRONMENT').

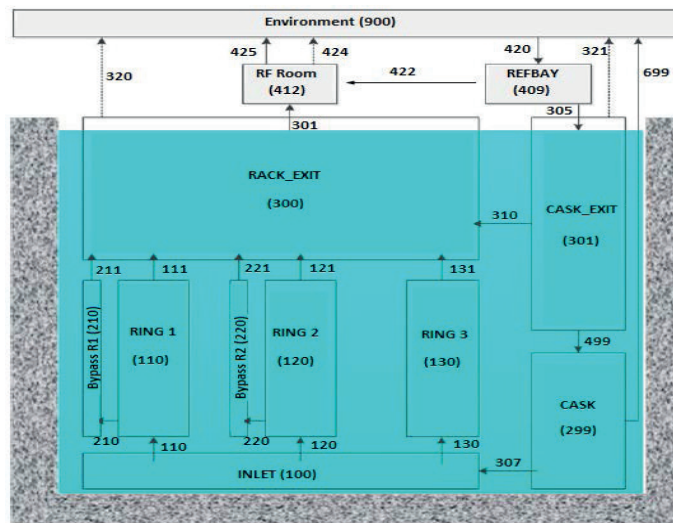


Fig. 1 Control volumes and flow paths in SFP model

Warm water in its natural circulation comes out of racks, enters the RACK_EXIT volume, radially extends to the edge of the pool and enters the CASK_EXIT volume. Furthermore, the water descends to the CASK volume, passes through the INLET at the bottom and re-enters the racks. The space inside the metal racks is divided into 3 Rings and 2 Bypass. The volumes are interconnected by the flow paths, shown by the arrows in Fig 1.

The spent fuel inside the pool is modeled in a similar way to the core in the reactor using the COR package [4]. Due to initial program constraints, fuel is modeled as a cylindrical structure with axial and radial splits. The fuel is divided

into 14 axial layers and 3 radial rings (Fig 2.). For large pools the new approach using interacting channels instead of the fuel rings is able to provide more realistic results.

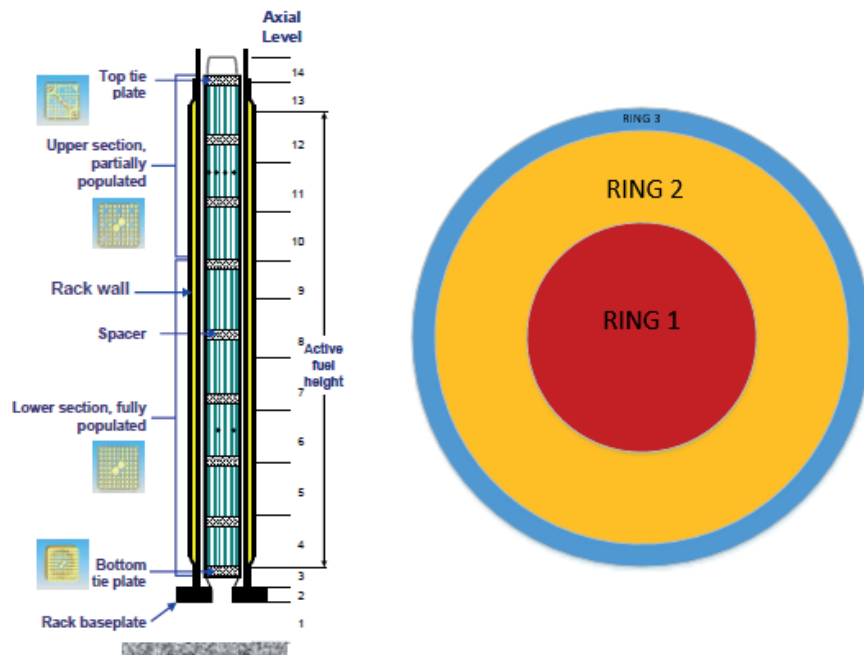


Fig. 2 Spent fuel model

The current configuration of NPP Krsko SFP, having old and new racks, is result of first phase of reracking program. The first ring (Ring 1) is made up of all fuel elements in the old section of the SFP (old racks), i.e. the fuel with larger decay heat. The second ring consists of cooler elements in the new section of the SFP, while the third ring represents a small amount of water between racks and side walls of SFP.

Concrete walls of SFP with metal liner, metal walls of FHB (Fuel Handling Building) and concrete floors on top of the pool (operating deck) represent the heat structures modeled in the HS package [5]. The concrete floor of SFP is modeled in the COR package due to the requirement to define the lower plenum and the reactor cavity below the fuel in MELCOR. Four concrete floors at the elevation of the pool top (11.8 m) were defined, with a total thickness of 0.5 m, surrounding all sides of SFP. Floors are rectangular geometries in which 9 temperature nodes are defined. The boundary condition on the left (inner) side were set as the convective heat transfer coefficient calculated by the HS package. On the right (outer) surface, a symmetric boundary conditions were defined, which represents an isolated surface. Due to program requirements, it was necessary to divide the side walls of the pool on the 17 axial layers and define the boundary (metal) structures above each radial ring of the fuel model in the COR package. Depending on the type of defined boundary condition, it was necessary to define the associate control volume for some heat structures. Therefore, the lowest two wall segments are connected with the INLET volume, the next 14 segments are connected with the RING 3 volume, while the last three segments are connected with the RACK_EXIT volume (Fig. 3).

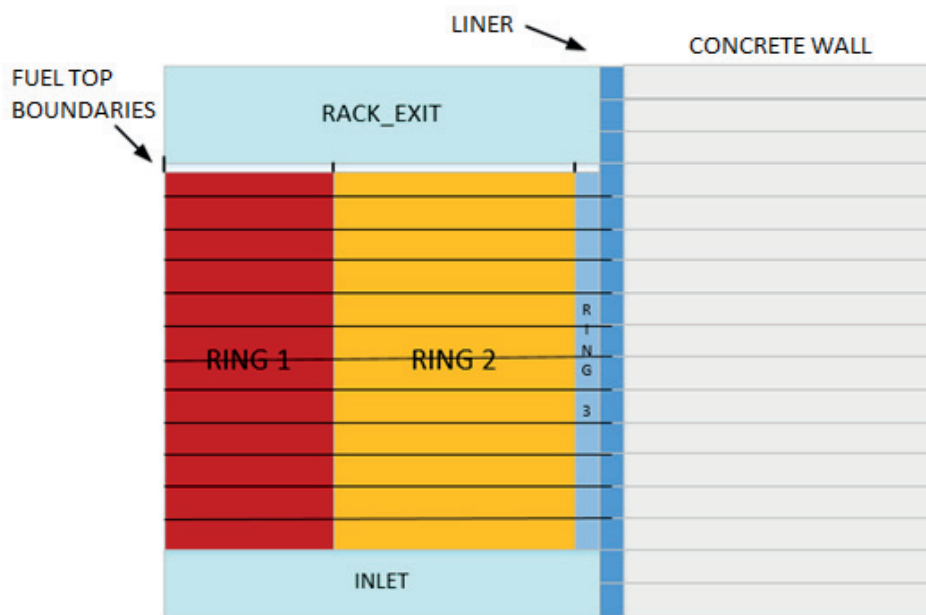


Fig. 3 Heat structures and neighboring volumes

4. RESULTS AND DISCUSSION

The calculations were carried out for a moment in which the fuel, during the refueling, was completely transferred from the reactor to the pool (09.10.2016.). The total decay heat in the old part of the pool was 5.71 MW, with the total fuel mass (metal uranium) 147.315 t, while the decay heat in the new part was 0.573 MW with a uranium mass of 372.035 t. Some MELCOR calculation results were compared with an application that uses simple conservative models (mass and energy balances) for estimating basic data related to the safety of the spent fuel pool - SFPFA.

4.1 Loss of coolant through a 1 cm² crack

This scenario describes the loss of the coolant through the hole at the bottom of the pool having cross section area of 1 cm². A hole of such size is used in NEK in design bases water pool drainage analyzes. Fig. 4 depicts the inventory loss of the pool by the height of water in the control volumes 300, 110 and 100 (they extend through the entire height of the pool). The result shows that the water after 6.0e5 s drops to 0.5 m height. Fig. 5 shows comparison of MELCOR and SFPFA results. In the MELCOR results, the effect of water level stagnation to about 7.0e4 s is noticed even though the mass is lost, which can be explained by the increase in water volume due to heating, i.e., density reduction (Fig. 6).

Fig. 7 shows the temperature of the axial segments of the fuel rod cladding, showing a sudden rise of the temperature after the fuel has become uncovered.

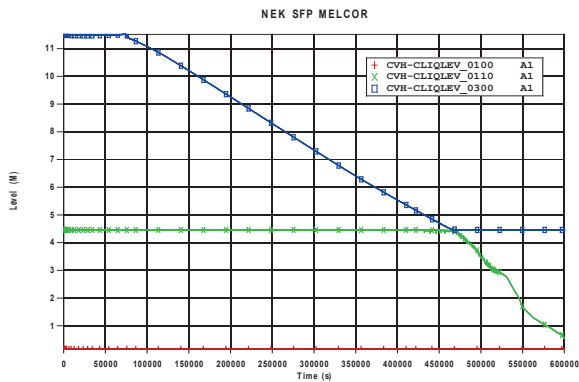


Fig. 4 Water elevation change in MELCOR

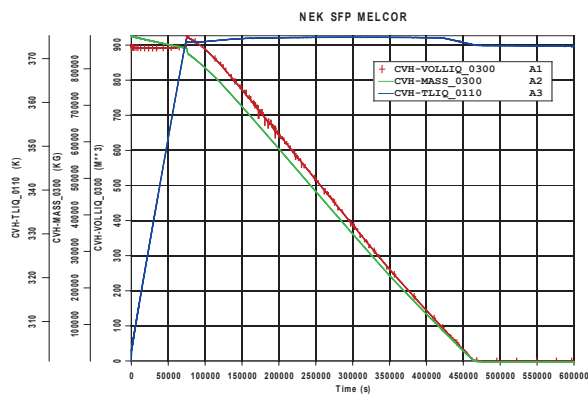


Fig. 6 Water level swelling explanation

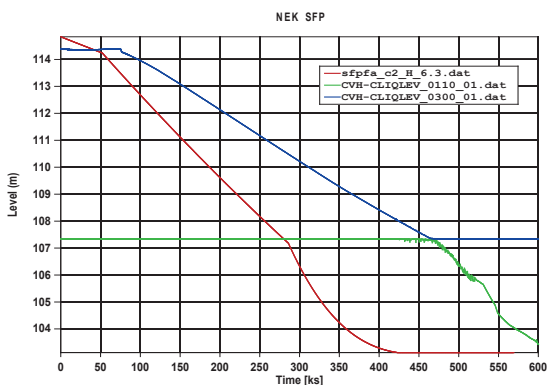


Fig. 5 MELCOR and SFPFA water elevation comparison

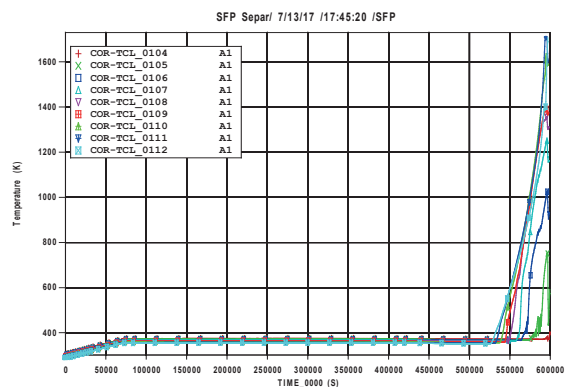


Fig. 7 Fuel cladding heatup in Ring 1

4.2 Loss of coolant through a 0.23 m² crack

The second case analyses the crack of a very large cross section located at the bottom elevation and at 0.5 m above the bottom. The crack of such size area is possible only during major seismic event (beyond design bases event), but it shows the fuel behavior in the case of almost instantaneous loss of coolant inventory. Water drains from the pool after 600s, except in the case of hole at 0.5 m where it stagnates below that elevation (Fig. 8). The water mass flow rate through the crack is exceptionally high (initial flow rate about 3000 kg/s) as can be seen in Fig. 9. The temperature of the fuel cladding in region 1 (Ring 1) is shown in Fig. 10 and 12. On those figures can be observed the effect of breakaway oxidation, which influences the significant cladding temperature rise. Fig. 11 shows the heat produced and exchanged within SFP by various types of heat transfer. The decay heat power (EFPD-RAT) is shown, which due to radionuclide release partially decreases over time. In addition, the convective heat transfer from the fuel, water oxidation, and heat transfer to the surrounding heat structures are shown. Fig. 13 shows the energy balance of the COR model.

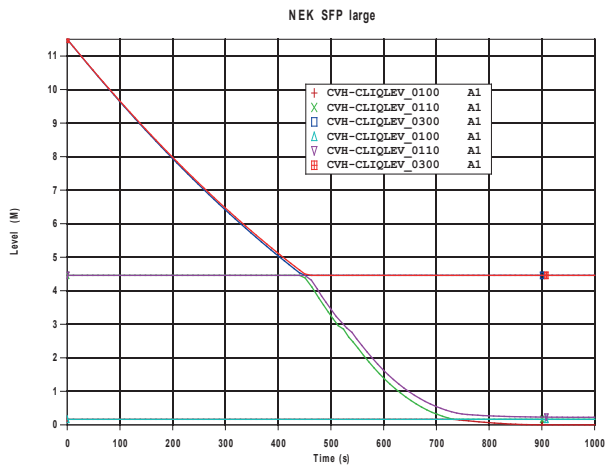


Fig. 8 Crack position impact on water level

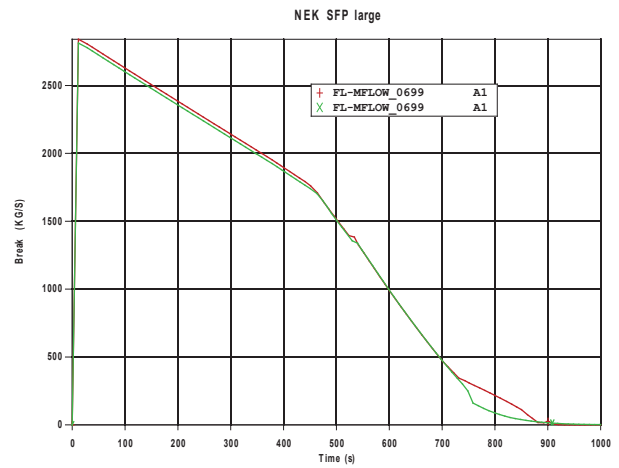


Fig. 9 Water flow through liner crack

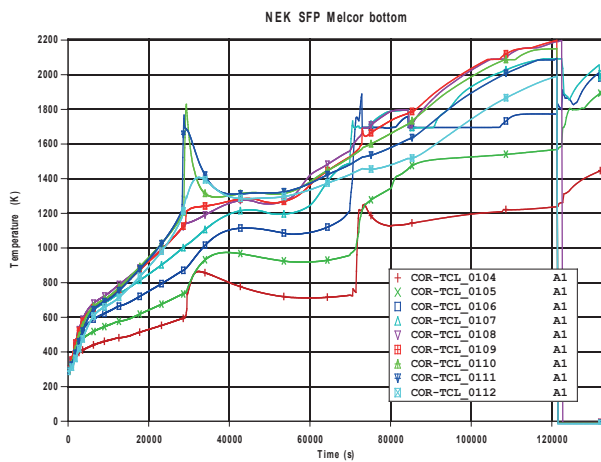


Fig. 10 Cladding temperature in Ring 1 (crack on bottom)

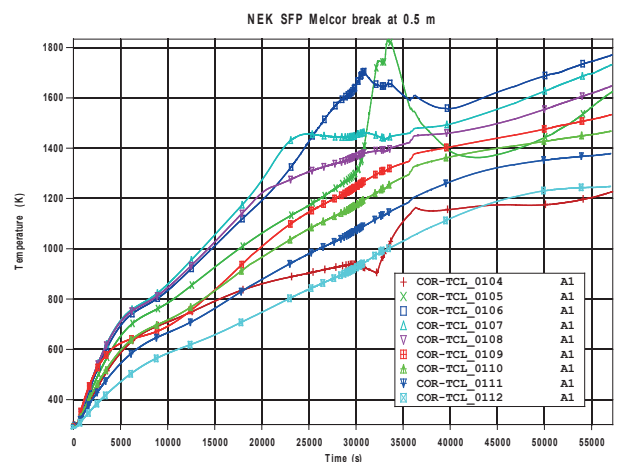


Fig. 12 Cladding temperature in Ring 1 (crack at 0.5m height)

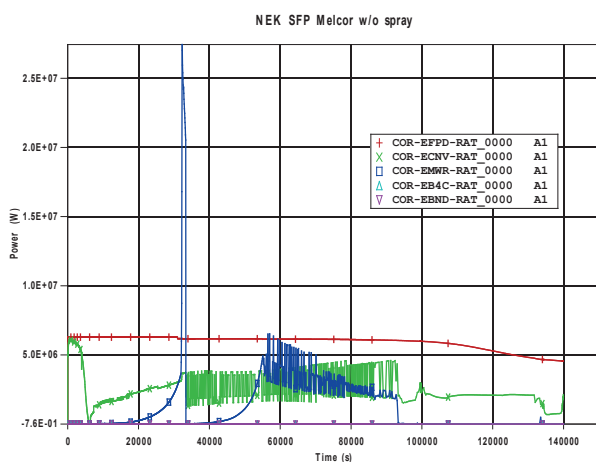


Fig. 11 Heat balance of pool contents - power

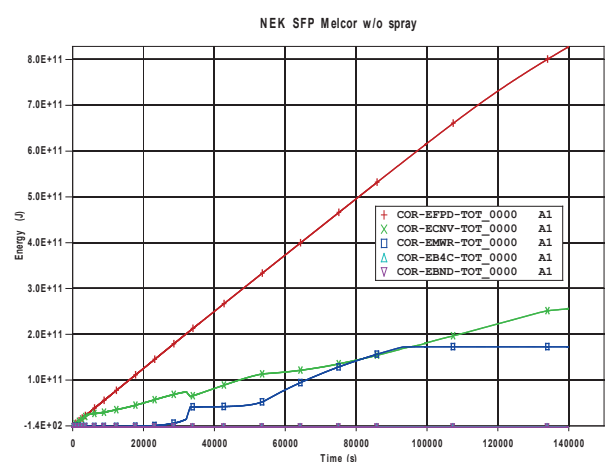


Fig. 13 Heat balance of pool contents - energy

5. CONCLUSIONS

In this paper the Spent fuel pool model of the NPP Krško was used for evaluation of loss-of-coolant inventory accident response using severe accident code MELCOR. Model has been used for partial (slow water drainage) and complete loss of coolant analysis. The case of coolant loss through a small hole prolongs fuel uncovering and consequent fuel heat-up. If the sudden loss of the coolant from the SFP occurs, natural circulation of air is established through the racks, but the results show that it is insufficient to prevent the overheating of the fuel elements with high decay heat. Accident mitigation measures should prevent fuel uncovering in case of partial loss of coolant by enabling water makeup. Due to the different phenomenology of the complete loss of coolant accident, the uncovered fuel should be cooled by allowing convective airflow through the racks, which can be achieved by the implementation of spray nozzles.

6. REFERENCES

- [1] Wagner, K. C., Gauntt, R. O. Mitigation of Spent Fuel Pool Loss-of-Coolant Inventory Accidents And Extension of Reference Plant Analyses to Other Spent Fuel Pools. SANDIA Letter Report revision 2, Sandia National Laboratories, November 2006.
- [2] Barto, et al. Consequence Study of a Beyond-Design-Basis Earthquake Affecting the Spent Fuel Pool for a U.S. Mark I Boiling Water Reactor. NUREG-2161, US Nuclear Regulatory Commission, September 2014.
- [3] Humphries, L.L., B.A. Beeny, F. Gelbard, D.L. Louie, J. Phillips. MELCOR Computer Code Manuals; Vol. 1: Primer and Users' Guide; Version 2.1. SAND2015-6691R, Sandia National Laboratories, 2015.
- [4] Cardoni, Jeffrey. MELCOR Model for an Experimental 17x17 Spent Fuel PWR Assembly. SAND2010-8249, Sandia National Laboratories, November 2010.
- [5] Kromar, Marjan, Kurincic, Bojan. Criticality Safety Analysis of the NPP Krško Storage Racks. Nuclear Energy for New Europe 2002, Kranjska Gora, Slovenia, 2002.

KRISTINA PANDŽIĆ

kristina.pandzic@fer.hr

ANTE MARUŠIĆ

ante.marusic@fer.hr

**University of Zagreb Faculty of Electrical Engineering
and Computing**

SMV TO COMTRADE DATA CONVERSION

SUMMARY

New achievements in the field of communication technology enabled an innovative approach in the solving of the existing problems in the power system. The IEC 61850 norm provides a standardized communication among the secondary equipment devices. Numerical relays have limited internal memory in terms of data storage and limited capability in subsequent analysis. Therefore the feasibility of making high resolution long term records using open-source hardware and software is tested. The observed restrictions on the driver in the SMV to COMTRADE data conversion are documented in this paper.

Key words: COMTRADE, IEC 61850, process bus, SMV

1. INTRODUCTION

Modern communication between transformer substation is achieved through optical connections. In the initial stage of digital substation development, a number of advanced numerical devices have emerged very quickly, however, without the possibility of interaction or connectivity. Devices of various manufacturers, and often the devices of the same manufacturer from different generations, could not communicate without expensive and complicated communication protocol conversion devices. The development of IEC 61850 is a step towards solving this problem and has been one of the biggest challenges in the field of automation [1].

Figure 1 shows three levels of digital substation architecture and the historical development.

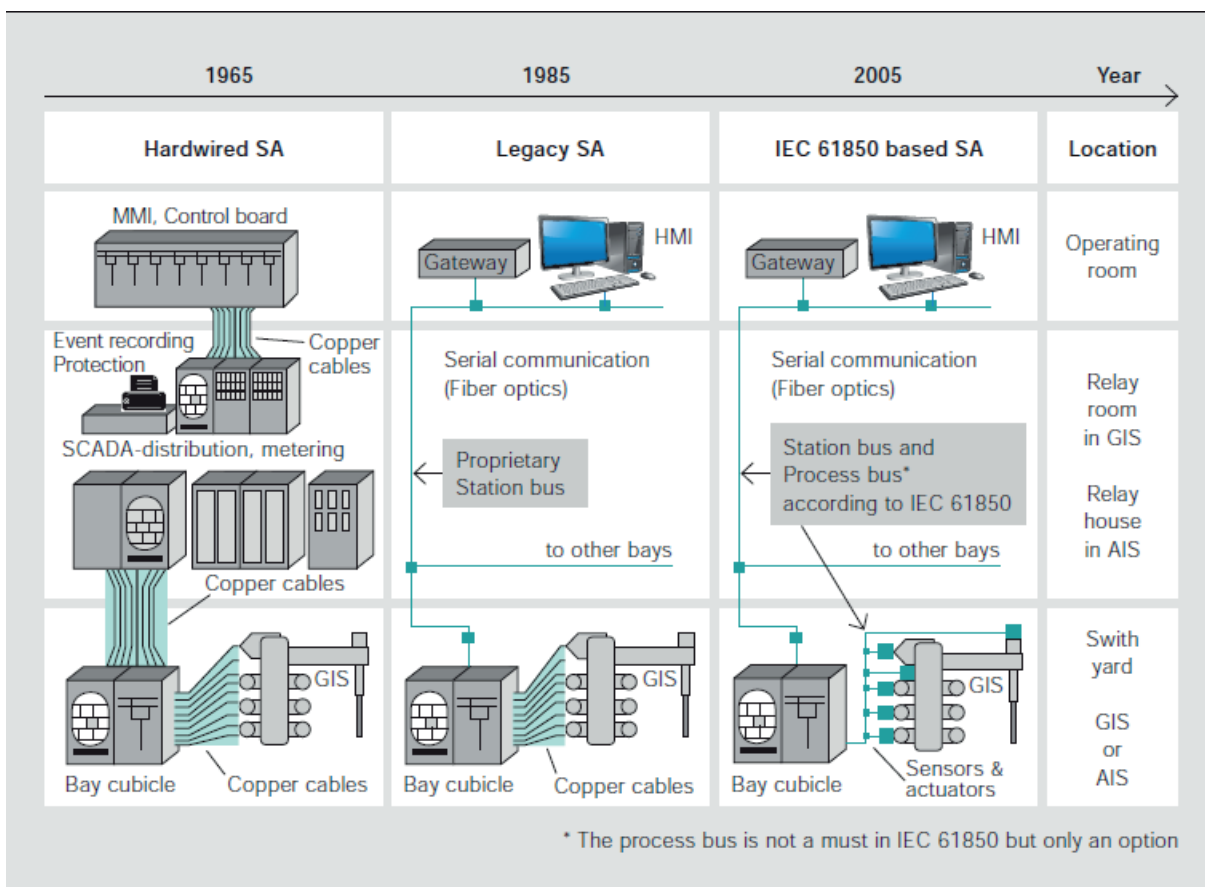


Figure 1. Digital substation development [2]

Norma IEC 61850 standard defines standardized object models, their names, parameters, and meanings that are required for all functions used in transformer substation. These unique features can significantly reduce the cost of designing, installing, commissioning, and generally running the power system.

IEC 61850-8-1 part defines the communication in station bus level and allows peer-to-peer communication by exchanging the GOOSE (Generic Object Oriented Substation Event) message between the connected LAN (Local Area Network).

IEC 61850-9-2 part describes how analogue current and voltage signals can be transmitted as Sampled Values through unconventional metering transformers or conventional metering transformers with the merging unit.

Measured data needs to be converted from analog to digital values, which is done with the help of a merging unit. The merging unit can be located within a measuring transformer or a stand alone unit that allows the use of conventional metering transformers [3][4].

The existing primary equipment is intended to be used as long as it is functional by merging the unit serving as a medium and a protocol converter [5].

1.1. Sampled measured values - SMV

Sampled values are transmitted as SMV (*Sampled Measured Values*) frames.

Figure 2 shows the Ethernet frame containing SMVs.

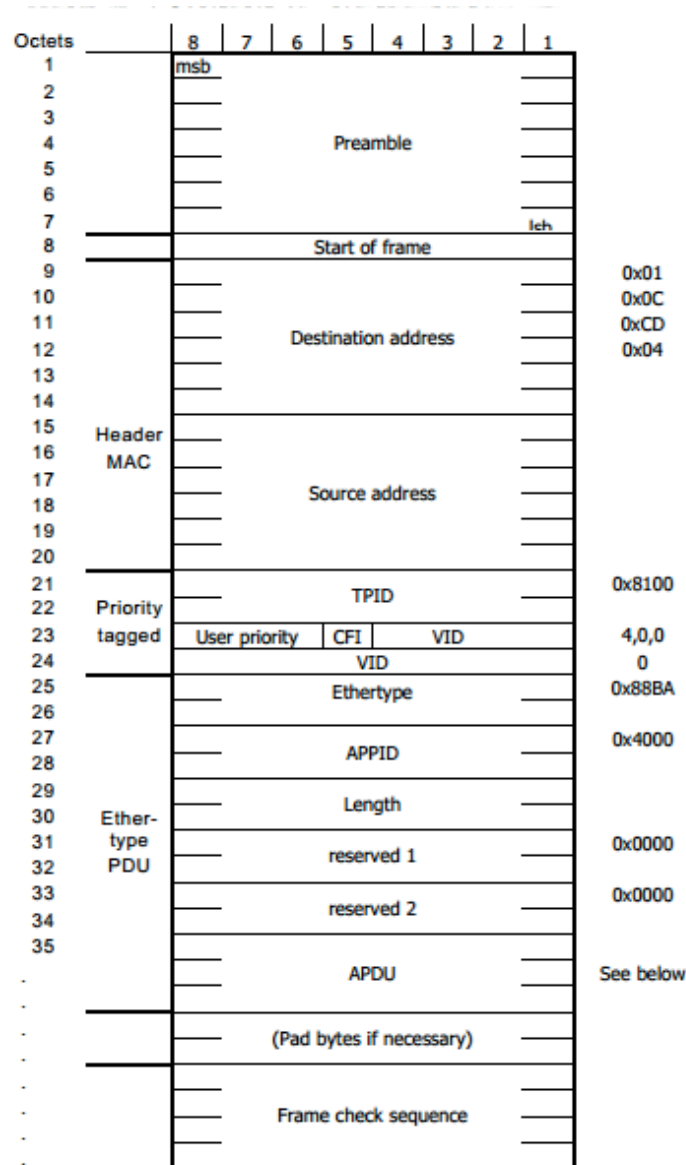


Figure 2. SMV Ethernet frame

The ethernet frame starts with preamble octets, MAC addresses and Ether type. APDU part contains the data.

Figure 3 shows the APDU segments.

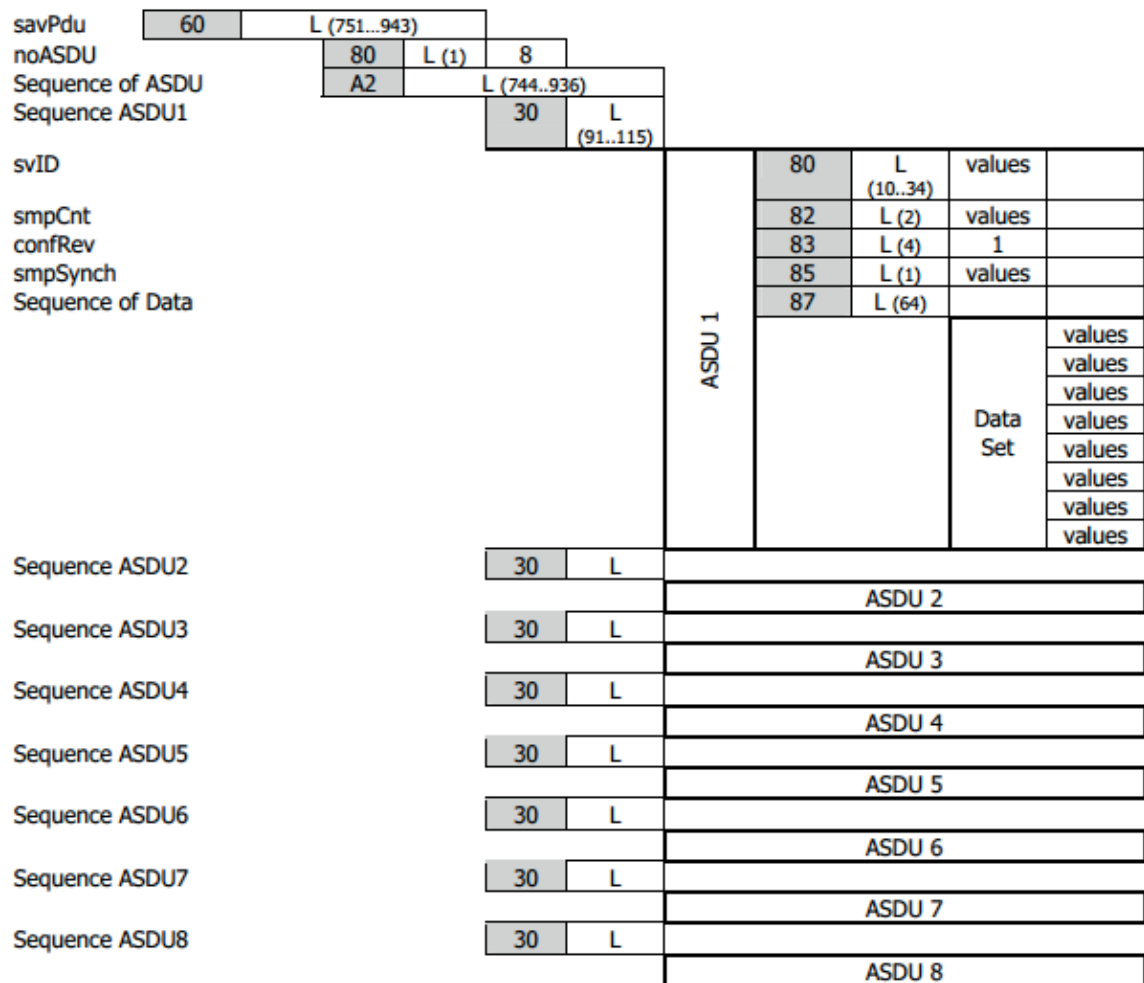


Figure 3. APDU

There may be one or eight ASDU parts in the APDU part, depending on the sample purpose. The total APDU depends on the number of ASDUs as well as on the value of the sample representing the sample value identifier and can be in the range of 10 to 34 octets. Current and voltage values are found under Data Set, the segment shown in Figure 3, under the values. Each voltage and current value is contained in two octets, where the first represents the amount, and the second quality of a certain value.

This paper deals with SMV frames intended for protection. The number of packets per second is 4000 and each packet received contains information on the size and quality of three phase currents and voltages, as well as zero current and zero voltage.

1.2. COMTRADE

COMTRADE (**C**ommon format for **T**ransient **D**ata **E**xchange for power systems) is a file format for storing oscillography and status data related to transient power system disturbances.

The *.DAT file contains the digitized sample data in an ASCII text format. The *.CFG file contains configuration data on what is in the *.DAT file including information such as signal names, start time of the samples, number of samples, min/max values, and more.

The feasibility of a functional program device to write string contained in SMV data frames directly from the Ethernet process bus to COMTRADE files will be verified. The motivation is to create a larger resolution and duration record than the standard fault logs in numeric relays.

2. SMV TO COMTRADE REAL TIME DATA CONVERSION

Omicron device was used to generate sampled values. Figure 4. shows the test environment. The Windows computer is connected to the testing device and is required for its configuration and management. Communication between computers and Omicron is "Ethernet proprietary". Omicron sends the SMV data frames via the LAN network cable to the Ethernet switch, from where the data is read on the Linux computer [6].

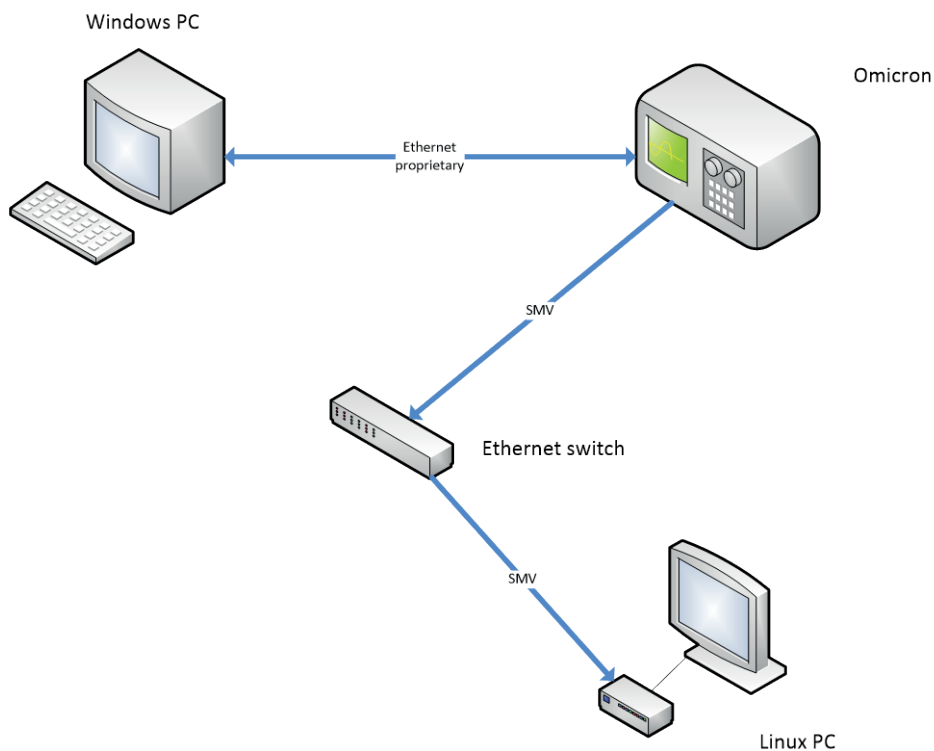


Figure 4. Test environment

2.1. SCAPY library

Using the *sniff* function integrated within the Linux SCAPY library we read ethernet data frames and converted them to COMTRADE file format.

Software is called from the terminal:

```
sudo python <software_name> -i <interface> [-s <file size>] [-t <cfg refresh time>]
```

Necessary argument is *-i*, interface. Additional arguments are *-s* (data file size) and *-t* (time to refresh configuration file). Default values of additional arguments are *s = 1MB* *i t = 10s*.

Function that reads the data frames can have several parameters:

```
sniff(prn = None, lfilter = None, count = 0, store = 1, offline = None, L2socket =  
None, timeout = None)
```

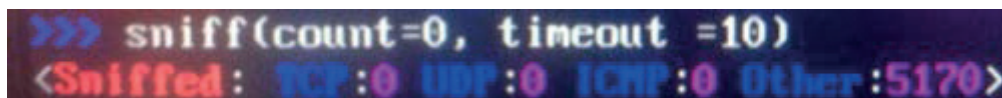
A function can be applied to the data frame (*prn*), data frame can be filtered (*lfilter*) or stored (*store*). We can also limit the number of frames to be read (*count = 0* – unlimited).

We applied a function *write_to_file* that analyzes the frame and rewrites it in COMTRADE file format. A new data file is created when the current one reaches its size limit. Configuration file is refreshed every 10 seconds.

Upon inspecting the data file we observed frame loss as shown in bold.

```
387,93003,0,0,0,0,0,0,0,0,3504,0  
388,93214,0,0,0,0,0,0,0,0,0,3505,0  
389,93516,0,0,0,0,0,0,0,0,0,3506,0  
390,95008,0,0,0,0,0,0,0,0,0,3512,0  
391,100001,0,0,0,0,0,0,0,0,0,3532,0
```

We tested the sniff function with the arguments *count* and *timeout*. First we assigned *timeout* argument – 10 seconds. In that time frame OMICRON sent 40 000 data frames, but our function managed to read only 5170 frames as shown in Figure 5.



```
>>> sniff(count=0, timeout=10)  
<Sniffed: TCP:0 UDP:0 ICMP:0 Other:5170>
```

Figure 5. Scappy test

Second we assigned the *count* argument. We measured time in which the function will read 40 000 data frames that Omicron sends in 10 seconds. It took 1:21,15 minutes.

2.2. PCAPY library

We tried using different Python library and we changed the way function writes the frames to COMTRADE data file. We write 100 frames into a *string* that we write into a data file. We reduced frame loss, but it wasn't eliminated.

2.3. Feasibility check

Both PCAPY and SCAPY libraries use *tcpdump* function in order to read the data frames. The *tcpdump* tool itself has frame loss.

Upon inspecting the driver *sunxi_emac* we found out its *data rate* is between 4 and 6 *MByte/s*.

One data file with 16000 samples has a frame loss of 23,45%.

Complete frame consists of octets:

$$L_{uk} = L_{preamble} + L_{SDF} + L_{MAC_odredište} + L_{MAC_izvor} + L_{tag} + L_{EtherType} + L_{podatak} + L_{CRC} = 7 + 1 + 6 + 6 + 4 + 2 + 1500 + 4 = 1530$$

L_{uk} – frame octet number

$L_{preamble}$ – preamble = 7

L_{SDF} – start = 1

$L_{MAC_destination}$ – destination address = 6

L_{MAC_source} – source address = 6

L_{tag} – tag = 4

$L_{EtherType}$ – ethernet type = 2

$L_{podatak}$ – data length = 1500

L_{CRC} –CRC = 4

Interpacket gap of 12 octets makes for the frame length of 1542 octets.

Table 1 shows theoretical and real frame bandwidth calculated from eq (1):

$$Frame\ bandwidth = \frac{data\ rate}{L_{uk}} \quad (1)$$

Table 1. Frame bandwidth

	Real	Theoretical
<i>Data rate</i>	4 – 6 MB / s	12.5 MB / s
Frame bandwidth (L=1542)	2592 – 3892 frames / s	8106 frames / s

Although the driver's *data rate* is big enough the problem is the frame frequency. Sunxci_emac driver is optimized for sending large data frames with much slower refresh rate to read the incoming frames.

3. CONCLUSION

The standard IEC 61850 provides standardized communications using the latest advances in communications technology. The use of new technologies provides innovative approaches to solving problems, but it also carries certain risks that are not negligible in the power system. To reduce the risk, it is necessary to gain experience in using new technologies, which is possible only on real objects.

The motivation was to create a longer duration record of a larger resolution than the standard logs of numeric relays that have limited internal memory for the amount of data they can store for subsequent fault analysis.

It was necessary to check the feasibility of the functional program device that writes the data string contained in the SMV data frames directly to the COMTRADE file after reading it from the EtherNet process bus.

The calculations have shown the limit on the Ethernet driver for a large amount of data coming in a short time span.

Reprogramming of driver is recommended, which comes out of the domain of this paper.

4. REFERENCES

- [1] Bago, M., Leci, G., Benović, J., Eršek, A. (2014). Novi koncept sustava upravljanja i zaštita kao platforma za razvoj. *Hrvatski ogranak međunarodne elektrodistribucijske konferencije - HO CIRED*, Trogir
- [2] ABB (2010). Special report IEC 61850. *ABB review*, 8.

- [3] ALSTOM (2012). The complete digital substation solution. *Agile Digital Substation*.
- [4] Leci, G. (2013). Coordinated automatic voltage control of power transformers, PhD Thesis, Zagreb: Faculty of Electrical Engineering and Computing
- [5] CIGRE (2013). Application and Management of Cybersecurity Measures for Protection and Control Systems. *JWG B5-D2.46 Technical Brochure Draft 15*.
- [6] Jurković, K. (2014). Konverzija podataka iz SMV u COMTRADE format, Master Thesis, Zagreb: Faculty of Electrical Engineering and Computing

MARKO PIKUTIĆ¹ GORAN GRDENIĆ² MARKO DELIMAR²

marko.pikutic@relatio.hr goran.grdenic@fer.hr marko.delimar@fer.hr

¹ relatio ES Adria d.o.o.

² University of Zagreb Faculty of Electrical Engineering and Computing

COMPARISON OF RESULTS AND CALCULATION SPEEDS OF VARIOUS POWER SYSTEM POWER FLOW METHODS

SUMMARY

The theoretical part describes basic power flow methods Gauss-Seidel and Newton-Raphson in their practical forms for solving a load flow problem. In practical part, IEEE test 24, 48 and 72 node networks are used to compare basic methods in terms of calculation speed: on execution of one iteration, entire calculation and on given accuracy influence. Also is analyzed optimal acceleration factor for Gauss-Seidel method and convergences of methods. On the end, final conclusions are obtained after analyzing comparison results.

Keywords: calculation speed, iteration, Load Flow, Gauss-Seidel, Newton-Raphson

1. INTRODUCTION

Power flow or often called load flow calculation is one of the most important calculations in the power system analysis, and the basic calculation for determining the state of the power system. Equations describing power system stationary state form the system of nonlinear equations. Therefore, to determine the state of the system iterative mathematical methods must be applied. Problems that occur during calculations of power flow can be divided into the problem of selecting the most efficient iterative mathematical calculation method and the problem of efficient software program execution of these numerical operations over a limited period. Mostly used methods for solving a power flow problem are Gauss-Seidel and Newton-Raphson method. Number of university textbooks describe and analyze these methods for power flow solution [1-5] and one of the aim of this article is to succinctly and concisely present this methods, so it can serve as additional working material for power system students.

Important features of these methods are number of necessary iterations or convergence rate to the correct solution, and the credibility of the final result (system of nonlinear equations has multiple solutions). Methods are applied on IEEE standard test networks with 24, 48 and 72 nodes [6, 7] and compared with respect to the necessary time for one iteration step (which depends directly on the number of operations performed in iteration), overall calculation time (which along with time for one iteration step also depends on number of iteration steps), accuracy condition and convergence rate.

2. GAUSS – SEIDEL METOD FOR LOAD FLOW CALCULATION

A method for solving nonlinear equations by Gauss-Seidel iteration procedure is also known as a sequential shift method. This method is in fact a complement to the method for solving the linear equations developed by Gauss. The Gauss method calculates all the unknown variables of the equations in the iteration k , and then with these new solutions goes to $k+1$ iteration. Gauss-Seidel's calculate the unknown variables in the iterative step k with all the calculated variables to that point in that step k and the others from the iterative step $k-1$.

Applying Gauss-Seidel method for the solution of power system equations, however, faces certain difficulties. Every node in the network is described by four quantities: voltage magnitude, voltage phase angle, active and reactive power. In every node two of these quantities are known, and two are unknown – and based on these – classification of nodes is obtained:

- load nodes or PQ nodes (active and reactive power are known variables)
- generator or PV nodes (active power and voltage magnitude are known variables)
- reference node (voltage magnitude and phase angle are known variables)

There are two variants of Gauss-Seidel method for solving load flow problem: variant using power system impedance matrix and variant using power system admittance matrix. In the sequence, more used variant with admittance matrix (abbreviated GSY) is described and later applied for solving load flow problem.

Voltage in node i in k th iteration step $\bar{V}_i^{(k)}$ is calculated according to equation:

$$\bar{V}_i^{(k)} = \frac{1}{\bar{Y}_{ii}} \left(\frac{P_i^{sch} - jQ_i^{sch}}{\bar{V}_i^{(k-1)*}} - \sum_{j=1}^{i-1} \bar{Y}_{ij} \bar{V}_j^{(k)} - \sum_{j=i+1}^n \bar{Y}_{ij} \bar{V}_j^{(k-1)} \right), \quad \forall i \neq ref \quad (1)$$

where P_i^{sch} , and Q_i^{sch} are scheduled active and reactive power in specific network nodes, and \bar{Y}_{ii} , \bar{Y}_{ij} are the elements of network admittance matrix Y . These voltages are calculated in every network node, except referent node. At the beginning of calculation procedure all voltages are set to initial values equal to 1 p.u. – also called flat start. At the end of every iteration step, accuracy of obtained solution is checked, i.e. difference of voltages in two consecutive iteration steps must be smaller than in advanced given accuracy condition ε :

$$|\bar{V}_i^{(k)} - \bar{V}_i^{(k-1)}| < \varepsilon, \quad \forall i \neq ref \quad (2)$$

Here, needs to be emphasized that this is simplified description without PV nodes in the grid.

A Gauss-Seidel method for load flow calculation is mostly long-term procedure and many iterations steps are necessary for achieving set accuracy which is typically in the range from 10^{-3} to 10^{-5} . It converges with geometrical speed. An algorithm can be accelerated by using acceleration factor α between two iteration steps for calculating node voltages according to expression:

$$\bar{V}_{i,acc}^{(k)} = \bar{V}_i^{(k-1)} + \alpha \cdot (\bar{V}_i^{(k)} - \bar{V}_i^{(k-1)}) \quad (3)$$

Instead of using voltage $\bar{V}_i^{(k)}$ in the k th iteration step, accelerated voltage $\bar{V}_{i,acc}^{(k)}$ is used. Attention is necessary for the selection of acceleration factor. Choosing to high value can lead to divergence of solution. An optimal acceleration factor depends upon network configuration and grid's operating point. Typical values are in the range from 1.3 to 1.8 [3].

3. NEWTON-RAPHSON METHOD FOR LOAD FLOW CALCULATION

The second method which is used for solving the system of nonlinear equations is Newton-Raphson method which is based on differential calculus. Starting point for load flow calculation using Newton-Raphson method are expressions for active and reactive power in grid nodes:

$$P_i^{(k)} = |V_i^{(k)}| \sum_{j=1}^n |V_j^{(k)}| |Y_{ij}| \cos(\delta_i^{(k)} - \delta_j^{(k)} - \theta_{ij}), \quad \forall i \in PV, PQ \quad (4.1)$$

$$Q_i^{(k)} = |V_i^{(k)}| \sum_{j=1}^n |V_j^{(k)}| |Y_{ij}| \sin(\delta_i^{(k)} - \delta_j^{(k)} - \theta_{ij}), \quad \forall i \in PQ \quad (4.2)$$

where δ is a phase angle of node voltage and θ is a phase angle of the corresponding element of network admittance matrix which is expressed in polar coordinates. In every iteration step, using node voltages, active power is calculated for all load and generator nodes, which is altogether $PV+PQ$ or $n-1$ equations, where n is a number of network nodes. Reactive power is calculated only in load nodes, which is altogether PQ or $n-1-g$ equations, where g is a number of PV nodes.

Thus calculated active and reactive powers are compared with scheduled or known values:

$$|P_i^{(k)} - P_i^{sch}| < \varepsilon, \quad \forall i \in PV, PQ \quad (5.1)$$

$$|Q_i^{(k)} - Q_i^{sch}| < \varepsilon, \quad \forall i \in PQ \quad (5.2)$$

An iterative procedure is finished when given accuracy condition is satisfied. If accuracy condition is not satisfied, it is necessary to approach to calculation of voltages in the next iteration. This is done by using Jacobian matrix or often called just Jacobian.

Jacobian is a matrix of the first partial derivatives of given expressions for active and reactive power in network nodes (5.1 and 5.2):

$$\begin{bmatrix} \Delta P_1 \\ \vdots \\ \Delta P_{n-1} \\ \Delta Q_1 \\ \vdots \\ \Delta Q_{n-1-g} \end{bmatrix} = \begin{bmatrix} \frac{\partial P_1}{\partial \delta_1} & \cdots & \frac{\partial P_1}{\partial \delta_{n-1}} & \frac{\partial P_1}{\partial |V_1|} & \cdots & \frac{\partial P_1}{\partial |V_{n-1-g}|} \\ \vdots & \ddots & \vdots & \vdots & \ddots & \vdots \\ \frac{\partial P_{n-1}}{\partial \delta_1} & \cdots & \frac{\partial P_{n-1}}{\partial \delta_{n-1}} & \frac{\partial P_{n-1}}{\partial |V_1|} & \cdots & \frac{\partial P_{n-1}}{\partial |V_{n-1-g}|} \\ \frac{\partial Q_1}{\partial \delta_1} & \cdots & \frac{\partial Q_1}{\partial \delta_{n-1}} & \frac{\partial Q_1}{\partial |V_1|} & \cdots & \frac{\partial Q_1}{\partial |V_{n-1-g}|} \\ \vdots & \ddots & \vdots & \vdots & \ddots & \vdots \\ \frac{\partial Q_{n-1-g}}{\partial \delta_1} & \cdots & \frac{\partial Q_{n-1-g}}{\partial \delta_{n-1}} & \frac{\partial Q_{n-1-g}}{\partial |V_1|} & \cdots & \frac{\partial Q_{n-1-g}}{\partial |V_{n-1-g}|} \end{bmatrix} \times \begin{bmatrix} \Delta \delta_1 \\ \vdots \\ \Delta \delta_{n-1} \\ \Delta |V_1| \\ \vdots \\ \Delta |V_{n-1-g}| \end{bmatrix} \quad (6)$$

Jacobian matrix in power flow calculation is usually divided into four submatrices:

$$[J] = \begin{bmatrix} J_1 & J_2 \\ J_3 & J_4 \end{bmatrix} = \begin{bmatrix} \left(\frac{\partial P}{\partial \delta}\right) & \left(\frac{\partial P}{\partial V}\right) \\ \left(\frac{\partial Q}{\partial \delta}\right) & \left(\frac{\partial Q}{\partial V}\right) \end{bmatrix} \quad (7)$$

so equation (6) in abbreviated form can be written as:

$$\begin{bmatrix} \Delta P \\ \Delta Q \end{bmatrix} = \begin{bmatrix} J_1 & J_2 \\ J_3 & J_4 \end{bmatrix} \times \begin{bmatrix} \Delta \delta \\ \Delta V \end{bmatrix} \quad (8)$$

Changes of voltage phase angles and magnitudes in the k th iteration are therefore calculated as:

$$\begin{bmatrix} \Delta \delta_{n-1}^{(k)} \\ \Delta |V|_{n-1-g}^{(k)} \end{bmatrix} = \begin{bmatrix} J_1^{(k)} & J_2^{(k)} \\ J_3^{(k)} & J_4^{(k)} \end{bmatrix}^{-1} \times \begin{bmatrix} \Delta P_{n-1}^{(k)} \\ \Delta Q_{n-1-g}^{(k)} \end{bmatrix} \quad (9)$$

Finally, voltage phase angles and magnitudes in the next iteration are simply calculated:

$$|V_i^{(k+1)}| = |V_i^{(k)}| + \Delta|V_i^{(k)}| \quad \forall i \in PV, PQ \quad (10.1)$$

$$\delta_i^{(k+1)} = \delta_i^{(k)} + \Delta|\delta_i^{(k)}| \quad \forall i \in PQ \quad (10.2)$$

Jacobian matrix and its inverse needs to be calculated in every iteration step what is for large networks (with several hundred nodes) time consuming process which requires large memory allocation. To combat this drawbacks, simplifications of Newton-Raphson method are used.

3.1 Fast Newton-Raphson method

In this variant of Newton-Raphson method, Jacobian matrix is only calculated in the first iteration step. These leads to the obvious advantage of time savings in every subsequent iteration step. On the other side, this can lead to the increased number of iteration steps, increased overall time or even divergence of the method, but in most cases will not. Jacobian matrix can also be calculated afterwards, after several iteration steps, which will decrease divergence probability.

3.2 Decoupled Newton-Raphson method

An influence of small changes of voltage magnitude on nodal active power is negligible, as also small changes of voltage phase angles on nodal reactive power. Jacobian matrix can therefore be simplified on the following way:

$$[J] = \begin{bmatrix} J_1 & J_2 \\ J_3 & J_4 \end{bmatrix} = \begin{bmatrix} \left(\frac{\partial P}{\partial \delta}\right) & 0 \\ 0 & \left(\frac{\partial Q}{\partial V}\right) \end{bmatrix} \quad (11)$$

Submatrices J_2 and J_3 are zero matrices. Corrections of voltage phase angles and magnitudes can now be calculated in two separate matrix equations:

$$\left[\Delta\delta_{n-1}^{(k)}\right] = [J_1]^{-1} \times \left[\Delta P_{n-1}^{(k)}\right] \quad (12.1)$$

$$\left[\Delta|V|_{n-1-gen}^{(k)}\right] = [J_4]^{-1} \times \left[\Delta Q_{n-1-gen}^{(k)}\right] \quad (12.2)$$

Main advantage of this method is lower memory allocation during calculation [2]. Dimension of matrix which needs to be inverted is halved, but inversion of two matrices must be done instead.

3.3 Fast decoupled Newton-Raphson method

Fast decoupled Newton-Raphson method is simply a combination of two previously described methods. Jacobian matrix is only calculated in the first iteration step, and instead of calculating full Jacobian matrix only J_1 and J_4 submatrices are calculated.

4. COMPARISON OF METHODS FOR LOAD FLOW CALCULATIONS

Load flow calculations were executed on IEEE test network with 24 nodes [10]. Networks with 48 and 72 nodes are made by expansion of IEEE 24 network according to [11].

4.1 An optimal acceleration factor for Gauss-Seidel method

Acceleration factors were varied in Gauss-Seidel method to obtain the minimum number of iterations for given voltage accuracy $\varepsilon=10^{-5}$ p.u. Thus attained acceleration factors were used in subsequent calculations and comparisons. On Figure 1a are presented results for IEEE 24 grid with x-axis resolution of 0.1 for which optimal acceleration factor is equal to 1.7 and on Figure 1b x-axis resolution is 0.01 and thus obtained acceleration factor equals to 1.71. For acceleration factor 1.7 number of iteration steps is 38, while for the acceleration factor 1.71 further reduces to 35. For needs of other calculations, acceleration factor 1.7 for IEEE 24 grid is used. An optimal acceleration factor for 48 and 72 node networks acceleration factor 1.8 is obtained and further used.

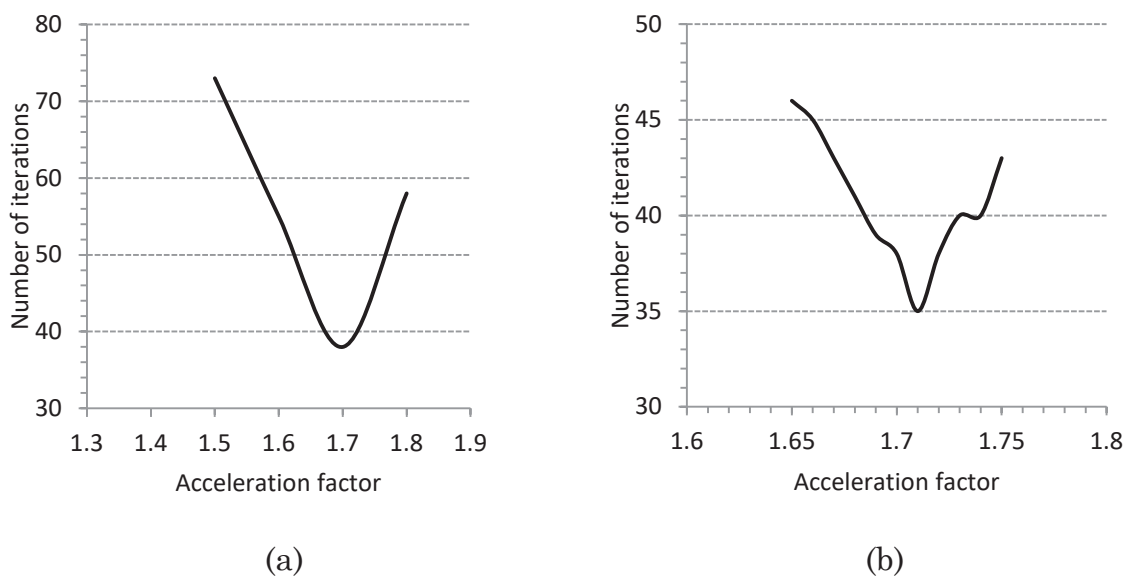


Figure 1: Optimal acceleration factor for 24 node network with given voltage accuracy 10^{-5} [p.u.] (a): Number of iterations for acceleration factor resolution of 0.1 (b): Number of iterations for acceleration factor resolution of 0.01

4.2 Time comparison of one iteration step

Time of one iteration step is an average time of one iteration, obtained as overall time divided by the number of iterations. In the average calculation does not enter zero iteration because in data analysis was shown data it differs significantly from time execution of other iterations. Final iteration is not included also because involves additional operations. Time comparison of one iteration step is shown on

Figure 2 for all three networks and for Gauss-Seidel and different variants of Newton-Raphson method.

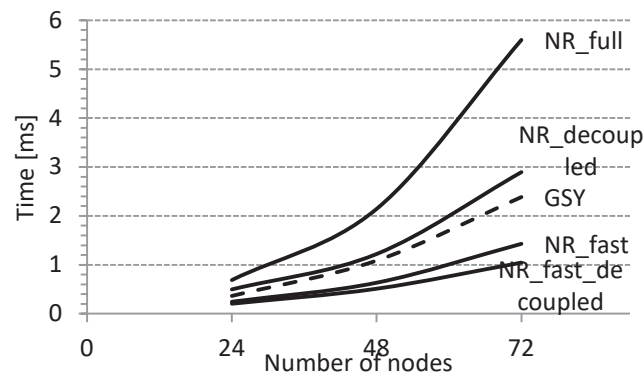


Figure 2: Time comparison of one iteration step for Gauss-Seidel and different variants of Newton-Raphson method

From the figure it can be seen, obviously, that execution time of one iteration rises with number of nodes and more importantly that time execution for Gauss-Seidel method is smaller than for the full Newton-Raphson method. With increasing number of nodes this difference becomes greater. Reason for this lies in the calculation of inverse of Jacobian matrix what requires more time. Calculation of one iteration of decoupled Newton-Raphson method is obviously smaller than for full Newton-Raphson method (instead of calculation of inverse of n -dimension matrix, calculation of two $n/2$ -dimension matrices is necessary), but still greater than for Gauss-Seidel method. Smaller times of one iteration step in relation to Gauss-Seidel method have Fast and Fast-decoupled Newton-Raphson method. However, it needs to be emphasized, that in these cases, necessary Jacobian is only calculated in the zero iteration which does not enter into average calculation. Therefore, time execution with number of nodes rises with slower rate for these two methods.

4.3 Time comparison of overall calculation time

In Gauss-Seidel method optimal acceleration factor determined in subsection 4.1 was used. Voltage ε_U and power accuracies ε_{PQ} were chosen differently in order to make methods comparable. According to [4] voltage accuracy $\varepsilon_U=10^{-5}$ p.u. for Gauss-Seidel method corresponds to power accuracy $\varepsilon_{PQ}=10^{-3}$ p.u. for Newton-Raphson method.

From Figure 3 it can be seen main reason why in power flow calculations Newton-Raphson method is mostly used. Although time of one iteration is smaller for Gauss-Seidel method, overall time is much greater because of necessary number of iteration steps to reach required accuracy. This is especially emphasized in the grids with higher number of nodes where number of iterations for Gauss-Seidel method increases, while for the Newton-Raphson method remains nearly the same. Overall execution time for Fast and Fast-Decoupled Newton-Raphson is the least, but interestingly overall execution time for Decoupled Newton-Raphson is greater than for full Newton-Raphson method. A cause again lies in the greater number of

iterations. Nevertheless, decoupled Newton-Raphson has some other advantages, such as necessary memory demand.

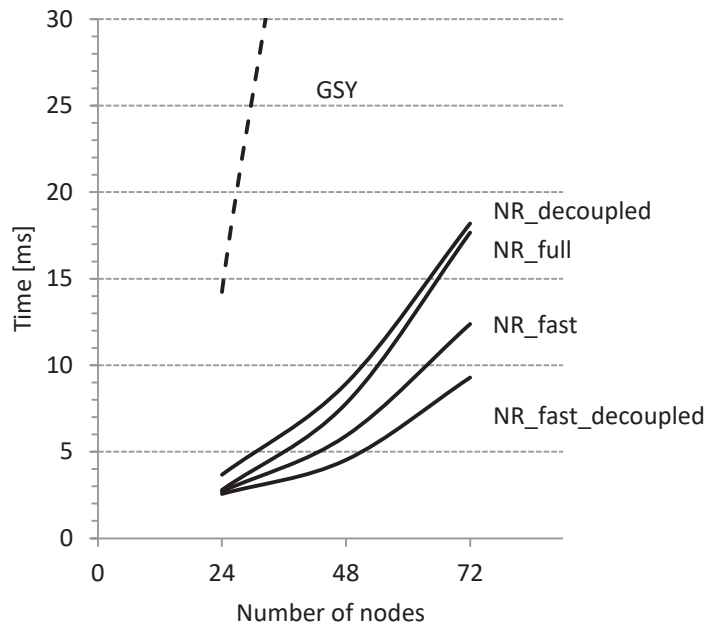


Figure 3: Time comparison of overall calculation time for Gauss-Seidel and different variants of Newton-Raphson method

4.4 Convergence comparison

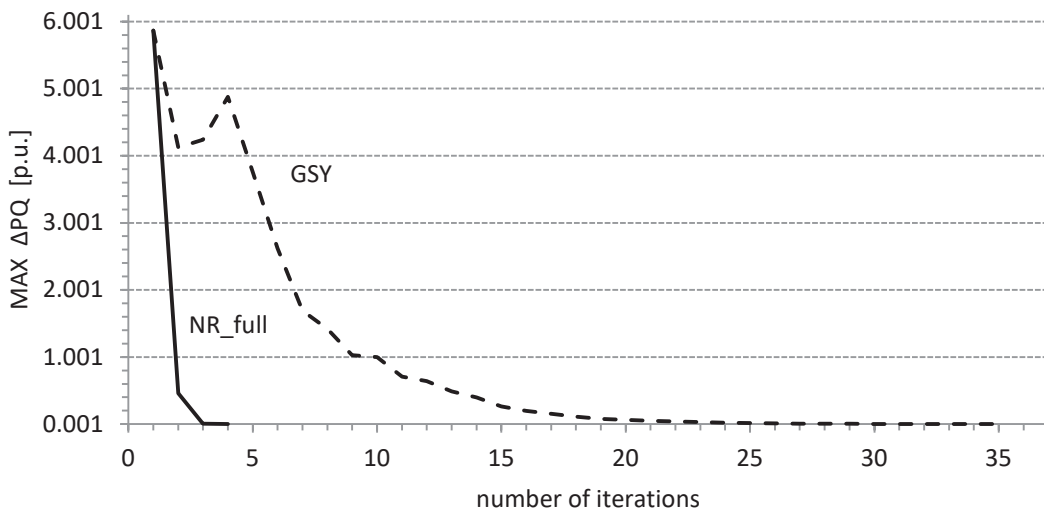


Figure 4: Convergence comparison for Gauss-Seidel and Newton-Raphson method

Comparison of convergence was performed using same power accuracy condition equal to 10^{-3} p.u. This is somewhat different than in previous subsection where for Gauss-Seidel equivalent voltage accuracy was used. Iterations were executed in Gauss-Seidel method until power accuracy was satisfied. Thus, two

more calculations – of active and reactive power – were performed in each iteration step in Gauss-Seidel method. Given accuracy for Newton-Raphson is obtained in four iterations, and for Gauss-Seidel in 35 iterations. On Figure 4 quadratic convergence of Newton-Raphson and geometric convergence of Gauss-Seidel can be observed. It is interesting to notice that Gauss-Seidel at some point starts to diverge, but soon after takes the right direction. One of the possible reasons for this is using acceleration factors. While approaching correct solution, acceleration factors could run away voltage iterations from the correct solution.

4.5 Calculation time dependency on given accuracy

For both methods calculations for given power accuracy in the range from 10^{-1} to 10^{-4} p.u. were conducted on network with 24 nodes.

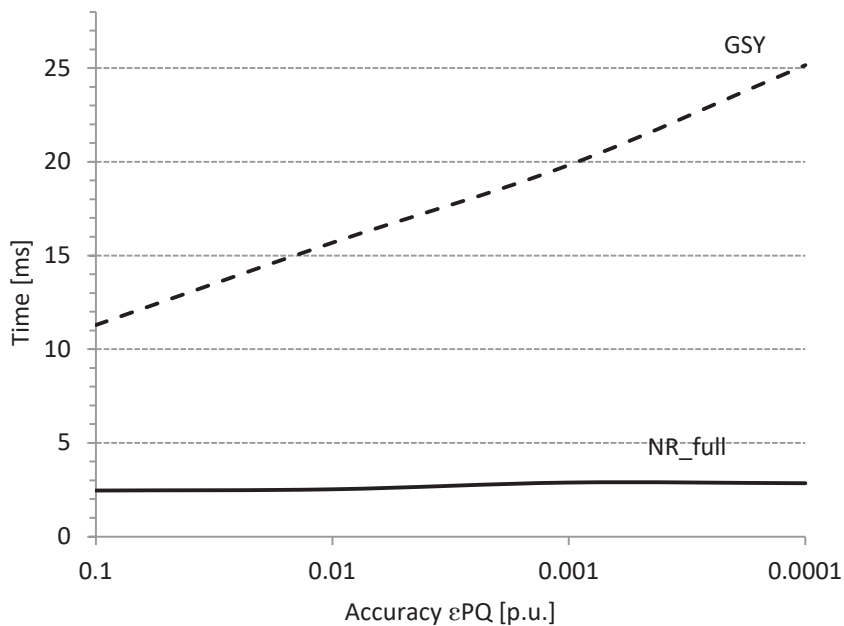


Figure 5: Calculation time dependency on given accuracy

From the Figure 5 it can be seen that overall calculation time for Gauss-Seidel method increases linearly with increasing given accuracy, while for the Newton-Raphson method it does not have large influence. With increasing accuracy Gauss-Seidel method requires greater number of iterations, i.e. converges more slowly which increases overall computation time. On the other side, Newton-Raphson reaches greater accuracy very fast.

4.6 Case of voltage deviation from the allowed limits

According to grid rules which are valid for certain power system, normal system operation state presumes node voltages inside allowable range. In case of a disturbance in the system, e.g. big load switching on or off, line outage, generator outage and similar, voltages may not be any more in allowable limits. Higher deviations appear in case of a fault, most often short-circuit occurrence, when voltage deviation of faulted node become incomparable to other voltages

(theoretically, in case of a direct short-circuit, node voltage becomes zero). This also has great impact on power flow calculation. A short-circuit was simulated on the IEEE 24 grid by changing corresponding diagonal element of admittance matrix. Conditions on short-circuit location are very low impedance, or respectively, very high admittance.

Short-circuit was simulated in node 20 and results of calculations are shown in Figure 6. A Newton-Raphson method has not reached final solution (it diverged – mark NR: $U_{20}=1$ p.u. on the Figure 6), while the Gauss-Seidel has converged to the solution. Improvements can be made during initialization of voltage variables by setting voltage of faulted node closer to zero. When setting faulted node voltage to 0.1 p.u., which corresponds to value obtained by Gauss-Seidel method, Newton-Raphson also converged to the correct solution (solid line on Figure 6). It can be concluded that Gauss-Seidel method converges better to solution when initial variable values are further from the correct solution. Therefore, often in power flow calculations, Gauss-Seidel and Newton-Raphson are used together: Gauss-Seidel in the first several iterations – to ensure convergence of iteration process, and Newton-Raphson to the end of calculation – to achieve greater speed.

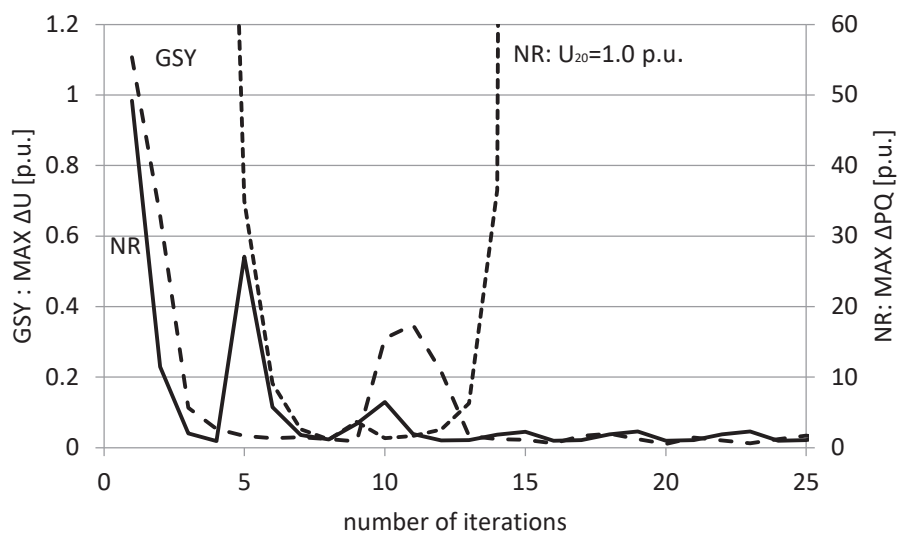


Figure 6: Convergence of a Gauss-Seidel and Newton-Raphson method in case of a short-circuit occurrence

5. CONCLUSION

For networks with small number of nodes, iteration and total calculation times are in comparable domain, and to make specific decision about which method to use can depend upon other things. Decision can be made by the impact of the method on the requirements on the hardware and software support. An advantage of Gauss-Seidel method is its simpler performance, as well as the lower requirement in terms of memory space allocation for execution. A time of one iteration step is also faster in the Gauss-Seidel method, but it will require a greater number of iterations to reach final solution due to geometric convergence. On the other side, Newton-Raphson method converges squarely in the total time of the calculation,

and hence overall computation time is reduced. However, in specific cases, like short-circuit simulations, Gauss-Seidel nevertheless benefits when initial conditions are far from finite solution. On contrary, a Newton-Raphson method is highly dependent on initial input conditions. Simplified Newton-Raphson methods can also achieve faster times of total calculation, and by increasing the number of nodes, they have a significant advantage over the Gauss-Seidel method.

In real-world power management, the choice of method will depend on the specificity of the problem being analyzed, as well as on the importance and responsibility behind the results of the method. Today, the importance of accuracy and speed of achieving results plays a major role in the emergence of new, dynamic participants in the power grid. Smart grids, electricity market, energy efficiency systems are just some of the areas where it is important to operate and make decisions with the results obtained.

REFERENCES

- [1] M. Ožegović and K. Ožegović, *Električne energetske mreže IV*. FESB, Split, 1999.
- [2] D. P. Kothari and I. J. Nagrath, *Modern Power System Analysis (Fourth Edition)*. Tata McGraw-Hill Education Pvt. Ltd, 2011.
- [3] J. J. Grainger and W. D. Stevenson Jr, *Power System Analysis*. McGraw-Hill Book Co.-Singapore, 1994.
- [4] H. Saadat, *Power System Analysis*. McGraw-Hill Book Co.-USA, 1999.
- [5] G. W. Stagg and A. H. El-Abiad, *Computer methods in power system analysis*, McGraw-Hill Inc, 1968.
- [6] Reliability Test System Task Force, “IEEE RELIABILITY TEST SYSTEM”, *IEEE Trans. on Power Apparatus and Systems*, Vol. PAS-98, No. 6 Nov. /Dec. 1979.
- [7] Reliability Test System Task Force, “The IEEE Reliability Test System – 1996”, *IEEE Trans. on Power Systems*, Vol. 14, No. 3, August 1999.

SARA RAOS¹sara.raos@hep.hr**ŽELJKO TOMŠIĆ²**zeljko.tomsic@fer.hr**IVAN RAJŠL²**ivan.rajsl@fer.hr¹ HEP – ODS d.o.o, Elektra Karlovac² University of Zagreb Faculty of Electrical Engineering and Computing

ROLE OF PUMPED-STORAGE HYDROELECTRIC POWER PLANTS AND LARGE PENETRATION OF ELECTRIC VEHICLES IN INCREASING POWER SYSTEM FLEXIBILITY WITH LARGE SHARE OF RENEWABLE SOURCES

SUMMARY

The European Union's (EU) goals of reducing energy dependence and reducing greenhouse gas emissions (GHG) are to be achieved primarily by increasing production from renewable energy sources (RES). However, due to the features of renewable sources such as unpredictability and lack of availability, it is necessary to increase the flexibility of the systems themselves. In other words, large penetration of RES into the power system requires a substantial increase in the capacity of various energy storage technologies. Pumped storage hydroelectric power plants (HPPs) represent 99% of global installed capacity of energy storage and are widely spread, providing energy storage capacity and transmission grid ancillary benefits in the US and Europe since 1920s, as well as in the rest of the world. Besides, new technologies are considered worldwide, and as one of the most prominent options considered today is the penetration of electric vehicles (EVs) into the power systems. The use of EVs reduces air pollution while connecting them to the smart grids creates the possibility of increasing the flexibility of the power

system since vehicle batteries could be used as storage but also as sources of electricity.

Using the PLEXOS energy market simulation software, the power system of the Republic of Croatia was modelled in this paper and based on the results of different scenarios, the role of pumped-storage power plants and large penetration of electric vehicles in increasing the power system flexibility with a large share of renewable sources was observed.

Keywords: greenhouse gas emissions, renewable energy sources, electric vehicles, pumped-storage power plants, energy storage technologies, power system flexibility

1 INTRODUCTION

The growing dependence on energy imports, the obligation to reduce GHG emissions, as well as older power plants are just some of the problems that the European energy systems are facing. Challenges such as climate change, security of electricity supply, and competitiveness in energy markets are multilayer and complex and require a profound change in the ways that Europe generates, distributes, and uses energy. Namely, 53.5% of primary energy is imported into the European Union (EU), at a cost of € 1 billion per day, and it is anticipated that for about twenty to thirty years this figure would be around 70%. [1] Moreover, fuel combustion in the transport sector contributes significantly to the total GHG emissions. Namely, transport in the EU member states accounts for 33.1% of total final energy consumption [2] while the share of transport in total GHG emissions is 23% [3]. Joining the EU, Croatia has agreed to fulfil the obligations of the Directive 2009/28/EC, which among other things require that each member state by 2020 achieves a minimum share of renewable energy in the finale energy consumption in transport by 10%. Furthermore, in accordance with the EU framework and other international agreements, Croatia was committed to presenting the Low-Carbon Strategy. The strategy will be a fundamental document in the area of climate change mitigation, but also the roofing economic, development and environmental strategy. The goals of the strategy are based on the European Union's policy on the low-carbon economy, which aims to reduce greenhouse gas emissions by 80-95% by 2050. Accordingly, in October 2014, the European Council adopted the Climate and Energy Framework of 2030, setting the target of reducing CO₂ emissions by 40% by 2030, increasing the share of renewable energy sources (RES) by 27% and the indicative target of 27% reduction in energy consumption. The goals of reducing greenhouse gas emissions by 2030 and 2050 will be implemented in the Republic of Croatia within the framework of the political framework adopted by the European Union.

In order to achieve the set goals it is necessary to change the way in which electricity is produced, distributed and consumed. Namely, modern power systems, mostly built in the 20th century, have been developed in such a way that large

generators inject electric power thru transformers into a high voltage power grid, and this power is then transported by a transmission system, very often at long distance. At the end of the transmission system, through a series of distribution transformers, the transported power is directed to medium and low voltage network and to the final consumers. However, the idea of connecting production units to the distribution network has become more and more present and these sources are mainly renewable energy resources since environmental impact is one of the most important factors while considering the connection of new production facilities to the power grid. While RES contribute to reducing environmental impact and increasing self-sustainability of national energy systems, it is important to point out that the increased construction of such sources affects many aspects of the power system such as power generation, frequency control, voltage control and reserve maintenance. In other words, due to the large fluctuations in natural water inflow and intermittent electricity generation of renewable sources, the power systems must provide substantial reserves in conventional sources or significant capacity of electricity storage. This leads to an increase in the price of electricity as well as the costs of the whole power system and limits further development to a greater integration of renewable sources. Electric vehicles and pumped-storage HPPs provide the possibility of storing electricity which opens new possibilities for the integration of RES into the grid.

2 RENEWABLE ENERGY SOURCES

Renewable energy is energy that is collected from renewable resources, also referred to as unconventional sources, which are naturally replenished on a human timescale, such as sunlight, wind, tides, waves, geothermal heat, biomass and biogas. Although renewable resources have significantly lower energy value compared to the fossil fuels, as a result of which their power plants have smaller installed capacity, are geographically more distributed, and are mainly connected to the distribution network, such production units considerably increase the ability to meet the requirements for reducing GHG emissions in accordance with national and international goals and agreements. Unlike conventional energy sources, renewable sources are impossible to exhaust over the time. However, it is possible to completely exhaust their potentials, therefore a careful and long-term planning of production capacities and location of their construction is required. The most significant feature of RES is the possibility of diversified applications. Further, RES have enormous potential, although some more than other considering that production from small hydroelectric power plants depends on natural water inflow and location or that the geothermal energy cannot be fully exploited since the technologies available are not sufficiently developed yet. Also, for most unconventional sources, there is no energy consumption when it comes to obtaining the original form nor is the energy consumed for the transport of the original form because transport is usually impossible. The undesirable general properties of unconventional sources are low surface density, partly inability of transport and

storage, and mostly usage in its original form, high oscillation of the natural inflow, small annual usage of installed capacity, which leads to the necessity of accumulating energy or making reserves in conventional sources. [4]

Fulfilled desirable property	
Partially fulfilled desirable property	
Unfulfilled desirable property	

Properties	Desirable state	Small hydro power plants	Collector thermal use of solar radiation	Photovoltaic Use of solar radiation	Wind	Using internal heat of the environment with a heat pump	Biomass and waste	Geothermal energy
Potential	big							
Renewability	yes							
Possibility of transport in natural form	exists							
Possibility of storage in natural form	exists							
Oscillating natural inflow	small							
The cost of obtaining the natural form	Doesn't exist							
Occupation of space at the site of transf.	small							
Emissions at the place of transformation	Doesn't exist							
CO ₂ neutrality, cumulative	yes							
Efficiency of the transformation process	high							
Duration of capacity utilization	high							
Reserve or accumulation	Not necessary							
Possibility of cogeneration	possible							
Possible diversification	yes							

2.1 Costs of RES integration

RES (wind and Sun) represent three unique problems that lead to a higher costs of their integration in the power system:

- Variability of energy resources i.e. output power of wind and solar power plants depends on the weather conditions and cannot be controlled in the way that it is done with conventional power plants.
- Unpredictability of production for shorter periods. Therefore, every deviation between the planned production and the actual production has to be balanced in the short term, which leads to the need of maintaining reserves in the power system.
- RES cannot be transported, with the common occurrence that suitable construction locations for RES aren't located on or near the sites of high energy demand.

According to [5] costs of RES are divided into groups:

- Direct costs
- System costs
- Macroeconomic impact

Direct costs represent levelized cost of electricity (LCOE¹) i.e. they consist of the costs of construction and financing costs, fixed operating and maintenance costs (FO&M), variable operating and maintenance costs (VO&M) and fuel costs. System costs represent additional costs incurred by connecting the production unit to the network and consist of balancing costs (balancing energy), network costs (upgrading/construction of the grid, transmission losses, congestions etc.), and integration costs (needed reserve). Macroeconomic impact is related to the effects of GDP and social welfare, the unemployment rate and the distribution of damage or benefits within individual sectors. Analysis at the level of the overall economy is of crucial importance given the significant expansion of RES over the last few years and since the spread of certain technologies can lead to unexpected consequences for other economic entities and sectors.

3 ENERGY STORAGE TECHNOLOGIES

Energy storage will have an important role in enabling the development of Low Carbon power systems, which is one of the main goals of the EU in the near future. Energy storage technologies can provide additional flexibility for the power system, which is needed to better the balance between production and consumption

¹ LCOE allocates the costs of and energy plant across its useful life, to give an effective price per each unit of energy (kWh). In other words, it's averaging the up-front costs across production over a long period of time.

of electric energy, since we are facing increasing penetration of RES into the grid. Namely, energy storage technologies would support the system in the case of intermittent and relatively unpredictable production from RES. Locally, at the distribution level, their implementation could improve distribution network management, decrease the costs of production, and increase efficiency. In this way, that may facilitate the introduction of RES on the market, accelerate the decarbonisation of power systems, improve the safety and efficiency of transmission and distribution of electricity (reduce unplanned congestions, reduce fluctuation of voltage and frequency etc.), stabilize market prices of electricity while simultaneously ensuring the security of energy supply.

The need for energy storage technologies derives from the basic characteristics of electricity. Namely, the electricity demand varies depending on the time of observation, geographic position, established patterns of electricity consumption etc., and accordingly the price of electricity changes. At peak loads, the price of electricity is higher because more flexible production units, such as gas power plants, have to be engaged, whose production costs are much higher than the base power plants (nuclear power plants). While in off-peak periods, when the electricity demand is lower, according to the law of supply and demand, the price of electricity decreases. This is exactly the opportunity for energy storage owner to profit financially. Namely, from the point of view of the power utility there is a great potential to reduce total production costs by eliminating the more expensive peak production units by storing energy during the night when the electricity price is lower and returning it to the grid over the peak periods the next day. Also, with a high percentage of penetration of wind and PV in some regions, there is excess energy, which is actually cost-free. This surplus could be stored in energy storage technologies such as EVs or pumped storage HPPs and used later on and thus also reduce production costs. On the other hand, from the consumer's point of view, energy storage can lead to a reduction in the electricity costs. Namely, consumers can buy energy at lower prices, store it and use it during the peak load periods. Also, consumers who have battery systems, such as EVs, can charge them during off-peak period and sell the same to power utility or other consumers during peak load period. The fundamental feature of electricity generates another problem for power utilities, which is to maintain a constant and flexible supply of consumers. If the amount of electricity demanded by consumers at a particular moment cannot be met, the quality of electricity is disturbed and in the worst case, this may lead to a disruption of supply. In order to meet changing energy demand, the appropriate amount of electricity should be continually produced, relying thereby on accurate forecasts of demand. However, today it is still impossible to predict accurately the current consumption of electricity, which results in a difference between forecasted and realized consumption. Therefore, some production units are required to participate in voltage (U-Q regulation) and frequency regulation (f-P regulation) in order to maintain the balance between production and consumption at any time. However, RES such as solar panels and wind power plants do not have any of above-mentioned regulation functions. Therefore, it is expected that energy storages will facilitate the mentioned regulations. For a number of years, pumped-storage HPPs have been used to provide auxiliary services, i.e. production of electricity when there is a lack of production from other production units due to different

reasons. Furthermore, energy storage technologies are useful in the events of failures in the power system, which can result in a supply disruption, but the consumption can still be satisfied with the energy stored in the energy storage technologies. Portable batteries can also serve as an urgent resource for electrical devices. Power utilities attempt to predict the future congestions in the power grid to avoid overloads, for example by building new transmission lines or by dispatching generators but they cannot be avoided. However, by installing energy storage technologies at appropriate locations, such as transformer stations at the end of heavily loaded lines, it is possible to reduce congestion by storing energy when transmission lines have sufficient capacity to transmit the required energy, and when the lines are unavailable due to congestion, the stored energy is used.

3.1 Pumped-storage hydroelectric power plants

Pumped-storage hydroelectric power plants, with over 168 GW installed capacity worldwide represent 99% of the world's installed energy storage capacity, which also represents 3% of total global electricity production. Conventional pumped-storage contain upper and lower basins between which there is a height difference. The bottom pool is mostly located either on a river waterway or it is a natural lake or sea. Pumped-storage power plants are most often used in terms of energy arbitrage, i.e. during off-peak periods (when the electricity prices are lower) the electricity is used for pumping the water from the lower to the higher water tank, and in periods of higher demand (when the electricity prices are higher) water flows through the turbine, which drives the generator, into the lower tank, and the electricity is produced. The generators in pumped-storage can operate in two modes, both as a pump and as a turbine/generator (usually Francis). Taking into account the losses due to evaporation of accumulated water and losses due to transformation, approximately 70% to 85% of the electricity used to pump the water into the higher tank can be recovered. Typical discharge time ranges from a few hours to a few days. The benefits of this technology are a very long life span and almost unlimited cycle stability, while the main drawbacks are dependence on topographic conditions and large land use. This technology is currently the most profitable in terms of storage large amount of electricity, but investment costs and the presence of problems of a suitable geographic position (the height elevation between water tanks) are critical factors in decisions regarding the building of such production units and storage technology.

There are three pumped-storage hydropower plants in Croatia, Fužine (operating since 1957), Lepenica (1985) and Velebit (1984). However, HPP Velebit is the only large pumped-storage power plant in Croatia with installed capacity of 276/240 MW (turbine/pump), and an annual production of 430 GWh. The HPP Fužine with installed capacity 4.666/4.8 MW (turbine/pump) uses a water drop between the Lokvarsko Lake and artificial Lake Bajer. The small HPP Lepenica with installed power 1.14/1.25 MW is located in the valley of the Lepenica Stream which is the tributary of the artificial Lake Bajer. So far there are no plans for installing new pumped-storage HPP, though they would be an ideal complement to

exploiting the full potential of wind and solar power plants that are particularly present on the Adriatic coast. Also, pumped-storage HPP largely fit into the concept of low-carbon strategy, as their work does not produce harmful GHG emissions.

3.2 Electric vehicles (EVs)

Electric vehicles are powered by an electric motor powered by a battery or other power source. The first electric vehicle originates from the 19th century, and was constructed by Scotland inventor Robert Anderson. Due to the advancement of the internal combustion engine during 20th century, the production and development of EVs fell in the second plan. At the beginning of the 21th century the interest in EVs was renewed, primarily due to the tendency of reducing emissions of pollutants associated with environmental protection and sustainable development, and thus the production of EVs is considerably present. Depending on the type of the engine and how the battery is charged, EVs can be divided into:

- Hybrid electric vehicles (HEVs)
- Plug-in hybrid electric vehicles (PHEVs)
- Battery electric vehicles (BEVs)

In this paper, only battery electric vehicles are modeled, therefore the description of this type of EVs is given below. BEVs are fully electric vehicles, meaning they are only powered by electricity and do not have a petrol engine, fuel tank or exhaust pipe. The basic parts of BEV are rechargeable battery, electric motor and engine controller. The electric engine is the central part of BEV, and this is the only type of drive engine in such types of electric vehicles. It turns the electrical energy from the battery into the mechanical and thus drives the vehicle. The motor is controlled by an engine controller, and the engine controller is operated by pushing the accelerator pedal, which has the role of an analogue-to-digital converter, or by pressing the brake (if the EV has a regenerative braking function). [6]

The most widely used battery technology used in BEVs is Lithium Ion. One of the biggest problems that the EV buyers are facing are high battery prices, inability to charge in the households, underdeveloped battery filing, and still a long charging time. Namely, although the market prices of the batteries are in the downward trend, they are still too expensive to increase the competitiveness of the EVs because the current market price of a new battery is about 80.000 \$ (about 500-600 \$/kWh). In addition, EVs charging equipment alternates the necessary time to charge a fully depleted battery. Level I equipment provides charging through a 120 V alternating-current (AC) plug and requires a dedicated circuit, and it generally refers to the use of a standard household outlet. Depending on the battery technology used in the EV, Level I charging generally takes 8 to 12 hours to completely charge a fully depleted battery. Level II equipment offers charging through a 240 V, AC plug and requires installation of home charging or public charging equipment. Depending on the battery technology used in the vehicle, Level

2 charging generally takes 4 to 6 hours to completely charge a fully depleted battery. Charging time can increase in cold temperatures. Level 2 chargers are commonly found in residential settings, public parking areas, places of employment and commercial settings. Level 3 equipment with CHAdeMO technology, also commonly known as DC fast charging, charges through a 480V, direct-current (DC) plug. Most Level 3 chargers provide an 80% charge in 30 minutes. Cold weather can lengthen the time required to charge. When connected to the grid EV can operate in four different ways. [7] Grid-to-Vehicle (G2V) when the battery of an EV is charged directly from the grid, Grid-to-Vehicle Half (G2V/2) when the battery does not charge but would otherwise be charged, thus EV is helping the system by providing up-regulation, Vehicle-to-grid (V2G) when the battery is discharged, providing the appropriate reserve, and Vehicle-to-Vehicle (V2V) when instead of taking the electricity from the grid, one EV discharges the battery giving the electricity to another connected EV whose battery is then being charged.

4 ELECTRICITY MARKET MODELING SOFTWARE PLEXOS

For the purpose of analysis in this paper, PLEXOS software tool has been used. [8] Modelling in PLEXOS can be carried out using deterministic or stochastic techniques that aim to minimize an objective function to the modelled cost of electricity dispatch and to a number of constraints including availability and operational characteristics of generating plants, licensing environmental limits, fuel costs, and operator/transmission constraints. After entering all the required system parameters, defining scenarios and setting the planning period, PLEXOS launches a program specialized in solving mathematical optimization problems. The simulation of the solution is based on the MIP mathematical programming technique - mixed integer programming. Also, PLEXOS supports the use of several commercially available solvers: *MOSEK*, *Gurobi*, *Xpress-MP* and *CPLEX*. With the completion of solving the mathematical problem, PLEXOS prepares the data for preview in the graphical user interface based on the obtained solutions.

PLEXOS is a simulation-optimization tool based on the object model of the electricity market. The object model defines the set of classes and their hierarchy. The class of objects implies a set of rules and definitions pertaining to a particular type of object. During the preparation of input data, the user creates objects representing each element of the model, whether it is a generator, a network, or a market. All supported elements of the power model and the simulation process are defined by different classes of object model. A well-constructed object model provides wide-ranging capabilities and provides a tool suitable for examining the impact of different energy strategies.

PLEXOS provides different possibilities including:

- Capacity expansion planning – optimization of new generation and transmission capacities with decommissioning of the existing power plants

- Modeling production costs
- Forecast of gas and electricity market prices – based on operational constraints on system and market rules
- Planning of gas and water supply infrastructure
- Market analysis
- Analysis of Transmission Restrictions – prediction and control of congestions in transmission system, transmission within security limits (N-x), outage planning, optimized power flows modeling
- Operational planning and stochastic optimization
- Analysis of the integration of RES – detailed (5 minutes) production and transmission analysis
- Smart grid planning – modeling of smart consumption, analysis of investments
- Management of hydro resources - modeling of storage, inlet and water flow
- Risk management – through scenario analysis comes the decision on optimal allocation of resources over a short or long period

5 TEST MODEL – POWER SYSTEM OF THE REPUBLIC OF CROATIA

Electricity needed to meet the consumption within the power system is produced in power plants, industrial power plants, and small-scale distributed sources or purchased from the energy market. Within the power system of the Republic of Croatia, the vast majority of electricity is produced in conventional power plants (thermos, hydro, including half production in the Krško nuclear power plant located in Slovenia). A significant part (sometimes more than 50%) of electricity needs are bought on energy markets and imported. Moreover, more than half of the total installed capacity within the Croatian power system consists of HPPs. Furthermore, some large industrial customers have their own energy sources (refinery in Rijeka etc.), and the share of small distributed sources such as small hydropower plants or photovoltaic cells is still not significant at this time. In recent years, installation of wind power plants has been intensified, and in August 2016 a total of 18 were connected to the transmission and distribution grid, with a total installed power of 420.95 MW.

All data used in modelling is used according to [9] and the low-carbon scenario of strong transition was taken into account. In (Table 1.) the production structure for the base year 2015 is presented as well as the planned installed power for 2030, 2040 and 2050. Figure 1 shows the geographic distribution of modeled existing thermal power plants and hydroelectric power plants. Moreover, an important part of the power system is a power grid that connects production capacities and consumers and provides safe, adequate and high quality electricity supply. The power grid is divided into two parts: transmission and distribution. The liberalization of the energy market brought the separation of transmission and distribution so now they belong to regulated market activities. The transmission

network in the Republic of Croatia is owned by Croatian transmission system operator (cro. *HOPS*) while the distribution network is owned by Croatian operator of the distribution system (cro. *HEP ODS*). In this paper, a 400 kV transmission network with the largest nodes (Žerjavinec, Tumbri, Erenstinovo, Melina, Velebit and Konjsko) is modeled, and all the modelled production units are assigned to the particular node to the one they are geographically the closest. The predicted consumption is divided by nodes based on percentages of actual electricity consumption in those regions.

Based on the available hourly load profile from 2015, with a proportional annual increase in energy consumption, hourly electricity consumption was estimated and created up to 2050. Due to the electrification of transport and the anticipated higher consumption of electricity in industry and services, electricity consumption is estimated to have an average growth rate of 1.2% per annum from 2014 to 2030, and 1.7% growth from 2030 to 2050. In 2050 the consumption should be by 70.1% higher than consumption in 2014. The new production capacities of conventional power plants, with planned start-up dates, were determined based on data available from Croatian National Power Utility - HEP. New coal-fired power plants are not envisaged after decommissioning the existing power plants. In modelling the natural inflow for hydropower plants the average hydrology was taken into account. The installed capacity of the RES for 2020 is determined according to the quotas set in the Changes of the Tariff System for the Production of Electricity from the RES and Cogeneration (NN 100/15) by 2020. Also, the model does not envisage incentives for new wind and solar power plants (which enter after 2020), and it is assumed to continue stimulating the capacity for biomass and biogas, small hydropower plants and geothermal power plants. Regarding the emissions, the emission prices are set, as well as the annual limits for the production of CO₂ emissions. Modeled power plant candidates include all commercially available technologies. The CO₂ price rises to 90 €/ton, limits on CO₂ emissions of 1725 ktonnes since 2030 and 555 ktonnes from 2050. The electricity market is not modeled after the year 2030. The model does not allow unserved and dump energy, meaning that the demand must be met all the time and also no extra energy should be produced.

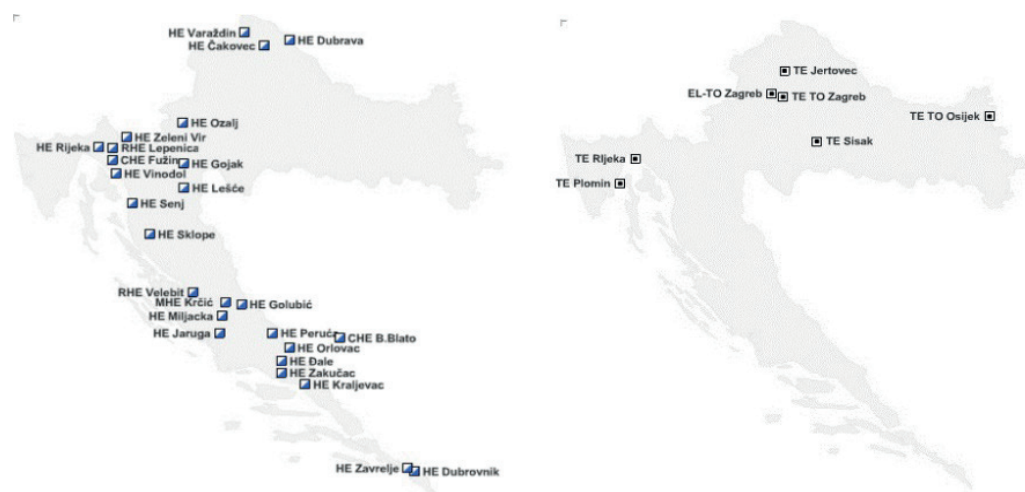


Figure 1. Geographical distribution of modelled existing hydroelectric power and thermal power plants

Table 1. Installed capacity

Installed power [MW]	2015.	2030.	2040.	2050.
TOTAL	4.786	8.434	10.718	12.643
Nuclear power plant	348	348	348	500
Gas-fired power plant	1.140	1.745	2.630	3.080
Coal-fired power plant	330	210	0	0
Gas-fired power plant with CCS	0	0	550	550
Heating oil-fired power plant	320	0	0	0
Hydroelectric power plants	2.095	2.567	3.107	3.107
Wind power plant	420	1.887	2.227	3.259
Solar power plant	48	1.300	1.400	1.667
Biomass power plant	28	94	140	150
Biogas power plant	21	100	128	136
Geothermal power plant	0	44	48	54
Small hydroelectric power plant	36	140	140	140

5.1 EV modeling

Battery electric vehicles (BEV) with vehicle-to-grid (V2G) technology were modeled. A total amount of EVs penetrating each year from 2020 to 2050 was divided into 20 EV objects that represent a set of EVs with corresponding annual capacity growth, according to the data available from [9]. The amount of EVs connected to the grid by 2030 is set to be 150,000, i.e. 4% of the total number of vehicles in 2030, and by 2050 a total of 1.5 million EVs or 75% of the total number of vehicles. Furthermore, it was necessary to set the maximum power that each vehicle has at a given time during the day (Figure 2. and Figure 3.). Hourly diagrams, made for working days and weekends or holidays, describe the movement of cars for each group of EVs object i.e. their consumption or production (Figure 4. and Figure 5.). Also, in order to successfully model the separation of EVs from the network, it was necessary to model the limitation related to their production. In other words, the production of each battery must be greater than or equal to the maximum power used by the EV at every hour of the day, so that there is a potential for EV to deliver power to the network and thus serve as an energy source. The anticipated consumption of EVs was added to the planned electricity consumption in Croatia by 2050. It should also be emphasized that, when modeling electric vehicles and their use in the system, investment costs for the construction of charging stations, as well as the supporting infrastructure and contents were not taken into account.

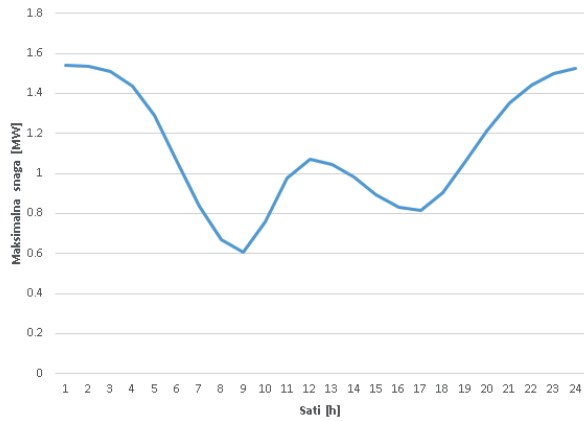


Figure 2. Hourly profile of maximum power of a group of EVs on working day

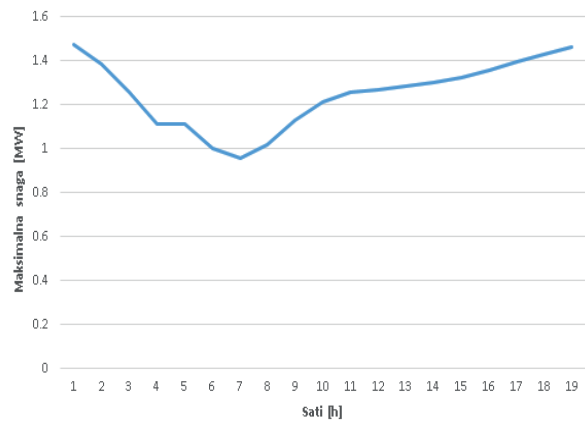


Figure 3. Hourly profile of maximum power of a group of EVs on weekends and holidays

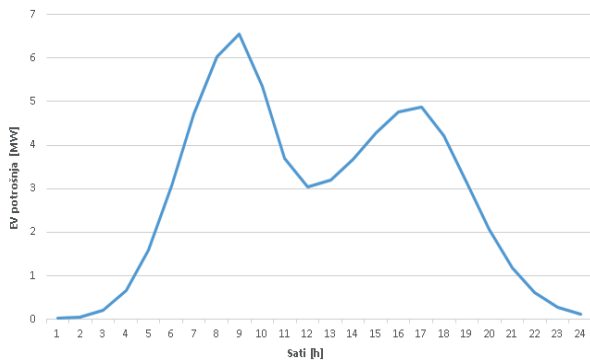


Figure 4. Hourly profile of energy consumption of a group of EVs on working day

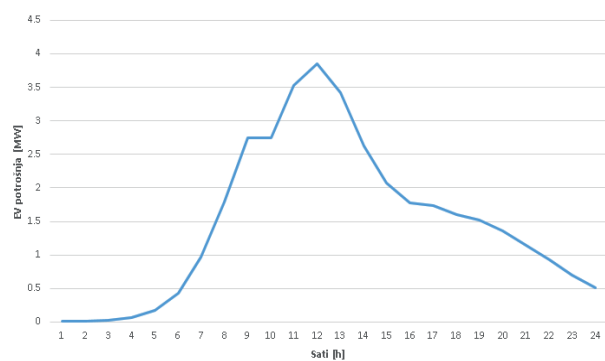


Figure 5. Hourly profile of energy consumption of a group of EVs on weekends and holidays

5.2 Wind power plants modeling

The existing installed capacity of the wind power plants as well as the anticipated entry of new production units into the grid in the period up to 2050 were modeled. Current and future production units are divided into nodes in the model by geographic position on the 'South Adriatic', 'Middle Adriatic' and 'North Adriatic'. For each area, based on the existing measurements and data from 2015 and forecasts, an hourly chart of wind farm production is defined by 2050. The generated hourly charts are associated with each existing and future production unit. An increase in installed wind power capacity for the analyzed years is shown in (Table 1.).

5.3 Solar power plants modeling

Existing solar power plants as well as anticipated production units are distributed into nodes in the model according to their geographical position to 'Inland', 'Primorje' and 'Dalmatia'. For each area, the hourly production diagram is defined by 2050, based on the measurements collected for the base year 2015 and the forecasts for the analyzed period. The increase of the installed capacity of solar power plants for the analyzed years is shown in (Table 1.).

6 RESULTS

According to the data described in Section 5, the test model of the Republic Croatia was created. The model consists of 12 nodes, of which 6 represent high voltage nodes, 3 high voltage nodes where the wind power plants are connected to the grid and 3 medium voltage nodes where the created solar power plants are connected. Furthermore, for the purposes of analysis, several scenarios have been created to help manipulate input data. The two main scenarios were observed and analyzed, scenario without EVs and pumped-storage HPPs and scenario with EVs and pumped-storage HPPs. Increase in the installed capacity of wind and solar power plants in the created model, for the observed years is shown in the following figure (Figure 6.).

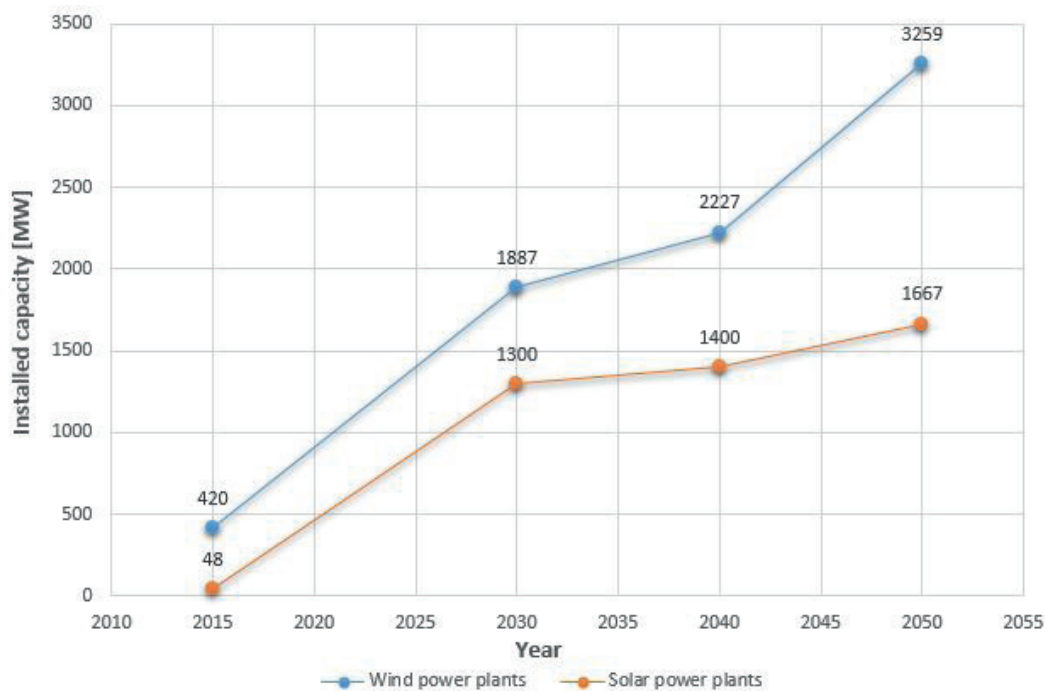


Figure 6. Increase in the installed capacity of wind and solar power plants for observed years

Impact on system flexibility can be observed by observing how much EVs and their quantity affect the production of certain power plants so that the lack or surplus production caused by intermittent production from RES is covered. Also, the production of RES themselves varies depending on whether there are or aren't EVs connected to the power system and whether the pumped-storage HPPs are constructed or not. When there are EVs and pumped-storage HPPs in the system, the total annual production from RES is higher (Figure 7. and Figure 8.).

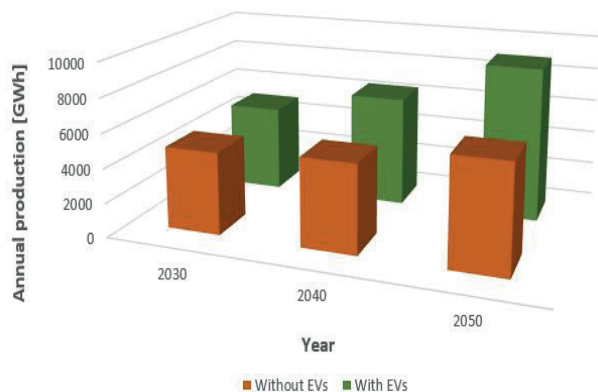


Figure 7. Annual production from wind power plants for both scenarios

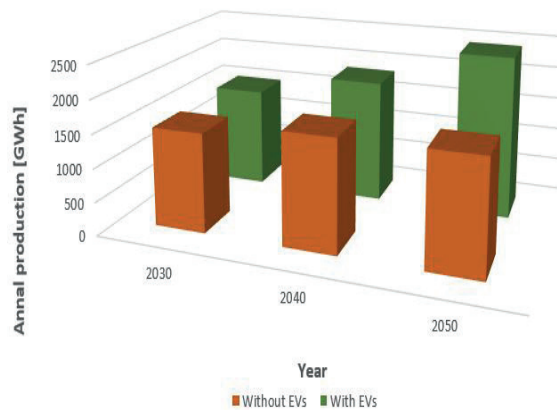


Figure 8. Annual production from solar power plants for both scenarios

An important influence on system flexibility is reflected in the production of fast ramping gas and slower coal thermal power plants, which in traditional systems without energy storage serve to cover the lack of electricity due to intermittent production from RES. In 2030 the increase of the EV capacity is relatively insignificant, therefore the increase of production from the wind and solar plants is only 270 GWh (Figure 9. and Figure 10.). However, it should be noted that the production from gas thermal plants is smaller in the EV scenario. Also, production from hydro plants is 2033 GWh smaller in the scenario without EVs. Results for 2040 are shown in (Figure 11. and Figure 12.). It is obvious that EVs cause a larger increase in total annual consumption than in 2030. For the scenario without EVs, the annual production from thermal plants is 33 GWh higher and the annual production from RES is 1441 GWh lower. Increased consumption caused by EVs is mostly covered by increased production from wind and solar plants, but also by an increase in production from hydro plants, which is 2907 GWh higher. In the case of 2050, the results are slightly different (Figure 13. and Figure 14.). Specifically, in the EV scenario, annual gas production is by 867 GWh higher than in the scenario without EVs. Obviously, the amount of 1.5 million EVs and modeled charging profiles cause a large increase in consumption in some periods (which coincides with the peak loads) that cannot be met by increased production from the installed RES and hydro plants, therefore the fast gas thermal plants increase their production.

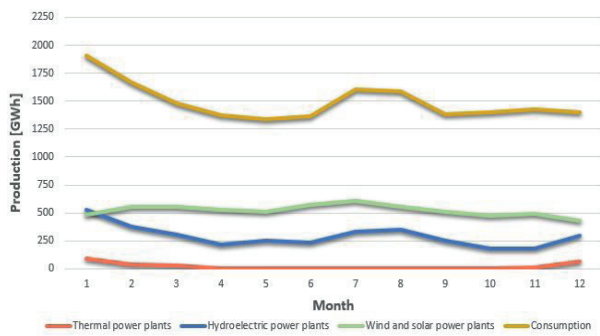


Figure 9. Production from wind and solar, gas thermal and hydro power plants for 2030 without EVs

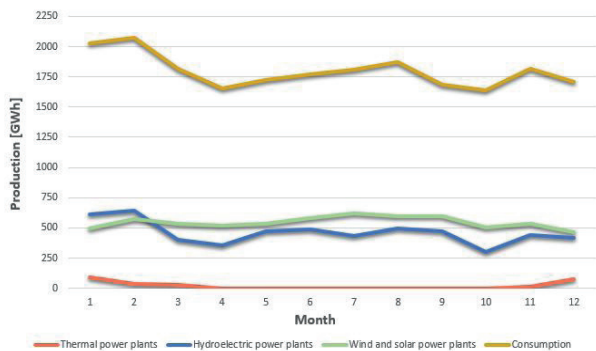


Figure 10. Production from wind and solar, gas thermal and hydro power plants for 2030 with EVs

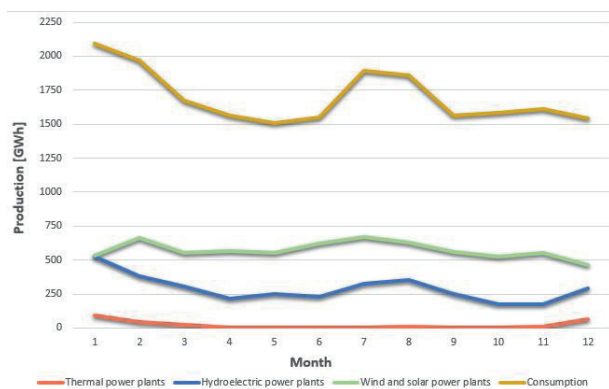


Figure 11. Production from wind and solar, gas thermal and hydro power plants for 2040 without EVs

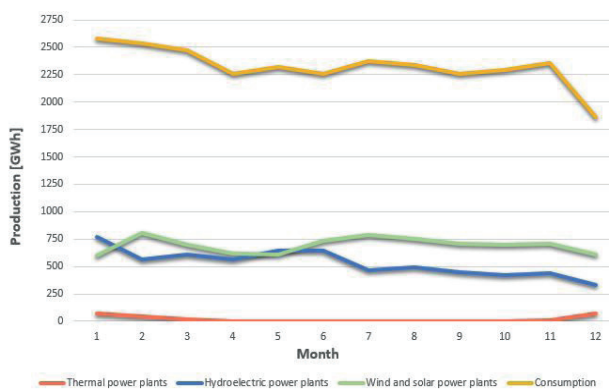


Figure 12. Production from wind and solar, gas thermal and hydro power plants for 2040 with EVs

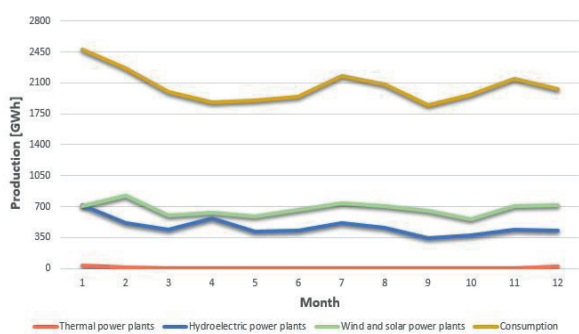


Figure 13. Production from wind and solar, gas thermal and hydro power plants for 2050 without EVs

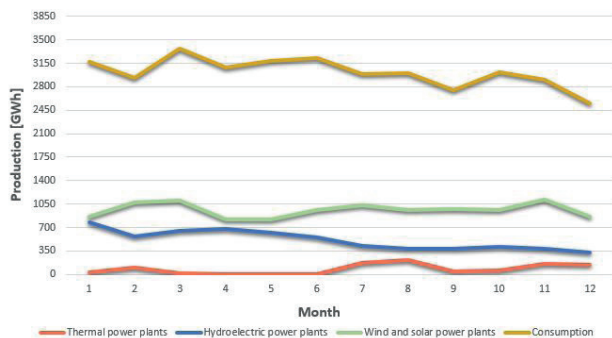


Figure 14. Production from wind and solar, gas thermal and hydro power plants for 2050 with EVs

In order to further examine the flexibility of the system, a new scenario has been made in which all thermal power plants, that can provide fast support for system balancing in the event of sudden changes in production from RES (primarily from wind power plants), have been excluded from the power system. After the simulation for the given scenario for three different observed years, the following data and conclusions are made and shown in (Table 2.).

Table 2. Flexibility of the power system for the new scenario

Year \ Scenario	2030.	2040.	2050.
Without EVs and pumped-storage HPPs	It was not possible to satisfy all the simulation conditions	It was not possible to satisfy all the simulation conditions	It was not possible to satisfy all the simulation conditions
With EVs and pumped-storage HPPs	In the basic scenario, the number of EVs is insufficient to store enough energy	In the basic scenario, the number of cars is insufficient to store enough energy	The number of EVs in basic scenario (about 1.5 million EVs) allows the operation of the system without starting the thermal power plant

When there are no modelled EVs and pump-storage HPPs in the system, the simulator cannot find the optimal solution since the system does not allow unserved energy, i.e. the demand must be met at any period of time. In such a scenario, neither the newly installed capacity of renewable sources along with other conventional ones is sufficient or sufficient to keep the system in balance at all times.

For scenarios when there are electric vehicles and pump-accumulating hydroelectric power plants, the results differ depending on the number and capacity of the EV. Namely, from all scenarios and years only in the scenario with EVs and pumped-storage HPPs in 2050, it is possible to fulfil all the limitations of system and simulation settings.

For more detailed analysis one day was taken into observation. The selected day was July 15, 2050 since it is one of the months where production from wind and solar power plants is smaller, and hydroelectric power plants are also producing less because of a reduced natural water inflow. The year 2050 was chosen because the system has the largest available EV capacity in that observed period.

In (Figure 15.) it is clear that in the periods between 4 – 11 and 13 – 23 hours during the day the EVs provide the power into the power grid so that the lack of production from installed and operating power plants (conventional and RES) is satisfied. It is only around noon that the energy that the EVs are consuming from the grid is larger than the total energy that is delivered into the grid, so the net production is negative. The picture also shows the net production of pumped-storage

HPPs. It is obvious that in the moments when the EVs cannot deliver power into the grid, or at night when the batteries are being charged, pumped-storage HPPs produce electric power to meet consumption. The figure clearly show how modelled energy storage technologies complement each other.

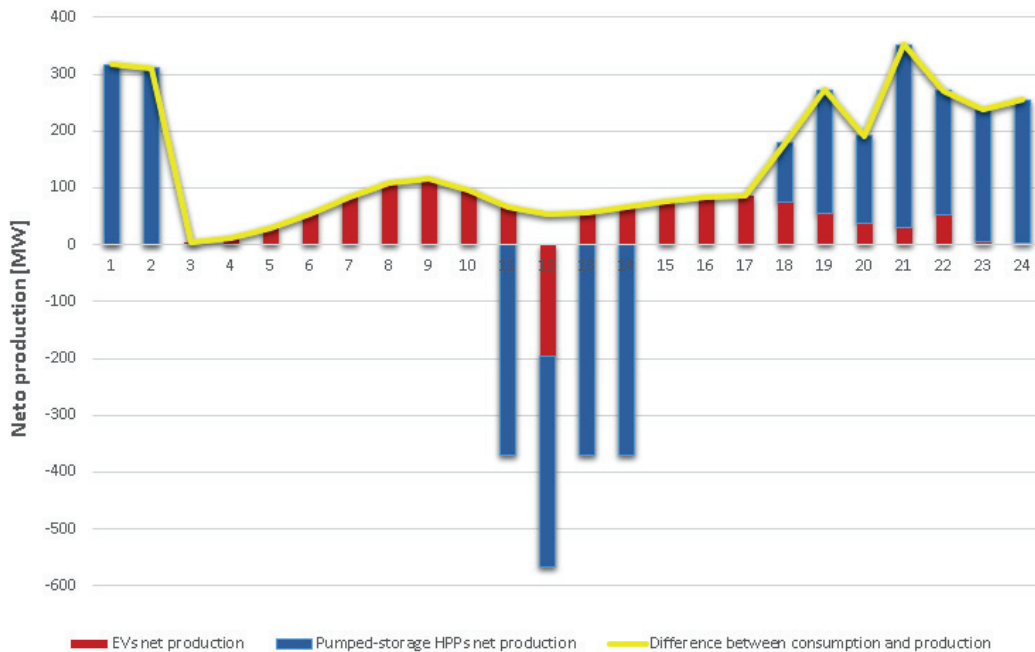


Figure 15. Net production of energy storage technologies in the system for 15.7.2050. for the scenario with EVs and pumped-storage HPPs

The impact of EVs on CO₂ emissions is one of the key parameters when analyzing the application of such energy storage technology. Namely, by increasing the share of EVs, emissions from the transport sector are shifted to the electricity production sector. Respectively, the emissions are shifted from non-ETS to ETS, which allows fulfillment of the targets set by the European Union for the observed period. The results suggest that in 2050 the additional load caused by EVs results in a small increase in CO₂ emissions since the EV charging was not modelled completely according to off-peak charging, therefore the EVs charging during peak load hours causes higher production from conventional fast power plants which contributes to CO₂ emission production. (Figure 16.) It can also be concluded that although RES capacity increases each year, the modelled growth around 2050 is not sufficient to cover the demand of the anticipated amount of EVs so the fast thermal power plants are started during some periods. Moreover, total production in both scenarios decreases over the years, which is expected as more and more RES enter the grid and conventional power plants are decomposed or they're production is not needed.

Total production costs are calculated as the sum of all production costs, including fuel costs, variable operating and maintenance costs (VO&M), start-up

cost, shutdown costs and emission costs. Comparing both scenarios it can be seen that in the case of the model with EVs the total production costs are lower during most of the analyzed period. Namely, as it was already mentioned, the production from RES in the scenario with EVs is higher and the costs of the production of such units are lower than conventional production units, hence the total production costs are somewhat smaller as shown in (Figure 17.). However, as in the case of CO₂ emissions, the higher production from thermal power plants in 2050, caused by the high number of EVs as much as the modelled charging profiles results in higher total generation cost.

Furthermore, the impact of modelled EVs and pumped-storage HPPs on total annual transmission losses is positive. Namely, due to the possibility of energy storage at locations closer to actual consumption, power flows are reduced and transmission losses in the power network are lower. (Figure 18.)

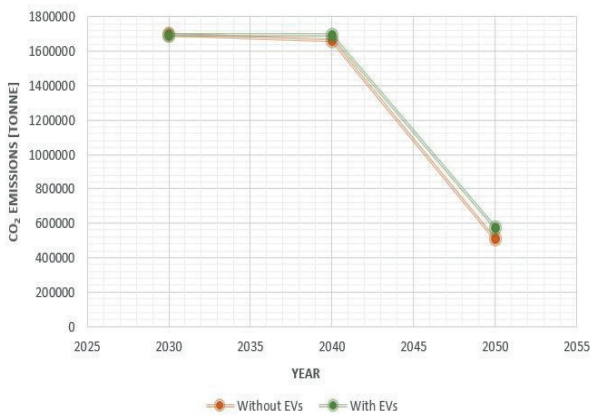


Figure 16. CO₂ Emissions for both scenarios

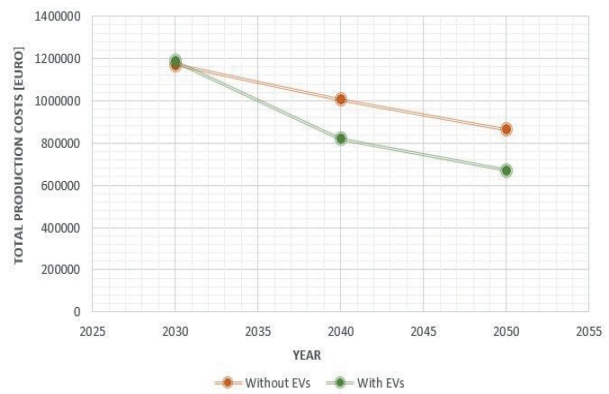


Figure 17. Total production costs for both scenarios

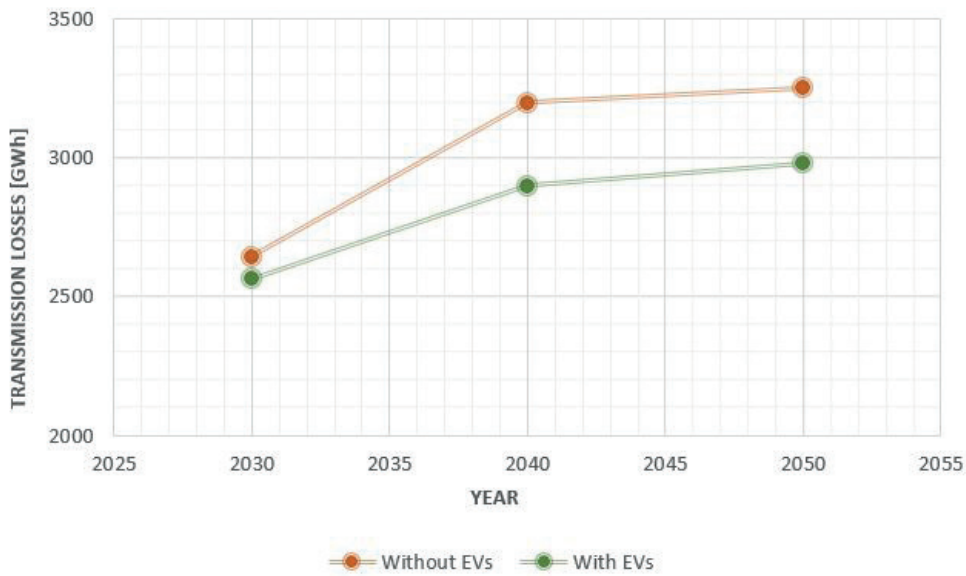


Figure 18. Transmission losses for both scenarios

6.1 Advantages and disadvantages of connecting EVs to power system

Based on the carried out analyses, and the results obtained in the previous chapter, the following advantages and disadvantages of electric vehicles can be concluded:

Advantages:

- Increase in production from variable RES – a higher increase in production from wind power plants.
- Reduced need for building additional conventional power plants to cover peak loads (with an increase in the number of EVs over the years the need for additional capacities of conventional power plants is decreasing).
- Decreased total production costs due to larger production from RES.
- Reduction of annual transmission losses.

Disadvantages:

- The need for a relatively large number of EVs to ensure sufficient capacity of energy storage.
- If the EVs are charging in periods of peak load, the conventional power plants with quick response must generate so that the additional load caused by high number of EVs is covered.
- Slight increase in CO₂ emissions compared to the scenario without EVs due to modelled charging profiles.

7 CONCLUSION

The European Union is the leader in the integration of renewable energy sources in the world. The latest directives intensify the construction of power plants using renewable sources. With the increase in production from renewable energy sources, or by increasing share of renewable energy sources in total consumption, it is being endeavored to reduce the dependence on energy imports as well as to contribute to the reduction of GHG emissions. The largest share in newly-installed capacities around the world is occupied by wind power plants. Wind power plants cause instability of the power system because of the volatility and unpredictability of the wind (especially on the long term basis) as a source of the energy. This raises the costs of maintaining the system in balance and in certain situations can lead to instability and even system breakdown. There are being options discussed, and as one of the most possible and prominent option are integration of EVs into the grid. The role of pumped-storage HPPs has already been recognized and there is a total installed capacity of 168 GW in the world. Pumped-storage HPPS are most often used in terms of energy arbitrages, i.e. during the off-peak periods, when the

electricity price is lower, electricity from the grid is used for the pumping of water from the lower to the higher water tank, and in the periods of higher demand, when the electricity price is higher, water flows through the turbine, which drives the generator, into the lower water tank, and produces electricity. One of the main advantages of pumped-storage HPPs is their synergy with variable energy sources, such as wind and solar power plants. This is due to the fact that pumped-storage HPPs can provide an instant reserve that can be utilized for a period of several seconds to several minutes when other variable RES are unavailable or their production is sudden abrupt.

The results based on the analysis made for both scenarios without and with EVs in the power system show that additional storage in a form of EVs allows increased production from RES, decreased need for building additional conventional fossil fueled thermal power plants to cover peak loads. Thus the total generation costs are lower and also the transmission losses are decreased. The observed deficiencies in this model are that a relatively large number of EVs is needed to ensure sufficient energy storage and if the EVs are charging in periods of peak load, the conventional power plants with quick response must generate so that the additional load caused by high number of EVs is covered. This as well causes a slight increase in CO₂ emissions compared to the scenario without EVs.

Further development of the model would include more detailed data on production units as well as expansion of the model of the whole region by creating production and consumption of neighboring countries, thus giving a better picture of cross-border transmissions, which would ultimately result in a more accurate picture of the Croatian power system. It would certainly be desirable to analyze scenarios with and without electric vehicles, but including the costs of the building of the charging stations. Also, further upgrading would be a detailed analysis (say, on a monthly basis) on how much wind and solar power plants are producing depending to their maximum capacity factor when there are no EVs in the system and when they are included in the model.

8 REFERENCES

- [1] European Commission, Energy, *Imports and secure supplies*, [online] <https://ec.europa.eu/energy/en/topics/imports-and-secure-supplies> Accessed on December, 12, 2017.
- [2] European Commission, Energy [online] http://ec.europa.eu/eurostat/statistics-explained/index.php/Consumption_of_energy. Accessed on November, 20, 2017.
- [3] European Commission, Energy [online] <http://ec.europa.eu/eurostat/statistics->

[explained/index.php/Greenhouse_gas_emission_statistics_-_emission_inventories](#). Accessed on November, 20, 2017.

- [4] M. Kalea, *Nekonvencionalni izvori energije*. (2006) lectures, ETF Osijek
- [5] G. Bachner, A. Tuerk, K. Williges i K. Steininger, D4.2. *Economic costs and benefits for renewables deployment in the EU*, CARISMA, innovation for Climate Change Mitigation, European Commission, Graz, 2017.
- [6] M. Rekić i Z. Klaić, *Utjecaj električnih vozila na opterećenje i kvalitetu električne energije u distribucijskoj mreži* (2016) HO CIRED, Osijek
- [7] <http://www.evtown.org/about-ev-town/ev-charging/charging-levels.html>
Accessed on November, 23, 2017.
- [8] Energy Exemplar, Concise user guide for the PLEXOS for power system software. [online]
<https://wiki.energyexemplar.com/index.php?n=Article.ConciseModellingGuide>
Accessed on December, 15, 2017.
- [9] MZOIP, Bijela knjiga. [online]http://mzoip.hr/doc/16062017_-_bijela_knjiga.pdf. Accessed on December, 10, 2017.

IVAN PAVIĆ**TOMISLAV CAPUDER****IGOR KUZLE**Ivan.pavic@fer.hrTomislav.capuder@fer.hrIgor.kuzle@fer.hr**University of Zagreb Faculty of Electrical Engineering and
Computing**

GENERATION SCHEDULING IN POWER SYSTEMS WITH HIGH PENETRATION OF RENEWABLE ENERGY

SUMMARY

Share of renewable energy sources increased rapidly over last two decades primary as wind and solar power plants. Their increase was driven by governmental subsidies and priority access and dispatch regarding conventional units. Wind and solar power plants are inflexible sources because their generation depends on exterior, weather conditions and they cannot be controlled as conventional units. This paper will define term power system flexibility and provide an insight into flexibility of conventional and modern power systems. Detailed mathematical model of power system and all its components has been created and explained. Modeling has been executed as mixed integer linear program using Fico Xpress optimization suite. Using those models, flexibility analyses of power systems with different renewable energy sources share has been conducted.

Key words: Mixed Integer Linear Programming, Power System Flexibility, Renewable Energy Sources, Unit Commitment, Wind Power Plants

1. INTRODUCTION

Penetration of renewable energy sources in power system have numerous advantages for the society in general, such as: lower energy costs, greenhouse gas emission decrease, decrease in dependence on fossil fuels, new vacancies [1] etc. But from the technical point of view, it changes conventional power system paradigm where power plants were controllable and used to cover demand variations and equipment failures. If renewable energy sources take higher share in total installed power, it effectively means increase in power variations and lower share of controllable units. Power system operators and planners must prepare for such transition in order to maintain continuous and reliable power supply. First step is do determine the cumulative impact of renewable source on power system costs and behavior through certain period. Second step should be testing of novel technologies in order to lower the costs and increase reliability. For mentioned reason, this paper aims to build a mathematical model of a power system and use the created model for analyzing the system flexibility with different shares of intermittent renewable energy resources. The paper is divided into three main parts. The first section briefly explains the characteristics of the power system now and in the past, and gives insight into further development of the system. Section also explains the concept of flexibility and applies it to the entire system and its components. The second part focuses on the development of mathematical model of the power system whose goal is optimization of generation scheduling minimizing operational costs. Final chapter tests performance of the model on different power systems. Used systems are constructed of thermal power, hydropower, renewable energy, energy storage and demand response. It analyzes the behavior of various power systems by adding new wind farms, photovoltaic power plants, energy storage and demand response into calculation. Finally, results are summarized, systems are evaluated regarding flexibility.

2. FLEXIBILITY

Power consumption is time-varying value observing different timescales: day (high consumption at daytime, low at night), week (higher consumption at work days then weekends), year (seasonal fluctuations) and long-term (in general, demand increase every year). In conventional vertically integrated power system, power system operator must commit units to cover total demand. Base load is usually covered by highly inflexible units such as nuclear and run-of-river hydro power plants, while intermediate load is usually covered by fossil fuel (coal and oil) power plants and hydro power plants with low accumulation. Peak load is covered by flexible units such as hydro power plants with large accumulation, pump storage or gas fueled thermal power plants.

Flexibility of units is determined by their technical parameters:

- Technical minimum,

- Ramping,
- Minimum up time,
- Minimum down time,
- Maximum generation.

Another flexibility barrier is the cost of generation. Each unit have several costs associated with its generation:

- No-load cost,
- Variable cost,
- Startup cost,
- Greenhouse gas emission cost.

Nuclear power plants have inadequate technical parameters for flexibility, high startup and low variable cost. Therefore, once when they are started their power is maintained fixed. Hydro power plants possess good technical flexibly parameters and low startup costs, so if there is sufficient accumulation they are generally driven in load-following regime. Thermal power plants have better technical parameters for flexibility then nuclear but lower then hydro power plants. Coal and oil have relatively high startup costs and low variable cost, whereas gas have low startup cost and high variable cost. In other words, coal and oil units are used as base or intermediate units and gas as peak units.

Due to variability and demand forecast mistakes each power system must have sufficient flexibility to maintain generation and load balance. In order to be sure that the system will be balanced in each time period sufficient reserves must be committed. Eventhough demand forecast are getting better and better and mistakes are very low, still we can model them with normal probability function with average value zero and standard deviation of 1% of current demand. If range of 3σ is considered, 99,7% of load deviations will be covered. Another big issue is probability of failure of power system equipment such as generators and lines. Simple way to address this issue is to incorporate the size of the biggest generator in the equations for reserve calculation. Equations

$$R_{Tup}(t) = \sqrt{(3 * \sigma_d(t))^2 + (P_{Gmax}(t))^2}, \quad t \in [1, N_t] \quad (1)$$

$$R_{Tdn}(t) = 3 * \sigma_d(t), \quad t \in [1, N_t] \quad (2)$$

- R_{Tup} , R_{Tdn} – Up and Down reserve of traditional power system,
- σ_d – Standard deviation of load,
- P_{Gmax} – Installed power of the biggest generator.

Increasing share of variable renewable energy sources such as wind, run-of-river hydro, solar, waves etc. increase the flexibility requirements as well. Solar and

wind power plants are the most widespread renewable energy technology and they will be used as representatives for the group. Neither solar nor wind do not have storage capability, so they must generate and inject power into the grid when meteorological conditions are met. Wind variability can be observed on different timescales. Statistical analyses of long-term observations indicate certain regularity due to seasonal methodological patterns. On second timescale, wind speed and direction variations are notable, but they are mitigated through relatively slow wind turbine response. The biggest problem for the system are wind speed and direction variations on minute timescale because the system must have enough flexible units to change their direction when wind turbines change their generation. Variations of solar irradiation can be divided into those caused by Earth's movement around the Sun and those caused by atmospheric dispersion. First ones are easily predictable (both daily and seasonally), but cloud movements through atmosphere are not and they bring forecast errors into prediction of output power generation of solar panels. In order to take into account both wind and solar prediction errors Eq. 1. and 2. should be modified with standard deviations of wind and solar generation to equations:

$$R_{Mup}(t) = \sqrt{(3 * \sigma_d(t))^2 + (3,5 * \sigma_w(t))^2 + (3,5 * \sigma_{pv}(t))^2} + P_{Gmax}(t) \quad (3)$$

$$R_{Mdn}(t) = \sqrt{(3 * \sigma_d(t))^2 + (3,5 * \sigma_w(t))^2 + (3,5 * \sigma_{pv}(t))^2}, \quad t \in [1, N_t] \quad (4)$$

- R_{Mup} , R_{Mdn} – Up and Down reserve of modern power system,
- σ_d , σ_w , σ_{pv} – Standard deviation of load, wind and solar generation,
- P_{Gmax} – Installed power of the biggest generator.

Forecast errors are increasing as period of forecasting increases. In this paper, 24 hour ahead forecasts are taken as inputs and reserve is therefore modeled in a way that it increases every hour. In the last observed hour, reserve is 10% higher than without the increase.

Power system flexibility can be increased through:

- Reconstruction of existing generators (updating their technical characteristics, lower technical minimum, faster ramping, shorter up and down times...),
- Investment in new flexible generators (gas turbines),
- Investment in new interconnectors (adjacent power systems coupling),
- Integration of energy storage technologies,
- Activation of demand, enabling demand response...

Energy storage technology are gaining a lot of attention last few years, mostly as a direct consequence of RES integration and increased system flexibility needs. Energy storage systems increase total system efficiency and can make some of the peak plants unnecessary. Still, energy storage systems are too expensive to be cost effective. One why is to subsidize them in a similar manner as governments created subsidies for RES technologies. On competitive electricity market energy storage technologies should be equal to production units and should be able to provide different services (reserves, voltage regulation, black start etc.). Similar to energy storage, demand response could be used to provide flexibility to power system. The highest investment to enable demand response is investment in ICT equipment to create conditions for automatic response of flexible demand.

3. MATHEMATICAL MODEL

Mixed integer linear program has been created in Fico Xpress optimization suite [2]. Modeling is divided into several parts: definition of variables, initialization of input parameters, modelling of constraints, objective functions and verification through results. Input parameters have been read from excel file where the output results are printed and graphically processed. Observed power system is composed of

N_t thermal power plants (fossil and nuclear), N_{ih} hydro power plants and pump storage, wind turbines, photovoltaics, battery storage systems and demand response. Each of the technologies have specific constraints modeled so the system is as close to real as possible. In each time period N_t power generation and demand must be balanced. For more information, similar modeling can be found in [3],[4], and [5].

3.1. Objective function

Objective function is summation of thermal and hydro generation costs. Thermal power plant costs are given through Eq. (5) as summation of five parts:

- Startup costs,
- Shut-down costs,
- No-load fixed costs,
- Variable fuel costs, and
- Greenhouse gas emissions costs.

$$C_{TE}(t, i) = v_{on}(t, i) * C_{start}(i) + v_{off}(t, i) * C_{shut}(i) + A(i) * n(t, i) + B(i) * P(t, i) + Em(t, i) * Em_c(i), t \in [1, N_t], i \in [1, N_i] \quad (5)$$

Vector n shows how many thermal power plants from each of the subgroup (nuclear, coal, gas CCGT, gas OCGT) is online, whereas vectors v_{on} and v_{off} show how many thermal power plants is startup or shutdown each discrete time step.

$$v_{on}(t, i) \geq n(t, i) - n(t - 1, i) \quad (6)$$

$$v_{off}(t, i) \geq n(t - 1, i) - n(t, i) \quad (7)$$

Greenhouse gas emissions have two parts, one concerning startup emissions and variable emissions connected with each new generated unit of electricity:

$$Em(t, i) \geq v_{on}(t, i) * Em_{rstart}(i) + P(t, i) * Em_r(i), \quad t \in [1, N_t], i \in [1, N_{ih}] \quad (8)$$

Hydro power plant costs are composed of fixed and variable costs, where variable cost is concerning maintenance not fuel cost as with thermal power plants.

$$C_{HE}(t, i) = A_h(i) * n_h(t, i) + B_h(i) * P_h(t, i), \quad t \in [1, N_t], i \in [1, N_{ih}] \quad (9)$$

Two additional terms were added to objective function in Eq. 10 in order to ensure feasibility of the model. Variables e_{minus} and e_{plus} represent lack and surplus of power within the system.

$$f_{cilj}^{min} = \sum_{t=1}^{N_t} \left\{ \sum_{i=1}^{N_i} [C_{TE}(t, i)] + \sum_{i=1}^{N_{ih}} [C_{HE}(t, i)] + e_{minus}(t) * C_{shed} + e_{plus}(t) * C_{ove} \right\} \quad (10)$$

2.2. System constraints

There are two main constraints in observed power system: power generation-demand balance represented with Eq. 11, and reserve provision-requirements balance for up and down reserve represented with Eq. 12 and 13. Terms in Eq. 11 from left to right: thermal power plants generation, hydro power plants generation (minus potential pumping of pump storage facilities), wind generation, photovoltaics generation, battery charging/discharging power, feasibility variables (up and down) and on the right-hand side total system demand.

$$\sum_{i=1}^{N_i} P(t, i) + \sum_{i=1}^{N_{ih}} [P_h(t, i) - P_p(t, i)] + w(t) + pv(t) + P_b(t) + e_{minus}(t) - e_{plus}(t) = \dots$$

$$t \in [1, N_t] \quad (11)$$

$$\sum_{i=1}^{N_i} r_{up}(t, i) \geq R_{up}(t), \quad t \in [1, N_t] \quad (12)$$

$$\sum_{i=1}^{N_i} r_{dn}(t, i) \geq R_{dn}(t), \quad t \in [1, N_t] \quad (13)$$

Please note that only one type of reserves has been observed due to simplicity.

2.3. Component constraints

This Subsection is going to define constraints for each of the technologies observed in model.

Eq. 14 represents generators technical minimum and maximum generation constraint (vector $n(t, i)$ is number of online units in the system). In Eq. 15 total number of thermal generators has been defined, while Eq. 16 and 17 define number of units started up and shut down each time step.

$$n(t, i) * P_{max}(i) \geq P(t, i) \geq n(t, i) * P_{min}(i), \quad t \in [1, N_t], i \in [1, N_i] \quad (14)$$

$$n(t, i) \leq G(i), \quad t \in [1, N_t], i \in [1, N_i] \quad (15)$$

$$v_{on}(t, i) \leq n(\tau, i), \quad \tau \in [t + 1, \min(t + T_{up}(i) - 1, N_t)], \quad t \in [1, N_t - 1], i \in [1, N_i] \quad (16)$$

$$v_{off}(t, i) \leq G(i) - n(\tau, i), \quad \tau \in [t + 1, \min(t + T_{dn}(i) - 1, N_t)], \quad (17)$$

$$t \in [1, N_t - 1], i \in [1, N_i]$$

Thermal power plants ramping has been defined in Eq. 18-20, while thermal power plants reserve provision capability has been defined in Eq. 21-24.

$$P(t, i) - P(t - 1, i) \leq n(t - 1, i) * V_{up}(i) * \Delta + v_{on}(t, i) * P_{min}(i), \quad t \in [2, N_t], i \in [1, N_i] \quad (18)$$

$$P(t, i) - P(t - 1, i) \leq (P_{max}(i) * n(t - 1, i) - P(t - 1, i)) + v_{on}(t, i) * P_{min}(i), \quad (19)$$

$$t \in [2, N_t], i \in [1, N_i]$$

$$P(t - 1, i) - P(t, i) \leq n(t, i) * V_{dn}(i) * \Delta + v_{off}(t, i) * P_{min}(i), \quad t \in [2, N_t], i \in [1, N_i] \quad (20)$$

$$r_{up}(t, i) \leq P_{max}(i) * n(t, i) - P(t, i), \quad t \in [1, N_t], i \in [1, N_i] \quad (21)$$

$$r_{dn}(t, i) \leq P(t, i) - P_{min}(i) * n(t, i), \quad t \in [1, N_t], i \in [1, N_i] \quad (22)$$

$$r_{up}(t, i) \leq V_{up}(i) * n(t, i) * \Delta, \quad t \in [1, N_t], i \in [1, N_i] \quad (23)$$

$$r_{dn}(t, i) \leq V_{dn}(i) * n(t, i) * \Delta, \quad t \in [1, N_t], i \in [1, N_i] \quad (24)$$

Hydro power plants possess energy storage capabilities in the form of water accumulation. Main hydro power plant equation is water balance equation defined as Eq. 25. Variables in Eq. 25 from left to right: usable water volume of observed time step, usable water volume of last time step, inflow, turbine flow, overflow. Eq. 26 defines upper and lower boundaries for usable water volume, Eq. 27 and 28 define the same boundaries for turbine flow and overflow, respectively.

$$V_k(i) * G_h(i) \geq V(t, i) \geq 0 \quad t \in [1, N_t], i \in [1, N_{ih}] \quad (25)$$

$$Q_{max}(i) * n_h(t, i) \geq Q(t, i) \geq Q_{min}(i) * n_h(t, i) \quad t \in [1, N_t], i \in [1, N_{ih}] \quad (26)$$

$$2 * G_h(i) * Q_{max}(i) \geq S(t, i) \geq 0 \quad t \in [1, N_t], i \in [1, N_{ih}] \quad (27)$$

Eq. 28 and 29 tackle hydro power plant power generation. Eq. 28 define linearized hydro power plant generation and eq. 29 put upper and lower boundaries on it. Eq. 30 defines existing number of hydro power plants in observed power system.

$$P_h(i) = \eta_h(i) * H(i) * Q(t, i) * g * \rho_h \quad t \in [1, N_t], i \in [1, N_{ih}] \quad (28)$$

$$P_{max_h}(i) * n_h(t, i) \geq P_h(t, i) \geq P_{min_h}(i) * n_h(t, i) \quad t \in [1, N_t], i \in [1, N_{ih}] \quad (29)$$

$$n_h(t, i) \leq G_h(i), \quad t \in [1, N_t], i \in [1, N_{ih}] \quad (30)$$

Pump storage facilities have additional variable in water balance equation – pumping power defined as Q_p in Eq. 31. Eq. 32 uses variable Q_p for pumping power calculation, while Eq. 33 doesn't allow simultaneous pumping and generation. Reserve provision of hydro and pump storage plants has been modeled in the same manner as thermal power plants.

$$VL(t, i) = VL(t - 1, i) * kv(i) + Q(t, i) * 3600 * \Delta - Q_p(t, i) * 3600 * \Delta + S(t, i) * 360 * \Delta - S_l(t, i), \quad t \in [1, N_t], i = RHE \quad (31)$$

$$P_p(i) = \eta_{hp}(i) * H(i) * Q_p(t, i) * g * \rho_h \quad t \in [1, N_t], i = RHE \quad (32)$$

$$a_g(t) + a_p(t) \leq 1, \quad t \in [1, N_t] \quad (33)$$

Demand response has been modeled as increase or decrease of demand through Eq. 34 with the condition that total energy must be conserved in chosen time period through Eq. 35. Eq. 36 and 37 are upper and lower boundaries for demand increase and decrease, respectively.

$$D(t) = D_i(t) + D_{dn}(t) - D_{up}(t) \quad t \in [1, N_t] \quad (34)$$

$$\sum_{t=1+N_{t24}*k}^{\min(N_{t24}*(k+1), N_t)} D(t) = \sum_{t=1+N_{t24}*k}^{\min(N_{t24}*(k+1), N_t)} D_i(t), \quad k \in [0, N_t/N_{t24}] \quad (35)$$

$$D_{maxdn}(t) * N_d \geq D_{dn}(t) \geq 0 \quad t \in [1, N_t] \quad (36)$$

$$D_{maxup}(t) * N_d \geq D_{up}(t) \geq 0 \quad t \in [1, N_t] \quad (37)$$

Base battery storage system equation is energy conservation equation represented with Eq. 38, variables from left to right are: energy stored in battery storage in observed time period, energy stored in previous period and power charged/discharged from battery. Eq. 39 and 40 are upper and lower boundaries for battery storage capacity and charging/discharging power, respectively.

$$C(t) = C(t-1) * kb - ef_b * P_b(t) * \Delta \quad t \in [1, N_t] \quad (38)$$

$$C_{max} * N_b \geq C(t) \geq C_{min} * N_b \quad t \in [1, N_t] \quad (39)$$

$$P_{bmax} * N_b \geq P_b(t) \geq -P_{bmax} * N_b \quad t \in [1, N_t] \quad (40)$$

Renewable energy sources are bound just with their maximal possible generation which is directly connected with weather conditions. Eq. 41 represents wind power generation and eq. 42 photovoltaics.

$$w(t) + \Omega(t) = W(t) \quad (41)$$

$$pv(t) + \Omega_{pv}(t) = PV(t) \quad (42)$$

4. RESULTS AND DISCUSSION

The analyses was conducted in three separate ways. First, we defined 8 different energy mixes with thermal and hydro power plants and added different shares of wind power plants to those systems. Wind power plants were chosen as representatives of variable renewable energy sources. Secondly, we chose one of those energy mixes and added photovoltaics (and vary their and wind power plants installed power). And finally, we added energy storage and demand response and vary their share as well.

4.1. Different energy mixes with different wind penetrations

Table 1 defines percentages of different conventional technologies used in analyses.

Table 1 Different energy mixes used in analyses

Type [%] Energy mix	Nuclear (NE)	Coal (UTE)	CCGT (PTEk)	OCGT (PTEo)	Run-of-river (PHE)	Hydro small (AHEm)	Hydro large (AHEv)	Pump storage (RHE)
A	50	35	15	0	0	0	0	0
B	26	0	26	48	0	0	0	0
C	17	52	31	0	0	0	0	0
D	9	26	35	30	0	0	0	0
E	17	26	24	0	10	12	11	0
F	17	26	18	0	9	0	0	30
G	9	17	21	0	9	26	18	0
H	0	0	9	0	23	23	16	30

Figure 1 and 2 show cost decrease and wind curtailment increase for energy mixes A-D for different wind penetrations (0-80%). Figure 3 and 4 show weekly generation scheduling for D case with 0 and 40 % wind.

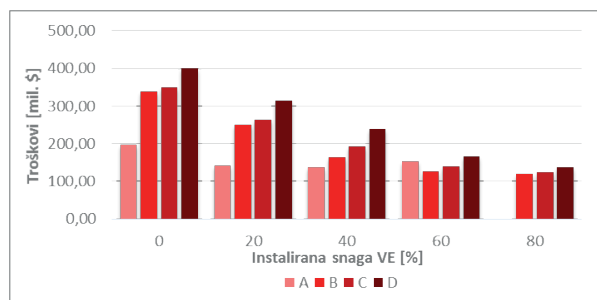


Figure 1 Total cost for A-D mixes

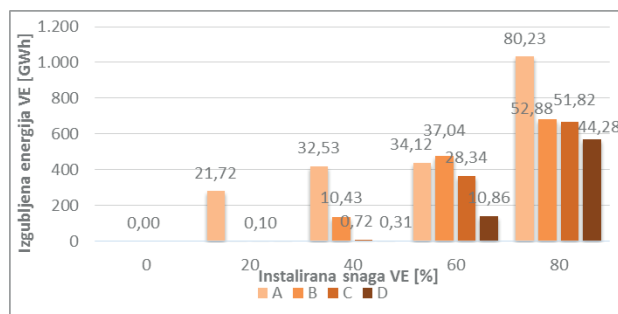


Figure 2 Wind curtailment for A-D mixes

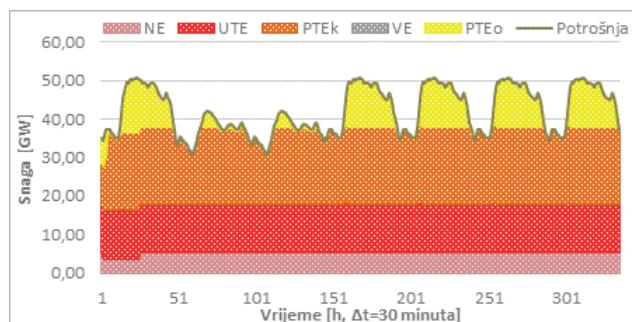


Figure 3 Generation scheduling for D mix with 0% wind

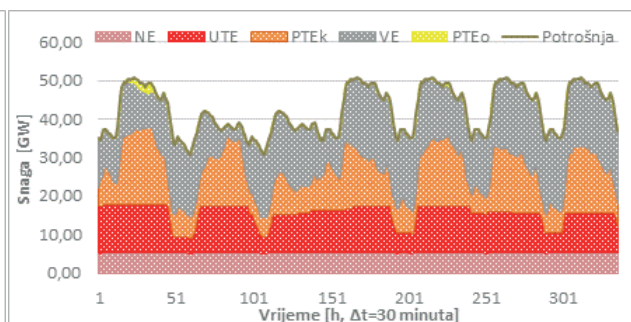


Figure 4 Generation scheduling for D mix with 40% wind

Figure 5 and 6 show cost decrease and wind curtailment increase for energy mixes E-H for different wind penetrations (0-80%). Figure 7 and 8 show weekly generation scheduling for F case with 0 and 40 % wind.

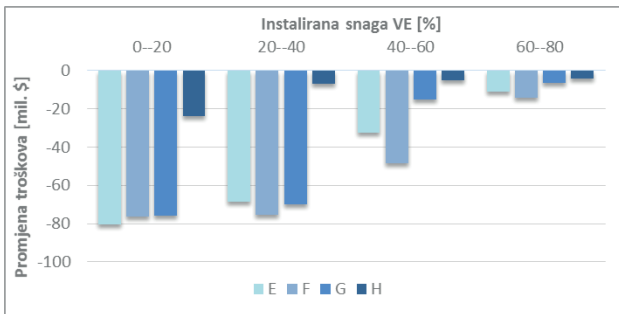


Figure 5 Total cost for E-H mixes

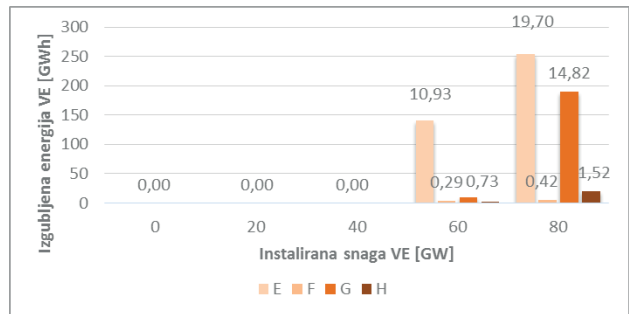


Figure 6 Wind curtailment for E-H mixes

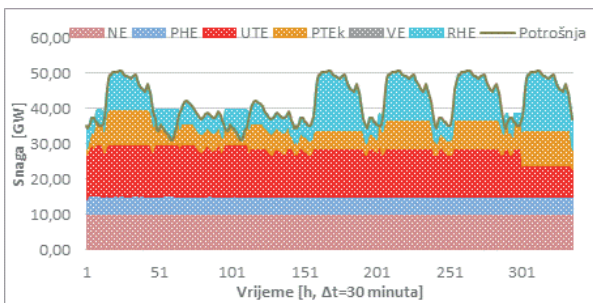


Figure 7 Generation scheduling for F mix with 0% wind

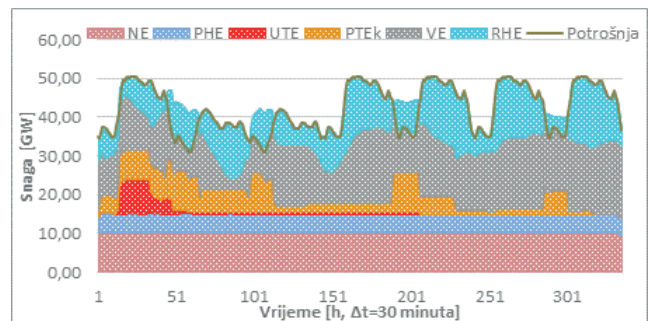


Figure 8 Generation scheduling for F mix with 40% wind

4.2. Different wind and solar power penetrations

Figures 9, 10 and 11 show cost decrease, wind and solar curtailment increase for energy mix D for different wind (0-80%) and solar penetrations (0-40%). Figures 12, 13 and 14 show weekly generation scheduling for D mix with wind penetrations (0, 40 and 80%, respectively) and 40 % solar.

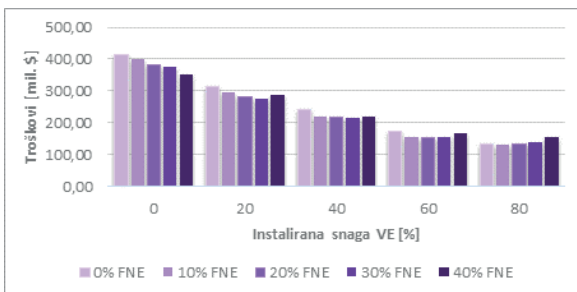


Figure 9 Total cost for mix D with different wind and solar shares

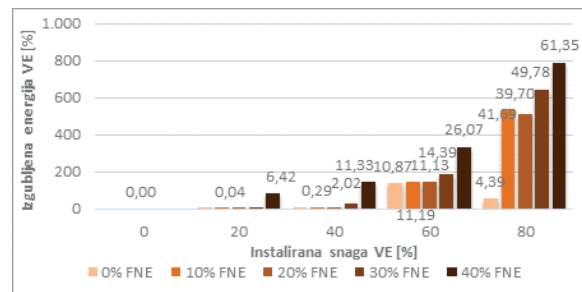


Figure 10 Wind curtailment for mix D with different wind and solar shares

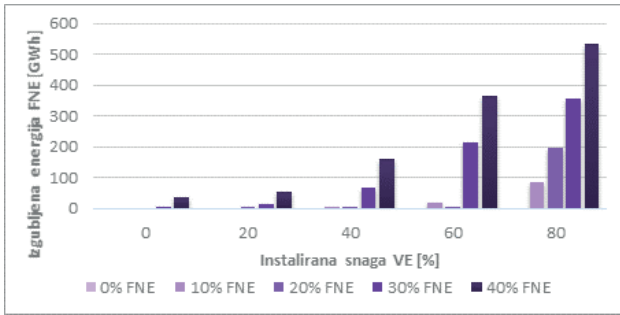


Figure 11 Solar curtailment for mix D with different wind and solar shares

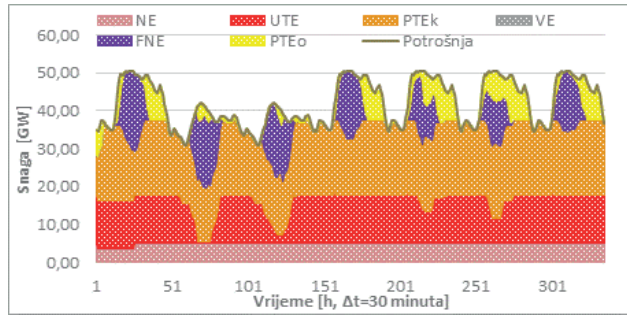


Figure 12 Generation scheduling for D mix with 0% wind and 40% solar

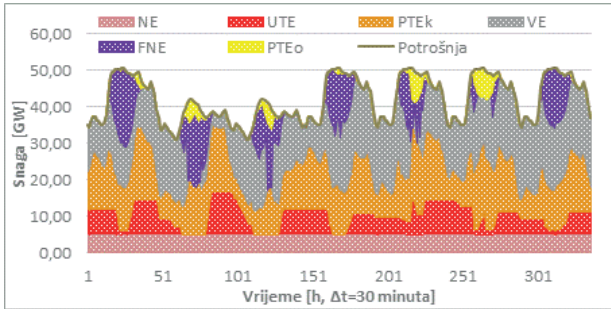


Figure 13 Generation scheduling for D mix with 40% wind and 40% solar

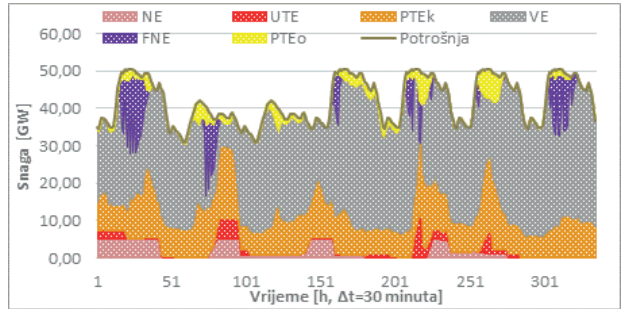


Figure 14 Generation scheduling for D mix with 80% wind and 40% solar

4.3. Introduction of energy storage systems and demand responses

Figures 15 and 16 show cost decrease and wind curtailment increase for energy mix B for different wind (0-80%) and adjustable demand penetrations (0-40% demand response+storage). Figures 17 and 18 show weekly generation scheduling for B mix with 80% RES penetrations (wind + solar) and 0% and 20% adjustable demand penetrations.

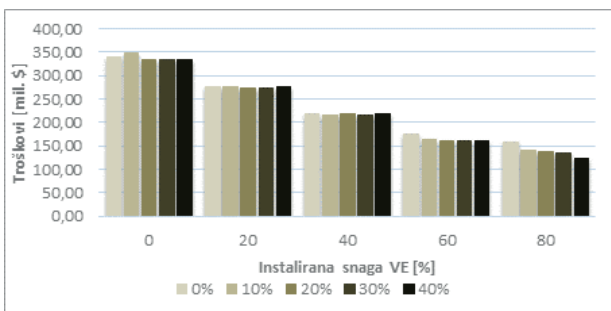


Figure 15 Total cost for mix B with different share of wind and adjustable demand (demand response+storage)

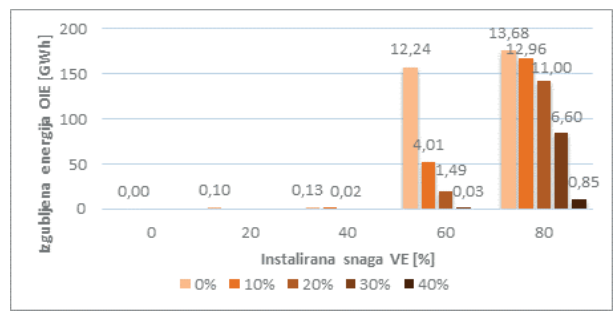


Figure 16 Wind curtailment for mix B with different share of wind and adjustable demand (demand response+storage)

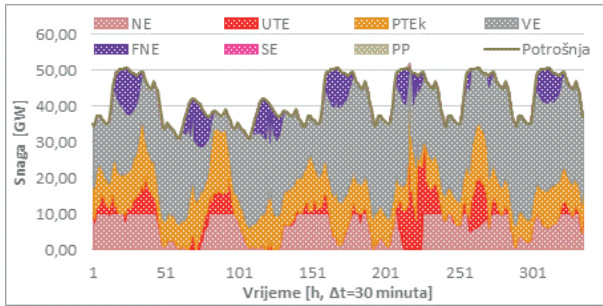


Figure 17 Generation scheduling for B mix with 80% RES (wind & solar) and 0% adjustable demand (demand response+storage)

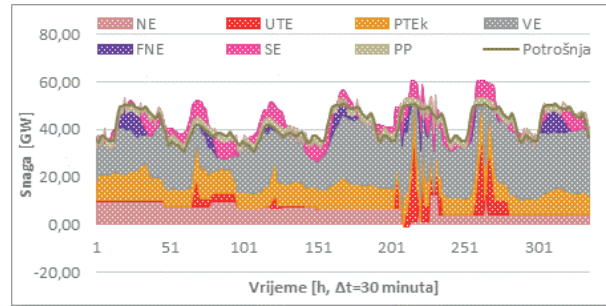


Figure 18 Generation scheduling for B mix with 80% RES (wind & solar) and 20% adjustable demand (demand response+storage)

5. CONCLUSIONS

The work presented mathematical optimization model of power systems primarily for renewable energy sources integration discussion. Model can be used as a tool to get a better insight into system's behavior under integration of different novel technologies. Model has been used with different energy mixes and penetration levels of RES technologies and the following can be concluded:

- Inflexible power plants, especially nuclear power plants, have major impact on power systems acceptance levels for renewable energy sources. More inflexible units within the system higher wind curtailment.
- Gas turbines, as the most expensive conventional power plants, are first to lose foothold when high share of RES is incorporated into system. It's cheaper for the system to curtail wind then to startup gas turbines.
- Hydro power plants drastically increase possible RES share due to their inherit flexibility.
- Pump storage facilities are the most flexible conventional units, and their proper share allows unlimited RES penetration share.
- Photovoltaics, when no wind is integrated, positively effect power systems behavior because they produce energy only during peak periods.
- High penetration of both wind and solar has negative affect on system's efficiency during periods of high generation of wind turbines and photovoltaics because large energy quantities are being curtailed.
- Energy storage and demand response have positive effect on systems with and without renewable energy sources. Without RES, they mitigate the need for peak plants, and with RES they decrease curtailed renewable power.

6. REFERENCES

- [1] US Energy Information Administration (EIA): „The International Energy Outlook 2013“, US Energy Information Administration, Washington DC, US, 205805, July 2013.
- [2] C. Guiret; C. Prins; M. Sevaux: „Applications of Optimization with Xpress-MP“, Editions Eyrolles, ISBN: 0-9543503-0-8, Paris, France, 2000.
- [3] M. Aunedi: „Generation Scheduling in Power Systems with High Penetration of Renewable Energy“, Imperial college London, London, 2009.
- [4] V. Silva: „Value of Flexibility in Systems with Large Wind Penetration“, Imperial college London, London, Listopad 2010.
- [5] J. Ma: „Evaluating and Planning Flexibility in a Sustainable Power System with Large Wind Penetration“, The university of Manchester, Manchester, 2012.

ANDREA STOŠIĆ¹ ANTE MARUŠIĆ² JURAJ HAVELKA²
andrea.stosic@aecom.com ante.marusic@fer.hr juraj.havelka@fer.hr

¹ AECOM, Manchester, UK

² University of Zagreb Faculty of Electrical Engineering and Computing

TRANSMISSION LINES PROTECTION USING SIPROTEC NUMERICAL RELAYS

SUMMARY

This paper analyses the fundamental principles of distance protection relays while highlighting the importance of correct relay parameterising through a set of relay tests. Numerical distance relays can have up to 6 distance zones, and nowadays most of them have a quadrilateral (polygonal) characteristic. The specific objective of this study was to apply those principles on a SIPROTEC distance protection 7SA611 relay with the help of Omicron CMC 56 testing device, as well as to describe the testing process. As a part of the testing, DIGSI and Test Universe Software were used. Experimental results confirm the theoretical principles of distance protection and show the advantages of numerical relays. This paper concludes that optimal choice of reach settings and time delays between the zones, as well as zone directions, can significantly impact the selectivity of the protection system, and therefore the scope and time of the outage.

Keywords: distance protection, numerical relay, polygonal characteristic, SIPROTEC, zone settings

1. INTRODUCTION

Transmission lines form a fundamental part of the electrical power system, as they present the path between generation and load. Often factors like deregulated market environment, economics, and environmental requirements urge utilities to operate transmission lines close to their limits. In a tightly interconnected system any fault, if not detected and isolated quickly, will cascade into a system-wide disturbance resulting in widespread outages. Consequently, it is crucial to equip transmission line terminals with relayed circuit breakers. Transmission protection systems are designed to identify the location of faults and isolate only the faulted section, that is to say, a minimum number of circuit breakers should trip, and preserve the selectivity of the system. The protection system selected should also provide redundancy to limit the impact of device failure, and backup protection to ensure dependability. For high-speed clearing times for faults occurring at any point on a transmission line, it is essential to produce some form of a communication channel between the transmission line terminals. This way, protective relaying systems can exchange information to determine whether the fault is internal or external to the protected line. The reliability of communications impacts the safety of the protection system. Thus its importance is vital. For transient faults such as lightning strikes, automatic reclosing may be applied, followed by fault clearance, to restore the line service [1].

2. DISTANCE PROTECTION

Bearing in mind that the line impedance is proportional to its length, it is appropriate to measure the impedance of a line up to a predetermined (reach) point. Such a relay described as distance relay, operates only for faults occurring between the point of relay location and the selected reach point, hence giving discrimination for faults that may occur in different line sections.

The fundamental principle of distance protection involves dividing short-circuit voltage (U_{SC}) and current (I_{SC}) at the relay location, as shown in Figure 1. So calculated apparent impedance (Z_{Lm}) is then compared with the impedance of the reach point (Z_1). If the reach point impedance is higher than the measured impedance, it is assumed that a fault had occurred on the transmission line between the relay and the reach point. For this basic protection decision, there is no requirement for further information and the protection, therefore, does not depend on any additional equipment or signal transmission channels.

Distance protection acts typically as primary protection for overhead lines and cables. Most commonly used numerical distance protection uses microprocessor technology with analogue to digital conversion of measured values (current and voltage), computed distance determination and digital processing logic. An extra advantage of numerical distance protection is integrated fault location function [2, 3].

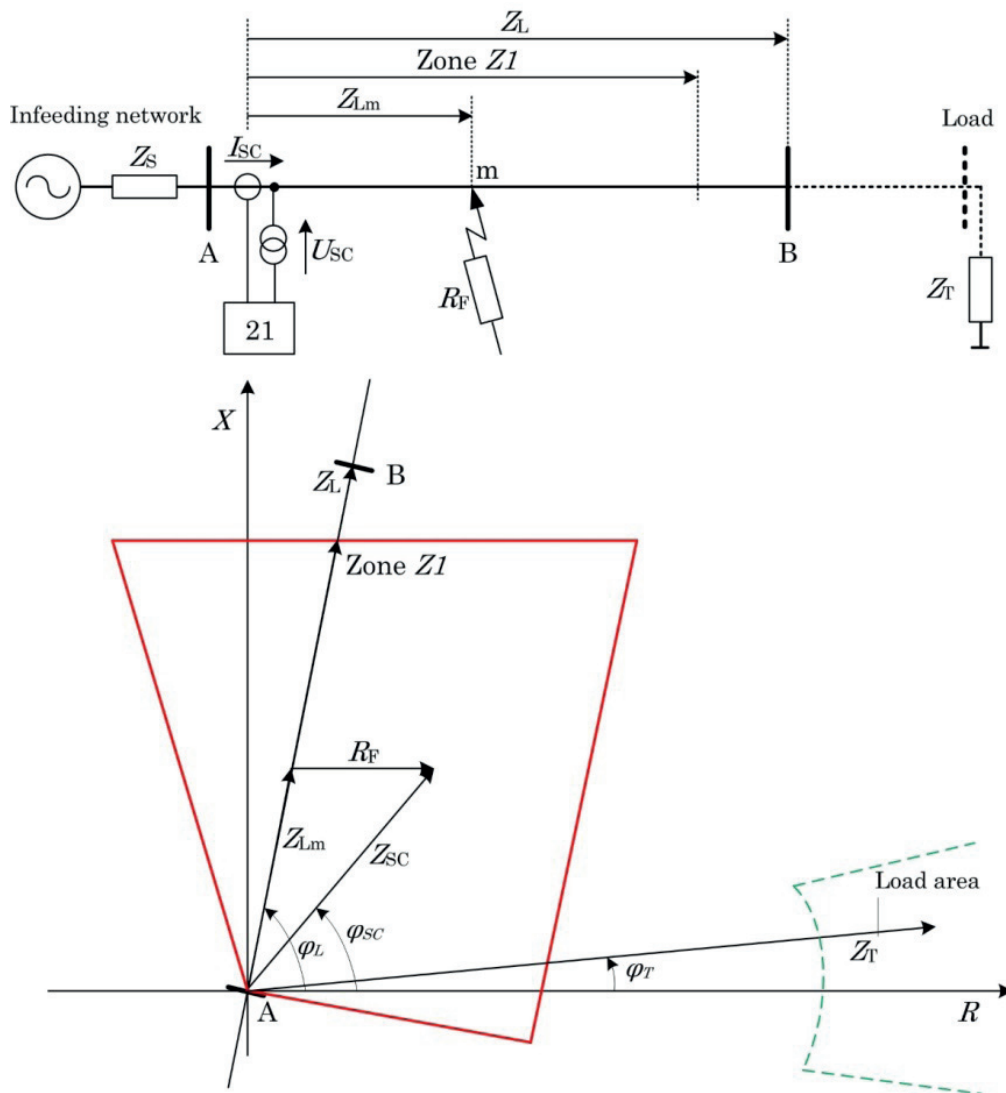


Figure 1 Distance protection fundamentals

2.1 Zones of Protection

Cautious choice of the reach settings and tripping times for different zones allow correct coordination between distance relays on a power system. Basic distance protection will compromise instantaneous directional Zone 1 protection and one or more time-delayed zones. Numerical distance relays may have more than five zones, some of which can be set to measure in the reverse direction. Typical settings for three forward-looking zones of basic distance protection are given in the following sub-sections.

2.1.1 Zone 1 Setting

Zone 1 is a high-speed, instantaneous zone with no deliberate delay and is typically set to provide 80-85 % coverage of a two-ended line. The resulting (15-20 %) safety margins ensure that there is no risk of Zone 1 protection over-reaching the protected line due to errors in the current and voltage transformers, inaccuracies in line impedance data provided for setting purposes (usually based on a calculation and not on a measurement) and errors of relay setting and measurement [3]. Otherwise, there would be a loss of discrimination with fast operating protection on the following line section. A time-delayed Zone 2 must cover the remaining 15-20 % of the line. Zone 1 should never overreach beyond the remote bus. Its tripping time approximately consists of one to two cycles (20 to 40 ms at 50 Hz) [2].

2.1.2 Zone 2 Setting

Distance protection additionally provides the option of backup protection for the adjacent line(s) (and for a failed Zone 1). The second stage (over-reaching zone) is used for this purpose. It reaches through the adjacent busbar and into the adjacent line(s). Additionally, it ensures full coverage of the line with allowance for the sources of error already listed (its primary purpose is to clear faults in the protected line beyond the reach of Zone 1). The reach setting of the Zone 2 is set to cover the protected line +50% of the shortest adjacent line at the remote bus or 120% of the protected line, whichever is greater. In many applications, it is common practice to set the Zone 2 reach to be equal to the impedance of the protected line section +50% of the shortest adjacent line. It ensures that the resulting maximum effective Zone 2 reach does not extend beyond the minimum effective Zone 1 reach of the adjacent line protection [1].

Zone 2 tripping time must be time-delayed to secure grading with the primary relay on the adjacent line(s) that fall within the Zone 2 reach. Thus complete coverage of a line section is obtained, with a fast clearance in the first 80-85% of the line and somewhat slower clearance of faults in the remaining part of the line [3]. The tripping time is approximately 250 to 300 ms [2].

2.1.3 Zone 3 Setting

Remote backup protection for all faults on adjacent lines can be provided by a third zone of protection which needs to be time delayed to discriminate with Zone 2 protection increased with trip time of circuit breaker for the adjacent line.

Zone 3 reach should cover at least 120% of the impedance given to the relay for a fault located at the remote end of the second line [1]. Zones 1 and 2 should never overreach the end of the remote line, and Zone 3 should never

underreach it. Equally, Zones 1 and 2 are set using the actual impedance of the protected line, ignoring current infeed at the remote busbar, while Zone 3 must be set for a fault at the end of the remote line with maximum infeed conditions at the remote bus.

The Zone 3 distance element rarely needs to operate; however, it must not work during extreme loading conditions, stressed power system conditions, or slow power swings [3, 4]. All three zones are presented in Figure 2.

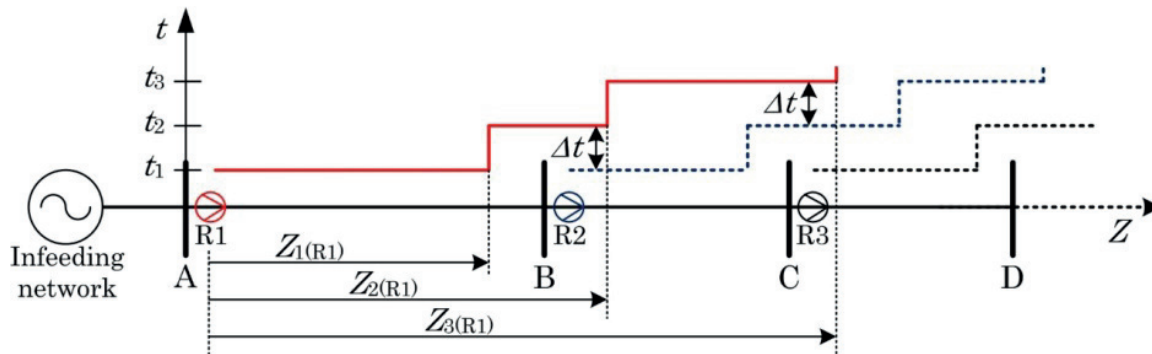


Figure 2 Zone reach and tripping time setting

2.2 Distance Relays Characteristics

Relay measurements are based on the comparison of either amplitude or phase quantities. In the case of a numerical relay, algorithms compare measured voltage and current. When plotted on a set of rectangular coordinates (resistance R as the abscissa and reactance X as the ordinate), the relay characteristics form geometric figures. Some of the most used characteristics are plain impedance characteristic, mho impedance characteristic, offset mho and lenticular characteristic, fully cross-polarised mho characteristic, partially cross-polarised mho characteristic and finally, a quadrilateral characteristic which is used by the SIPROTEC relay series.

2.2.1 Quadrilateral Characteristic

This form of polygonal impedance characteristic is shown in Figure 3. The characteristic consists of forward and resistive reach settings that are impartially changeable. As a result, it offers better resistive coverage than any mho-type characteristic for short lines. This is principally the case for earth fault impedance measurement, where the arc resistances and fault resistance to earth contribute to the highest values of fault resistance.

Regarding avoiding unnecessary mistakes in the zone reach accuracy, it is common to dictate a maximum resistive reach in regards to the zone impedance reach.

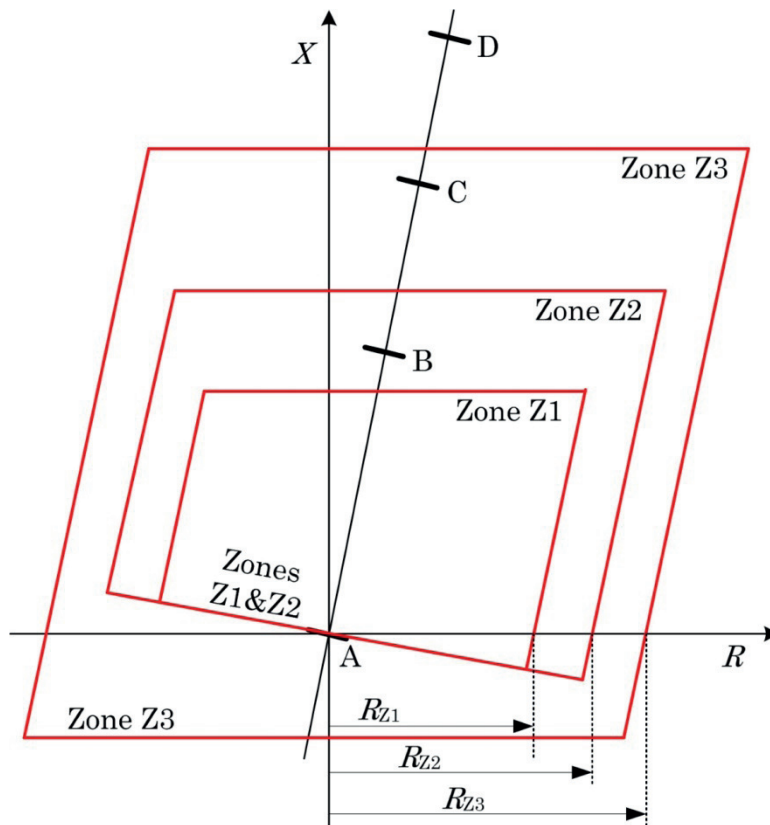


Figure 3 Quadrilateral characteristic

Quadrilateral elements with plain reactance reach lines can introduce reach error problems for resistive earth faults where the angle of total fault current differs from the angle of the measured current. This occurs when the local and remote source voltage vectors are phase shifted due to pre-fault power flow. However, it can be overcome by selecting an alternative use of a phase current for polarisation of the reactance reach line. Polygonal impedance characteristics are exceedingly flexible regarding fault impedance coverage for both phase and earth faults. Due to this, most digital and numerical distance relays now offer this form of characteristic [1].

2.3 Experimental Work

As one of the world's leaders in manufacturing protection equipment for power systems, Siemens has designed SIPROTEC relay series which was chosen for testing. It implements integrated protection, control, measurement and automation functions in the same device. Another benefit is the possibility of both local (via integrated keypad and display) and remote (via PC) control [7].

2.3.1 Distance Protection 7SA611 Relay

The following parameterisation and testing were performed on SIPROTEC 4 7SA611 relay which is used for protection of overhead lines and cables at all voltage levels from 5 to 400 kV. The unit also enables single-pole, three-pole and multiple auto-reclosures. Therefore, it can detect power swings and prevent non-selective tripping. 7SA6 contains a powerful 32-bit microprocessor which allows utterly numerical processing of all functions in one device, starting from the acquisition of the measured values to the output of commands to the circuit breakers. For the quick location of the damage to the line after a short circuit, there is an integrated fault locator which may also compensate for the influence of a parallel line and load [5]. The tripping characteristic is polygonal with separate setting along the X-axis (reach) and R-axis (arc resistance reserve) and separate R-setting for earth faults. Furthermore, it offers six distance zones, selectable as forward, reverse or non-directional reaching, and nine time stages [8].

2.3.2 DIGSI software

The PC operating program DIGSI is the user interface to the SIPROTEC devices, regardless of their version. The word DIGSI is an abbreviation of a German expression "Digitalizer Simulator", which means a digital simulation of a relay [6]. Its design has a modern and intuitive user interface. It is often referred to as a powerful all-in-one tool for configuring, setting, testing and communicating with the device. Moreover, it offers the possibility to display signals from various fault records in one diagram and synchronise these signals to a common time base. In addition to finding out the details of the line fault, the localisation of the fault is of particular interest in order to save time used for on-site inspection of the fault.

2.3.3 Parameterising Distance 7SA611 Relay

There are two different approaches to parameterisation. The first one is to proceed in offline mode and later switch to online mode and transfer all the settings into the relay. The second one (used here) is to parameterise the relay directly, that is to say, as soon as settings are changed, they are immediately transferred to the relay. For this experiment, the relay parameterisation contains data of a real 400 kV line of the length of 79, 9 km (Figure 4).

Some of the critical parameterising settings necessary to set up correctly are considering transformers, power system, and circuit breakers as shown in the following figure.

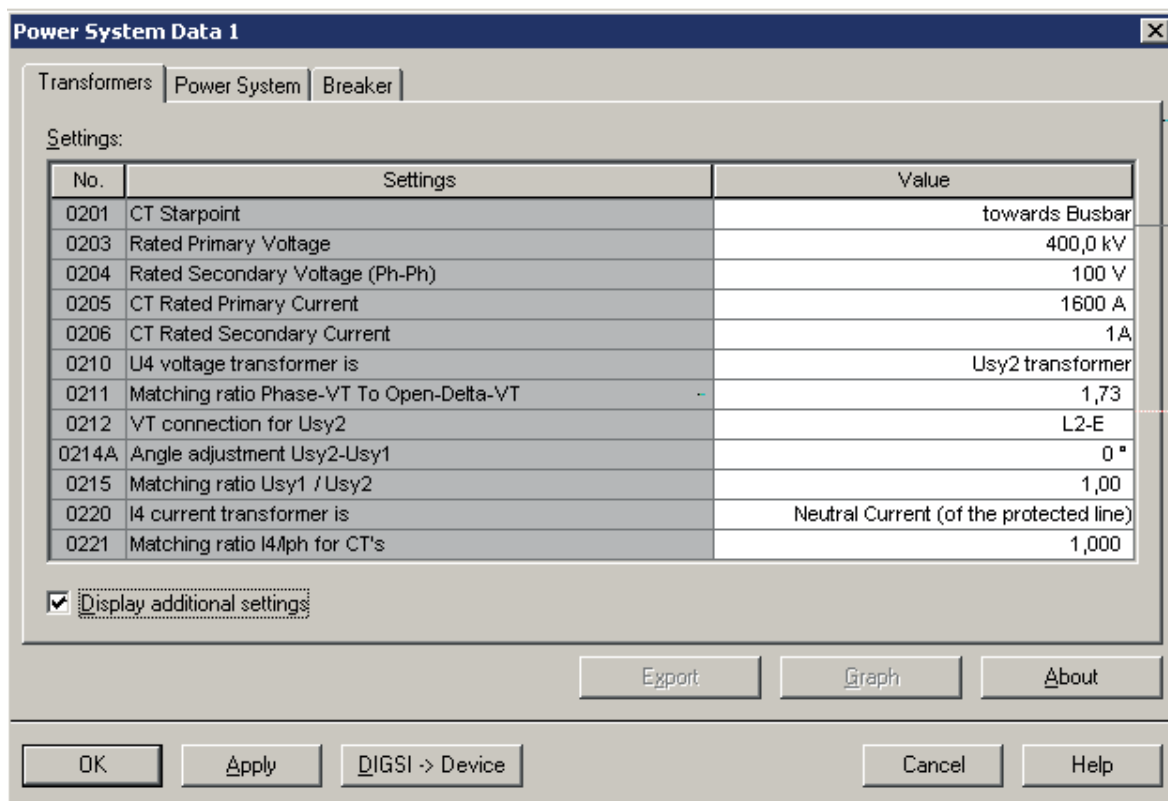


Figure 4 Relay parameterising

Several further physical quantities are adjustable in different Settings Groups as shown in Figure 5.

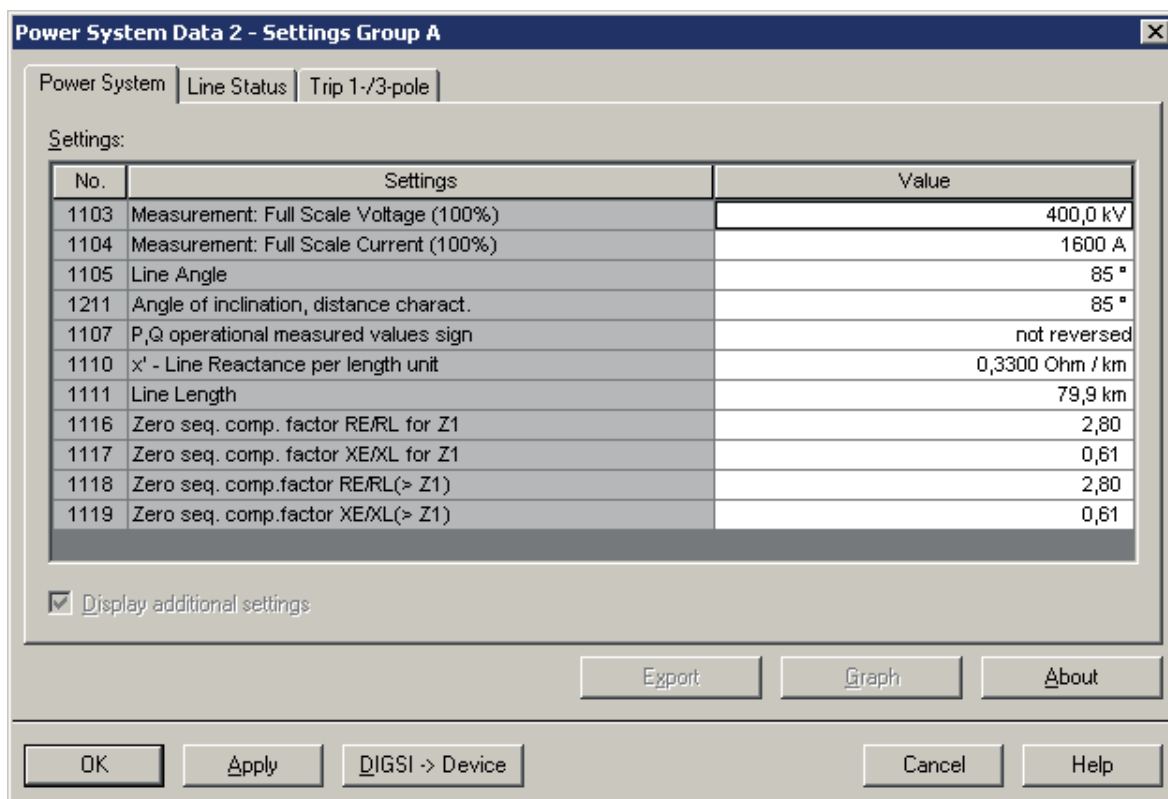


Figure 5 Relay settings group

As the calculation of the line impedance on a phase to ground loop is not possible only with measured values, additional information regarding the ratio, Z_L/Z_E needs to be provided to the relay. Here, it is assumed that the ratio is constant along the line. After individually setting the distance zones (Figure 6), a graph of the characteristic can be plotted (Figure 7) in which the dotted lines represent the tolerances of each zone. The type of the characteristic is quadrilateral, and although the reach of every single zone can be edited, the form of the characteristic cannot be changed once it is integrated into the relay. Additionally, it is possible to export the relay characteristic in an RIO File which then enables easy import into Omicron (test device used).

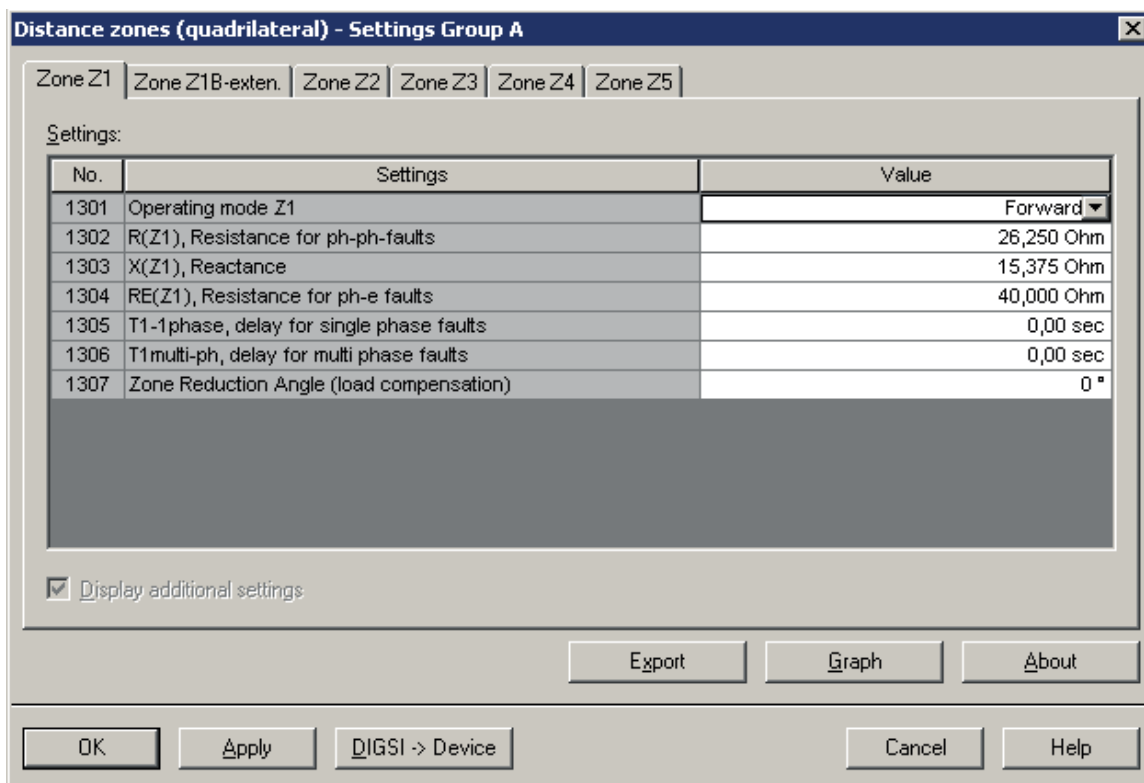


Figure 6 Distance zones settings

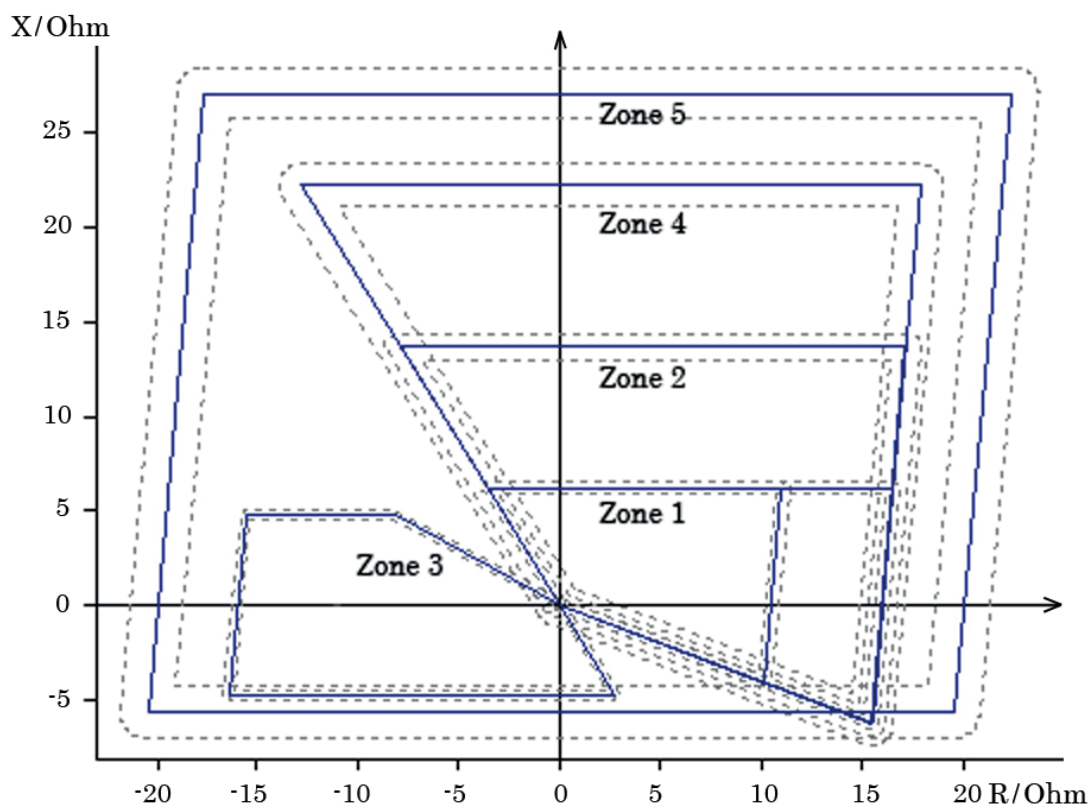


Figure 7 Relay characteristic

2.3.4 Testing Distance 7SA611 Relay

The relay was tested with Omicron CMC 56, a device created for testing all generations and types of protection relays. Its software, Test Universe, is a helpful tool for advanced secondary testing of protection and measuring devices. It enables a range of approaches, from manual to entirely automated and standardised tests, running on a PC or a laptop. For this testing process, the adequate test module was Distance.

It is possible to test each adjusted distance zone separately, or more zones at the same time. Different types of faults (one-pole, two-pole or three-pole short circuit) need to be tested independently. According to the previously set up parameters in DIGSI, the nominal values for tripping time for each zone are as following:

- for Zone 1: 0 ms (instantaneous),
- for Zone 2: 350 ms,
- for Zone 3: 800 ms,
- for Zone 4: 700 ms,
- for Zone 5: 1,5 s.

Table 1 Zone settings (Test Universe)

Label	Type	Fault loop	Trip time	Tol.Trel	Tol.T abs+	Tol.T abs-	Tol.Z rel.	Tol.Z abs
Z1	Tripping	L-L	0,000 s	1,000 %	100,0 ms	100,0 ms	5,000 %	100,0 mΩ
Z1	Tripping	L-E	0,000 s	1,000 %	100,0 ms	100,0 ms	5,000 %	100,0 mΩ
Z2	Tripping	L-L	350,0 ms	1,000 %	100,0 ms	100,0 ms	5,000 %	100,0 mΩ
Z2	Tripping	L-E	350,0 ms	1,000 %	100,0 ms	100,0 ms	5,000 %	100,0 mΩ
Z4	Tripping	L-L	700,0 ms	1,000 %	100,0 ms	100,0 ms	5,000 %	100,0 mΩ
Z4	Tripping	L-E	700,0 ms	1,000 %	100,0 ms	100,0 ms	5,000 %	100,0 mΩ
Z3	Tripping	L-L	800,0 ms	1,000 %	100,0 ms	100,0 ms	5,000 %	100,0 mΩ
Z3	Tripping	L-E	800,0 ms	1,000 %	100,0 ms	100,0 ms	5,000 %	100,0 mΩ
Z5	Tripping	L-L	1,500 s	1,000 %	100,0 ms	100,0 ms	5,000 %	100,0 mΩ
Z5	Tripping	L-E	1,500 s	1,000 %	100,0 ms	100,0 ms	5,000 %	100,0 mΩ

3. TEST RESULTS AND DISCUSSION

3.1 Testing Zone 1 for Single-Pole Short Circuits

Ten different impedances were tested and successfully passed the test as shown in the results from the Test Universe report.

As expected, the relay tripped for all impedances less than the Zone 1 impedance within the Zone 1 tripping time, whereas for the impedances bigger than the Zone 1 impedance, it tripped within the Zone 2 tripping time. Nominal tripping time for Zone 1 is instantaneous, and for Zone 2 equals 350 ms. In both cases, for every selected impedance, there was an inevitable time delay within the permitted tolerances which illustrates the real-life situations in power systems.

Test results consist of the value and the angle of the impedance, nominal and activating time of the relay, time deviation and the decision of the testing as presented in the following figure.

Table 2 Zone 1 test results for one-pole short circuit

Z	Phi	t nom	t act.	Dev.	I _{Test}	Result
5,869 Ω	85,00 °	0,000 s	33,60 ms	33,60 ms	2,000 A	Passed
6,062 Ω	74,86 °	0,000 s	34,20 ms	34,20 ms	2,000 A	Passed
6,602 Ω	63,76 °	0,000 s	34,00 ms	34,00 ms	2,000 A	Passed
7,459 Ω	50,00 °	0,000 s	34,00 ms	34,00 ms	2,000 A	Passed
8,494 Ω	42,89 °	0,000 s	34,30 ms	34,30 ms	2,000 A	Passed
6,575 Ω	94,58 °	350,0 ms	384,1 ms	9,743 %	2,000 A	Passed
6,596 Ω	85,00 °	350,0 ms	383,7 ms	9,629 %	2,000 A	Passed
6,834 Ω	73,55 °	350,0 ms	384,3 ms	9,8 %	2,000 A	Passed
7,263 Ω	64,47 °	350,0 ms	383,5 ms	9,571 %	2,000 A	Passed
8,890 Ω	46,83 °	350,0 ms	383,8 ms	9,657 %	2,000 A	Passed

Furthermore, if the test impedances successfully pass the test, they become visually green in the graph (Figure 8).

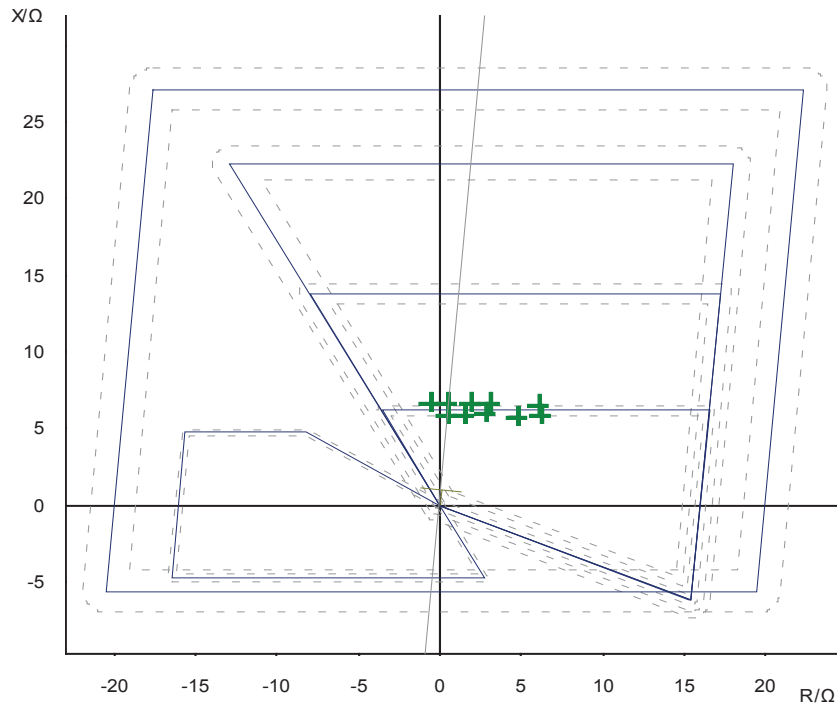


Figure 8 One-pole short circuit (Zone 1 test)

Further fault analysis results become available as well, such as fault physical quantities. These test results point out the voltage and the current of the fault, and consequently, show that the fault had occurred in Phase One.

Table 3 Physical quantities for one-pole short circuit

VL1:	50,7V	0,00 °
VL2	57,7V	-120,00 °
VL3:	57,7V	120,00 °
IL1:	2,00A	-24,31 °
IL2:	0,00A	n/a
IL3:	0,00A	n/a
VFault:	50,7V	0,00 °
IFault:	2,00A	-24,31 °

Additional graphs of fault voltage and current, as well as tripping time of the relay, are available for analysis.

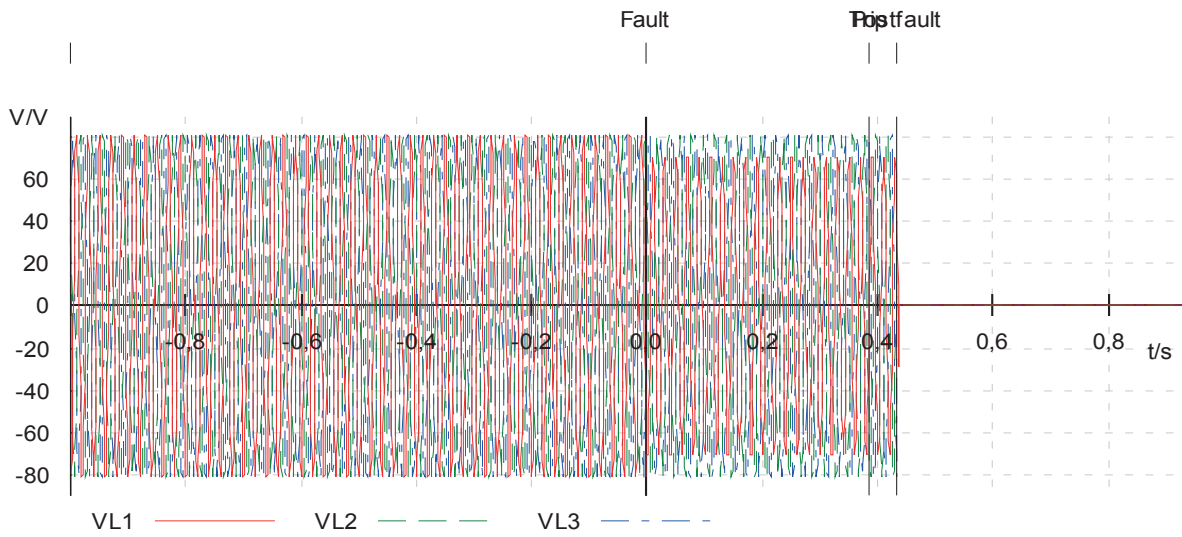


Figure 9 Short circuit voltage

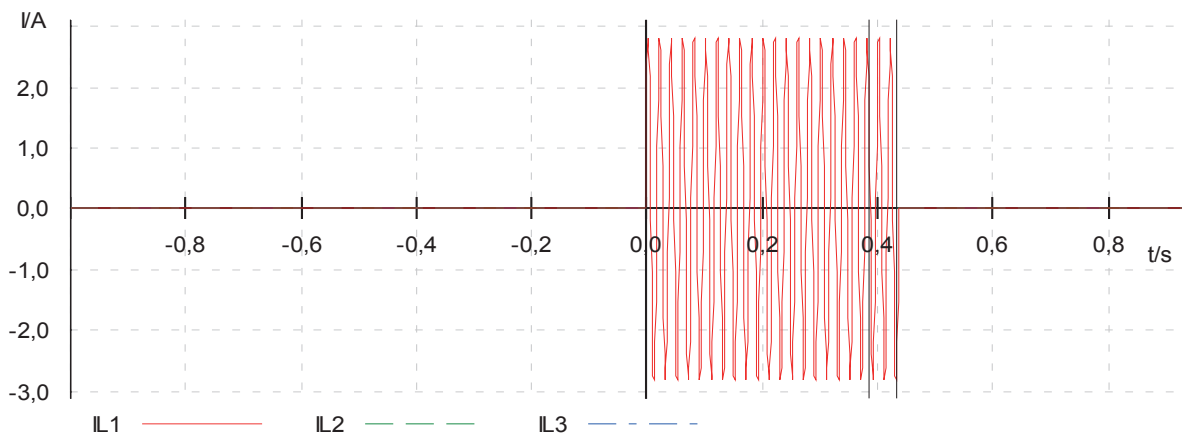


Figure 10 Short circuit current

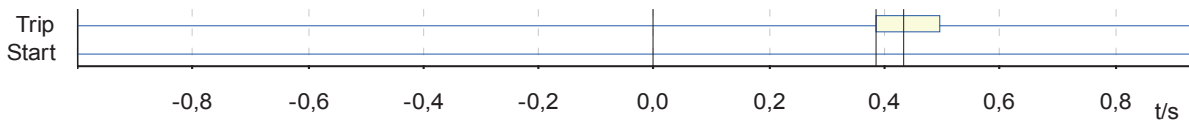


Figure 11 Relay tripping time

3.2 Testing Zone 3 for Single-Pole Short Circuits

As shown in the graph below, Zone 3 was set to have a reversed direction. As a result, it provides distance protection against faults behind the relay (busbar) of the protected transmission line. It is also the reason that the Zone 4 tripping time can be less than the Zone 3 tripping time; otherwise, the zones would not discriminate.

Eight impedances selected are located within the Zone 3 setting, and one within Zone 5 and its relay tripping time, thus, equals the Zone 5 nominal time increased with time deviation.

Table 4 Zone 3 test results for three-pole short circuit

 Z 	Phi	t nom	t act.	Dev.	I_{Test}	Result
8,402 Ω	150,00 °	800,0 ms	855,4 ms	6,925 %	2,000 A	Passed
7,174 Ω	150,00 °	800,0 ms	859,7 ms	7,462 %	2,000 A	Passed
5,855 Ω	150,00 °	800,0 ms	853,8 ms	6,725 %	2,000 A	Passed
4,000 Ω	150,00 °	800,0 ms	860,0 ms	7,5 %	2,000 A	Passed
2,649 Ω	160,00 °	800,0 ms	834,2 ms	4,275 %	2,000 A	Passed
2,455 Ω	140,00 °	1,500 s	1,553 s	3,56 %	2,000 A	Passed
4,776 Ω	150,00 °	800,0 ms	853,9 ms	6,738 %	2,000 A	Passed
6,334 Ω	150,00 °	800,0 ms	854,2 ms	6,775 %	2,000 A	Passed
8,000 Ω	150,00 °	800,0 ms	853,9 ms	6,738 %	2,000 A	Passed

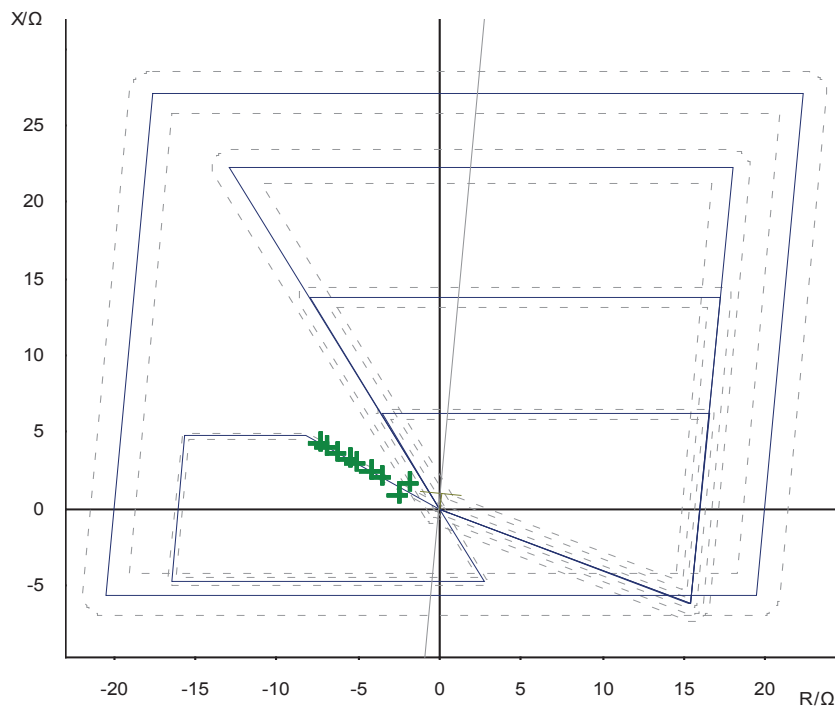


Figure 12 Three-pole short circuits (Zone 3 test)

3.3 Testing Zone 4 for Three-Pole Short Circuits

Due to Omicron's restraints, tests for Zones 4 and 5 were only possible for three-pole short circuits; otherwise, impedances selected would appear to be out of range. In this experiment, six impedances were less than the Zone 4 impedance. Hence the tripping times corresponded to the tripping time of the Zone 4 (nominal time 700 ms + time deviation). On the other hand, the remaining four impedances selected were higher than the Zone 4 impedance and their tripping times consequently corresponded to the tripping time of the Zone 5 (nominal time 1, 5 s + time deviation) as expected. For all the impedances selected, the relay tripped within the correct times, depending on the zone.

Table 5 Zone 4 test results for three-pole short circuit

Z	Phi	t nom	t act.	Dev.	I _{Test}	Result
21,20 Ω	82,85 °	700,0 ms	733,5 ms	4,786 %	2,000 A	Passed
21,25 Ω	85,00 °	700,0 ms	734,2 ms	4,886 %	2,000 A	Passed
21,12 Ω	92,00 °	700,0 ms	734,1 ms	4,871 %	2,000 A	Passed
21,55 Ω	79,30 °	700,0 ms	733,6 ms	4,8 %	2,000 A	Passed
21,96 Ω	74,68 °	700,0 ms	733,5 ms	4,786 %	2,000 A	Passed
24,55 Ω	60,00 °	700,0 ms	733,6 ms	4,8 %	2,000 A	Passed
26,26 Ω	62,80 °	1,500 s	1,534 s	2,28 %	2,000 A	Passed
25,23 Ω	70,00 °	1,500 s	1,534 s	2,26 %	2,000 A	Passed
23,52 Ω	85,00 °	1,500 s	1,540 s	2,667 %	2,000 A	Passed
24,00 Ω	100,00 °	1,500 s	1,554 s	3,567 %	2,000 A	Passed

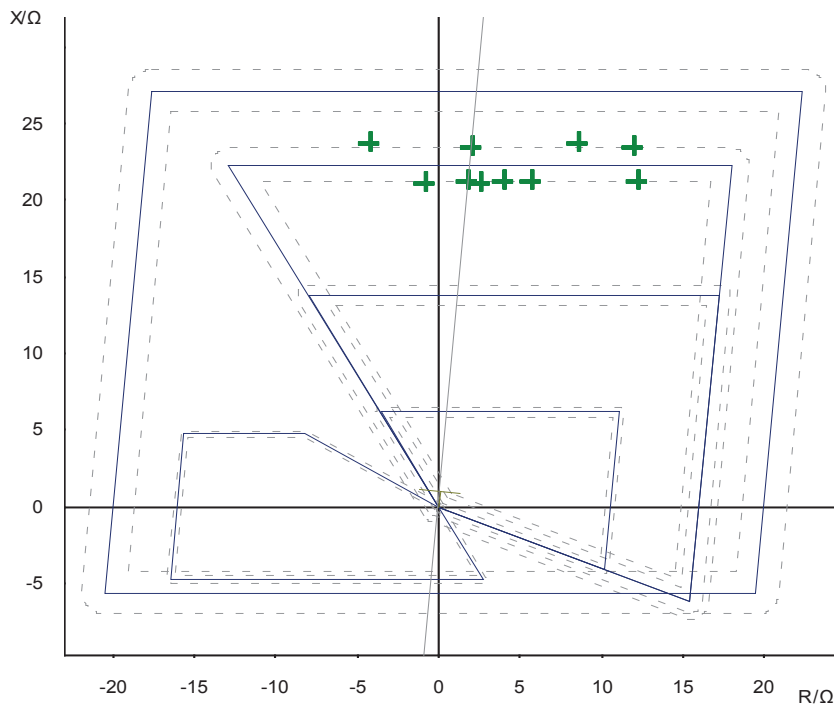


Figure 13 Three-pole short circuits (Zone 4 test)

3.4 Testing the Complete Characteristic for Three-Pole Short Circuits

In this test, impedances were selected within various zones of the polygonal relay characteristic and understandably, the tripping times were different as well.

Bearing in mind that the largest zone determines the fault detection characteristic of the relay, for two tested impedances which are bigger than the Zone 5 impedance, as predicted, there was no trip. This means that these impedances are not part of the protected area and that the protection of this relay will not interfere with the protection of another relay protecting that area.

For other cases there was always a trip within the nominal tripping time of the corresponding zone, increased with time deviation within permissible tolerances. The quickest way to establish which fault impedance belongs to which zone is by its nominal tripping time. From the results summary, it is evident that the first fault is located within Zone 1 reach (instantaneous trip), following three faults are part of Zone 2, further two fit within the Zone 4 reach, and the next two within Zone 5. Additionally, there is a no trip case for an impedance outside of the protected area, and there are two simulated faults within the Zone 3 (reversed direction zone), another one within the Zone 5, and finally, the last case simulated a fault located outside of the characteristic.

Table 6 Complete characteristic test results for three-pole short circuit

Z	Phi	t nom	t act.	Dev.	ITest	Result
5,808 Ω	85,00 °	0,000 s	34,30 ms	34,30 ms	2,000 A	Passed
6,329 Ω	80,00 °	350,0 ms	389,8 ms	11,37 %	2,000 A	Passed
6,758 Ω	85,00 °	350,0 ms	389,8 ms	11,37 %	2,000 A	Passed
13,53 Ω	85,00 °	350,0 ms	383,6 ms	9,6 %	2,000 A	Passed
14,24 Ω	85,00 °	700,0 ms	734,2 ms	4,886 %	2,000 A	Passed
21,93 Ω	85,00 °	700,0 ms	734,5 ms	4,929 %	2,000 A	Passed
22,89 Ω	85,00 °	1,500 s	1,534 s	2,24 %	2,000 A	Passed
22,33 Ω	26,43 °	1,500 s	1,534 s	2,253 %	2,000 A	Passed
24,00 Ω	24,74 °	no trip	no trip		2,000 A	Passed
659,1 m Ω	-95,00 °	800,0 ms	819,0 ms	2,375 %	2,000 A	Passed
3,591 Ω	-95,00 °	800,0 ms	813,6 ms	1,7 %	2,000 A	Passed
5,204 Ω	-95,00 °	1,500 s	1,534 s	2,287 %	2,000 A	Passed
6,387 Ω	-95,00 °	no trip	no trip		2,000 A	Passed

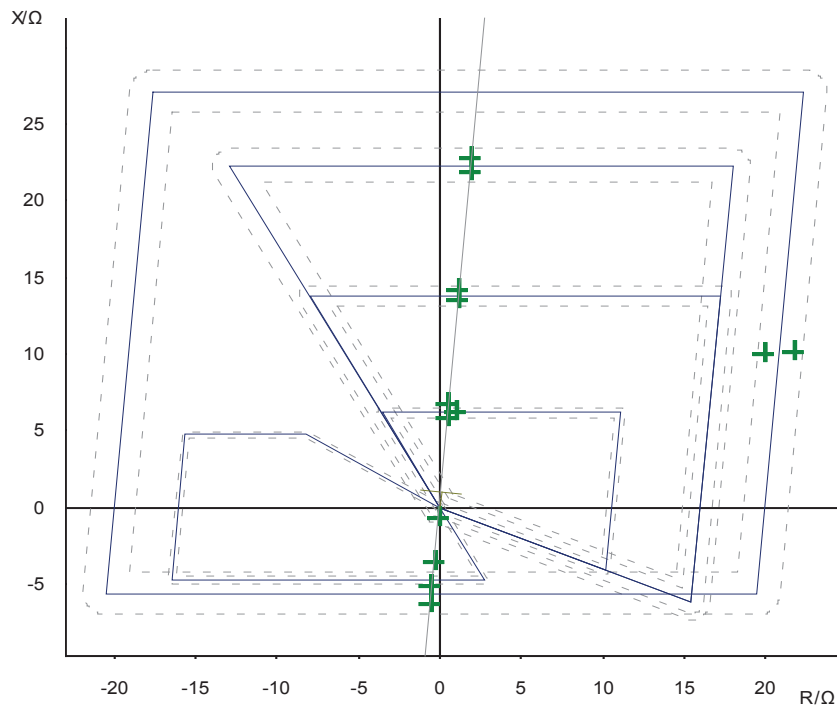


Figure 14 Three-pole short circuits (complete characteristic test)

4. CONCLUSION

This study set out to describe the principles of transmission lines distance protection and to emphasize the importance of correct relay parameterizing as it is crucial for the security and stability of any power system. The challenge today is to implement cost-efficient solutions in modern, intelligent and smart grids where communication and monitoring of the system would enable optimal functioning of power systems across the globe. Hence, setting the adequate protection systems, to provide selective tripping, will minimize the extent and time of the outage. Their communication protocols and precise determination of the fault location, therefore, contribute to the reduction of the on-site inspection time.

In this investigation, the aim was to evaluate adequate zone reach settings and corresponding tripping times of a numerical distance relay and to illustrate the selectivity between different zones of the characteristic.

The results of this study indicate that correct reach settings and tripping times of different zones result in the selective acting of a relay on the protected transmission line and further adjacent line(s), whether in forward or reversed direction. The analysis undertaken here has also confirmed our knowledge on the basic protection principles and applied it to a specific relay type.

5. LITERATURE

- [1] Stosic, A.: Transmission Lines Protection Using SIPROTEC Numerical Relays. Master Thesis. Faculty of Electrical Engineering and Computing, Zagreb, 2015.
- [2] Ziegler, G.: Numerical Differential Protection: Principles and Applications. Second Edition. Germany: Publicis Publishing, Erlangen, 2005.
- [3] Rush, P.: Network Protection and Automation Guide. First Edition. France: Flash Espace, 2002.
- [4] Power Swing Detection, Blocking and Out - of - Step Relays, <http://nptel.ac.in/courses/108101039/download/Lecture-26.pdf>, Accessed: November 19, 2014.
- [5] Distance Protection 7SA6 Manual, http://www.automationberlin.com/downloads/siemens/energy_ptd/7SA6xx_Manual_A7_V047001_en.pdf, Accessed: December 17, 2014.
- [6] DIGSI software, http://www.answers.com/Q/Abbreviation_of_digsi_software, Accessed: January 17, 2015.
- [7] Group of Authors: SIPROTEC 4 – Using Numerical Protection Devices. Germany: Siemens AG, 2008.
- [8] Group of Authors: Power Engineering Guide. Edition 7.0. Erlangen, Germany: Siemens Aktiengesellschaft, 2012.
- [9] Blackburn, J. L., Domin, T. J.: Protective Relaying: Principles and Applications. Third Edition. CRC Press Taylor & Francis Group, Boca Raton, Florida, USA 2007.
- [10] Elmore, W. A.: Protective Relaying Theory and Applications. Second Edition. Marcel Dekker, Inc., New York, USA 2003.
- [11] Transmission Line Protection Principles, <https://www.gedigitalenergy.com/smartgrid/Dec07/1-transmission.pdf>, Accessed: November 16, 2014.
- [12] SIGRA 4, <http://w3.siemens.com/smartgrid/global/en/products-systems-solutions/Protection/Engineering-Evaluation-Diagnostic-Software/Pages/SIGRA-4.aspx>, Accessed: January 10, 2015.
- [13] Pradhan, A. K., Jena, P.: Solution to Close-in Fault Problem in Directional Relaying. Power Delivery, IEEE Transactions on (Volume: 23, Issue: 3). July, 2008, pages: 1690. – 1692.
- [14] Omicron CMC 56 User manual. OMICRON electronics, Klaus, Austria
- [15] SIPROTEC 4 – 7SA6, http://ftp.soups.ru/RZA/Siemens/SIPROTEC%20SA6/7SA6_Catalog.pdf, Accessed: January 4, 2014.

- [16] Tziouvaras, D., Mooney, J., Alexander, G.: Functional Integration in Modern Distance Relays Improves the Reliability of Power Systems. Schweitzer Engineering Laboratories, Inc., USA, 2004.
- [17] Tziouvaras, D.E., Altura, H., Benmouyal, G., Roberts, JR.: Line Differential Protection with an Enhanced Characteristic. Pullman, Washington, USA, 2014.

GORAN GRDENIĆ

goran.grdenic@fer.hr

ŽELJKO TOMŠIĆ

zeljko.tomsic@fer.hr

**University of Zagreb Faculty of Electrical Engineering
and Computing**

RENEWABLE ENERGY SOURCES AND OTHER ENERGY TECHNOLOGIES AS A MEASURE FOR MITIGATING THE IMPACT OF URBAN HEAT ISLANDS.

SUMMARY

Urban heat islands (UHI) represent increase of temperature inside of cities in regard to their rural environment. Causes of their formation are diverse and multiple: reduced amount of vegetation and waterproofing of surfaces, changed radiation and thermal characteristics of materials, urban geometry. Consequences are also diverse and significant: increasing consumption of energy for cooling, negative impact on human health, deterioration of air quality. Conventional methods for mitigating their impact include reflective and green roofs and introduction of green and water surfaces in cities. Different renewable energy technologies can also have positive impact on urban heat islands, but at the same time they contribute to greater energy independency of cities what is goal of future urban development. Proposed and described technologies are solar cooling, ground-air heat exchanger, passive cooling, solar pond.

Key words: ground-air heat exchanger, passive cooling, renewable energy sources, solar pond, urban heat islands

1. INTRODUCTION

Cities around the world are facing growing problem of urban heat island, UHI, a temperature increase within the city with respect to its rural surrounding. This problem becomes more frequent as consequence of climate change as heat waves becomes more frequent and prolonged, although there are multiple causes for UHI occurrence. Consequences of UHI are also significant and diverse: negative impact on human health during summer months, and on the other side – increase of energy consumption for building cooling – which is contrary to European directives of energy consumption decrease.

Urban space cannot be longer observed only through its functional and aesthetic role. In urban planning more and more prominent becomes energy component because of interdependence of urban heat islands and energy consumption. Goals are energy independent cities developed on ecological principle, pleasant for life of humans and other living creatures. While accessing these goals, renewable energy sources can help us in achieving this idealized city image to which we definitely should tend.

2. URBAN HEAT ISLANDS

Built environment has significant impact on air temperature in the cities which is significantly higher with respect to rural and suburban surrounding (Figure 1), This phenomenon is called urban heat island and it is one of the most investigated effect of urbane climate. Urban surfaces and structures absorb sun heat during the day and emit it during the night. An average annual temperature of cities with more than one million inhabitants is typically from 1 to 3 °C higher with respect to their surroundings [1]. During bright and calm summer nights this difference can increase even up to 12 °C, thus creating extremely unpleasant atmosphere for urban population, Consequently, these higher temperatures increase cooling energy needs and increase peak electricity consumption because most of the cooling devices use electricity.

An energy balance equation for flat, horizontal and homogenous surface is given by (1):

$$(1 - a) \cdot I + L + Q_F = H + \lambda E + G \quad (1)$$

where a - surface albedo (ratio of reflected and incoming radiation), I - incoming sun radiation, L - net value of longwave radiation, Q_F - anthropogenic heat, H - convection heat, λ - latent heat of evaporation, E - evaporation quantity and G - conduction heat.

The left side of equation represents thermal gains, and the right side of equation thermal losses. Every part of energy balance equation is changing in urban surrounding and contributes to formation of UHIs. Main causes, processes and belonging quantities from equation which they affect are listed in Table I.

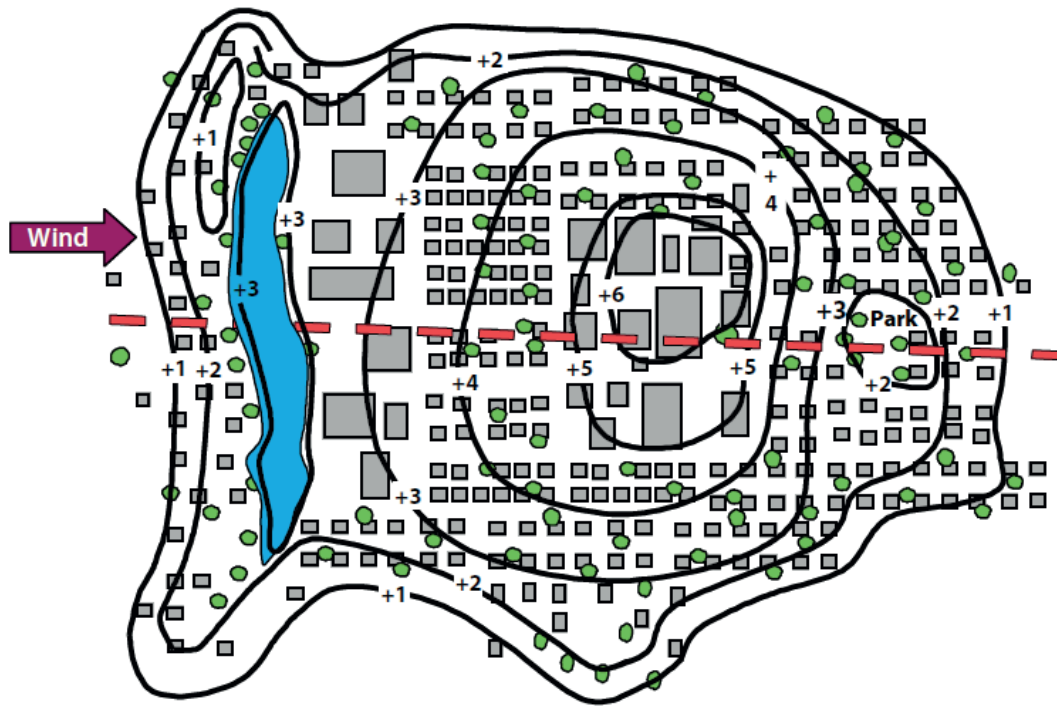


Figure 1 Isothermal map of nocturnal atmospheric urban heat island [1]

Table I Occurrence causes of urban heat islands and corresponding processes

Causes	Members of energy balance equation	Corresponding processes
Decreased amount of vegetation and impermeability of surfaces	λE	Decreased latent heat of evaporation
Changed radiation and thermal material properties	G, a	Increase of absorption and thermal capacity of surfaces
Urban geometry	I L $H, \lambda E$	Multiple shortwave reflections Decreased loss of longwave radiation (smaller sky-openness coefficient) Decreased wind speed
Anthropogenic heat	Q_F	Cooling and heating of the buildings, industry, traffic
Air pollution	L	Increased absorption and re-emission of longwave radiation

The goal is to decrease thermal gains and to increase thermal losses. From the thermal balance equation, we can extract main factors on which we can affect: surface albedo, anthropogenic heat and evaporation quantity.

Considering that free surface in cities is quite limited and of high economic value, it is relatively hard to implement large projects of mitigating influence of heat islands on earth surface. Therefore, the main, conventional methods in combating urban heat island are the following: cold or reflecting roofs and green (or live) roofs. To these two methods we need to add and the third method which is connected to earth surface, and those are green and water surfaces.

Despite few positive effects of urban heat islands during winter months (smaller energy consumption for heating, ice and snow melting), much greater and more serious are negative consequences: increase of energy consumption for cooling, impact on human health, poorer air quality, increase of rainwater temperature.

3. INTERDEPENDENCY OF URBAN HEAT ISLANDS AND RENEWABLE ENERGY SOURCES

While fighting negative impact of urban heat island, we need to bear in our minds broader perspective – especially sustainable development. Can we, by lowering their impact, at the same time contribute to higher energy independence of today cities? Cities, during their existence are transforming and developing and they are never finished, so that today urban developers start to think about the cities as complex biological and natural system analogous to self-sustained living organism. Demand for energy and free space will continue to grow, also as material consumption and waste generation. At the same time, economy of size in cities gives a chance of increasing renewable energy profitability.

In order to lower the impact of urban heat island, urban communities are focused on changing characteristics of urban materials and increasing green surfaces, while changing urban geometry and anthropogenic heat is in the second plan. Communities can lower created anthropogenic heat by help of energy efficiency technologies in buildings and traffic, and renewable energy sources. Beside this, new researches show that waste heat has far greater impact on formation of UHI than was thought earlier – which is an additional stimulus to cut down anthropogenic heat sources. Solar cooling technologies and ground-air heat exchangers, which are described in the sequel of this paper, are the most promising technologies for lowering quantity of anthropogenic heat. On this way, at the same time, we contribute to energy independency of the cities, lowering electricity production in conventional power plants and decreasing human impact on environment. The benefits we get are multiple and diverse.

Beside anthropogenic heat we can make impact on other causes of creation of urban heat islands. By using functional water surfaces, e.g. solar pond for heat collecting or roof pond for cooling, we insure necessary water for evaporation and to some extent we change thermic characteristics of urban materials. With different

shadowing solutions we are changing characteristics of urban geometry. Introducing changes in traffic (limited number of vehicles in city center, bicycles, pedestrian areas, electric vehicles, public transport) decrease quantity of waste heat but also air pollution. Methods for combating urban heat islands are listed concisely in Table II and Figure 2, where they are also connected with their emergence causes.

Table II Interdependency of urban heat islands and renewable energy sources

Causes	Renewable energy sources
Decreased amount of vegetation and impermeability of surfaces	Water surfaces: solar and roof pond
Changed radiation and thermal material properties	Water surfaces: solar and roof pond
Urban geometry	Shadowing (passive cooling)
Anthropogenic heat	Solar cooling technologies Ground-air heat exchanger RES in traffic Passive cooling
Air pollution	RES in traffic

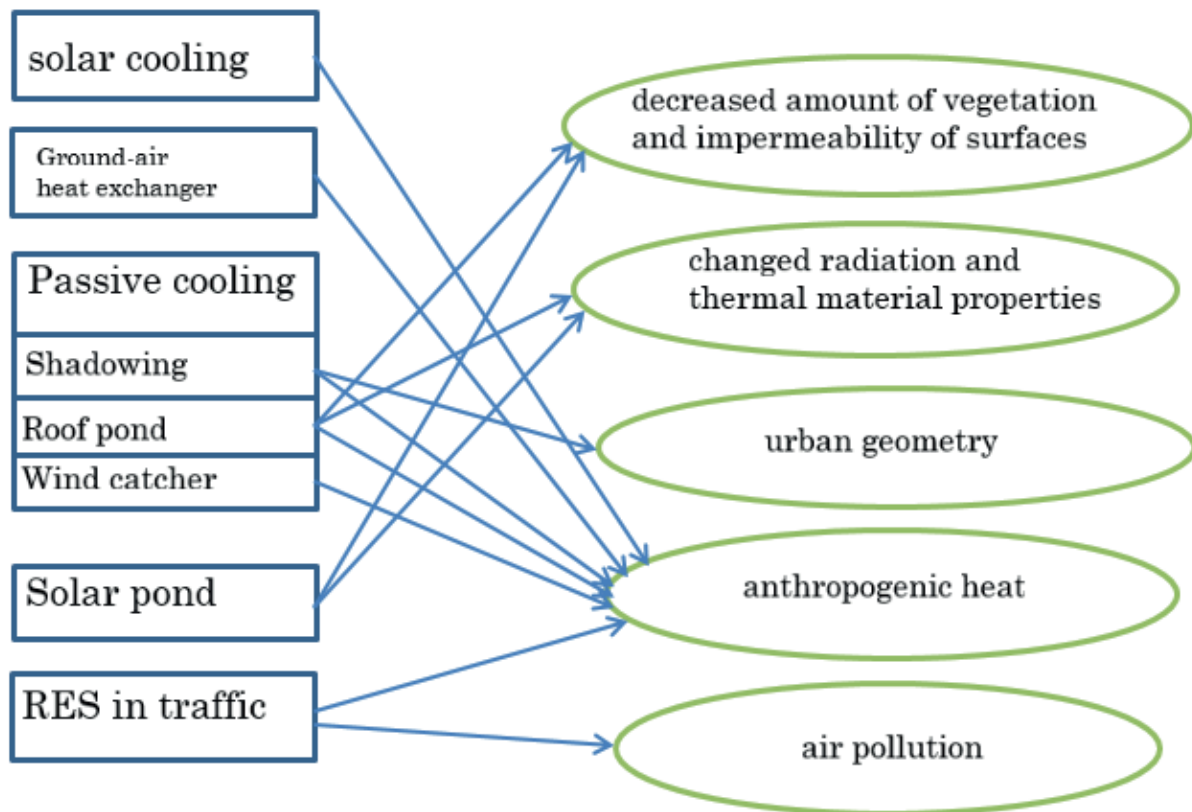


Figure 2 Interdependency of urban heat islands and renewable energy sources

4. ENERGY TECHNOLOGIES

4.1. Solar cooling

The main advantage of building acclimatization powered by sun energy is simultaneous availability of source (Sun) and cooling need in the same season (during summer), which is not the case for building heating. Solar cooling systems consist of two main parts: solar thermal technology for transformation of solar heat into hot water and solar cooling technology for production of cooling energy. Solar thermal technologies are the following:

- Flat collectors
- Vacuum pipe collectors
- Concentrating collectors (static and dynamic)
- Solar pond
- Photovoltaic panels

Solar cooling technologies are mainly classified into two main groups with respect to energy source: system initiated by heat or work and systems initiated by electricity. Systems initiated by heat or work are the following:

- Absorption cycle
- Adsorption cycle
- Cycle with dry evaporation
- Jet (ejector) cycle

Systems initiated by electricity are:

- Steam compression cycle
- Thermoelectric cooling cycle
- Stirling cooling cycle

The main problems of solar cooling in achieving economic competitiveness are high investing costs and system complexity. Therefore, this area of technical science is permeated with new solutions which tend at the same time to simplify and lower system costs.

4.2. Ground-air heat exchanger

A principle of using ground-air heat exchanger is based on the seasonal earth thermic capacity which causes time shift with respect to air temperatures. This temperature difference enables using earth for cooling during summer and for heating during winter. Ground-air heat exchanger is suitable for application in climates with high temperature differences between summer and winter, and between day and night, which corresponds to areas of moderate geographic latitudes and deserts. Simplified concept of such system is shown on Figure 3.

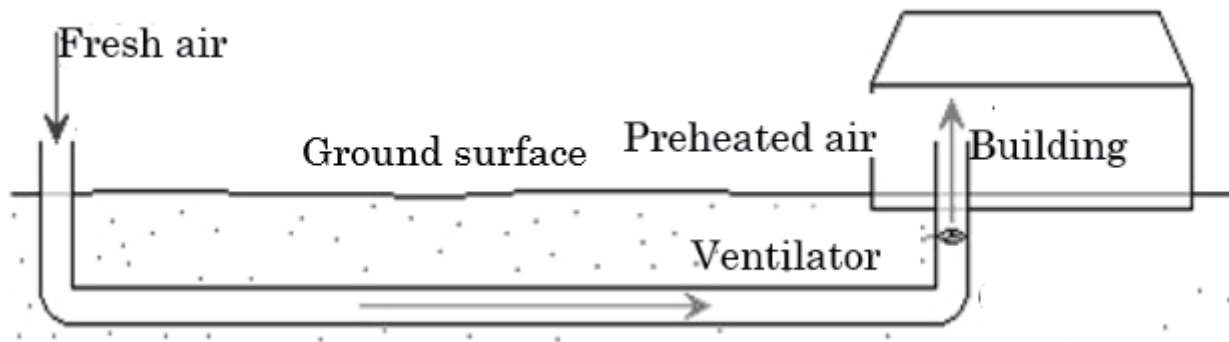


Figure 3 Simplified concept of ground-air heat exchanger

4.3. Passive cooling

Passive solar design incorporates application of natural processes for heating and cooling in order to achieve desired conditions inside the building. Energy flow in such buildings contain natural processes of heat exchange: radiation, conduction and convection without use of electric devices.

Prior to revolution of mechanic cooling machines in the middle of the last century, people were using different natural and clever methods for cooling (and for heating) of indoor spaces. Living spaces and also habits of their inhabitants, have been adjusted to outdoor conditions and to possible means of their cooling. “High technology” application resulted in negligence of natural cooling techniques. In the last few decades, in circumstance of fossil fuels exhaustion and ecological problems caused by their usage, we have become aware that is unreasonable to spend large amount of energy for cooling when our ancestors had managed to achieve thermal comfort by natural processes.

Maintaining comfort conditions inside the building, especially in the hot climates, is relied on decreasing heat incomes and removing heat excess from the building. Achieving above processes depends upon two conditions: cool tank availability which is on the lower temperature than inside air and possibility of heat transfer towards that tank. Tanks which are present in the nature are:

- Outdoor air (heat transfer by convection through openings in the building)
- Water (heat transfer by evaporation inside and/or outside of the building)
- (Night) sky (heat transfer by longwave radiation of roof and/or other building surfaces)
- Ground (heat transfer by conduction through building envelope)

The main techniques of passive cooling are [2]:

- Shading of sun radiation (eaves, awnings, different methods of roof shading, trees and vegetation)
- Isolation (walls and roof)
- Inducted ventilation technique (solar chimney, wind catcher, ventilation openings)
- Radiation cooling (metal roof, roof ponds)
- Evaporation cooling (water spraying inside wind catcher or on the roof)
- Connection to ground (digging in)

In the sequel are described two interesting ways of passive cooling: roof pond and wind catcher. A roof pond is a simple system of shallow water on the flat roof with good thermic conductivity and movable thermic isolation cover [2]. Pool is covered during the day in order to prevent heating of the water, while during the night is open and is cooling by longwave radiation. Covered pool during the day provides cooling thanks to effect of cooled water during the night and thermic isolation of the water on the other side. This system can be used for heating during the winter, but then isolation is moved during the day in order to heat water, while during the night pool is covered to prevent heat losses. On Figure 4 is shown working principle of roof pond.

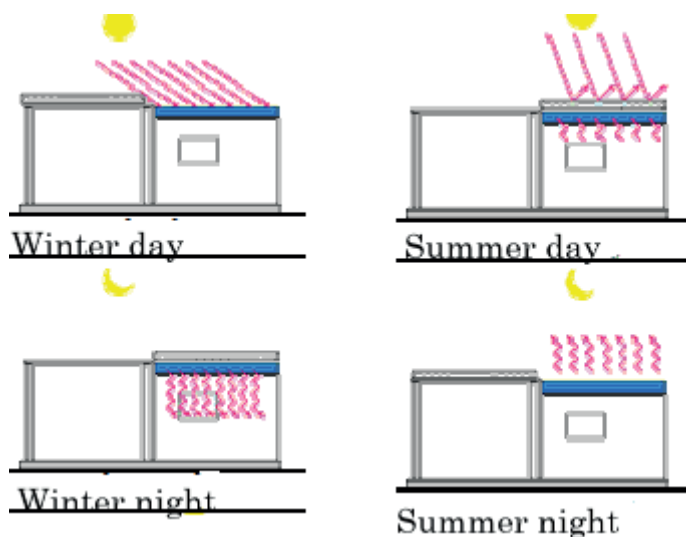


Figure 4 Roof pond operation principle

Wind catcher looks like a large chimney with openings on the top which lead wind into the inside of the building in order to enhance thermic comfort (Figure 5). Wind catchers had been using for centuries in countries with dry hot climate, especially in the Middle East where they are known under name “malqaf”. Opening on the top of the tower is oriented in the dominant wind direction in order to “catch” as much wind as possible during warm part of the year. In order to increase air humidity, inside the tower are placed water sprayers or inside pool or fountain.



Figure 5 Wind catcher in Iran [3]

4.4. Solar pond

Because of the positive role of the water on mitigating negative impact of urban heat island, solar pond is especially interesting technology for transformation of solar energy. A solar pond is a large surface sun collector which at the same time serves as an energy storage. There are several types of solar ponds: solar pond with salty water or gel, shallow ponds with cover, deep ponds with glass or plastic devices for retaining heat. The most frequently used are solar ponds with salty water and this type of pond is described in the remainder of this subsection. The main advantages of solar ponds are the following: simple construction, application of widely accessible salt and water, combined collecting and storing of sun energy. The key ingredient of solar pond with salt water, as its name say, is increased amount of salt dissolved in the water. There are three well defined zones or layers which can be seen on Figure 6: surface zone, gradient zone and storage zone. Salt concentration (salinity) and temperature are constant in the surface and storage layer, while in the transition layer are increasing with depth (Figure 7).

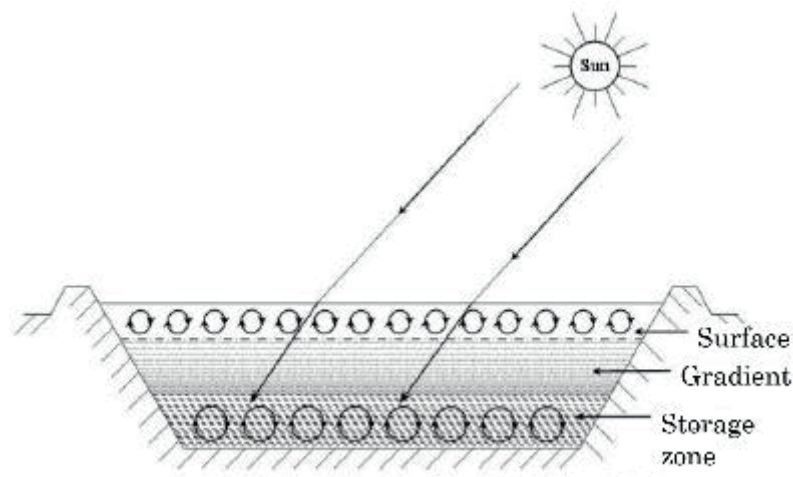


Figure 6 Solar pond system [3]

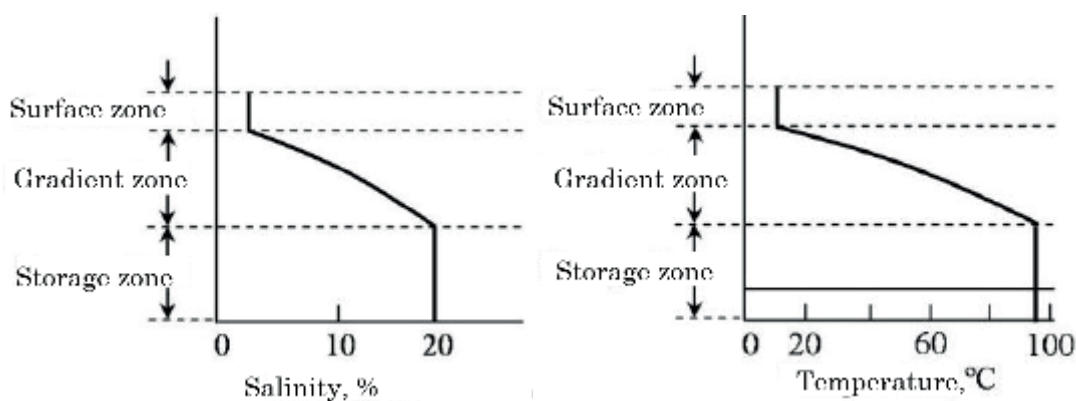


Figure 7. Salinity and temperature in the solar pond [3]

The most frequently used salts are magnesium chloride, sodium chloride and sodium nitrite. It is desirable that concentration in surface zone is low as possible

(lower than 5%), while in the storage zone is from 20 to 30%. Typical depths of certain layers are 0.5, 1 and 1 m for surface, gradient and storage layer, and they vary with respect to specific application of the pool and meteorological conditions. Overall depth of such pools is in the range from 2 to 3 m. In periods with high sun radiation, water in the storage layer can reach temperatures around 80 to 90 °C. Increased temperatures with respect to surrounding can be kept overnight and to certain point even over the winter. Storage layer approximately absorbs 20-25% of incoming sun radiation that falls on pond surface. After considering ground losses, we come to the thermic efficiency between 15 and 20%.

Solar ponds generate thermal energy with lower costs with respect to burning of the fossil fuels. Solar ponds find their application in the conditions where water of low and medium temperature is necessary: heating and cooling of the buildings, heating of hothouses and farms, industrial process heat for preparing and treating materials, heat for biomass conversion, electricity production and desalinization. Especially is interesting application in combination with thermal cooling systems (absorption or adsorption) where warm water from the storage is used for generator operation and cool water from the surface layer is used for condenser cooling. Lack of this system is salt accumulation which decreases thermal efficiency.

4.5. Photovoltaic panels

Except electricity production, photovoltaic panels have positive impact on thermal characteristics of the building on which they are installed. Photovoltaic panels can be installed on several different ways: in immediate contact with roof surface, under certain incline or on the stands whereby they overshadow roof surface. If panels are installed under certain angle or on the stands, research has shown that this can significantly lower energy necessary for cooling inside the building [4]. Panels block direct sun radiation which directly decreases roof temperature and wind drift between panels and roof additionally increases the positive effect by convection cooling. At the same time, efficiency degree of the photovoltaic panels is increased because of their negative power-temperature coefficient.

Combine application of solar systems and cold reflecting roofs increases efficiency of solar systems thanks to better collection of diffuse and reflected sun radiation. Different institutions which have installed photovoltaic panels on cold reflecting roofs have reported photovoltaic electricity production 10 to 20% higher than expected [5].

5. CONCLUSION

This paper presents problematics related to urban heat islands: occurrence causes, consequences, conventional problem-solving methods and then tries to answer a question whether renewable energy sources and other energy technologies can contribute to reduction of negative impact of urban heat islands.

One of the conventional methods for mitigating UHI effect is broad use of water surfaces in towns: fountains, wells, artificial lakes. This way, necessary water is provided which by evaporation decreases air temperature. On the basis of investigated and described technologies, the main method which this research suggests is application of functional water surfaces, especially solar pond and then roof ponds. Solar pond collects and stores sun energy which can afterwards be used in different purposes.

Besides functional water surfaces, recommendation is combined application of other technologies: solar cooling systems, ground-air heat exchangers and passive cooling methods. For ventilator operation in ground-air heat exchange systems we can use for example small wind turbine. In order to improve image of the city as energy independent, sustainable entity, holistic approach is necessary. As air pollution also influence occurrence of urban heat islands, it is one more reason for transforming traffic patterns in cities, especially in their centers. In this area, renewable energy sources also play important role.

Besides well-known advantages of application of renewable energy sources, this research has additionally increased their cost-effectiveness, giving them one new dimension and specific benefit, which is rarely taken into account. Renewable energy sources can contribute to reduction of negative impact of urban heat islands.

6. REFERENCES

- [1] „Reducing Urban Heat Islands: Compendium of Strategies, Urban Heat Island Basics“, U.S. Environmental Protection Agency
- [2] A. Akbarzadeh, J. Andrews, P. Golding, „Solar Ponds“, Solar Energy Conversion and Photoenergy Systems, Vol. 1
- [3] M.A. Kamal, „An Overview of Passive Cooling Techniques in Buildings: Design Concepts and Architectural Interventions“, Acta Technica Napocensis: Civil Engineering & Architecture, Vol. 55, No. 1, 2012.
- [4] A. Dominguez, J. Kleissl, J.C. Luvall, „Effects of solar photovoltaic panels on roof heat transfer“, Solar Energy 85, (2011), str. 2244-2255
- [5] M. Magallanes, „Cool roofs and photovoltaics work together to enhance generation performance“, 2011.

MIRNA GRŽANIĆ MARKO DELIMAR TOMISLAV CAPUDER

mirna.grzanic@fer.hr marko.delimar@fer.hr tomislav.capuder@fer.hr

Faculty of Electrical Engineering and Computing, University of Zagreb

FINANCIAL TRANSMISSION AND STORAGE RIGHTS

SUMMARY

The paper presents concepts of Financial Transmission Rights (FTRs) and Financial Storage Rights (FSRs) as key market concepts for alleviating congestion issues in transmission networks. These instruments are in place in markets where prices differ depending on the location/node due to congestions. They serve as a tool for transmission system operators TSO (or independent system operators; ISOs) for eliminating congestions by remunerating entities who make it possible. The paper further discusses different aspects of FTRs, which are traditional financial instruments used to hedge the risk of high cost occurrence associated with transmission congestion. By owning and trading with FTRs, through auction or via bilateral contracts, market participants can gain additional profit. More variable and uncertain power system environment, characterized by high penetration of renewable energy sources (RES), creates potential for storage units to assist TSO/ISO in maximizing social welfare through FSR. As storage has the capability to move energy in time, it can alleviate transmission lines congestion and create profit through intertemporal arbitrage (by load shifting and peak shaving) improving return rate of its investment. These concepts are additionally explained by intuitive examples showing how, when congestion occurs and TSO/ISO awards market participants who own transmission and storage rights, price volatility is reduced.

Key words: auction markets, congestion management, financial storage rights, financial transmission rights, strategic bid

1. INTRODUCTION

Congestion management and financial transmission rights (FTRs) are key financial elements ensuring reliable and secure operation of power systems in deregulated electricity market [1]. However, the presumption of their existence is that markets incorporate Locational Marginal Pricing mechanisms in which prices differ depending on the both the location in power system and time of electricity production (examples of such systems are New England, North and South America and Nordic countries). These price differences are a result of transmission line congestion and FTRs are financial instruments that allow market participants to hedge against the extra cost caused by congestions. FTRs entitle their owners to the revenue collected during the congestion time, meaning market participants can buy or sell this right for any line in the transmission grid in order to avoid congestion and at the same time maximize their own profit. The FTR owners receive payments based on price differences between two nodes for which the right is bought. As the prices can vary, FTRs protect their owners from price volatility and provide them trading at the price agreed in contracts.

In power systems with larger integration of renewable energy sources, new challenges arise when it comes to power system operation and participant behavior [2]. This is where energy storage can find its business case, by enhancing power system flexibility, efficiency and reliability [3]. From the market perspective, transmission lines move power spatially while energy storage has the additional capability to move power forward also in time; this is called energy arbitrage [4]. Storage units have high initial investment costs and low marginal operating costs. Using storage only for one service highly underestimates their value and does not justify investments in such units. Financial storage rights (FSRs) are seen as a potential service to increase storage profitability; the same way market participants hedge against the congestion and price volatility in transmission lines with FTRs, they can also hedge against congestion by utilizing storage units and maximize revenues through provision of additional services.

The paper is organized as follows; Section 2 gives a general overview of different market principles and transmission rights pricing, explaining the main concepts and differences between market set-ups. Section 3 explains the concept of Financial Transmission Rights and mathematical modelling background supported with examples. Section 4 explains Energy Storage Rights with auction examples. Section 5 concludes the article.

2. LOCATIONAL MARGINAL PRICING

2.1. Pricing transmission congestion

There are three different methods for pricing in transmission system: locational or nodal pricing, zonal pricing and uniform pricing. In locational pricing, the price of electricity at each bus reflects the marginal cost of providing electricity at that location. It is used in the USA, South America, New England and Nordic countries. It maximizes social welfare considering transmission and generators constraints, as well as losses in the power system and is performed by the system operator. If the system is not congested all prices are equal, however if the transmission line is congested or there is a loss of a transmission line, nodal prices will differ by location. These locational prices are based on the principles of economic dispatch. Transmission congestion prevents energy from low-cost generators from meeting all load requirements and, consequently, from clearing the market. This means that low-cost generators dispatch will be constrained to lower power output values (or even shut down) and higher-cost generators will be dispatched to serve load and will thereby raise the market price.

Zonal pricing is similar to locational pricing. Several buses are grouped into zones and there are price differences between the zones. Prices are calculated from simplified models. Zonal pricing implies higher operating cost [5]. When uniform pricing is used and location is neglected social welfare is often reduced even if the transmission is not congested, which can give incorrect investment signals in the long term [6].

2.2. Locational Marginal Prices

Prices are determined by generator bids for producing energy. If there is no congestion, the charge for using transmission lines is zero and marginal prices at all nodes are the same (this does not include charges for using transmission grid for transferring electricity). However, in case of congestions the transmission network usage charges are defined as the incremental cost of redispatch that satisfies transmission lines limit. This means that if transmission lines are congested, some low-cost generators will have to be replaced by more expensive generators resulting in higher marginal prices. Locational Marginal Prices (LMPs) values are calculated for different time periods and are a result of the optimization process which finds least cost dispatch while maintaining production consumption equilibrium and satisfies all system technical constraints [7]. There are many factors that affect LMPs: the electrical characteristics of the system, generators' bid prices, generators' limit, the transmission system elements that are experiencing congestion (line thermal limit) and the losses in the system (if they are taken in the account) [8]. The calculation process combines shadow prices of transmission system constraints with the impact on transmission constraints due to supplying additional load at a

bus to determine the LMPs values. In short, LMPs can be defined as “the price of supplying an additional MW of load at each location (bus) in the system. [9]” This results in generators selling energy at one price (the price calculated for that location) and suppliers (or consumers) buying energy at a different price because of congestion and differences in LMPs. As a way of protecting buyers from price volatility efficient mechanisms such as FTRs are put in place to deal with congestions in transmission system.

3. FINANCIAL TRANSMISSION RIGHTS

FTRs are used to mitigate market participants’ exposure to price risks when congestion occurs in transmission network, they are a financial entitlement used for hedging against congestion charges. The economic value of an FTR is determined by the difference in the hourly locational marginal prices between its source and sink and by the MW reservation level of the financial transmission right. The FTR is independent of actual energy delivery since its value is determined by the reservation MW [10]. The marginal cost of energy (energy component of LMP) has the same value throughout the system. On the other hand, values of loss and congestion components may vary from one location to another. The congestion component of the LMP is calculated as a congestion difference between sink and source location (bus), while the difference between loss components of sink and source LMPs determines the loss component of the LMP differences. However, currently FTRs are determined only according to the congestion components of LMP differences. Energy component of the LMP differential is always zero. This is because the energy component of the LMP at a certain location is always the same as that at any other location [11].

When losses are neglected, nodal price difference reflects the existence of transmission constraints or transmission congestion (1):

$$\Delta LMP = W_i - W_j \#(1)$$

where $W_i - W_j$ is price difference in congestion cost between bus i and bus j .

FTRs can be acquired through four market mechanisms: Long-term FTR Auctions, Annual FTR Auction, Monthly FTR Auction or FTR Secondary market.

3.1. Obligation and Option

There are two different types of Financial Transmission Rights: obligation and option. The hourly economic value of FTR Obligation is based on the MW reservation and the price difference between sink (point of delivery) and the source point (point of receipt). The hourly economic value of an FTR Obligation is positive (a benefit) when the path designated in the FTR is in the same direction as the

congested flow. This occurs when the price at the sink point is higher than the price at the source point. An FTR Obligation is negative (a liability) if the designated path is in the direction opposite of the congested flow (price at the source point is higher than the price at the sink source), as shown in Figure 1.a) and 1.b). Since FTR payoff is related to LMP differences, potential FTR owners will try to forecast LMP in order to choose FTR injection and withdrawal locations with only positive payoff.

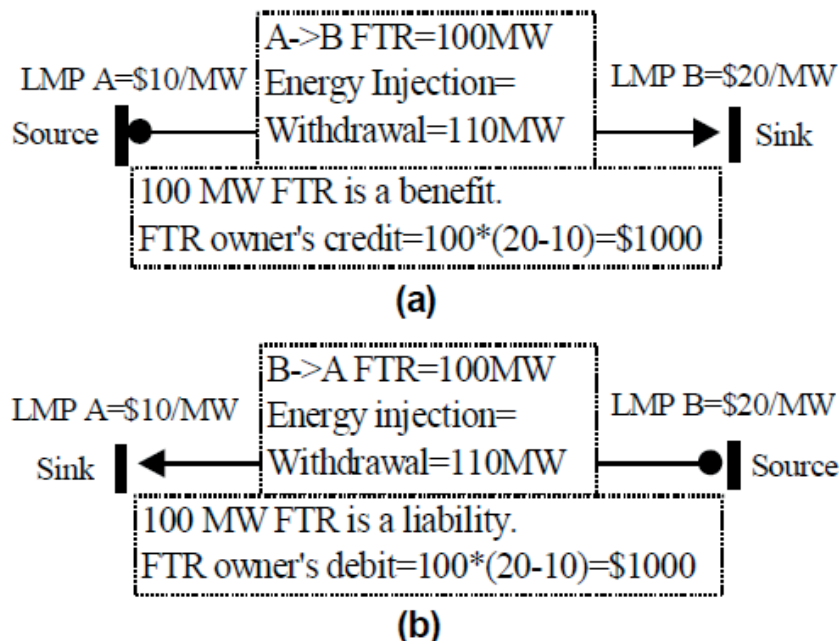


Figure 1 a) FTR as a benefit b) FTR as a liability [12]

The hourly economic value of an FTR Option is based on the FTR MW reservation and the price difference between sink point (point of delivery) and the source point (point of receipt). The hourly economic value of an FTR Option can only be positive. This occurs when path designated in the FTR is in the same direction as the congested flow. When the designated path is in the direction opposite to the congested flow the economic value of an FTR Option is zero.

FTR is a financial instrument. The payment ISO collects from congestion charges will be allocated to the FTR owners regardless if they actually use the transmission lines or not. Payment is independent of real physical power transfer since it is based on reservation of MW for specified lines.

3.2. Mathematical background for calculating FTRs

DC optimal power flow method is used to calculate minimal cost of generation and financial transmission rights. The goal is to minimize generators cost functions for meeting the load (2):

$$\text{minimize } \sum_{i \in G} f_i(p_{g_i}) \#(2)$$

where G is the set of all generators in the system, $f_i(p_{g_i})$ is generator cost function for generator at node i and p_{g_i} is the amount of power produced by the generator at the node i .

λ_i is nodal price for node i (dual variable). The power injected in the node or withdrawn from the node p_i is equal to sum of all power flows on the transmission lines p_{ij} that start (end) at that node (3):

$$\lambda_i: p_i = \sum_j p_{ij} \#(3)$$

Generators have lower p_{min} and upper p_{max} power limit (4):

$$p_{min} \leq p_{g_i} \leq p_{max} \#(4)$$

μ_{ij} is the dual variable for line shadow price. Power flow on each transmission line is constrained by thermal capacity $limit_{ij}$ (5):

$$\mu_{ij}: p_{ij} \leq limit_{ij} \#(5)$$

The complementarity conditions enforce that the inner product of an inequality constraint and the primal or dual variable is zero, and the nonnegativity of both the inequality constraint and primal or dual variable. This means that either the inequality constraint holds as an equality, i.e. is binding, or the primal or dual variable is zero. If $p_{ij} < limit_{ij}$, then the dual variable for shadow price μ_{ij} is equal to zero. If $p_{ij} = limit_{ij}$, then the value of μ_{ij} is greater than zero and that is the value for financial transmission right [13].

3.3. 3-bus example

There are two generators in the system, one located at the bus 1 with marginal cost 10 €/MWh and the other at the bus 2 with marginal cost 20€/MWh. Load is located at the bus 3. Transmission lines capacity between two nodes are 40 MW and the impedances are equal for all three lines. Nodal price can be a combination of two marginal costs of generators and it can be lower than the cheapest generator's marginal cost and higher than the most expensive marginal cost. The system is shown in Figure 2:

Generator G_1 and G_2 each have the capacity of 100 MW. In the first case example, load at the bus 3 is equal to 55 MW. The power flow and nodal prices are calculated in MATLAB. The best solution for this case is to dispatch generator G_1 for serving the load at the bus 3. Transmission line constraints are not violated. Nodal price is 10€/MWh at each bus.

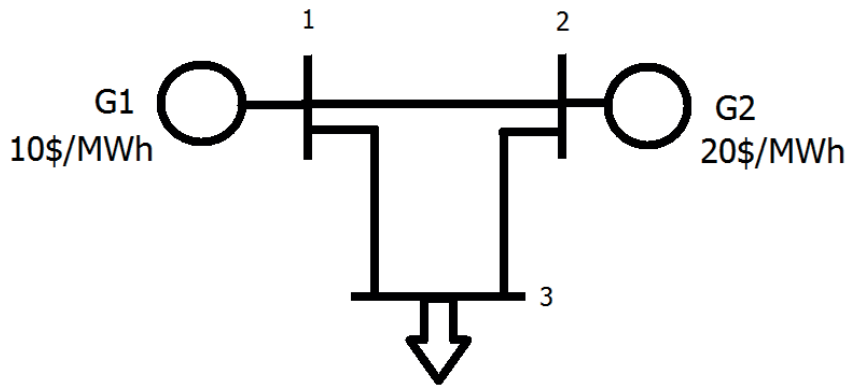


Figure 2 3-bus system

In the second case load is increased by 5 MW. Generator G_1 produces 60 MW and nodal prices are not unique in the entire system. Nodal price at bus 1 is 10 €/MWh, at bus 2 is 20€/MWh and at bus 3 is 30€/MWh. Increasing the load for 1 MW at bus 1 can be served by Generator G_1 . If load at bus 3 is increased for 1 MW, generator G_2 must increase its power production for 2 MW and generator G_1 must decrease the power generation by 1 MW. That is the reason why the nodal price at bus 3 is 30€/MWh. Generator's profit at the bus 1 is 10€/MWh*60MW*1h=600€. The load has to pay 30€/MWh*60MW*1h=1800€. The difference between generators' profit and consumers' cost is collected by the system operator. The FTR price for transmission line between bus 1 and bus 3 is 30 €/MWh. If that price is multiplied by amount of power transferred over that line (40 MW), 1200 € revenue is collected for consumer at bus 3. If the consumer at bus 3 buys the FTR from bus 1 to bus 3, he can hedge against the price volatility.

3.4. IEEE 9-bus example without congestion

9-bus example is shown in Figure 3:

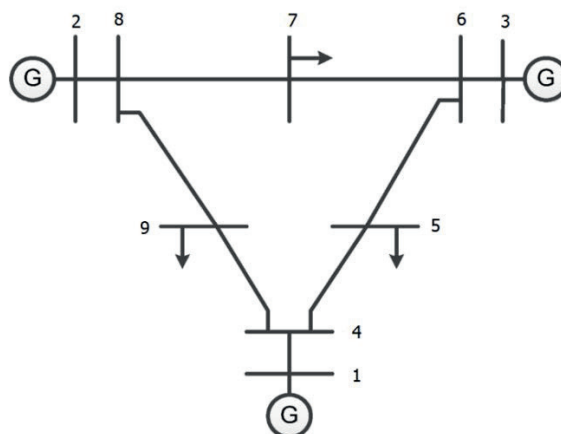


Figure 3 9-bus example

The generators' cost function, transmission line limits and reactance are given in Table I and Table II:

Table I Generators' cost function

Generator	Cost function (€)
G ₁	$0.11p^2 + 5p + 150$
G ₂	$0.085p^2 + 1.2p + 600$
G ₃	$0.1225p^2 + 1p + 335$

where p is the amount of produced power in MW.

Table II Transmission line characteristics

Line	From	To	Reactance (p.u.)	Limit (MW)
1	1	4	0.0576	250
2	2	8	0.0625	250
3	3	6	0.0586	300
4	4	5	0.092	250
5	4	9	0.085	250
6	5	6	0.17	150
7	6	7	0.1008	60
8	7	8	0.072	250
9	8	9	0.161	250

Load is located at buses 5, 7 and 9, as shown in Figure 3, and the generators are located at buses 1, 2 and 3. The objective is to minimize the generation cost considering transmission line limits. In the first example, 90 MW load is located at bus 5, 100 MW load at bus 7 and 125 MW load at bus 9, as shown in Table III. After running the optimization algorithm, the minimum cost of supplying the load in the system is 5216.03 € and generators are dispatched as shown in Table III:

Table III Load and generators' production

Load bus	Load (MW)	Gen bus	Gen (MW)
5	90	1	86.56
7	100	2	134.38
9	125	3	94.06

The system is operating within technical limits and constraints and prices are equal at every bus (24.04 €).

Power flow on each line and comparison with thermal line limits is shown in Table IV:

Table IV Power flow compared to line limit

Line	From	To	Limit (MW)	Power flow (MW)
1	1	4	250	86.5614
2	2	8	250	134.3633
3	3	6	300	94.0753
4	4	5	250	33.7322
5	4	9	250	52.8292
6	5	6	150	-56.2678
7	6	7	60	37.8075
8	7	8	250	-62.1925
9	8	9	250	72.1708

3.5. IEEE 9-bus example with congestion

Load is increased in all buses of the system. Loads at the buses 5,7 and 9 are 155 MW, 190 MW and 200 MW, respectively. The production cost is 12619.1 € and the generators dispatch is shown in Table V:

Table V Load and generators dispatch for constrained case

Load bus	Load (MW)	Gen bus	Gen (MW)
5	155	1	157.14
7	190	2	243.96
9	200	3	143.90

Figure 4 shows absolute value of power flow in constrained case. Thermal limit on line 7 is enforced:

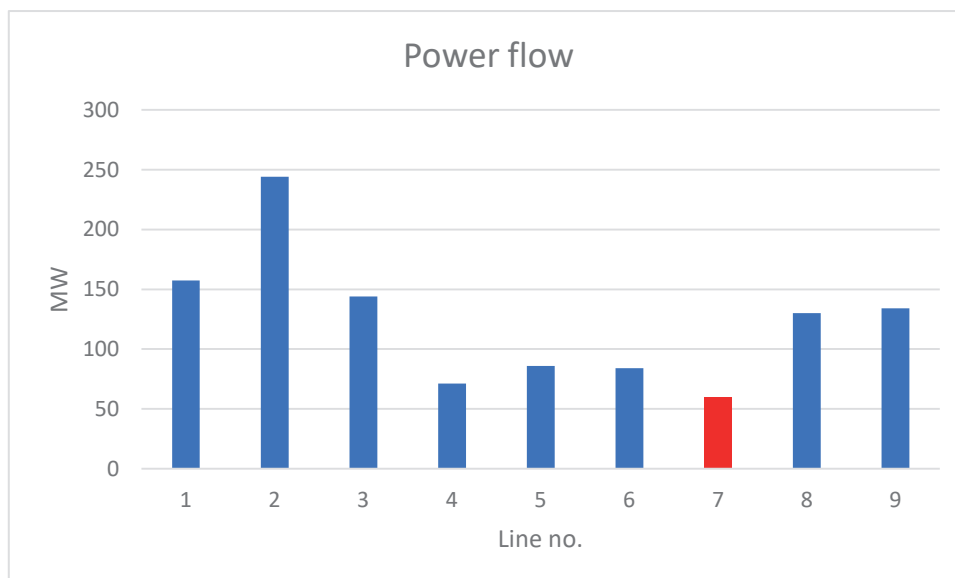


Figure 4 Power flows in constrained case

This results in different nodal prices as shown in Table VI:

Table VI Nodal prices

Bus	Price (€/MWh)
1	39.56
2	42.67
3	36.26
4	39.56
5	38.41
6	36.26
7	43.58
8	42.67
9	40.64

After the optimization process, shadow price for the constrained line is 8.6095 €/MW. Every participant who requested the FTR for that line will be paid 8.6095€/MW times reserved amount of MW.

Market participants can hedge against the price differences or make profit by owning FTRs. Next section demonstrates maximization of revenue from owning the FTR through auctions.

3.6. Auction model

The main goal of auction process is maximizing ISO profit. Bidders make offers of lower and upper amount of MW they are willing to buy and the price they are willing to pay. There are 3 types of FTRs that can be bought in an auction: flow-based financial transmission option or flowgate rights (in this case presented as bidder a_i), point-to-point financial transmission obligation (presented as b_i) and point-to-point financial transmission option (presented as c_i). Market participants develop a bidding strategy by calculating the flowgate capacity required by their transaction and often change the bid price or quantity required to adjust their portfolios. Willing to obtain more rights or trying to get a better price for desired right, bidders attempt to eliminate other markets participants, as explained later in 3.7. The auction model is taken from [14].

The objective is presented as (6):

$$\max \sum_i a_i \cdot price(a_i) + \sum_i b_i \cdot price(b_i) + \sum_i c_i \cdot price(c_i) \#(6)$$

where a_i , b_i and c_i are required amount of MW in auction for flowgate right, point-to-point obligation and point-to-point option, respectively and $price(a_i)$, $price(b_i)$ and $price(c_i)$ are prices that bidders are willing to pay for a certain right.

Constraints are lower and upper bounds of required MW (7):

$$lower_{bound_i} \leq x_i \leq upper_{bound_i}, \forall i, x \in a, b, c \#(7)$$

There is also constraint connected with flowgate limit on every line in each direction (the FTR flow on the same line does not have to be equal for both directions). This can be described by equation (8) and described as:

$$\sum_i a_i \cdot \alpha_i + \sum_i b_i \cdot \beta_i + \sum_i c_i \cdot \gamma_i \leq \text{line}_{limit\#}(8)$$

where a_i , b_i and c_i are required quantities of MW in auction for flowgate right, point-to-point obligation and point-to-point option, respectively. α_i , β_i and γ_i are coefficients that determine power flow for flowgate right, point-to-point obligation and point-to-point option.

3-bus system is shown in Figure 5 with equal transmission line reactance of $X = 1$ p.u. for all lines and thermal line limits of 100 MW:

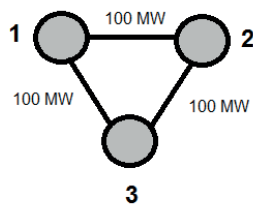


Figure 5 3-bus system and thermal limits

When bidder a_i is willing to buy a flowgate right for certain line and direction, his coefficient for that flowgate will be 1 and for the other lines 0. Flowgate or flow based option is an option for a line in specified direction. As one can see in Table VII bidder a_1 is willing to buy the right for flowgate 1->3, bidder a_2 is willing to buy the right for flowgate 3->2 and bidder a_3 is willing to buy the right for flowgate 3->1. Bidder b_1 is buying point-to-point obligation from node 1 to node 3. As it is a point-to-point obligation, there is negative Power Transfer Distribution Factor (PTDF) on opposite direction. This means if required FTR is in the same direction as congested flow, he will receive payment, and if it is in opposite direction he has to pay the ISO. If he injected 1 MW of power in node 1 and extract it from node 3, that will increase a power flow on line 1->3 by 2/3 MW (in opposite direction -2/3 MW), on line 1->2 and 2->3 by 1/3 MW (with negative sign in opposite directions). Bidder c_1 is willing to buy a point-to-pont option from node 1 to node 2. As he is buying an option, there is just a positive sign because if required FTR is in opposite direction as the congested flow, he does not have to pay the ISO anything. Injecting 1 MW at node 1 and extracting from node 2 will cause a power flow of 2/3 MW on the line 1->2 and 1/3 MW on the lines 3->2 and 1->3.

Table VII Flowgate and PTDFs factors for each bid

Flowgate	Bidder a ₁	Bidder a ₂	Bidder a ₃	Bidder b ₁	Bidder c ₁
1->2	0	0	0	1/3	2/3
2->1	0	0	0	-1/3	0
2->3	0	0	0	1/3	0
3->2	0	1	0	-1/3	1/3
1->3	1	0	0	2/3	1/3
3->1	0	0	1	-2/3	0

Lower bounds are FTRs that bidders already own and do not want to trade with. Bidding prices, lower and upper bound of required FTRs are given in Table VIII:

Table VIII Bidding prices, lower and upper bounds of FTRs

Bidder	a ₁	a ₂	a ₃	b ₁	c ₁
Bid (€/MW)	4	7	8	10	5
Lower bound (MW)	0	0	50	20	0
Upper bound (MW)	100	100	100	80	50

After the auction, comparing the line limits with power flow in Table IX, one can notice that flowgate 1->3 is congested and the shadow price is 4€/MW (given later in the section).

Table IX Line limit, actual power flow and shadow prices

Line	Line limit (MW)	Power flow (MW)	Shadow price (€/MW)
1->2	100	60	0
2->1	100	-26.6667	0
2->3	100	26.6667	0
3->2	100	90	0
1->3	100	100	4
3->1	100	46.6667	0

Awarded FTRs, upper bound of required FTRs and ISO revenue from auction are given in Table X:

Table X Awarded FTRs and ISO receipt

Bidder	a ₁	a ₂	a ₃	b ₁	c ₁
Upper bound (MW)	100	100	100	80	50
Awarded MW	30	100	100	80	50
ISO revenue (€)	120	0	0	213.33	66.67

As one can notice from Table X, ISO revenue depends on bidding prices and MW awarded to each bidder. The main goal of the auction is to maximize the profit taking into account transmission line limit. As shown in Table IX, thermal limit of line 1->3 is violated and shadow price for that line is not 0. Shadow prices depend on the latest bid which could not be awarded. For example, we can notice that bidder a_1 got 30 MW (and he was willing to buy 100 MW). His bidding price was 4 €/MW for flowgate 1->3. After the auction, the shadow price for flowgate 1->3 is 4 €/MW because this is the last bid that could not be awarded (he could not get the required amount because of congestion, his price reflected the shadow price for that flowgate).

Bidders have to be careful in auction process. For example, bidder a_1 wanted to buy 100 MW for flow gate 1->3. As that flowgate is very valuable, he pays dearly for his 30 MW because this flowgate is also very valuable to other bidders. In next hour auction bidder a_1 can change his strategy and bid only for 30 MW and if others do not change their strategy, he would get 30 MW of that right. However, now the shadow price will be 0 and he would not have to pay anything for holding that right because there are no more rights that have to be awarded for that flowgate.

As it can be seen in Table X, bidders a_2 and a_3 do not have to pay the ISO for awarded FTRs because there are more rights available. This can also be subject to changes in next hour auction. Flowgates 3->2 and 3->1 can become more valuable and price can change.

Bidders b_1 and c_1 have to pay for holding the congested flowgate 1->3 depending on the PTDFs factor. Bidder b_1 has to pay $80 \text{ MW} * 2/3 * 4 \text{ €/MW} = 213.33 \text{ €}$ and bidder c_1 $50 \text{ MW} * 1/3 * 4 \text{ €/MW} = 66.67 \text{ €}$.

Bidder a_1 could not get the full 100 MW for his right since his bidding price was too low. As ISO objective is to maximize the profit from auction, and bidders b_1 and c_1 had higher prices, they are the first to be awarded their FTRs.

If bidder b_1 changes his bid price (e.g. from 10€/MW to 2€/MW wishing to pay less for FTRs) situation will change as shown in Table XI and XII:

Table XI Changes in awarded FTRs and ISO receipt

Bidder	a ₁	a ₂	a ₃	b ₁	c ₁
Awarded MW	50	100	100	50	50
ISO revenue (€)	200	200	0	100	100
Previous awarded MW	30	100	100	80	50
Previous ISO revenue (€)	120	0	0	213.33	66.67

Table XII Changes in power flow and shadow prices

Line	Line limit (MW)	Power flow (MW)	Shadow price (€/MW)
1->2	100	50	0
2->1	100	-16.6667	0
2->3	100	16.6667	0
3->2	100	100	2
1->3	100	100	4
3->1	100	66.6667	0

ISO would award more MW to bidder a_1 since this would increase its profit. As one can notice, shadow prices and power flow changed as well.

3.7. Bidder a_1 strategy for awarding more MW

Bidder a_1 would like to gain more than 50 MW of FTR on line 1->3. To achieve this, he can choose from different strategies. His first option would be rising his bidding price from 4 €/MW to 7€/MW. The choice of 7€/MW follows from the logic of 6€/MW being sufficient only for awarding him 50 MW, as shown in the previous case. The shadow price for flowgate 1->3 is 6€/MW and ISO receives 300€ from bidder a_1 , 200€ from bidder b_1 and 100€ from bidder c_1 . Raising his price to 7€/MW, he gets 70 MW for flowgate 1->3. At the same time ISO reduces FTRs to the bidder b_1 from 50 MW to 20 MW. The shadow price for flowgate 1->3 is now 7€/MW and ISO receives 490 € from bidder a_1 , 93.33 € from bidder b_1 and 116.67€ from bidder c_1 .

Second choice for bidder a_1 is to buy the FTR for different flowgate and try to eliminate other market players. He wants to buy 70 MW for flowgate 1->2 (this bid is presented as a_4). Choosing the right bidding price is the most important if he chooses this strategy. He bids 4€/MW for flowgate 1->3 (as he did in previous auction) and he bids 3€/MW for flowgate 1->2. This bid is too low to eliminate other market participants and he cannot get more than 50 MW for the flowgate 1->3 (it is still more profitable for ISO to award more MW to bidders b_1 and c_1). This means he has to give a higher bid of 4€/MW. Results of the auction and payments to the ISO compared to the previous case are given in Table XIII:

Table XIII Compared awarded MW and payment to ISO

Bidder	a_1	a_2	a_3	a_4	b_1	c_1
Awarded MW (case 1)	70	90	100	-	20	50
Payment to ISO (€)	490	490	0	-	46.67	233.33
Awarded MW (case 2)	70	100	100	70	30	30
Payment to ISO (€)	280	500	0	210	80	150

As the results show, better strategy for a bidder is to participate in auctions by bidding for different rights instead of increasing the bid for the same right. As opposed to the previous example, now bidder a_1 is awarded 70 MW for the flowgate 1->3 and he needs to pay 280 € for holding that FTR, instead of 490 €. He could additionally make more profit by selling the right for flowgate 1->2 through bilateral contract if he does not need that right. By choosing the right bidding price for the flowgate 1->2, he was awarded more MW for the flowgate 1->3 and paid less for it. The shadow prices for the flowgates 1->2, 3->2 and 1->4 are 3€/MW, 5€/MW and 4 €/MW, respectively.

3.8. Rising shadow prices

Assume that the second scenario explained in section 3.7. occurs. Only flowgates 3->2 and 1->3 are congested and shadow prices are 2€/MW and 4€/MW. Shadow price for flowgate 2->3 is 0 which means there are more rights on that flowgate that can be awarded. Only bidder b_1 is holding point-to-point obligation for that flowgate. The flowgate is 16.67 MW and there is additional 83.33 MW that can be awarded. If new bidder wants to buy flow-based option for flowgate 2->3, regardless the price he offers, he can get a maximum of 93.33 MW. This comes from the fact that bidder's b_1 lower bound is 20 MW ($20 \cdot 1/3 = 6.667$ MW) and does not want to trade with that amount. Depending on the price and the upper bound of required amount of MW offered by new bidder for flowgate 2->3, flowgates, awarded FTRs and shadow prices change. Table XIV presents shadow prices and power flow on flowgates when bidding price for flow-based option 2->3 is 4€/MW and required upper bound is 80 MW. Compared to the previous case, shadow prices are still the same for flowgate 3->2 and 1->3 (2€/MW and 4 €/MW). Power flow changed only on the flow gate 2->3 and is increased by 80 MW.

Table XIV Shadow prices and power flow for bidding price 4€/MW and upper bound 80 MW

Flow gate	Shadow price (€/MW)	Power flow (MW)
1->2	0	50
2->1	0	-16.667
2->3	0	96.667
3->2	2	100
1->3	4	100
3->1	0	66.667

If the new bidder increases his required upper bound up to 100 MW and the price remains the same (4€/MW), he will be rewarded 83.33 MW (others get the same amount as in previous case), but his upper bound reflects the shadow prices, as shown in Table XV:

Table XV Shadow prices and power flow for bidding price 4€/MW and upper bound 1000 MW

Flow gate	Shadow price (€/MW)	Power flow (MW)
1->2	0	50
2->1	0	-16.667
2->3	4	100
3->2	6	100
1->3	4	100
3->1	0	66.667

If the new bidder wants more MW, he should rise his price. Shadow prices and power flow, when the price is 5€/MW and upper bound 100 MW, is shown in Table XVI:

Table XV Shadow prices and power flow for bidding price 5€/MW and upper bound 1000 MW

Flow gate	Shadow price (€/MW)	Power flow (MW)
1->2	0	40
2->1	0	-6.667
2->3	4	100
3->2	7	100
1->3	5	100
3->1	0	86.667

This also changes the awarded MW for bidders as shown in Table XVII (second and third column presents the situation when bidding price is 4€/MW and 5€/MW, and the upper bound is 100 MW):

Table XVII Differences in awarded MW depending on different bidding price

Bidder	Awarded MW	Awarded MW
a₁	50	70
a₂	100	90
a₃	100	100
a₄	83.333	93.333
b₁	50	20
c₁	50	50

The new bidder will receive 93.333 MW, which is maximum since bidder b_1 already owns 6.667 MW for the specified flowgate. His bidding price changed awarded FTRs to bidders a_1 , a_2 and b_1 . As one can notice, this can also be a good strategy for bidder a_1 if he wants to get more MW for flowgate 1->3. If bidder a_1 request 100 MW for flowgate 2->3 at the price 5€/MW or higher, he will get 70 MW on the flowgate 1->3. As the shadow price is 5€/MW, he needs to pay 350 € for 70 MW and 373.33€ for 93.333 MW on the flowgate 2->3. This is a suboptimal case is compared to the one described in section 3.8. On the other hand, if he would choose to sell the right for flowgate 2->3 via bilateral contract, there is an opportunity to increase the profit and still get 70 MW for flowgate 1->3.

3.9. FTR auction in 6 bus system

Line parameters are obtained from [15] and shown in Table XVIII.

Table XVIII Line parameters 6 bus system

Line	From bus	To bus	X (p.u.)	Flow limit (MW)
1	1	2	0.20	100
2	1	4	0.20	100
3	1	5	0.30	100
4	2	3	0.25	60
5	2	4	0.10	60
6	2	5	0.30	60
7	2	6	0.20	60
8	3	5	0.26	60
9	3	6	0.10	60
10	4	5	0.40	60
11	5	6	0.30	60

6-bus system is given in Figure 6:

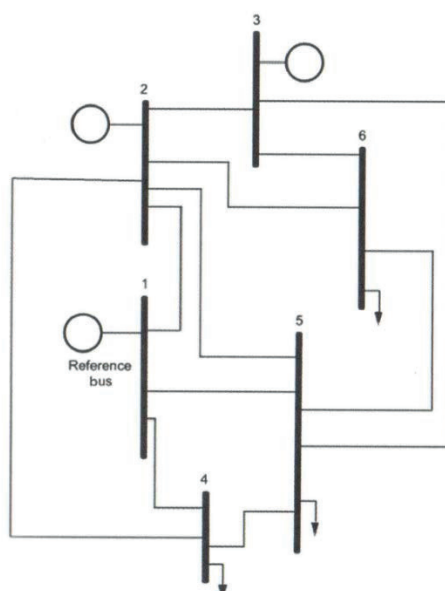


Figure 6 6-bus system [15]

Generators' cost function is a quadratic function given in Table XIX, as well as lower and upper bound:

Table XVIII Generators' parameters

Generator	P_{\min} (MW)	P_{\max} (MW)	Cost function
1	50	200	$213.1+11.669p_1+0.00533p_1^2$
2	37.5	150	$200.0+10.333p_2+0.00889p_2^2$
3	45	180	$240.0+10.833p_3+0.00741p_3^2$

where p_1 , p_2 , p_3 are power produced by generator at bus 1,2 and 3, respectively. Load at the bus 4,5 and 6 is 80 MW, 90 MW and 70 MW. Generator at the bus 1 produces 50 MW, generator at bus 2 produces 101.696 MW and generator

at the bus 3 produces 88.304 MW. Thermal line limits are not violated and nodal prices are the same all over the network 12.14€/MWh.

If the demand increases, congestion will occur and the nodal price will be different depending on nodes. Assume there is 120 MW, 120 MW and 100 MW load at buses 4,5 and 6. Lines 5 (between bus 2 and 4) and 9 (between bus 3 and 6) are congested and nodal prices are different. Shadow prices for congested lines are 3.86 €/MW and 1.59€/MW. ISO collects 327.10 € for transmission congestion.

If participants want to hedge against price volatility, they can buy flow based option, firm point-to-point option or obligation. As lines 5 and 9 are congested, market participants compete to buy rights for those lines. Bidder a_1 wants to buy flow based option for flow gate 2->4; his bidding price is 3.5 €/MW and maximum bound of FTR he is willing to buy is 10 MW. Bidder a_2 competes for flowgate3->6 with the bidding price 1.5 €/MW and upper bound 15 MW. They chose their prices according to the shadow prices in congested system. If they make bids with higher prices they can get more rights, but also they will pay more than the right is worth. Bidders b_1 and b_2 are buying point-to-point obligation (b_1 from bus 2 to 4 and bidder b_2 from bus 3 to 6). Upper bounds for both are 60 MW and bidding prices are 2€/MW and 3€/MW. Flow based options and calculated PTDFs are shown in Table XX:

Table XIX Flow based options and PTDFs for auction

Flowgate	Bidder a_1	Bidder a_2	Bidder b_1	Bidder b_2
1->2	0	0	-0.1555	+0.004
2->1	0	0	+0.1555	-0.004
1->4	0	0	+0.1895	+0.001
4->1	0	0	-0.1895	-0.001
1->5	0	0	-0.0337	-0.005
5->1	0	0	+0.0337	+0.005
2->3	0	0	+0.0384	-0.1508
3->2	0	0	-0.0384	+0.1508
2->4	1	0	+0.69	-0.006
4->2	0	0	-0.69	+0.006
2->5	0	0	+0.07	-0.0077
5->2	0	0	-0.07	+0.0077
2->6	0	0	+0.045	+0.1675
6->2	0	0	-0.045	-0.1675
3->5	0	0	+0.0438	+0.1362
5->3	0	0	-0.0438	-0.1362
3->6	0	1	-0.006	+0.7120
6->3	0	0	+0.006	-0.7120
4->5	0	0	-0.12	-0.0043
5->4	0	0	+0.12	+0.0043
5->6	0	0	-0.04	+0.1193
6->5	0	0	+0.04	-0.1193

After the auction, ISO awards maximum amount to every bidder. Shadow prices are 0 because there are more rights that can be awarded and none of them has to pay for awarded FTRs. Bidder a_1 gets 10 MW and receives 38.6 € for holding the FTR for flow gate 2->4. Bidder a_2 gets 15 MW and receives 23.85 €. Bidder b_1 gets for flow gate 2->4 41.4 MW and 159.80 €. Bidder b_2 gets 42.7 MW for flow gate 3->6 and 67.92 €.

If in the next auction bidders a_1 and a_2 will try to get more FTRs, meaning they will rise their upper bound to e.g. 30 MW. ISO awards them 30 MW and 17.564 MW. Bidder b_1 gets 44 MW and bidder b_2 gets 60 MW. Shadow prices for flow gates 2->4 and 3->6 are 2.91 €/MW and 1.5 €/MW. Bidder a_1 pays 87.35 € (30 MW at the price 2.91 €/MW) and receives 115.80 € for holding the FTR (30 MW multiplied by 3.86 €/MW). Bidder a_2 pays 26.32 € and receives 27.90 €. Bidder b_1 pays 88.35€ and gets 117.19 €. Bidder b_2 pays 64.08 € and gets 67.92€.

4. ENERGY STORAGE

Utilizing electricity storage flexibility can increase the reliability of supply for the consumers, especially with the increased integration of renewable energy sources characterized by limited controllability and predictability. Flexibility is the ability to provide upward and downward power adjustments to deal with short-term imbalances between generation and consumption of electric energy. This flexibility can be provided by flexible generation and consumption and electricity storage, but can also be activated in neighboring regions through interconnection capacity and by further integration of adjacent markets [16]. Electricity storage has the ability to compensate temporary power surpluses and shortages by decoupling the generation of electric energy from its consumption over time. The extent of this ability is limited by storage capacity. Although there is an increasing need for flexibility, market participants are incentivized to integrate new flexible resources only if the investment is profitable.

4.1. Financial storage rights

Model for calculating Financial Storage Rights is obtained from [6]. System is modeled with multiperiod DC optimal power flow. The objective is to minimize the intertemporal production cost. Constraints and dual variables are given in (9):

$$\lambda_{i,t} : p_{i,t} = \sum_{j \in \mathcal{S}_i} (\text{charge}_{j,t} + \text{discharge}_{j,t}) + \sum_j p_{ij,t} \quad \#(9)$$

Where $\lambda_{i,t}$ is nodal price for bus i in the time t . Power $p_{i,t}$ injected in the bus or withdrawn from bus i is equal to sum of all power flow on the transmission lines

that start (end) at that bus plus power charged into storage $charge_{j,t}$ or discharged from storage $discharge_{j,t}$ (of course only if storage is installed at that bus).

All generators have lower p_{min} and upper p_{max} power limit, modelled by (10):

$$p_{min} \leq p_{g_{i,t}} \leq p_{max} \#(10)$$

$\mu_{ij,t}$ is dual variable for line shadow price of line between buses i and j . Power flow on each transmission line is constrained by thermal capacity, modelled by (11):

$$\mu_{ij,t} : p_{ij,t} \leq limit_{ij} \#(11)$$

State of charge of storage i ($SoC_{i,t+1}$) in the time $t + 1$ is equal to state of charge $SoC_{i,t}$ in previous time step t and reduced by leakage coefficient α_i , plus charging ($charge_{i,t}$) reduced by charge loss coefficient η_i^+ and discharging ($discharge_{i,t}$) reduced by discharge loss coefficient η_i^- (12):

$$SoC_{i,t+1} = \alpha_i \cdot SoC_{i,t} + \eta_i^+ \cdot charge_{i,t} + \eta_i^- \cdot discharge_{i,t} \#(12)$$

Storage state-of-charge at the beginning and at the end of the day is the same, as modelled by (13):

$$SoC_{i,0} = SoC_{i,24} = 0 \#(13)$$

Charging $charge_{i,t}$ and discharging $discharge_{i,t}$ are constrained by charge $charge_max_{i,t}$ and discharge rate limits $dicharge_max_{i,t}$ (14) and (15):

$$\vartheta_i^+ : charge_{i,t} \leq charge_max_{i,t} \#(14)$$

$$\vartheta_i^- : discharge_{i,t} \geq dicharge_max_{i,t} \#(15)$$

ϑ_i^+ and ϑ_i^- are dual variables for charging and discharging. If storage is charged or discharged at the maximum rate, $charge_{i,t} = charge_max_{i,t}$ or $discharge_{i,t} = dicharge_max_{i,t}$, dual variables ϑ_i^+ and ϑ_i^- are greater than 0. If congestion occurs, the owner of a power capacity right (PCR) collects $\vartheta_i^+ \cdot \overline{charge}_{i,t} - \vartheta_i^- \cdot \overline{discharge}_{i,t}$.

$\overline{charge}_{i,t}$ and $\overline{discharge}_{i,t}$ are quantities of power that power capacity right owner has.

Charging is always positive, meaning $charge_max_{i,t}$ has positive values as modelled by (16). Discharging is negative and $dicharge_max_{i,t}$ is a negative values (17).

$$charge_{i,t} \geq 0 \#(16)$$

$$discharge_{i,t} \leq 0 \#(17)$$

State of charge $SoC_{i,t}$ is constrained by storage capacity $SoC_max_{i,t}$ (18):

$$\delta_{i,t} : SoC_{i,t} \leq SoC_max_{i,t} \#(18)$$

State of charge is always greater or equal to zero (19):

$$SoC_{i,t} \geq 0 \#(19)$$

$\delta_{i,t}$ is dual variable for energy capacity right. If storage is congested $SoC_{i,t} = SoC_max_{i,t}$ and $\delta_{i,t}$ is greater than 0 and owner of energy capacity right collects $\delta_{i,t} \cdot \overline{SoC}_{i,t}$.

$\overline{SoC}_{i,t}$ is the quantity of energy that owner of the energy capacity rights owns and it has to be less than $SoC_max_{i,t}$.

Together, power capacity right and energy capacity right are financial storage rights. If the owner of storage rights has right for power and energy and if congestion occurs in storage, he will collect $\vartheta_i^+ \cdot \overline{charge}_{i,t} - \vartheta_i^- \cdot \overline{discharge}_{i,t} + \delta_{i,t} \cdot \overline{SoC}_{i,t}$.

4.2. 3-bus system with one energy storage

A 3-bus system, as shown in Figure 2, is analyzed. All transmission lines have the same reactance $X = 1 p.u.$ and thermal limit of 60 MW. Generators are located at the bus 1 and 2. Generator costs are 10€/MWh and 20€/MWh. Load and storage are located at bus 3. Energy storage is characterized as follow: capacity of storage is 18 MWh, charge and discharge rate limits are 10 MW and 9 MW, charge loss coefficient is 0.95 and discharge loss coefficient is 1/0.85. Energy leakage coefficient is 0.9. We consider the case with 6-time periods. Results are shown in Table XXI, Table XXII and Table XXIII:

Table XXI Generation, load, charging, discharging, state of charge

Time (h)	G ₁ (MW)	G ₂ (MW)	Load(MW)	Charge(MW)	Discharge (MW)	SoC (MWh)
1	30	0	20	10	0	9.5
2	77.2675	25.4650	110	0	-7.2675	0
3	59.9415	0	50	9.9415	0	9.4444
4	80	0	70	10	0	18
5	69	42	120	0	-9	5.6118
6	74.2930	31.4140	110	0	-4.2930	0

Table XXII Nodal prices

Time (h)	Bus 1 (€/MWh)	Bus 2 (€/MWh)	Bus 3 (€/MWh)
1	10	10	10
2	10	20	30
3	10	10	10
4	10	10	10
5	10	20	30
6	10	20	30

Table XXII Power flow

Time (h)	Line 12 (MW)	Line 23 (MW)	Line 13 (MW)
1	10	10	20
2	17.2675	42.7325	60
3	19.9805	19.9805	39.9610
4	26.6667	26.6667	53.333
5	9	51	60
6	14.2930	45.707	60

Total cost is 5882.6 €. As one can notice, congestion and different nodal prices occur in second, fifth and sixth hour. Line shadow prices for the congested line, in all three cases, are 30€/MW. When congestion occurs, owner of the Financial Transmission Right for the line 13 will be paid 30€/MW times the amount of reserved MW on the transmission line 13.

There is also congestion of energy storage. As one can notice, in first and fourth hour, energy storage is charged at the maximum rate 10MW and shadow prices for power capacity right are 11.80 €/MW and 1.11 €/MW. In fifth hour energy storage is discharged at maximum rate of -9MW and shadow price is 3 €/MW. In fifth hour energy storage is full and the shadow price for energy capacity right is 8.96 €/MWh.

Because of congestion and price differences in system, payment collected from load exceeds payment to generators. ISO has 5717.4 € surplus. Amount of 5400 € is reserved for FTRs owners and 317.4 € for Storage Rights owners (161.26 € for power capacity right and 156.14 € for energy capacity right).

If someone holds the transmission right for line 13 in second, fifth or sixth hour, he will be paid 30€ for each MW he owns. If storage right owner holds the right for power and energy capacity in fifth hour, he will be paid 3€/MW for reserved charging MW and 8.96€/MWh for reserved MWh.

4.3. 30-bus system

30-bus system is shown in Figure 7:

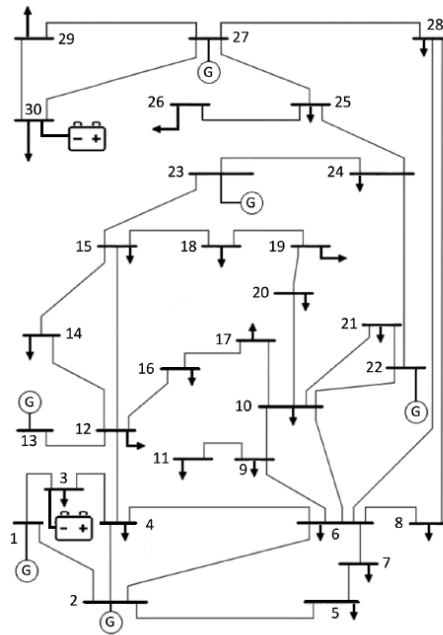


Figure 7 30-bus system [17]

There are 6 generators in the system located at buses 1, 2, 13, 22, 23 and 27. Generators' cost functions are given in Table XXIV:

Table XXIIIIV Generators' cost function

Generator	Cost function (€)
G ₁	$0.02p_1^2+10p_1$
G ₂	$0.0175p_2^2+15p_2$
G ₁₃	$0.0625p_{13}^2+15p_{13}$
G ₂₂	$0.00834p_{22}^2+17p_{22}$
G ₂₃	$0.025p_{23}^2+20p_{23}$
G ₂₇	$0.025p_{27}^2+16p_{27}$

Energy storages are located at buses 3 and 30. Storage parameters (charge and discharge rate limit, energy capacity, charge and discharge loss coefficient and energy leakage coefficient) are given in Table XXV:

Table XXIV Storage parameters

Storage	Charge limit (MW)	Discharge limit (MW)	Energy capacity (MWh)	Charge loss coefficient	Discharge loss coefficient	Energy leakage coefficient
S ₃	20	-15	100	0.98	1	0.98
S ₃₀	15	-20	100	0.98	1	0.98

Load is shown in Table XXVI:

Table XXVI Load characteristics

Hour	Load (MW)	Hour	Load (MW)	Hour	Load (MW)
1	523.60	9	652.70	17	751.50
2	458.40	10	723.80	18	773.40
3	428.10	11	749.10	19	789.40
4	404.90	12	800.00	20	855.50
5	404.20	13	809.30	21	910.80
6	421.40	14	779.60	22	897.80
7	433.50	15	758.30	23	852.70
8	498.90	16	740.60	24	756.50

Line parameters (reactance and thermal limit) are shown in Table XXVII:

Table XXVII Line parameters

Line	From bus	To bus	Reactance p.u.	Limit MW	Line	From bus	To bus	Reactance p.u.	Limit MW
1	1	2	0.26	87	22	12	13	0.22	80
2	1	3	0.19	112	23	12	14	0.13	60
3	2	4	0.17	120	24	12	15	0.27	60
4	2	5	0.24	90	25	12	16	0.21	50
5	2	6	0.20	130	26	14	15	0.28	50
6	3	4	0.18	95	27	15	18	0.27	60
7	4	6	0.24	95	28	15	23	0.15	65
8	4	12	0.22	90	29	16	17	0.22	50
9	5	7	0.28	70	30	18	19	0.20	50
10	6	7	0.24	75	31	19	20	0.18	50
11	6	8	0.21	70	32	21	22	0.27	80
12	6	9	0.56	95	33	22	24	0.33	50
13	6	10	0.21	70	34	23	24	0.38	50
14	6	28	0.11	70	35	24	25	0.21	55
15	8	28	0.26	70	36	25	26	0.40	55
16	9	11	0.24	75	37	25	27	0.42	90
17	9	10	0.26	75	38	27	28	0.60	55
18	10	20	0.13	60	39	27	29	0.45	50
19	10	17	0.20	60	40	27	30	0.20	50
20	10	21	0.20	60	41	29	30	0.30	55
21	10	22	0.19	65	-	-	-	-	-

The results are shown in Figure 8:

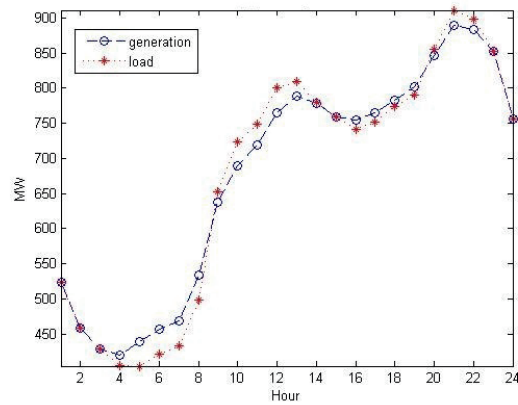


Figure 8 Load and generation curve

As one can notice that in the first, second and third hour generation is equal to the demand. Because system contains energy storages, from fourth to eighth hours generators produce more energy (demand is low and cheap generators can produce more energy to save money in the future when demand will be higher and system will need to use more expensive generators). Saved energy is discharged from storages during tenth, eleventh, twelfth and thirteenth hour. During four hours before daily peak, generators also produce more energy and then during twenty-first, twenty-second and twenty-third hour storages are discharged again.

Line 1 (between bus 1 and 2) is congested during the whole day and line 2 (between bus 1 and 3) is congested from thirteenth to twenty-fourth hour. When congestion occurs, there are differences between nodal prices and generators are redispatched from optimal production to satisfy line thermal limit. Line shadow price for line 1 and line 2 are shown in Table XXVIII and Table XXIX:

Table XXVIII Shadow prices for line 1

Hour	€/MW	Hour	€/MW	Hour	€/MW
1	3.62	9	5.15	17	4.94
2	2.91	10	5.67	18	4.89
3	2.66	11	5.92	19	4.84
4	2.62	12	6.46	20	4.95
5	2.51	13	6.32	21	4.61
6	2.61	14	5.68	22	4.71
7	2.70	15	5.89	23	4.28
8	3.50	16	5.19	24	5.94

Table XXVIII Shadow prices for line 2

Hour	€/MW	Hour	€/MW
13	1.31	19	5.79
14	2.52	20	7.64
15	1.02	21	10.52

16	2.64	22	9.94
17	3.82	23	9.64
18	4.80	24	0.84

Charging and discharging at bus 3 is shown in Figure 9 and state of charge during the day in Figure 10:

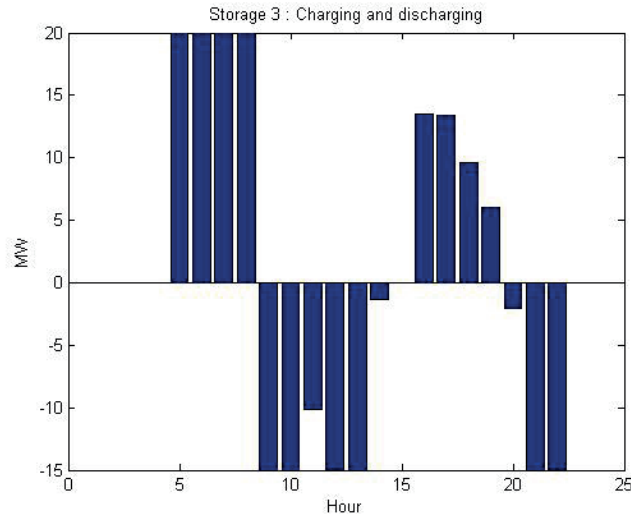


Figure 9 Charging and discharging – Storage 3

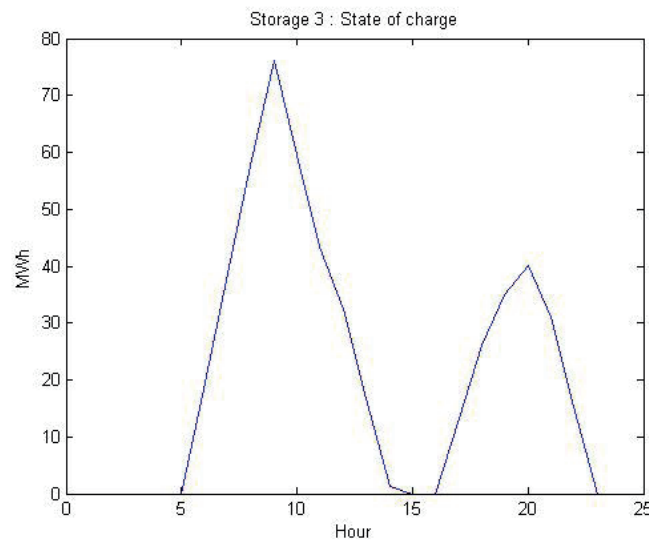


Figure 10 State of charge – Storage 3

Energy capacity is 100 MWh and, as we can see in Figure 10, storage is never full. Storage is charging in fifth, sixth, seventh and eighth hour at maximum rate and is discharging in ninth, tenth, twelfth, thirteenth, twenty-first and twenty-second hour at maximum rate. Owner of the power capacity right will collect for each hour price shown in Table XXX times reserved MW of charging/discharging capacity.

Table XXIX Price for power capacity right – Storage 3

Hour	5	6	7	8	9	10	12	13	21	22
PCR (€/MW)	0.0089	0.2627	0.5593	0.2393	0.0494	0.1271	0.0098	0.1756	0.7442	0.0053

Charging and discharging at the bus 30 is shown in Figure 11 and state of charge during the day in Figure 12:

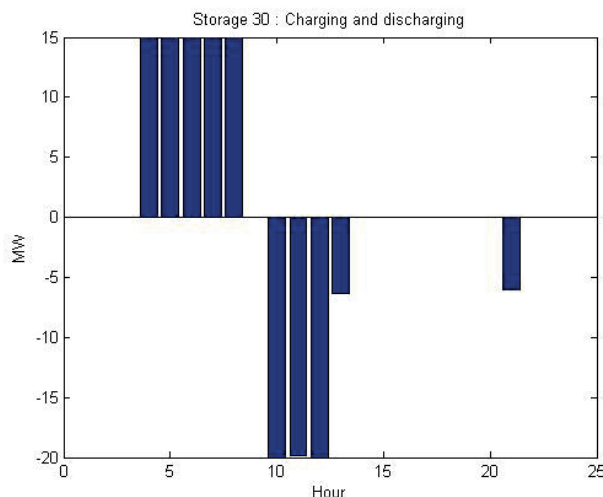


Figure 11 Charging and discharging – Storage 30

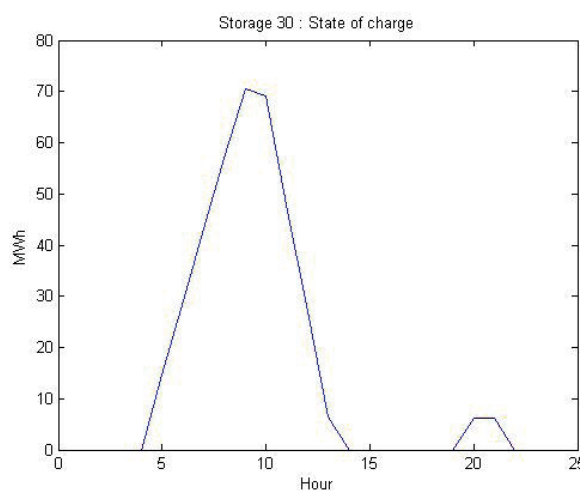


Figure 12 State of charge – Storage 30

Storage is charging at maximum rate during the fourth, fifth, sixth, seventh and eighth hour and is discharging at the maximum rate during tenth and twelfth hour. Owner of a power capacity right will collect revenue as shown in Table XXXI times reserved amount of MW:

Table XXXI Price for power capacity right – Storage 30

Hour	4	5	6	7	8	10	12
PCR (€/MW)	0.1597	0.4099	0.6638	0.9625	0.5375	0.1063	0.0734

4.4. Auction for Power Capacity Rights

The objective of the auction is to maximize profit. Bidders submit their offers for charging and discharging capacity they want to reserve and the price they are willing to pay. If charging and discharging for each hour are at the lower level than rate limits, bidders will get their maximum amount of preferred right and do not need to pay for those rights because there are still more rights that can be awarded. Maximum desirable capacity for charging has a positive sign and for discharging a negative sign.

Energy storage is empty in the beginning and it is characterized by energy capacity, charge and discharge rate limits and energy leakage coefficient. There is no charge and discharge loss coefficients. As charging and discharging have opposite sign and they are simultaneously feasible, more rights can be awarded. Dual variables are related to charge and discharge rate limits. For the purpose of this model, it is assumed that charging and discharging is the same variable. If the variable is positive, the storage is charging, and if it is negative, storage is discharging.

4.5. Auction example

Storage energy capacity is 60 MWh, energy leakage coefficient is 0.9, charge and discharge rate limits are 15 MW and -10 MW. Storage is operating for four hours.

There are three bidders (a_1 , a_2 , and a_3) competing for charging capacity and two bidders for discharging capacity (b_1 and b_2). Their prices and desirable power capacity are shown in Table XXXII and Table XXXIII:

Table XXXII Bidding prices (€/MW)

Bidder	a_1	a_2	a_3	b_1	b_2
Hour 1	0	6	7	5	8
Hour2	8	5	3	4	2
Hour 3	0	0	5	5	15
Hour 4	4	6	2	10	5

Table XXXIII Desirable charging and discharging capacity (MW)

Bidder	a_1	a_2	a_3	b_1	b_2
Hour 1	0	14	12	-7	-8
Hour2	12	10	11	-8	-5
Hour 3	0	0	8	-10	-10
Hour 4	10	12	10	-5	-10

Awarded charging and discharging capacity is shown in Table XXXIV:

Table XXXIIIIV Awarded charging and discharging capacity (MW)

Bidder	a₁	a₂	a₃	b₁	b₂
Hour 1	0	14	12	-7	-8
Hour2	12	10	6	-8	-5
Hour 3	0	0	8	-8	-10
Hour 4	10	12	8	-5	-10

As one can see, bidder a_3 did not get desirable amount of charging capacity in second and fourth hour because storage is charging at the rate limit 15 MW (red color in the Table XXXIV shows the differences between desirable and awarded amount of MW). Shadow price for second and fourth hour is 3 €/MW and 2 €/MW. In the third hour storage is discharging at rate limit -10 MW and discharging shadow price for third hour is 5 €/MW. In the first hour, storage is not congested and every bidder gets desirable capacity without paying for that right (there are still more rights that can be awarded). Table XXXV shows how much each bidder has to pay for awarded capacity rights:

Table XXXIV Payment (€)

Bidder	a₁	a₂	a₃	b₁	b₂
Hour 1	0	0	0	0	0
Hour2	36	30	18	24	15
Hour 3	0	0	40	40	50
Hour 4	20	24	16	10	20

5. CONCLUSION

When transmission lines are congested, differences in LMPs occur. Low-cost generators power is reduced (or are shut down) and high-cost generators are redispatched. Generators sell energy at one price and load buys at the different one. Payments which ISO collects from loads exceed payment to generators and the surplus ISO collects during congestion can be awarded to the market participants to hedge against congestion charges and price volatility. FTRs are financial instrument that enables market participants to avoid risk in price differences. Market players can require FTRs in the auction process (annual, monthly or daily auction) or via bilateral contracts. Once FTRs are awarded in auction, they can easily be traded in different auctions or bilateral contracts. Market players can require FTRs to avoid paying extra cost due to congestion or make profit by reserving some amount of MW (because FTRs are based on reserved amount of MW, not actual MW delivered). This means that everyone can participate in FTRs auction or bilateral contracts to increase their profit. For have more FTRs awarded,

market participants need to act strategically. This means they will change their bidding prices or even submit offers for other flowgates or point-to-point rights.

Energy storage are sources of flexibility and reliability, they enable lower operating cost in the power system and decrease generation during daily's peaks. Storages usually profit through intertemporal arbitrage (load shifting and peak shaving). Storages can be compared to transmission lines. Transmission lines move power spatially and storages move power forward in time. When storages are congested, owners of power and energy capacity rights (together known as financial storage rights) collect money from ISO. Passive storages profit through sales of rights.

6. REFERENCES

- [1] Hogan, W. W. 2000 Flowgate Rights and Wrongs, Center for Business and Government, JFK School of Government, Harvard University, 2000
- [2] Pavić I., Capuder T., Kuzle I. Value of flexible electric vehicles in providing spinning reserve services, *Applied Energy* 157, Pages 60-74
- [3] Zidar M., P. S. Georgilakis, N. D. Hatziaargyriou, Capuder T. Škrelc D. Review of energy storage allocation in power distribution networks: applications, methods and future research, *IET Generation, Transmission and Distribution*, 2016, Pages 645.-652.
- [4] Pandžić H., Wang Y., Dvorkin Y., Qiu T., Kirschen DS, Near-optimal method for siting and sizing of distributed storage in a transmission network, *IEEE Transactions on Power Systems* 30 (5), 2288-2300
- [5] Mohrhauer T., Comparison of Nodal, Zonal and Hybrid Market Structures with Respect to Operating Cost and Redispatch Volumes, *EEH – Power Systems Laboratory Swiss Federal Institute of Technology (ETH) Zurich*, 2016
- [6] Hogan, W. Contracts Network for Electrical Power Transmission. *Journal of Regulatory Economics* 4. January 1992, p.211-242
- [7] Locational Marginal Pricing (LMP): Basics of Nodal Price Calculation, CAISO Market Operations, CRR Educational Class #2, CALIFORNIA ISO
- [8] California ISO, Locational Marginal Pricing (LMP): Basics of Nodal Price Calculation (CRR Educational Class #2, CAISO Market Operations), ppt presentation
- [9] Frank Delea, Jack Casazza, *Understanding Electric Power Systems: An Overview of the Technology, the Marketplace, and Government Regulation*, March 2010, Wiley-IEEE Press

- [10] Xingwang Ma, David I. Sun, Andy Ott. Implementation of the PJM Financial Transmission Rights Auction Market System. Power Engineering Society Summer Meeting, 2002 IEEE (Volume 3). 25 July 2002. Pages 1360 – 1365
- [11] V. Sarkar, S. A. Khaparde. Introduction to Loss-Hedging Financial Transmission Rights. IEEE Transactions on Power Systems, vol. 24, no. 2, May 2009. Pages 621-630
- [12] Xingwang Ma, David I. Sun, and Andy Ott. Implementation of the PJM Financial Transmission Rights Auction Market System. Power Engineering Society Summer Meeting, 2002 IEEE (Volume: 3). 25-25 July 2002. Chicago, IL, USA. Pages: 1360-1365
- [13] Joshua A. Taylor. Financial Storage Rights. IEEE TRANSACTIONS ON POWER SYSTEMS, VOL. 30, NO. 2, MARCH 2015. Pages 997.-1005.
- [14] Richard P. O'Neill, Udi Helman, Benjamin F. Hobbs, William R. Stewart, Jr., and Michael H. Rothkopf. A Joint Energy And Transmission Rights Auction: Proposal and Properties. IEEE Transactions on Power Systems. November 2002. Pages: 1058-1067
- [15] Allen J. Wood, Bruce F. Wollenberg, Gerald B. Sheble. Power Generation, Operation and Control. Third edition. IEEE, Published by John Wiley & Sons, Inc., Hoboken, New Jersey, 2014.
- [16] Tom Brijs, Daniel Huppmann, Sauleh Siddiqui, Ronnie Belmans. Auction-Based Allocation of Shared Electricity Storage Resources through Physical Storage Rights. Conference in Berlin, 2016. Pages 1-21
- [17] Hamed Mohsenian-Rad. Coordinated Price-Maker Operation of Large Energy Storage Units in Nodal Energy Markets. IEEE Transactions on Power Systems, vol.31.no. 1, January 2016, page 791

BORNA POŠTA

borna.posta@fer.hr

SINIŠA ŠADEK

sinisa.sadek@fer.hr

**University of Zagreb Faculty of Electrical Engineering
and Computing**

MATHEMATICAL MODEL OF THE NPP KRŠKO PCFV SYSTEM FOR THE RELAP5 COMPUTER CODE

SUMMARY

Containment building is the final barrier for radioactive releases from a nuclear power plant (NPP). Preserving its integrity will minimize these releases even in a case of a severe accident with core degradation and melt discharge in the containment accompanied with the pressure and temperature increase. Installation of a venting system with ability to filter radioactive fission products is a preferred way to deal with the issue in present and future NPPs, especially after the Fukushima accident. Such system, called passive containment filtered venting system (PCFV), was installed in 2013 in the NPP Krško. Thermal hydraulic model of the PCFV system which included aerosol and iodine filters, associated pipings and valves was developed for the best-estimate computer code RELAP5. Main results and discussion are presented and compared with relevant plant documentation.

Key words: Containment, NPP Krško, PCFV system, RELAP5 code

1. INTRODUCTION

Upgrades of existing safety systems and installation of new systems are the most important actions in strengthening safety of nuclear installations and their ability to withstand accident conditions. Containment building represents the last physical barrier in the defence in depth concept for a nuclear power plant (NPP) because it prevents radioactive releases to the environment. Pressure increase caused by decay heat losses in the containment atmosphere and supported by the accumulation of incondensable gases produced during the molten corium concrete interaction may challenge the integrity of the containment wall. A containment filtered venting system based on the dry filter method (DFM) enables the plant to effectively mitigate the consequences of a severe accident by reducing the pressure and the level of fission products releases to the environment during the venting process. This system provides high decontamination factors for aerosols such as caesium iodide and caesium hydroxide and for both elemental and organic iodine. The system can operate in a fully passive manner and does not require other support functions like cooling or electricity and is therefore named as passive containment filtered venting (PCFV) system.

Following the lessons learned from the accident at the nuclear power plant Fukushima in Japan and according to the Slovenian Nuclear Safety Administration (SNSA) Decree No.: 3570-11/2011/7 on September 1, 2011 [1], the NPP Krško (NEK) decided to take the necessary steps for upgrade of safety measures to prevent severe accidents and to improve the means to successfully mitigate their consequences. Consequently, one of the first modifications that NEK implemented during the outage 2013 is the installation of the PCFV system. The system is based on the dry filter method and designed to be used in case of severe accident conditions involving core relocation from the pressure vessel. The resulting pressurizing gas-vapour mixture in the containment can be discharged through the PCFV to the environment. This pressure relief is used to prevent the failure of the containment as a result of slow containment pressurization to levels above the containment vessel design pressure. The filter system protects the environment and surrounding population from airborne radioactive aerosols containing caesium which can enter the food chain and gaseous radioactive iodine and its organic compounds which can accumulate in the human thyroid.

The system operation was simulated using the system code RELAP5. RELAP5 is a state-of-the-art thermal hydraulic code which has a broad verification basis and is able to simulate the complete venting process for the whole range of design conditions and the different operation modes. An explicit model was developed based on NEK isometric drawings [2] and component design data. Since the system is needed for beyond design basis accident situations, the verification analysis is based on best-estimate assumptions. The steady state calculation was performed to verify the nodalization by comparing the results with the design operating parameters (pressure, temperature, gas velocity). The transient calculation, in the absence of the measured data, was run with the boundary conditions extracted from the calculations performed with the code MELCOR in

scope of the supporting calculations for the plant reported in relevant documents [3] and papers [4], [5]. The knowledge gained in this analysis will be later used to develop a model for the integral plant simulation with explicit models of all power plant systems, including the model of the PCFV system.

2. PCFV SYSTEM DESCRIPTION AND MATHEMATICAL MODEL

2.1 PCFV system outline

The passive containment filtered venting system, a system specially designed for light water reactor NPPs to work without external power supply, is used to filter radioactive aerosols, gaseous iodine, iodine organic compounds and to control the containment pressure.

The PCFV system consists of aerosol filters, the iodine filter, the rupture disc, valves, expansion orifices, instrumentation and associated piping, Figure 1. The venting gas first passes aerosol filter modules, leaves the containment via piping through a containment penetration, passes the iodine filter and discharges to the environment through a stack.



Figure 1. PCFV system layout, taken from [6]

Aerosol filters (five units on the right hand side in Figure 1) remove solid particles and aerosols from the vented gases by mechanical filtering using a metal fiber filter. They are connected with piping, which leads the vent stream out of the containment through the containment penetration and then splits into a passive and an active actuation line. The passive actuation of the system will occur once the containment pressure exceeds the rupture disk burst pressure of 0.6 MPa. The vented gases will then flow through two normally-opened isolation valves and the pressure relief valve. The pressure relief valve isolates the passive actuation line at low containment pressure in order to prevent too low pressure conditions inside the containment. The valve maintains the pressure inside the containment between 0.41 MPa and 0.49 MPa. The active actuation of the system can be achieved through the opening of the two normally closed isolation valves, either manually with the remote handwheels or from a control room with motor actuators. In the analysis, only the passive line with the rupture disc and the relief valve was simulated.

Before entering the iodine filter, gases flow through an orifice which controls the mass flow and maximum humidity of the vented gas stream. In the filter beds, the gaseous radioactive iodine and its organic compounds are removed through chemical sorption with silver as an active material with the designed filter efficiency.

In addition, nitrogen is used for long term storage and inerting of the zeolite filter material of the iodine filter. Also, injection of nitrogen prevents too low pressure conditions due to steam condensation when venting is stopped and the system cools down. Nitrogen is provided by a separate nitrogen supply system connected to system piping downstream of the actuation lines.

2.2 RELAP5 model and nodalization

The code version used in the calculation was RELAP5/MOD3.3 [7]. The nodalization scheme of the PCFV system is shown in Figure 2. All major components which are required for the filtered venting functions of the PCFV have been considered and were implemented in the model. The model consists of 160 control volumes, 159 junctions and 154 heat structures with 924 mesh points. A PCFV system sketch with piping dimensions is shown in Figure 3 and its RELAP5 representation with the main control volume (CV) data is presented in Table I.

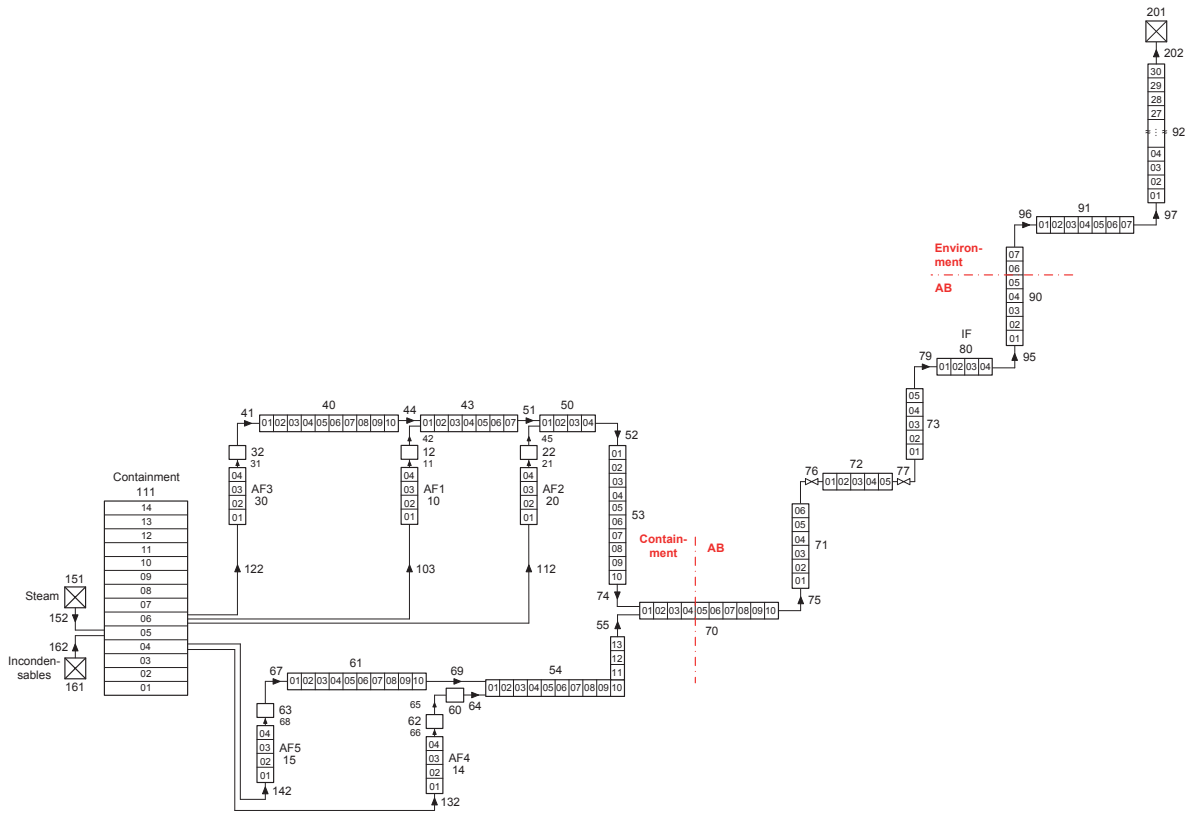


Figure 2. RELAP5 nodalization of the PCFV system

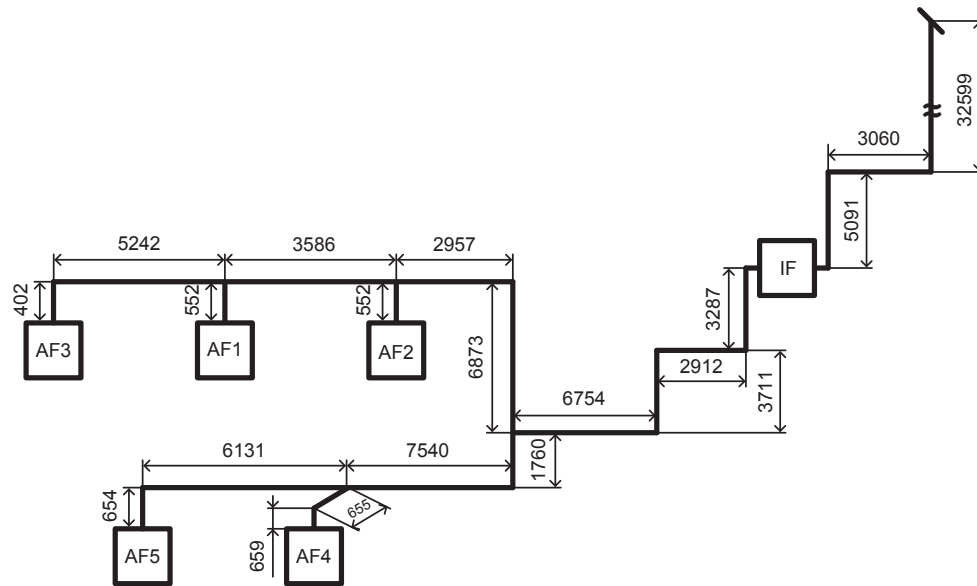


Figure 3. PCFV system piping outline

Table I. Description of RELAP5 control volumes

Control volume	Segments	Length [m]	Flow area [m ²]	Hydraulic diameter [m]	Vertical angle
111	14	61.46	650	14.4	90°
AF1-10	4	2.42	2.2149	1.484	90°
AF2-20	4	2.42	2.2149	1.484	90°
AF3-30	4	2.42	2.2149	1.484	90°
AF4-14	4	2.42	1.5356	1.2	90°
AF5-15	4	2.42	2.2149	1.484	90°
12	1	0.552	0.032	0.2032	90°
22	1	0.552	0.032	0.2032	90°
32	1	0.402	0.01824	0.1524	90°
40	10	5.242	0.01824	0.1524	0°
43	7	3.586	0.032	0.2032	0°
50	4	2.957	0.05	0.254	0°
53	10	6.873	0.05	0.254	-90°
62	1	0.659	0.032	0.2032	90°
63	1	0.654	0.032	0.2032	90°
60	1	0.655	0.032	0.2032	0°
61	10	6.131	0.01824	0.1524	0°
54	13	9.3	0.032	0.2032	0°/90°
70	10	6.754	0.05	0.254	0°
71	6	3.711	0.05	0.254	90°
72	5	2.912	0.05	0.254	0°
73	5	3.287	0.1	0.356	90°
IF-80	4	1.6	19.5	0.27	0°
90	7	5.091	0.29	0.6096	90°
91	7	3.06	0.29	0.6096	0°
92	30	32.599	0.29	0.6096	90°

Control volumes 10, 20, 30, 14 and 15 represent aerosol filters 1-5, respectively. The iodine filter is modelled with CV 80. Filters' flow areas, hydraulic diameters and friction factors were adapted to obtain correct steady state gas velocities. All other control volumes represent PCFV piping. Pressure loss coefficients have been modelled to account for elbows and branches. Wall roughness is set generally to 10^{-6} m. The volumes are nodalized in such way that the node length is approximately 0.5 m to accurately track the gas composition as well as to support computation of pressure wave loads. The general Courant rule that the minimal time step applied corresponds with flow velocity and the length of the nodes has been respected.

The rupture disc is modelled as a trip valve component 76 which opens when the containment pressure reaches 0.6 MPa. The relief valve (component 77) is also modelled as a trip valve but with pressure hysteresis behaviour. The valve needs to

keep the pressure inside the containment between 0.41 MPa, closing pressure, and 0.49 MPa, opening pressure, after the failure of the rupture disc. Thus, valve operation is characterized by two setpoint pressures: an opening pressure and a “reseat” (closing) pressure. As system pressure is increased, the valve opens at the opening pressure and remains open until the system pressure falls below the reseal pressure. This process therefore involves hysteresis; operation of the valve is not only dependent on the pressure but also on whether the valve is currently open or closed. This behaviour was modelled by a simple script:

```
20605020 p 111010000 gt null 0 4.1e5 n
20605030 p 111010000 gt null 0 4.9e5 n
20610010 502 and 1002 n
20610020 503 or 1001 n
```

First, variable trips 502 and 503 are defined to compare the current system pressure against the two setpoint pressures. Control volume 111 represents containment and 'p' stands for pressure. Next, logical trips 1001 and 1002 are used to combine the information from the variable trips with the information on the current valve status into a trip that will control the valve. Trip 1001 is true only if the valve was open on the previous time step and the current pressure is above the closing setpoint pressure. Trip 1002 is true only if the pressure exceeds the opening setpoint pressure or the valve was open on the previous time step and the current pressure is above the closing setpoint pressure. Therefore, the status of trip 1002 is used to control the model valve position: opened when the trip is true and closed when the trip is false.

The orifice at the inlet in the iodine filter used to control operating conditions in the filter is modelled as a single junction component with an abrupt area change option.

The heat losses to the environment through the pipe walls, aerosol and iodine filter internal and housing structures were modelled as heat structures. The conduction through these structures was assumed to be one-dimensional and a stainless steel heat conductivity and volumetric heat capacity data were used. Heat convection from the hot gases to the walls was calculated internally by the code and for the heat transfer to the environment three sets of data were used, according to [8], depending on the outside conditions:

- containment atmosphere: heat transfer coefficient (HTC) 20 W/m²K, temperature 443 K,
- auxiliary building atmosphere: HTC 10 W/m²K, temperature 353 K,
- outside air: HTC 20 W/m²K, temperature 318 K.

3. ANALYSIS RESULTS

3.1 Steady state calculation

The input model was verified by checking its output results and comparing them with design parameters reported in [8]. Boundary conditions for the steady state were modelled using the time-dependent volume 151 and time-dependent junction 152 components. The working fluid was pure steam, as specified in the afore-mentioned document, at pressure 0.6 MPa and temperature 443 K with a mass flow rate 7 kg/s. The outlet conditions were set to atmospheric pressure 101.325 kPa and temperature 293 K (time-dependent volume 201).

The main results of the steady state analysis are listed below:

- The designed relief capacity of 7 kg/s of pure steam at 0.6 MPa in the containment is reached (Figure 4).
- The average gas velocity in the aerosol filters does not exceed the limit of 0.22 m/s, while in the zeolite beds of the iodine filter steam velocity is less than 0.5 m/s (Figure 5).
- The maximum pressure in the piping system is below 0.65 MPa from downstream of aerosol filters to the main orifice and below 0.12 MPa downstream of iodine filter inlet orifices (Figure 6).
- The average temperature of the piping walls is less than 523 K in aerosol filters and 493 K in the iodine filter (Figure 7).
- No condensate accumulates in the piping during steady state downstream of the main orifice (Figure 8).

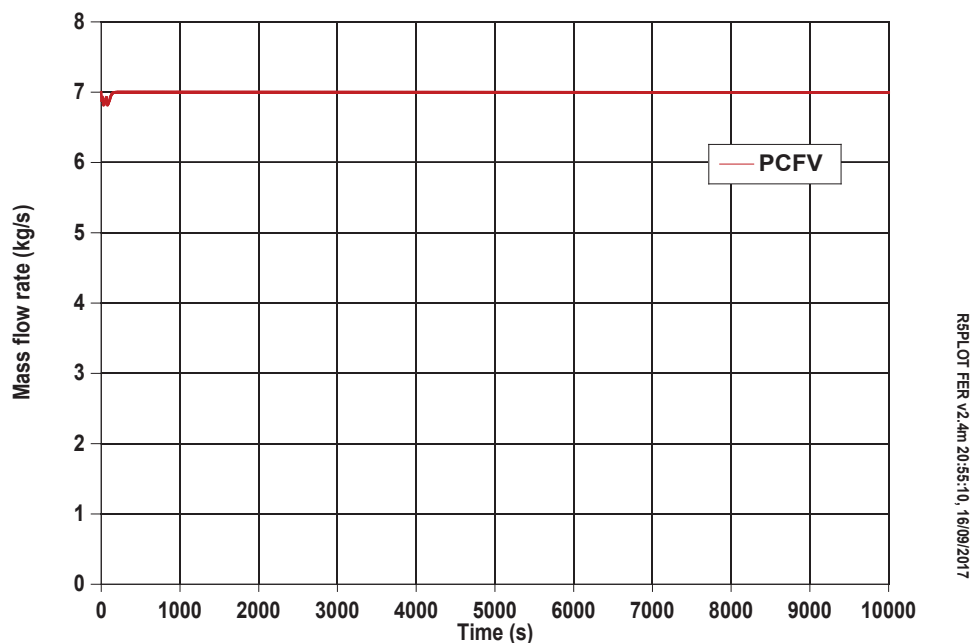
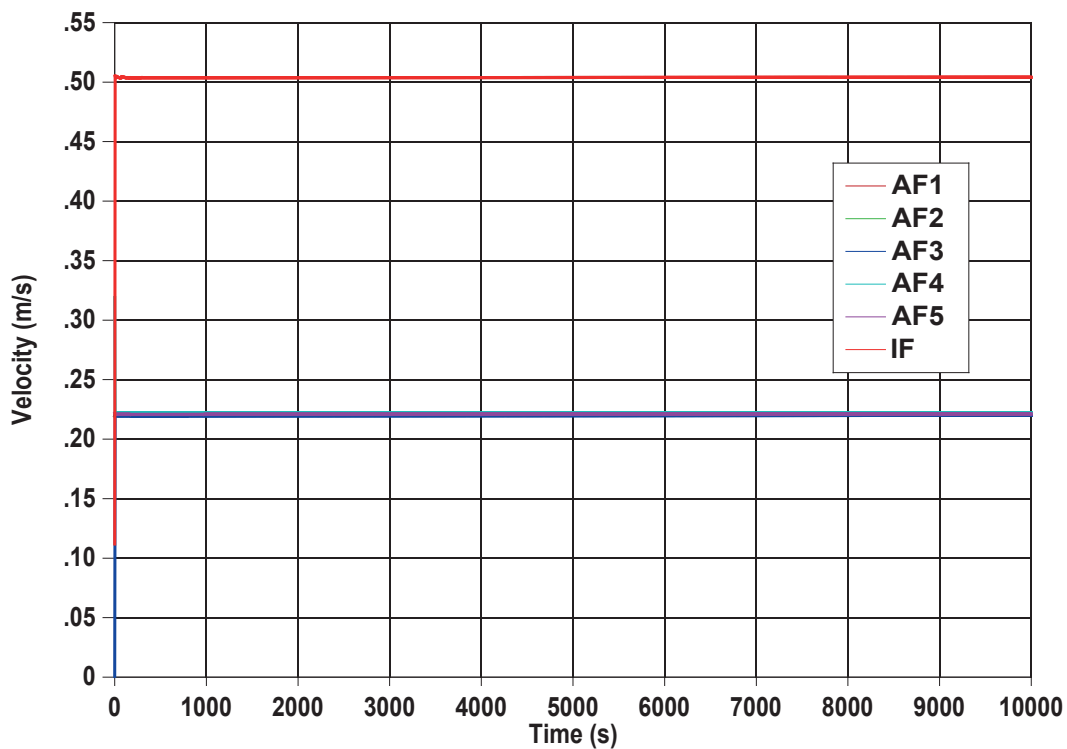
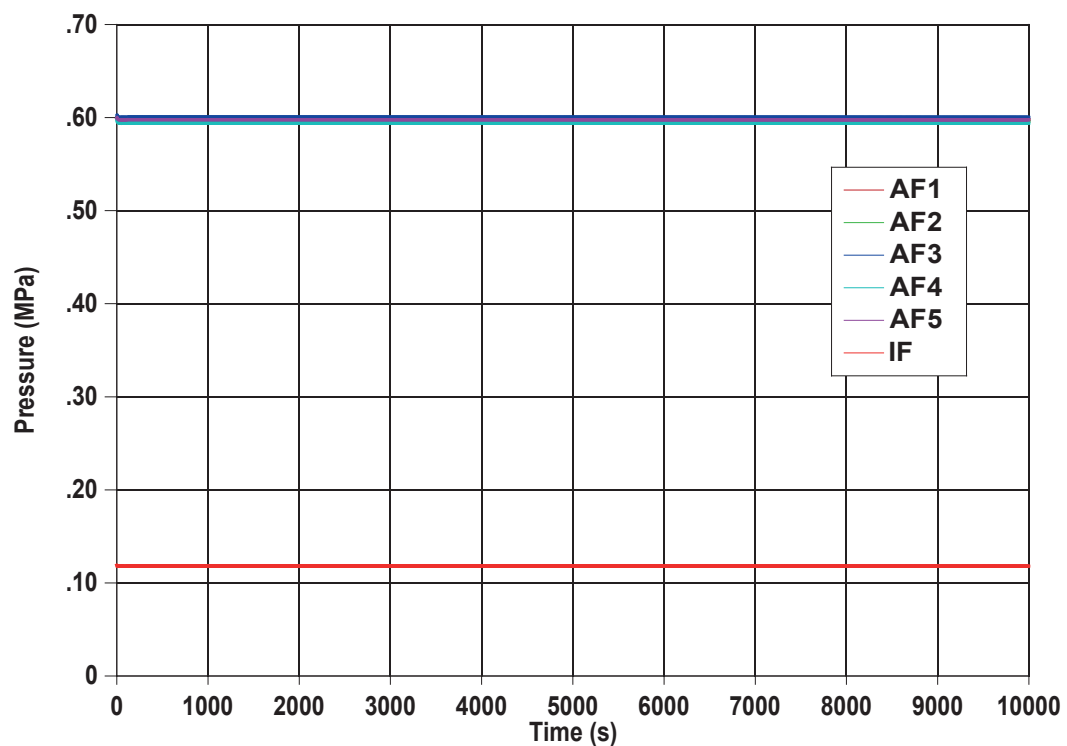


Figure 4. Steam mass flow rate through the PCFV system



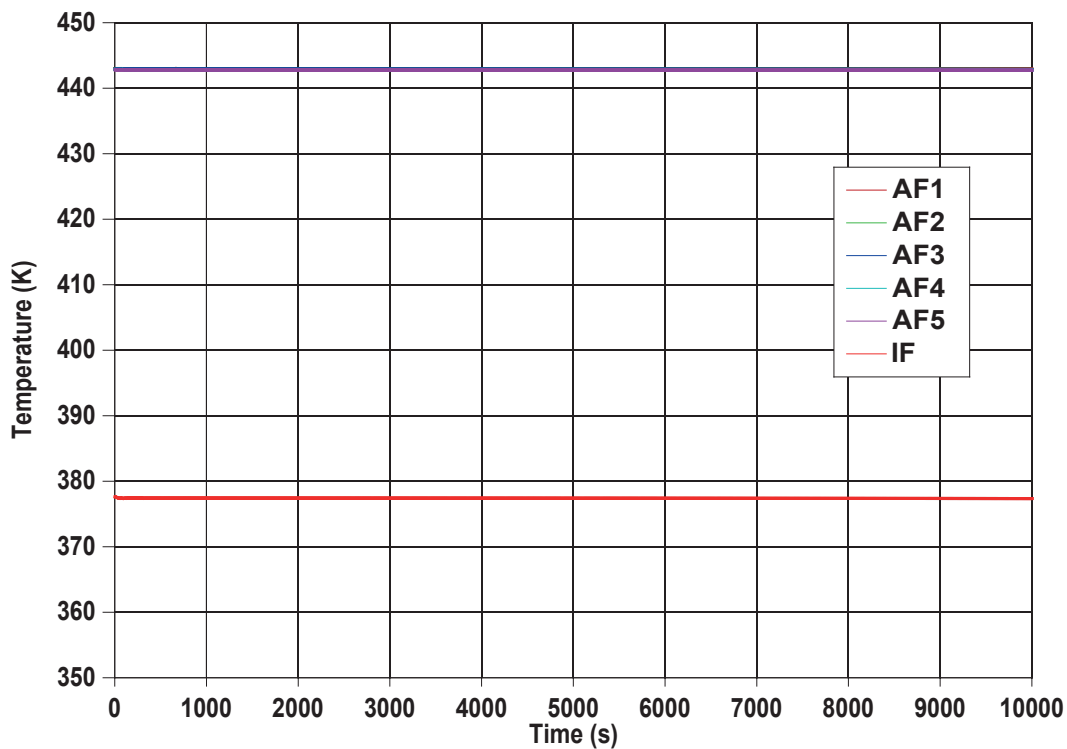
RSPLOT FER v2.4m 21:07:53, 16/09/2017

Figure 5. Gas velocities in aerosol and iodine filters



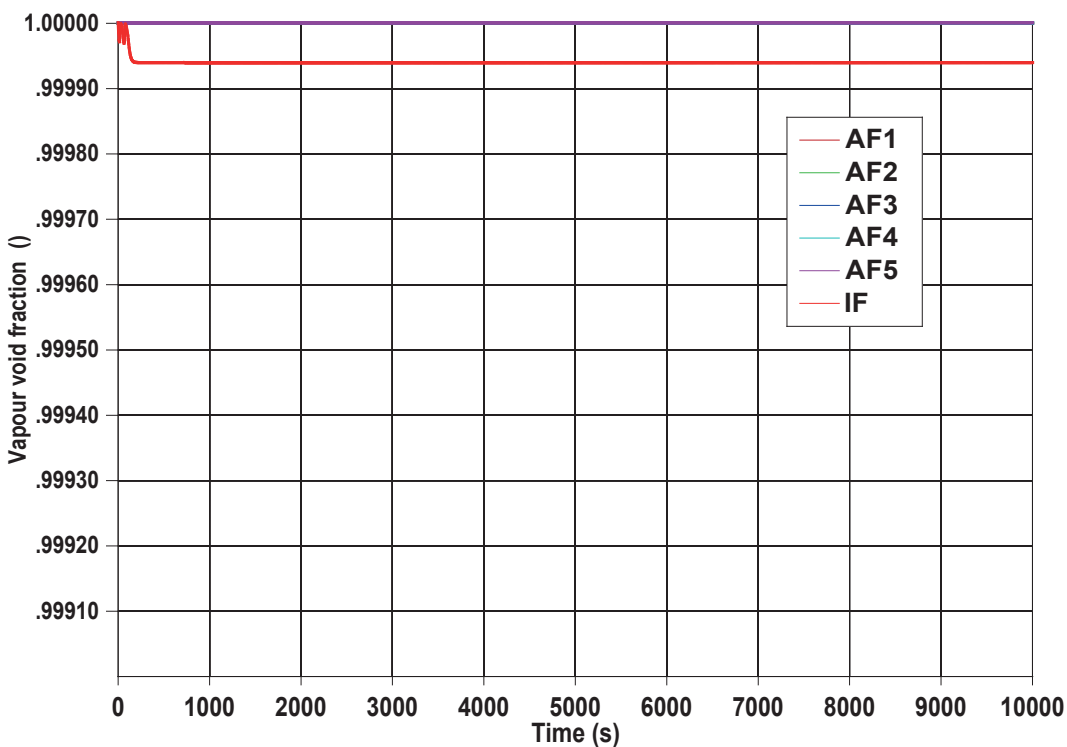
RSPLOT FER v2.4m 21:00:01, 16/09/2017

Figure 6. Gas pressures in aerosol and iodine filters



RSPLOT FER v2.4m 21:03:24, 16/09/2017

Figure 7. Gas temperatures in aerosol and iodine filters



RSPLOT FER v2.4m 18:51:03, 19/09/2017

Figure 8. Steam void fraction in aerosol and iodine filters

3.2 Transient calculation

In the absence of measured data, the transient calculation was performed with boundary conditions provided by the MELCOR run [3]. The scenario was a station blackout with core damage and the release of corium in the containment. The molten corium concrete interaction took place in the cavity compartment resulting with production of steam and incondensable gases, hydrogen, carbon dioxide and carbon monoxide. The majority of stem was released from the primary system through the breaks formed at the reactor coolant pumps after degradation of pump seals as a consequence of the loss of electrical power. The steam and incondensable gases mass flow rates were taken from the MELCOR calculation and used as input boundary conditions for this analysis (Figure 9). Initially, the steam flow rate was low to account for containment environmental conditions and the PCFV system that was filled with air. The steam fraction increased rapidly afterwards following the coolant release out of the primary system.

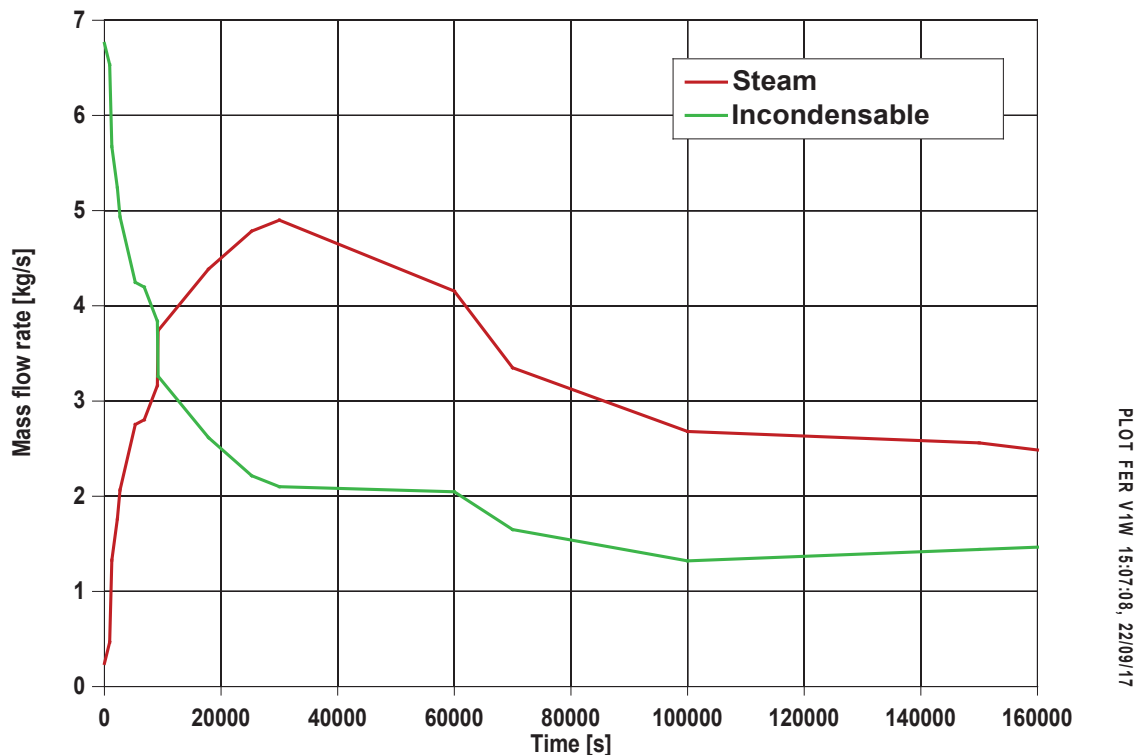


Figure 9. Steam and incondensable gases mass flow rates at the PCFV system inlet

Discharge of reactor coolant in the containment is responsible for the initial containment pressure increase. When the containment dome pressure reaches 0.6 MPa (the first pressure peak), the rupture disc in the PCFV line will break causing containment gases to be released in the environment. The pressure drops fast to 0.41 MPa prompting the relief valve in the PCFV line to close. Following the valve closure, the pressure rises once again. After reaching 0.49 MPa, the relief valve opens and again some containment inventory is released. Later, the pressure

continues to cycle between 0.41 MPa and 0.49 MPa by the operation of the PCFV pressure relief valve, Figure 10 (MELCOR result is shown in the same figure for the easier comparison). That kind of valve behaviour is important for preserving containment integrity and minimizing radioactive releases.

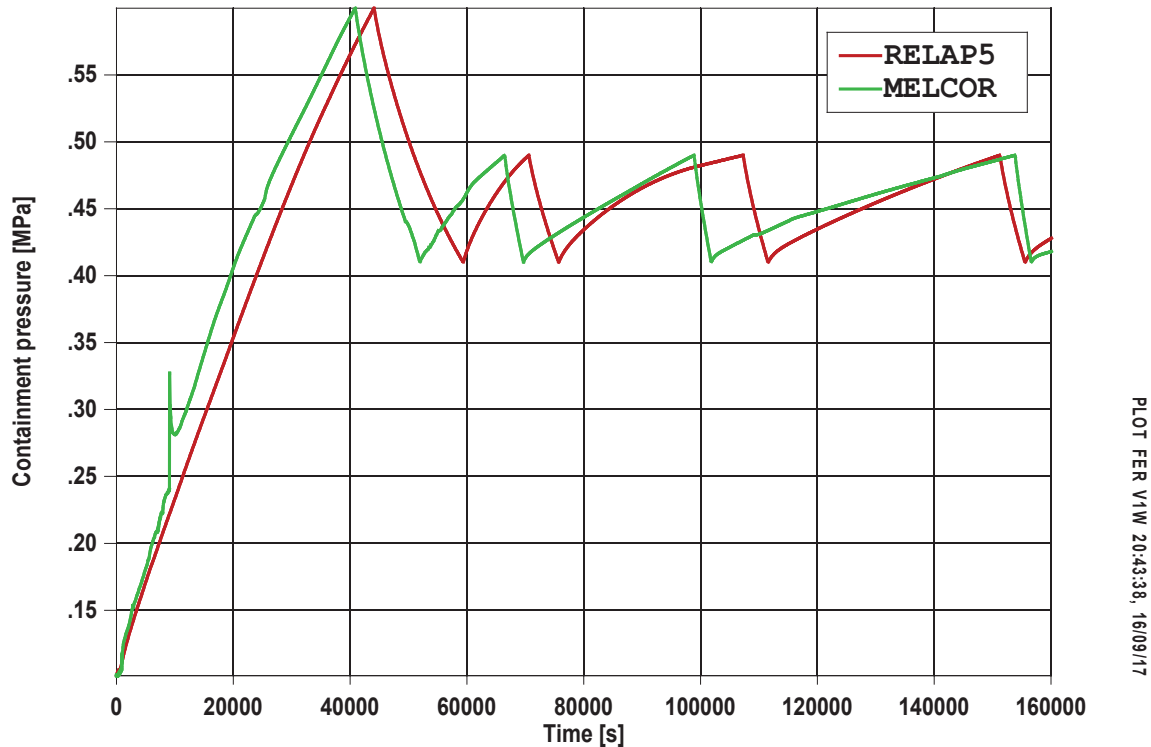


Figure 10. Containment upper plenum pressure

The big concern is the possibility of hydrogen ignition in the system components during the venting phase. There are two mechanisms of hydrogen production:

- Oxidation of zirconium fuel cladding alloy with steam at temperatures above 1200 K. Zirconium is transformed into zirconium dioxide in form of a ceramic oxide shell on the fuel rods, while hydrogen is released as another product of that reaction.
- Molten corium concrete interaction during which steam released from the concrete reacts with steel reinforcement iron. Here, iron oxide and hydrogen are the reaction products.

Hydrogen flammability depends on composition of air-steam-hydrogen mixture. The minimum mole fraction of hydrogen that could lead to its ignition is 4-5 % [9]. The maximum fraction calculated by the RELAP5 was less than 3% (Figure 11) and, thus, no ignition could take place. The figure indicates the rise in hydrogen concentration in the late venting phase but that is irrelevant since no more oxygen is released from the containment and, due to the high back-pressure, no oxygen could also enter in the system from the outside. The oxygen in the containment was consumed earlier by the operation of the hydrogen autocatalytic recombiners which

induce the reaction between oxygen and hydrogen until all oxygen has reacted. An integral analysis of the whole NEK containment was performed with three system codes: ASTEC, MELCOR and MAAP with emphasis on the containment thermal hydraulic behaviour when the PCFV system is in the operation [5]. Figure 12 shows the gas mixture composition throughout the transient and it is visible that conditions for possible hydrogen ignitions were not achieved in any time period during the calculation.

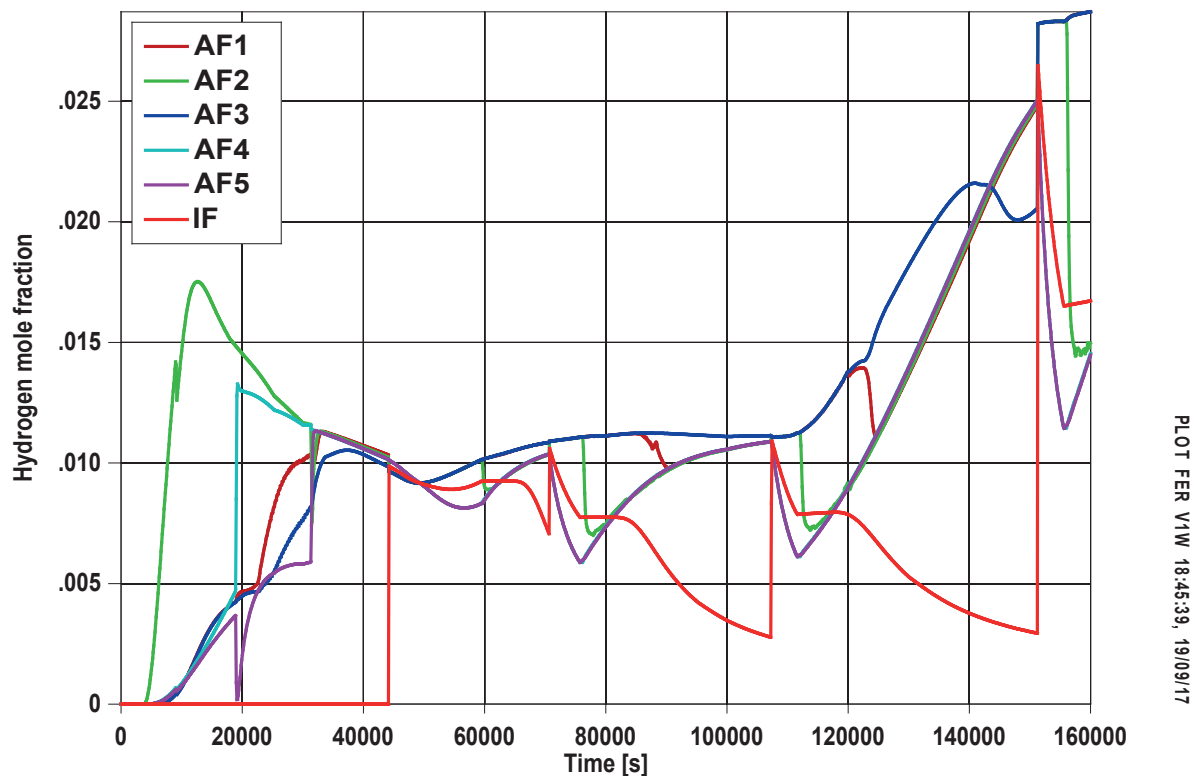


Figure 11. Hydrogen concentration in aerosol and iodine filters

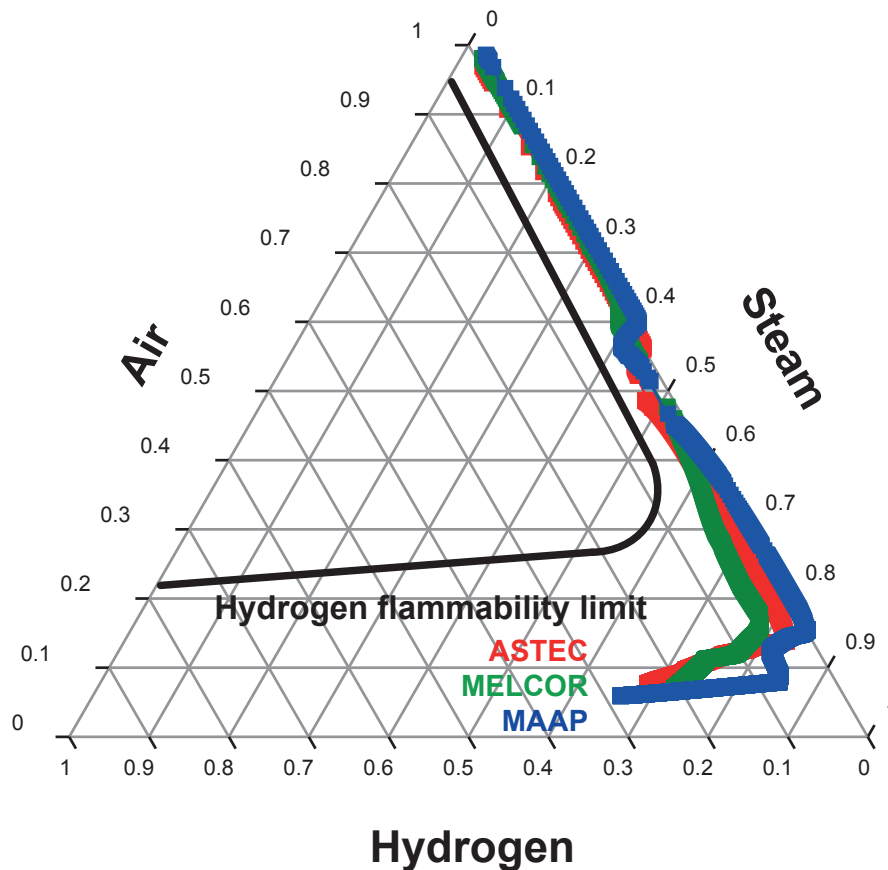


Figure 12. Containment conditions as calculated by 3 codes represented in ternary diagram of air-steam-hydrogen mixture

4. CONCLUSIONS

A detailed explicit model of the NPP Krško PCFV system was developed for the best-estimate thermal hydraulic code RELAP5. The best-practice code options in constructing the nodalization were adopted. The model was tested on the steady state and transient levels.

The steady state calculation was performed to verify the model by comparing the results with the system design parameters: gas mass flow rates and velocities, system pressure and heat structure temperatures. Pressure loss coefficients and hydraulic diameters for equipment with complex geometry, such as aerosol and iodine filters, were fine-tuned to obtain satisfactory steady state behaviour. The gas composition and boundary conditions were prepared to be in accordance with the plant documentation.

Transient calculation scenario was a station blackout with the complete loss of the electrical power. The simulation was used to check the system behaviour in accidental conditions, primarily the relief valve operation in keeping the pressure between prescribed setpoints: 0.41 MPa and 0.49 MPa. Results were compared with

a similar calculation conducted with the code MELCOR because this was the only relevant plant analysis with the PCFV system in operation. They showed similar trends in pressure evolution during several relief valve opening/closing cycles. The conclusion is that the RELAP5 model is qualified for safety analyses of both the steady state and transient scenarios. The last thing checked was the hydrogen concentration in the different parts of the system. The gas mixture was always below the hydrogen flammability limit and no fire danger, or explosion, exists when the PCFV system is in operation.

5. REFERENCES

- [1] SNSA Decree No. 3570-11/2011/7, “Odločba o izvedbi modernizacije varnostnih rešitev za preprečevanje težkih nesreč in blažitev njihovih posledic (SNSA Decree on Implementation of modernization of safety solutions for prevention of severe accidents and mitigation of their consequences)”, September 2011.
- [2] NPP Krško design modification package 1008-VA-L, Rev. 1, Section H: Drawings section, 2013.
- [3] S. Šadek, D. Grgić, V. Benčik, „Analysis of the NPP Krško Station Blackout Accident with PAR and PCFV Using MELCOR 1.8.6 Code“, Report No. FER-ZVNE/SA/DA-TR01/15-1, December 2015.
- [4] S. Šadek, D. Grgić, V. Benčik, „NPP Krško Station Blackout Analysis after Safety Upgrade Using MELCOR Code“, in *Proceedings of the 11th International Conference of the Croatian Nuclear Society*, Zadar, 2016, pp. 058-1 – 058-14.
- [5] S. Šadek, D. Grgić, Z. Šimić, „Application of ASTEC, MELCOR, and MAAP Computer Codes for Thermal Hydraulic Analysis of a PWR Containment Equipped with the PCFV and PAR Systems“, *Science and Technology of Nuclear Installations*, vol. 2017, pp. 8431934-1 – 8431934-16, May 2017.
- [6] D. Grgić, V. Benčik, S. Šadek, I. Bašić, “Independent Review of NPP Modifications and Safety Upgrades”, *International Journal of Contemporary Energy*, vol. 1, no. 1, pp. 41 – 51, 2015.
- [7] RELAP5/MOD3.3 Code Manuals, Vol. 1-8, NUREG/CR 5535, Rev. P3, Information Systems Laboratories, Inc., Rockville, Maryland, March 2006.
- [8] M. Frings, „Krško Passive Containment Filtered Venting System (PCFV) RELAP Design Calculation Work Report“, Westinghouse Proprietary Class 2, WENX-12-36, Rev. 1, May 2013.
- [9] Z.M. Shapiro, T.R. Moffette, “Hydrogen Flammability Data and Application to PWR Loss-of-Coolant Accident”, Technical Report No. WAPD-SC-545, Prepared for U.S. Atomic Energy Commission, 1957.

NINOSLAV HOLJEVAC

CATARINA SOARES

IGOR KUZLE

ninoslav.holjevac@fer.hr

catarina.soares@fer.hr

igor.kuzle@fer.hr

University of Zagreb Faculty of Electrical Engineering and Computing

SHORT-TERM POWER SYSTEM HOURLY LOAD FORECASTING USING ARTIFICIAL NEURAL NETWORKS

SUMMARY

Artificial neural networks (ANN) have been used for many application in various sectors. The learning property of an ANN algorithm in solving both linear and non-linear problems can be utilized and applied to different forecasting problems. In the power system operation load forecasting plays a key role in the process of operation and planning.

This paper present the development of an ANN based short-term hourly load forecasting model applied to a real data from MIBEL – Iberian power market test case. The historical data for 2012 and 2013 ware used for a Multilayer Feed Forward ANN trained by Levenberg-Marquardt algorithm. The forecasted next day 24 hourly peak loads and hourly consumptions are generated based on the stationary output of the ANN with a performance measured by Mean Squared Error (MSE) and MAPE (Mean Absolute Percentage Error). The results have shown good alignment with the actual power system data and have shown proposed method is robust in forecasting future (short-term) hourly loads/consumptions for the daily operational planning.

Key words: Artificial neural networks; Short-term load forecasting; Electric power system operation and planning;

1. INTRODUCTION

The importance of load forecasting power system planning and operation is gaining on significance with the increase of stochastic element associated with both supply and consumption side [1], [2]. The forecasts are one of the most important inputs for system analysis tools e.g. economic dispatch and short term unit commitment. The main goal of these planning techniques is to maintain the stability and efficiency of the system. The deregulation of the power system and market structures both in the USA and Europe in recent years has made short term load forecasting increasingly important [3]. In a deregulated, competitive electricity market environment, the ability to accurately forecast load in the short term is of interest to all participants in the power system.

Different forecasting techniques for short term load forecasting have been used. There are models based on Kalman filtering [4], dynamic linear and non-linear model, and optimization techniques [5]. Generally speaking two most common models are the Autoregressive Integrated Moving Average (ARIMA) models and the multiple linear regression models [6]. ARIMA based methods have shown to achieve good mean absolute percentage errors (MAPE) [7]. These methods have been in use for a number of years, however, they are not able to adapt to changes in weather conditions or other load affecting factors [8]. Furthermore, these methods rely primarily on historical data but realized load demands and consumptions do not necessarily need to resemble and be similar to future load demands (especially in recent decade) and cannot efficiently consider weather data [9].

Artificial intelligence (AI) techniques have come up as a potential load forecasting techniques such as the fuzzy-neural model, the artificial neural network (ANN) model and the genetic algorithm method and out of the AI techniques, the most widely used model of feed-forward ANN [10]. The ANN model is suitable for load forecasting due to its ability to model the nonlinear relationships between variables without making prior assumptions on the functional relationship among the variables. Artificial neural networks are able to learn and adapt to the data. Artificial neural networks learn the interdependencies between the variables and reach the conclusion based on that information [11]. They can be used as an integral part of different applications, such as secondary regulation of voltage and reactive power [12] or a potential prediction module inside of central control energy management systems [13].

One of the most important factors influencing the performance of neural networks is the choice of input variables. Input variables commonly used in short term load forecasting are hour and indicators, recent load realizations and temperature and other weather variables. The use of recent hours load is of particular interest as the load series is strongly auto-correlated. To evaluate the correlation of the current hour load with previous hours load correlation analysis is frequently performed [14]. Other commonly used approach is using Euclidean norm approach [15]. In both methods there is a possibility to discard certain hours in the past and looking only at the most recent ones

In this paper, an hour ahead load forecasting method using an ANN is proposed. The paper presents a two-layered feedforward artificial neural network for performing a short-term power system load forecast. Two different models of ANN (ANN mode 1 and ANN mode 2) were tested and their results were compared. The main difference between developed artificial neural networks models is in the inclusion of different weather data (temperature, rainfall, wind). Both models were applied to the real data set to real data from the MIBEL - Iberian power market for years 2012 and 2013. Both models use the entire load profile of the previous day. Simulation results show that ANN mode 2 gives a slightly better performance than ANN model 1 and the overall use of ANN in load forecasting is robust and precise enough.

The paper is structured as follows: after the introduction in section II describes most commonly used components of the artificial neural network. Section III describes the developed models and forecasting procedure. Section IV presents the results of the preliminary correlation studies (“time-series study”) and section V presents the ANN forecast results. Section VI concludes the paper and gives directions for potential future research work.

2. ARTIFICIAL NEURAL NETWORKS

An artificial neural network (ANN) consists of a series of interconnected systems of artificial neurons. Each neuron mimics the behaviour of a real neuron - receives data from multiple inputs, processes the data and responds with an output based on its characteristics as shown on figure below (Figure 1).

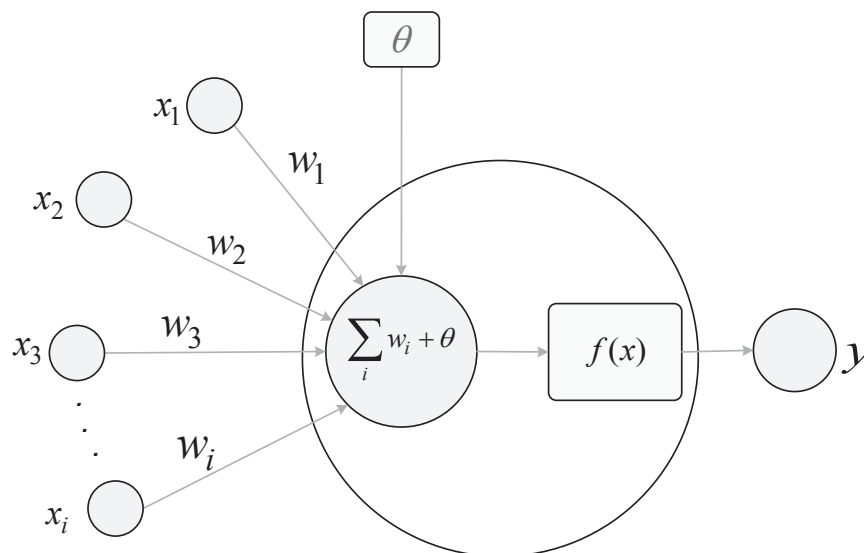


Figure 1. Basic schematic of the artificial neuron model (inputs, transfer function and output)

The output of the neuron can be given by equation (1):

$$y = f \left[\left(\sum_i w_i \cdot x_i \right) + \theta \right] \quad (1)$$

where x_i are neuron inputs, w_i are associated weights, θ represents the bias associated with the neuron and f is the transfer/activation function.

A feed-forward artificial neural network is used for the modelling of load forecasts. Basic schematic of feed-forward neural network (with the simple mark of the also commonly used back propagation) is represented on figure below (Figure 2). The choice of input variables and number of neurons in hidden layers affects the results.

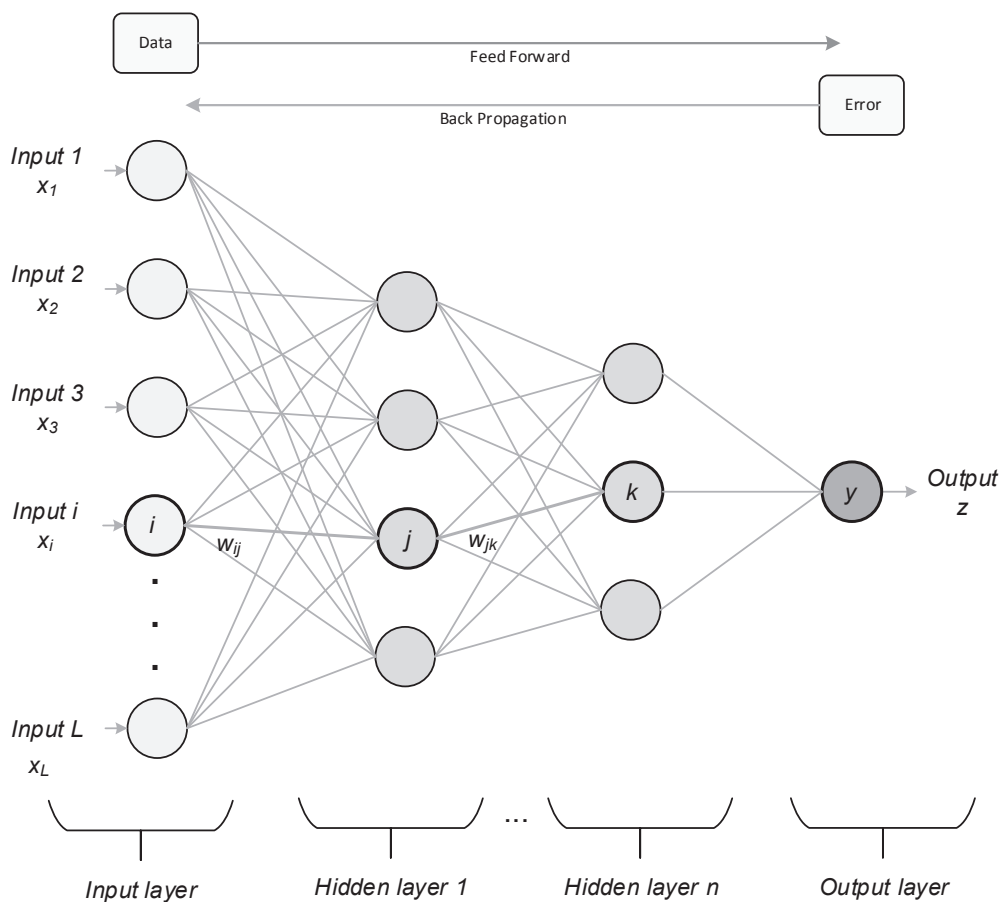


Figure 2. Artificial Neural Network (ANN) basic layout (with general multilayer structure)

Generally speaking there are three basic steps in creating (fitting) an artificial neural network model applied to load forecasting: selection of input variables, definition of neural network structure and determination of the training method.

2.1. Selection of input variables

The input variables used typically for short-term load forecasting are loads for previous hours, moment (time) indicators and weather conditions. In the process of ANN creation selection of different combination of input variables achieves different results. The performance is usually measured by means of mean squared error (MSE) given by equation (2) and then finally forecasts measured by means of absolute percentage error (MAPE) given by equation (3):

$$MSE = \frac{1}{N} \cdot \sum_{i=1}^N (l_i - a_i)^2 \quad (2)$$

$$MAPE = \varepsilon = \frac{1}{N} \cdot \sum_{i=1}^N \left| \frac{l_i - a_i}{a_i} \right| \quad (3)$$

where N is the number of data samples, l_i is the target output (actual historical load), a_i is the artificial neural network output. Furthermore usually it is a recommendation in accordance to parsimony rule that networks with smaller number of input nodes and similar performance are better to be chosen to prevent over parametrization. The most important input series are loads from realized/past hours that usually have a strong correlation with the predicted load. There is a trade-off between accuracy of the model and computational burden when selecting the “look back window” of realized loads that is used for the ANN. Second important input is the day identifier. It is used to present the seasonal, weekly and daily cycles. It can be a binary input variable that for example indicates weekdays (0 for workdays, 1 for weekends) and an input variable ranging from 1 to 12 to represent the months of the year, January through December and 0 to 24 for hours of the day. Third important input parameter are weather variables, mainly temperature with others like wind, clouds and humidity/rainfall have smaller influence [16]. The list and definition of possible inputs and outputs is given in the table below (Table I).

Table I. List of possible ANN inputs and outputs

No.	Inputs	Description
1	Time of day (hour)	Time of the day identifier
2	Time of Week	Week day identifier
3	Time of Month	Month identifier
4	Loads of the day D-1	Loads of the previous day
5	Temperature of the day D-1	Temperatures of the previous day
6	Loads of day the D-6	Loads of the day D-6
7	Temperatures of the D+1*	Temperature forecasts
8	Rainfall of the D+1	Rainfall forecasts
9	Wind of the D+1	Wind forecast
*time D+1 is the day for which the loads are to be forecasted		

2.2. Artificial neural network structure

When fitting and ANN model it is important to define the artificial neural network structure. A feed forward networks is used. A total of 17 hidden neurons is used. Neural networks are made up of process units (neurons) that are bind in layers, whose number is set by the user and with different weights in the links. Inputs that are used are as mentioned realized load hour, week, month identifier, loads of for the past day and weather conditions inputs. The transfer function used for the hidden layer is sigmoid transfer function and for the output layer is linear transfer function (Figure 3).

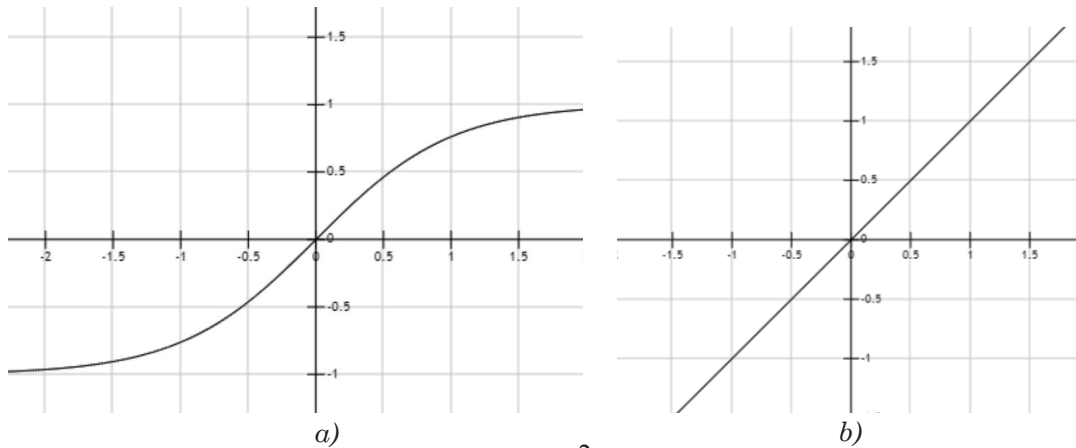


Figure 3. a) Tan-Sigmoid function $\frac{2}{1+e^{-2x}-1}$ b) Linear transfer function

2.3. Training method selection

The training algorithm determines the way the ANN adjusts the weights associated with different node connections. The algorithm that is used is Levenberg-Marquardt backpropagation and is used in combination with minimization of MSE. This method is quasi-Newton [17] method that is designed to approach second-order training without having to compute the Hessian matrix (\mathbf{H}) that can be approximated when the performance function has the form of a sum of squares (equation 4).

$$\mathbf{H} = \mathbf{J}^T \mathbf{J} \quad (4)$$

The gradient is then computed as:

$$\mathbf{g} = \mathbf{J}^T \mathbf{e} \quad (5)$$

where \mathbf{J} is the Jacobian matrix that contains first derivatives of the network errors with respect to weights and biases and \mathbf{e} is a vector of network errors. This algorithm uses the approximated Hessian matrix in the following cyclic update procedure:

$$\mathbf{x}_{k+1} = \mathbf{x}_k - [\mathbf{H} + \mu \mathbf{I}]^{-1} \mathbf{g} \quad (6)$$

where \mathbf{x}_k is the vector of current weights and biases, μ is the adaptive scalar (when small the method behaves like Newton's method and when big the algorithm acts as a gradient descent with a small step size. μ is decreased as long as the performance function of the network is improved (reduction in size) with each step and is increased only when a tentative step would increase the performance function. In this way, the performance function is always reduced at each iteration of the algorithm and ensures efficient training step. The Levenberg-Marquardt algorithm was the chosen, and is recommended for most problems because it appears to be the fastest method for training moderate-sized feedforward neural networks. For larger problems, however, Scale Conjugate Gradient algorithm is recommended as it uses gradient calculations which are more efficient than the Jacobian calculations.

3. CORRELATION STUDY RESULTS

Performing the preliminary study of the information available (inputs) is essential to the forecasting process, so that final forecasts are as close as possible to possible realizations. With that aim, so called "time-series" analysis is intended to determine what is the most relevant information contained in the input variables, in order to build the prediction model. The study can be performed using the analysis of correlations between specific data enabling the construction of correlation charts and offering the trend lines and the values of Pearson correlation coefficient r defined as shown in equation (7) that is a zero-dimensional index that ranges from -1 to 1, inclusive and reflects the existence of a linear relationship between two data sets.

$$r = \frac{\sum_{i=1}^n [(x_i - \bar{x}) \cdot (y_i - \bar{y})]}{\sqrt{\sum_{i=1}^n [(x_i - \bar{x})^2]} \cdot \sqrt{\sum_{i=1}^n [(y_i - \bar{y})^2]}} \quad (7)$$

where two sets are being compared, actual data $\{x_1, \dots, x_n\}$ and model output data $\{y_1, \dots, y_n\}$ with their mean values marked with \bar{x}, \bar{y} .

The Pearson coefficient was calculated for all variables (Table II) that could be used in the forecasting model for predicting consumption for the next day (D+1). The whole data set available (both the training and validation parts) for the MIBEL data for years 2012 and 2013.

The results show the best correlation was as expected for hour, consumption (D-1) and consumption (D-6). Based on this information, the correlation graphs

were made and are presented in the following figures (Figure 4, Figure 5 and Figure 6), confirming the relation between variables.

Table II. List of possible ANN inputs and outputs

	<i>Input data set</i>	<i>Pearson coefficient</i>
Time data	Hour	0.6540
	Day week (D-1)	-0.3120
	Day Week (D+1)	-0.1869
	Month (D-1)	-0.01293
	Month (D+1)	-0.1348
	Year (D+1)	-0.0519
Production data	Wind production (D-1)	0.0997
	Wind production (D-6)	0.1001
	Hydro production (D-1)	0.3889
	Hydro production (D-6)	0.5254
	Cogeneration + Solar (D-1)	0.4427
	Cogeneration + Solar (D-6)	0.5705
	Coal production (D-1)	0.1663
	Coal production (D-6)	0.3088
	Nuclear production (D-1)	0.0449
	Nuclear production (D-6)	0.0644
	Natural Gas production (D-1)	0.3929
	Natural Gas production (D-6)	0.5866
Weather data	Temperature (D-1)	0.1234
	Temperature (D+1)	0.0975
	Wind (D+1)	0.1735
	Direction (D+1)	0.0534
	Irradiance (D+1)	0.3620
	Rainfall (D+1)	0.0159
Price data	Price (D-1)	0.4111
	Price (D-6)	0.4614
Export data	Export (D-1)	0.1423
Consumption data	Hourly consumption (D-1)	0.7623
	Hourly consumption (D-6)	0.9122

The more precise statistical analysis could include larger amounts of data (e.g. 10 years of data) but most impactful values would remain the same with the weather forecast for the forecasting period always playing a significant role regardless of the statistical analysis results. The impact of the weather inputs in the artificial neural network will be shown in the following chapter that presents the results of the wholesome forecasting process.

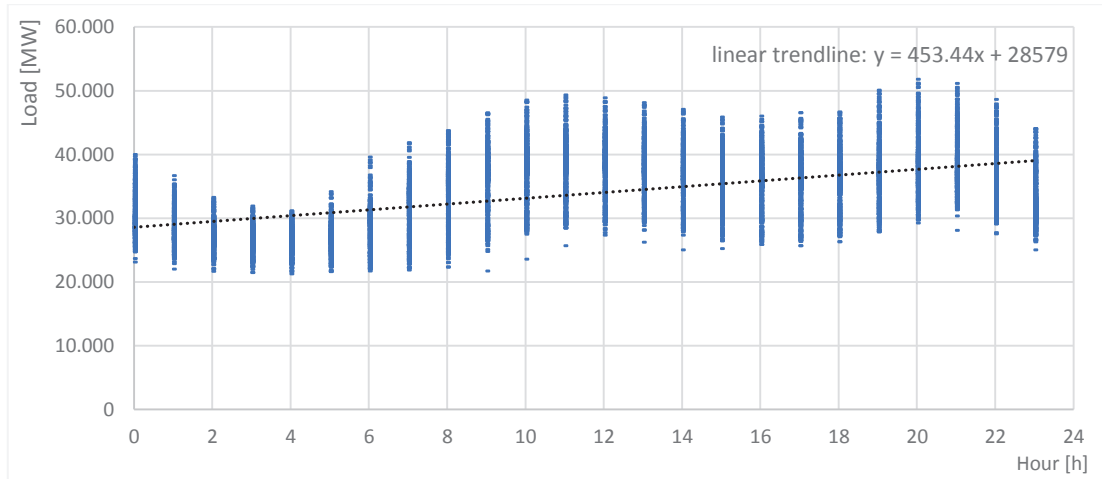


Figure 5. Hourly consumption (D+1) and hour identifier correlation coefficient

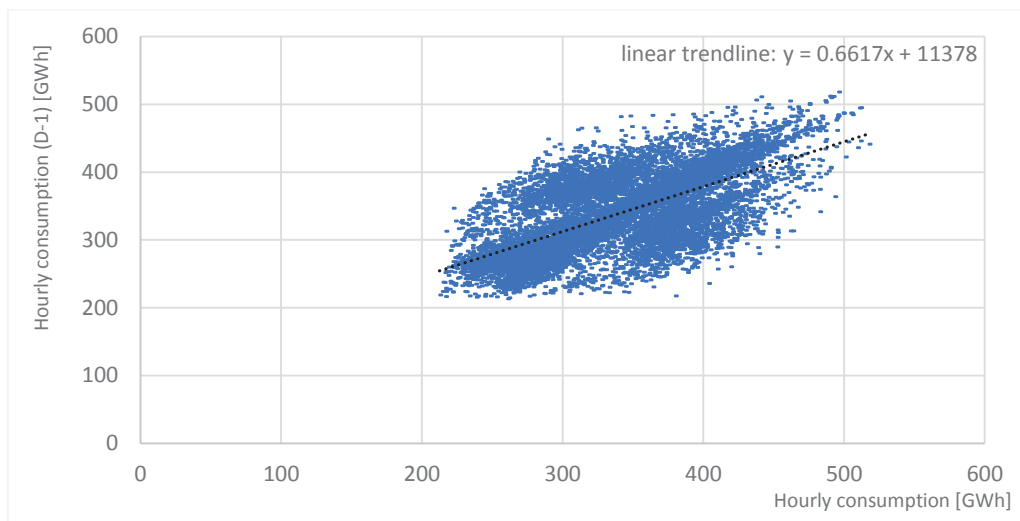


Figure 6. Hourly consumption/load (D+1) and hourly consumption/load (D-1) correlation coefficient (Pearson coefficient)

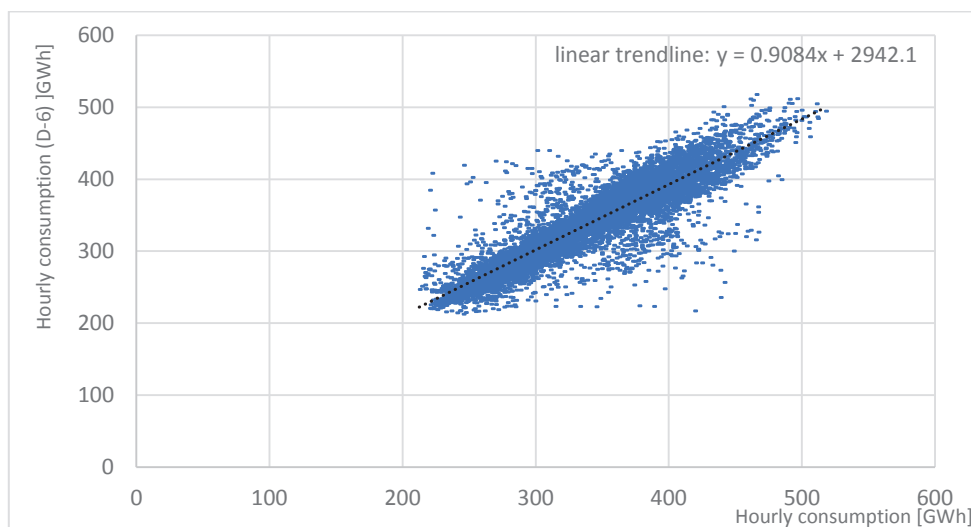


Figure 7. Hourly consumption/load (D+1) and hourly consumption/load (D-6) correlation coefficient (Pearson coefficient)

4. FORECASTING PROCESS AND RESULTS

The general forecasting process includes the creation of the artificial neural network model in the first phase and the usage of the model in the second phase to generate final outputs - next day load forecasts (Figure 4)

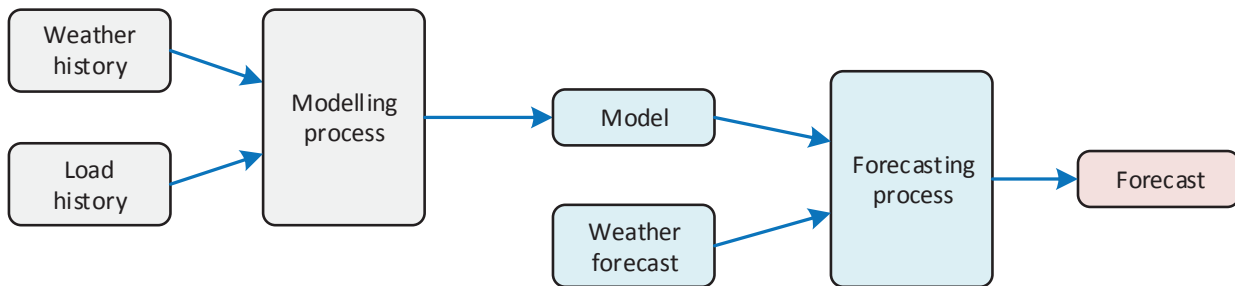


Figure 8. Load forecasting process diagram

With the purpose of obtaining best results different variations of input variables (Table I) can be considered. As was discussed some have more significant influence than the others and inclusion of some can improve the results. Furthermore pre-processing of the data was done. Loads and weather data for years 2012 and 2013 were obtained and prepared and as mentioned earlier part of it will be used for training part and part as a validation and testing set. Regarding the final implementation of neural network, it is necessary to pay attention to overfitting and the high computational effort. Overfitting happens when the error associated to the training set decreases in the same time as the error associated to the validation set increases. This means that the network over fits the training set which leads to a lack of generalization. Finally, weights are initiated randomly and backpropagation algorithm is used for the training and the network performance was tested on 3 different test sets.

From the used input data available 70% was used for training purposes (12264 samples), 15% (2628) or validation and 15% (2628) for testing of the developed artificial neural network. With these settings, the input vectors and target vectors are divided into three mentioned sets, 70% for training of the network where networks weights are adjusted, 15% to validate that the network is generalizing satisfactory and to stop training before overfitting (when generalization stops improving), 15% to test the network performance (this set has no effect on performance during training). The data set used in this paper is load data for years 2012 and 2013 of the MIBEL – Iberian power market. The neural network was trained using the neural network package in MATLAB 2013a [18].

The results (expressed as overall MAPE in Table III) of the artificial neural network design show the best performance of the test network 3. The validation performance of the network is shown on the Figure 9. It can be seen that after approximately 60 epochs the performance of the algorithm improves insignificantly and that it can be stopped.

Table III. Used variables/inputs for different test sets

No.	Inputs	MAPE (%)
Test 1	Time of day (hour)	2.67%
	Time of Week (day)	
	Time of Month (season)	
	Consumption (D-1)	
	Consumption (D-6)	
Test 2	Test 1 + Price (D-1)	2.68%
Test 3	Test 1 + Rainfall (D+1) + Temperature (D+1)	2.37%

The quality of neural fitting can be observed from the figure above (Figure 9). It can be seen that around 60 cycles/epochs are required for the algorithm to reduce the total amount of MSE to a point where no significant reductions are visible.

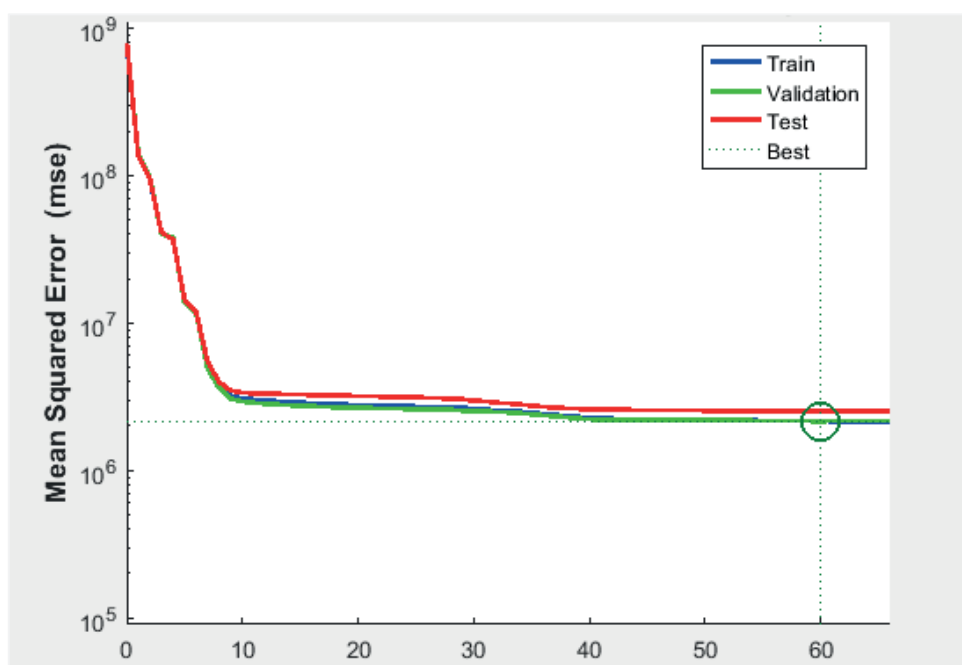


Figure 9. Ranges of error through neural network process epochs for different sets of data (training, validation, test)

The final forecast results are shown for test network 3 on the following figures ((Figure 10 and Figure 11).

As it can be seen from the comparison between historic data and output forecasts of the ANN for educational purposes it serves as a valid enough result since the curves align well with certain differences in forecasts of the peak values of some of the days (especially noticeable for Friday).

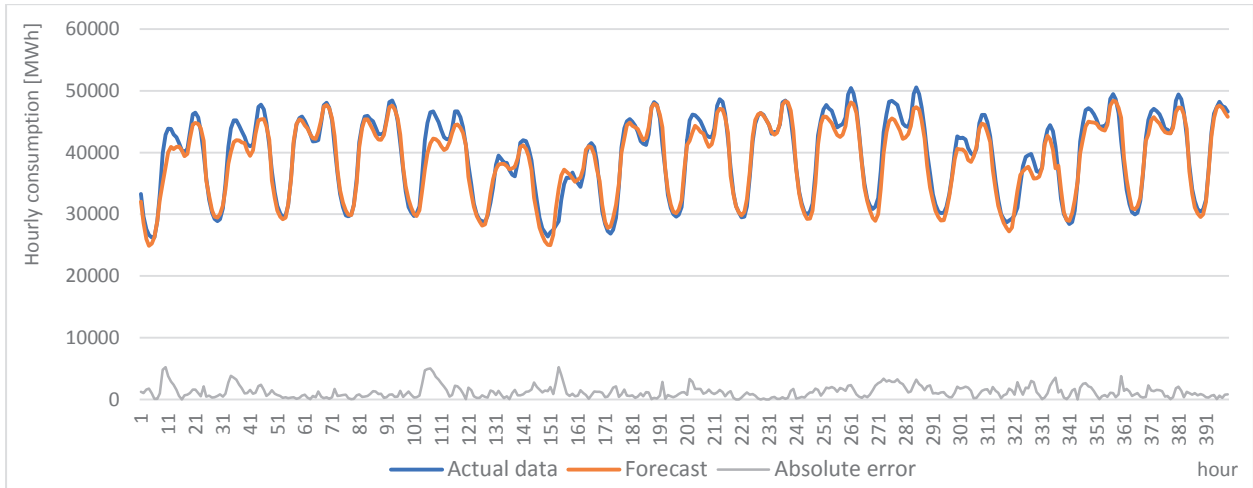


Figure 10. Comparison between actual data and ANN forecasts for a segment of test data set

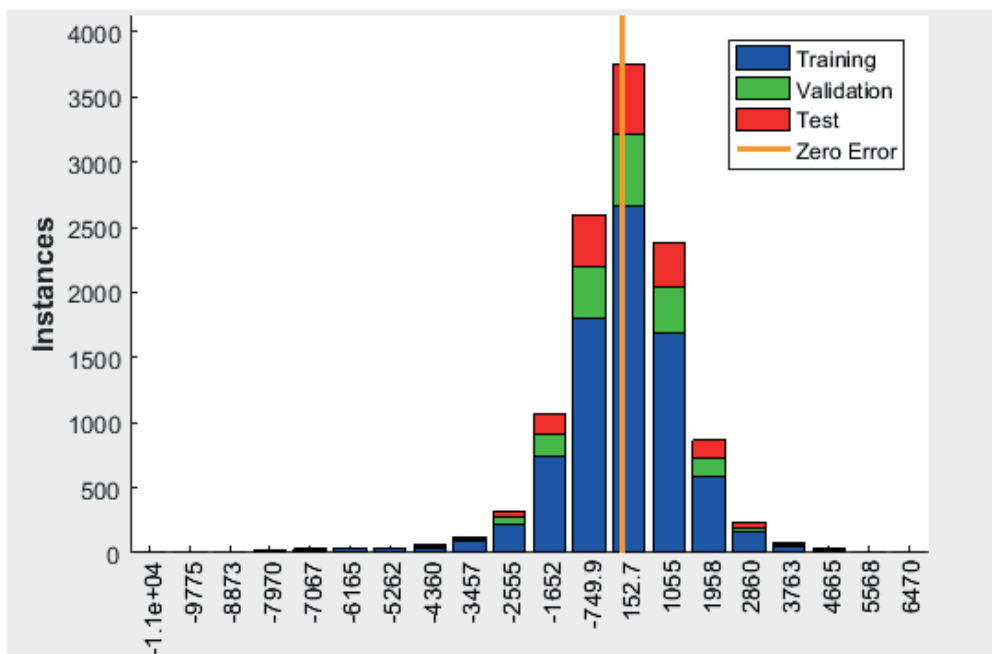


Figure 11. Error histogram showing error distribution between historic data and ANN outputs (Targets-Outputs)

5. CONCLUSIONS

In this paper, a feed-forward neural network model used for short term load forecasting is presented. This model makes use of past hours hourly consumptions, temperature, rainfall, day indices, weekend indices and month indices as the input variables. The MAPE of the load forecasted by this neural network was found to be

between 2% and 3% depending on the selection of input variables. The test-case data was for MIBEL - Iberian power market. The result presented in this paper suggests that the use of carefully selected input historic data can have a positive impact on results. For example, the structure of the neural network can be improved upon to take into account the effects of holidays or usage of more input samples (more years of past consumptions/load).

6. ACKNOWLEDGEMENT

The work of the authors is a part of the H2020 project CROSSBOW – CROSS BOrder management of variable renewable energies and storage units enabling a transnational Wholesale market (grant no.773430). This document has been produced with the financial assistance of the European Union. The contents of this document are the sole responsibility of authors and can under no circumstances be regarded as reflecting the position of the European Union. Additionally, this work has been supported in part by the Croatian Science Foundation under the project FENISG – Flexible Energy Nodes in Low Carbon Smart Network (grant no. IP-2013-11-7766).

7. REFERENCES

- [1] E. Ilseven and M. Gol, "Medium-Term Price Forecasting Considering Demand and Supply Uncertainty", *IEEE Transactions on Power Systems*, vol. PP, no. 99, pp. 1-1, 2017.
- [2] I. Kuzle, D. Bošnjak, H. Pandžić, "Comparison of Load Growth Prediction Methods in Distribution Network Planning", *The 20th International Conference and Exhibition on Electricity Distribution*, Prague, Check Republic, Paper 0765, pp. 1-4, 2009.
- [3] W. Taylor and P. E. McSharry, "Short-Term Load Forecasting Methods: An Evaluation Based on European Data", *IEEE Transactions on Power Systems*, vol. 22, no. 4, pp. 2213-2219, 2007.
- [4] S. Sargunaraj, D. Gupta, and S. Devi, "Short-Term Load Forecasting for Demand Side Management," *IEE Proceedings-Generation, Transmission and Distribution*, vol. 144, no. 1, pp. 68–74, 1997.
- [5] Z. Yu, "A Temperature Match Based Optimization Method for Daily Load Prediction Considering DLC Effect", *IEEE Transactions on Power Systems*, vol. 11, no. 2, pp. 728–733, 1996.

- [6] H. Steinherz, C. Pedreira, and R. Castro, "Neural Networks for Short- Term Load Forecasting: A Review and Evaluation", *IEEE Transactions on Power Systems*, vol. 16, no. 1, pp. 44–55, 2001.
- [7] C. Y. Tee, J. B. Cardell and G. W. Ellis, "Short-term load forecasting using artificial neural networks," *41st North American Power Symposium*, Starkville, MS, USA, pp. 1-6, 2009.
- [8] E. A. Feinberg, D. Genethliou, "Chapter 12 - Load forecasting", *Applied mathematics for power systems*, State University of New York, Stony Brook, pp 269-282, 2016.
- [9] D. Park, M. El-Sharkawi, R. Marks, L. Atlas, and M. Damborg, "Electric Load Forecasting Using an Artificial Neural Network," *IEEE Transactions on Power Systems*, vol. 6, no. 2, pp. 442–449, 1991.
- [10] D. Bunn and L. Sch, "Forecasting Loads and Prices in Competitive Power Markets", *Proceedings of the IEEE*, vol. 88, no. 2, pp. 163–169, 2000.
- [11] E. Banda and K. A. Folly, "Short Term Load Forecasting Using Artificial Neural Network", *2007 IEEE Lausanne Power Tech*, Lausanne, pp. 108-112, 2007.
- [12] I. Kuzle, T. Plavšić, S. Tešnjak, "Primjena neuronskih mreža za sekundarnu regulaciju napona i jalove snage", *Journal of Energy*, vol. 47, pp. 133-140, 1998.
- [13] N. Holjevac, T. Capuder, N. Zhang, I. Kuzle, C. Kang, "Corrective receding horizon scheduling of flexible distributed multi-energy microgrids", *Applied Energy*, Volume 207, pp. 176-194, 2017.
- [14] T. Senjyu, H. Takara, K. Uezato, and T. Funabashi, "One-Hour-Ahead Load Forecasting Using Neural Network", *IEEE Transactions on Power Systems*, vol. 17, no. 1, pp. 113–118, 2002.
- [15] N. Kandil, R. Wamkeue, M. Saad, and S. Georges, "An Efficient Approach for Short Term Load Forecasting Using Artificial Neural Networks", *International Journal of Electrical Power and Energy Systems*, vol. 28, no. 8, pp. 525–530, 2006.
- [16] A. Al-Shareef, E. Mohamed, and E. Al-Judaibi, "One Hour Ahead Load Forecasting Using Artificial Neural Network for the Western Area of Saudi Arabia", *International Journal of Electrical Systems Science and Engineering*, vol. 3, no. 1, pp. 35–40, 2008.
- [17] MATLAB and Simulink User's guide, R2013a, The MathWorks Inc., 2014.
- [18] <https://uk.mathworks.com>, available online, accessed 6th Dec 2017.

Journal
of Energy

AN
ENERGY